Advances in Planar Lipid Bilayers and Liposomes

Volume 10

EDITORIAL BOARD

Academic Press is an imprint of Elsevier
Linacre House, Jordan Hill, Oxford OX2 8DP, UK
32 Jamestown Road, London NW1 7BY, UK
30 Corporate Drive, Suite 400, Burlington, MA 01803, USA
525 B Street, Suite 1900, San Diego, California 92101-4495, USA

First edition 2009

Library of Congress Cataloging-in-Publication Data
A catalog record for this book is available from the Library of Congress

British Library Cataloguing-in-Publication Data
A catalogue record for this book is available from the British Library

ISBN: 978-0-12-374823-2
ISSN: 1554-4516

Printed and bound in USA

09 10 11 12 10 9 8 7 6 5 4 3 2 1

PREFACE

Volume 10 consists of several chapters devoted to the research on BLMs (bilayer lipid membranes) and also to liposomes. The BLMs started to be used in 1960s based on a historic perspective of the lipid bilayer concept and its experimental realization. Many of the contributing authors collaborated either directly in the past with late Prof. H. Ti Tien, the funding editor of this book series or learnt many leading ideas about BLMs from his many scientific publications and book chapters over the last four decades. The untimely 5th anniversary of his passing away was commemorated on May 30, 2009 by his colleagues and friends. Prof. H. Ti Tien, used in his experiments, also supported BLMs formed on metallic wire (s-BLMs) or on agar gel (sb-BLMs) and he predicted that this type of supported BLM is very suitable for molecular electronic devices development, especially for potential biosensors with a broad range of applications.

It belongs to the history when in 1961 at the Symposium on the Plasma Membrane, the group of researchers (Rudin, Mueller, Tien, and Wescott) reported the reconstitution of a bimolecular lipid membrane *in vitro*. At that time the scientific community was not very optimistic about it. One of the reasons was the fact that the group of four above-mentioned scientists started their presentation with a description of soap bubbles well known to children, followed by "black holes" in soap films, . . . ending with an invisible "black" lipid membrane, made from lipid extracts of cow's brains. The reconstituted structure (6–9 nm thick) was created in the same fashion like a cell membrane separating two aqueous solutions. As one of the members of the amused audience remarked, ". . . the report sounded like . . . cooking in the kitchen, rather than a scientific experiment!" We have to remember this story from 1961, as the four above-mentioned researchers published their first report a year later. In reaction to their publication, Bangham, the major researcher on liposomes, wrote in a 1996-article entitled "Surrogate cells or Trojan horses": ". . . a preprint of a paper was lent to me by Richard Keynes, then Head of the Department of Physiology (Cambridge), and my boss. This paper was a bombshell . . . . They (Rudin, Mueller, Tien, and Wescott) described methods for preparing a membrane . . . not too dissimilar to that of a node of Ranvier . . . . The physiologists went mad over the model, referred to as a 'BLM', an acronym for Bilayer or by some for Black Lipid Membrane. They were as irresistible to play with as soap bubbles."

Today, after nearly five decades, BLMs (bilayer lipid membranes or black lipid membranes), along with liposomes, have become very important experimental models in certain areas of membrane biophysics and cell biology and in biotechnology. The lipid bilayer, existing in all cell membranes, is most unique in that it serves not only as a physical barrier among cells, but functions as a two-dimensional matrix for all sorts of reactions. Furthermore, the lipid bilayer, after suitable modification, acts as a conduit for ion transport, as a place for antigen–antibody binding, as a bipolar electrode for redox reactions, and as a reactor for energy conversion (e.g., light energy to electric energy to

chemical energy). A modified lipid bilayer is used for signal transduction (i.e., sensing), and many other functions as well. All these countless applications require the ultra thin lipid bilayer of 5 nm thickness.

Nowadays, black lipid membranes (BLMs or planar lipid bilayers) have been used in a number of applications ranging from the core of membrane biophysics studies, including photosynthesis, practical AIDS research, and "microchips" study. In reactions involving light, BLMs have provided valuable insights to the conversion of solar energy via water photolysis, and to photobiology comprising apoptosis and photodynamic therapy. These topics are very much in line with the latest trends in energy studies, conservation, and transformation worldwide as well as with the latest exciting biomedical applications. Also, some special features of supported bilayer lipid membranes (s-BLMs) predestine them for the biosensors development. This volume reviews many studies performed by several scientific groups based on recent research using the BLMs as models for several types of biomembranes.

The present volume of *Advances* series on planar lipid membranes and liposomes continues to include invited chapters on a broad range of topics, ranging from theoretical research to specific studies and experimental methods, but also refers to practical applications in many areas. The author(s) of each chapter present the results of his/her laboratory. We continue in our endeavor to focusing with this Serial on newcomers in this interdisciplinary field, but we try to attract experienced scientists as well. All chapters in this volume have one feature in common: further exploring theoretically and experimentally the planar lipid bilayer systems and spherical liposomes. We are thankful to all contributor(s) for their expert knowledge in BLM research area, for the shared information about their work and also for their effort in preparation of this Volume 10. Their willingness to write these chapters in memory of the founding editor of this Serial—Prof. Hsin Ti Tien—is very much appreciated by the whole scientific community.

As in many previous volumes of this Serial, we intend to invite again some of those colleagues who already contributed to one of our previous volumes. Their work and continuous progress in this exciting field is a convincing proof about the importance of this research area and its practical applications worldwide.

We, the editors and the editorial board of this *Advances* series, would like to express our gratitude to all contributing authors for their effort spent on preparing their respective chapter and for sharing with us, the worldwide scientific community and their latest results in this volume. We also appreciate the continuous support and help of Dr. Kostas Marinakis, Publisher of Chemistry and Chemical Engineering Department in Elsevier together with his coworkers, particularly with Dr. Lyndsey Dixney and in Elsevier's Chennai Office in India with Dr. Gayathri Venkatasamy, who very effectively helped us, the editors, in many important stages of preparation of this latest Volume 10 of our Serial on "*Advances in Planar Lipid Bilayer and Liposomes*." We will also continue in the future with our effort to keep these *Advances* series alive. This is the best way to pay tribute to the founding editor Prof. Hsin Ti Tien and to commemorate with our research and its ongoing publication his great legacy.

Angelica Leitmannova Liu
Aleš Iglič

Contributors

Ingolf Bernhardt
Laboratory of Biophysics, Saarland University, P.O. Box 151150, 66041 Saarbruecken, Germany

G.J.C.G.M. Bosman
Department of Biochemistry, Radboud University Medical Center Nijmegen, P.O. Box 9101, 6500 HB Nijmegen, The Netherlands

David D. Busath
Department of Physiology and Developmental Biology, Brigham Young University, Provo, UT 84602, USA

J. Cluitmans
Department of Biochemistry, Radboud University Medical Center Nijmegen, P.O. Box 9101, 6500 HB Nijmegen, The Netherlands

Damjana Drobne
Department of Biology, Biotechnical Faculty, University of Ljubljana, SI-1000 Ljubljana, Slovenia

J. Clive Ellory
Department of Physiology, Anatomy and Genetics, University of Oxford, Oxford OX1 3PT, United Kingdom

W.T. Góźdź
Institute of Physical Chemistry, Polish Academy of Sciences, Kasprzaka 44/52, 01-224 Warsaw, Poland

John S. Gibson
Department of Veterinary Medicine, University of Cambridge, Cambridge CB3 0ES, United Kingdom

N. Gov
Department of Chemical Physics, The Weizmann Institute of Science, P.O. Box 26, Rehovot 76100, Israel

Aleš Iglič
Laboratory of Biophysics, Faculty of Electrical Engineering, University of Ljubljana, Tržaška 25, SI-1000 Ljubljana, Slovenia

Yasunaga Kameyama
Department of Oral Biochemistry, Asahi University School of Dentistry, 1851 Hozumi, Mizuho, Gifu 501-0296, Japan

Veronika Kralj-Iglič
Laboratory of Clinical Biophysics, Institute of Biophysics, Faculty of Medicine, University of Ljubljana, Vrazov trg 2, SI-1000 Ljubljana, Slovenia

Maruša Lokar
Laboratory of Biophysics, Faculty of Electrical Engineering, University of Ljubljana, Tržaška 25, SI-1000 Ljubljana, Slovenia

Šárka Perutková
Laboratory of Biophysics, Faculty of Electrical Engineering, University of Ljubljana, Tržaška 25, SI-1000 Ljubljana, Slovenia

P. Sens
Physico-Chimie Théorique (CNRS UMR 7083), ESPCI, 10 rue Vauquelin, 75231 Paris Cedex 05, France

Peter Veranič
Institute of Cell Biology, Faculty of Medicine, University of Ljubljana, Lipičeva 2, SI-1000 Ljubljana, Slovenia

Robert J. Wilkins
Department of Physiology, Anatomy and Genetics, University of Oxford, Oxford OX1 3PT, United Kingdom

CHAPTER ONE

Ion Permeability of Membranes: From Lipid Bilayers to Biological Membranes

Ingolf Bernhardt,[1,*] J. Clive Ellory,[2] John S. Gibson,[3] *and* Robert J. Wilkins[2]

Contents

Abstract

Although cells were first observed as early as in the 17th century, it is only over the last 100 years or so that our understanding of the permeability barrier imposed by the plasma membrane of cells started to emerge. The last

* Corresponding author. Tel.: +49 681 3026689; Fax: +49 681 3026690;
E-mail address: i.bernhardt@mx.uni-saarland.de

[1] Laboratory of Biophysics, Saarland University, P.O. Box 151150, 66041 Saarbruecken, Germany
[2] Department of Physiology, Anatomy and Genetics, University of Oxford, Oxford OX1 3PT, United Kingdom
[3] Department of Veterinary Medicine, University of Cambridge, Cambridge CB3 0ES, United Kingdom

Advances in Planar Lipid Bilayers and Liposomes, Volume 10
ISSN 1554-4516, DOI: 10.1016/S1554-4516(09)10001-7

50 years, in particular, has seen a marked development in our knowledge of the characteristics of this barrier. The membrane itself comprises in the most part a bilayer of phospholipids, asymmetrically distributed, together with cholesterol and intrinsic and extrinsic proteins. Simple diffusion through the lipid phase can occur for lipid soluble moieties. In other cases, intrinsic membrane proteins provide pathways for solutes and water. Three types of pathways are described: channels, carriers, and pumps. What is known about flux through these proteins, together with their structure and function, is discussed—illustrated with reference to particularly significant pathways. The important part played by the red blood cell as a paradigm for membrane transport is explained. Existing gaps in our understanding of transport across membranes are emphasized. For example, how pumps like the quintessential membrane, the Na^+–K^+ ATPase, operate remains unknown. In addition, the nature of the residual (or "leak") permeability, which remains when all such pathways are inhibited, is unclear. The residual permeability of biological membranes appears to be about 2 orders of magnitude greater than that of artificial lipid bilayers. An important caveat here is the existence of unknown pathways yet to be described. In this context, a novel permeability with characteristics of $K^+(Na^+)/H^+$ exchange is described which becomes manifest across the red blood cell membrane when cells are suspended in low ionic strength solution. Future discoveries will add to our understanding of membrane permeability. It is likely that the red blood cell will play an important part in this new chapter.

1. Introduction

Our knowledge of the structure of the cell membrane, as well as of solute transport mechanisms, has improved markedly over the last 100 years. Accordingly, we present first a historical overview concerning the development of this understanding. We then address the mechanism of the water transport, followed by that of ion transport through lipid bilayers as well as biological membranes. The four principal ion transport mechanisms of biological membranes (three protein-mediated and the residual transport) will be discussed in more detail. Finally, as an example of a biological membrane, the significant ion transport pathways of the red blood cell membrane are summarized, as a transport paradigm, with particular focus on the residual ("leak") membrane permeability for ions.

2. Historical Overview

The terms "cells, membranes, and membrane transport" have been in use for sometime but our understanding of them has changed markedly, especially during the last 100 years or so. The term "cells" was first used by

the English natural scientist Robert Hooke in 1665 upon observing the cell-like structure of cork slices under a microscope [1]. "Membrane," earlier plasmalemma, was first employed by the Swiss professor of botany Carl Wilhelm von Nägeli in 1855 to describe the boundary of a cell [2]. He investigated osmosis in plant cells. We now know that membranes also surround intracellular organelles, as well as the cell perimeter. Plant cells are distinct from animal ones in possessing an additional cell wall outside their cell membrane, providing them with rigidity and the ability to withstand pressure. The work of Nägeli as well as that of Brücke, Pfeffer, and Ostwald demonstrated that the cell membrane is permeable for water and small uncharged substances (e.g., [3]). It was Overton, however, who finally demonstrated the lipoid character of animal and plant cell membranes [4, 5], in publications still pertinent to this day. He discovered that the toxicity of organic compounds depends on their lipid solubility. An important finding was that the lipid-water distribution of different substances is crucial for their membrane passage. He assumed, however, that water filled areas exist in the cell membrane acting as transport pores.

At the end of the 19th century, knowledge of the cell membrane still remained vague. First, Gorter and Grendel [6] postulated that the cell membrane consists of a lipid double layer (bilayer), in which the hydrophilic lipid head groups are directed outwards to the water phases (of the intra- and extracellular media) and the hydrophobic fatty acids are directed inwards to the membrane center. Later, it became evident that proteins are located on the outer and inner surfaces of the cell membrane [7]. Polysaccharides on the external surface of the membrane were first shown in the membrane model of Robertson [8].

Our current understanding of a biological membrane is based on the fluid-mosaic model of Singer and Nicolson [9]. This model postulates that the membrane lipids are in the fluid-crystalline state and membrane proteins are embedded in the membrane (intrinsic proteins) or attached to the inner and outer surface like islands (peripheral proteins). This basic assumption was elaborated by subsequent observations. We know now that: (i) not all membrane lipids are in the fluid-crystalline state but some are exist in the crystalline (gel) state (the phase transition temperature of these lipids is higher than the surrounding temperature of the membrane); (ii) lipids, as well as proteins, are asymmetrically distributed around the circumference of the membrane and also between outer and inner faces [10]; and (iii) lipids do not only compose a bilayer structure in the membrane but can also form nonbilayer structures (polymorphism of the phospholipids; see, e.g., Ref. [11]). Neither lipids nor proteins are static, rather they can potentially move in both dimensions of the membrane.

By the end of the 19th century, it was already known that Na^+ and K^+ are nonequally (asymmetrically) distributed across the cell membrane. Based on chemical analysis of human red blood cells, it was demonstrated that the

intracellular Na^+ concentration is considerably lower than the extracellular (plasma) Na^+ concentration, whereas for K^+ the distribution is *vice versa* [12]. At that time it was possible to explain the existence of such gradients for Na^+ and K^+ by assuming the existence of a "dense" cell membrane, meaning that the membrane is impermeable for either ion (e.g., [13]). A very important finding concerning the membrane permeability for ions was the fact that Cl^- can pass across the red blood cell membrane relatively fast [14]. Later, it was shown that a muscle cell membrane is, in fact, permeable for Na^+ and K^+ [15]. It became evident that a cell membrane is generally permeable for ions. These findings were developed in 1941 by Dean into the postulate that an asymmetric distribution of Na^+ and K^+ can be realized only on the basis of an active ion transport or ion pump [16]. This hypothesis was represented by Krogh [17]. It took until 1957, however, for Skou to isolate the enzyme responsible from crab nerves, the Na^+, K^+-ATPase [18]. That this was the enzymatic manifestation of the Na^+/K^+ pump was not accepted unequivocally until the 1970s. Work by Sachs, in particular, characterized the ion fluxes mediated by the Na^+/K^+ pump [19].

Another milestone in the history of our knowledge about the permeability of a biological membrane was the work of Hodgkin and Huxley [20] who described quantitatively the action potential of excitable cells with its underlying membrane permeability changes. The original idea was based on the assumption that the increased ion transport was carried out by ion carriers, a feature now ascribed to ion channels [21]. The existence of ion channels in biological membranes was under discussion for a relatively long time (up to approximately 1976). The research of Hille [22] and Armstrong [23] contributed considerably to our understanding of the mechanism of an ion transport across a channel. We are now aware of the crucial part played by such ion channels in ion transport through biological membranes. Characteristic features of channels include their gating mechanism and the selectivity filter. Latterly, it has become commonplace to study single ion channels in detail by applying the patch-clamp technique of Neher and Sakmann [24].

3. The Water Permeability of a Bilayer Lipid Membrane

Simple planar lipid bilayer membranes (i.e., artificial bilayers) are permeable for water [25]. The water molecules partition into the lipid phase and move through the membrane via simple diffusion. The diffusion permeability for water (P_d) depends on the temperature and the lipid composition of the membrane. The activation energy is normally in the range of 10–20 kcal/mol [26, 27]. If an osmotic gradient is applied to the

lipid bilayer, the permeability under such conditions (P_f) is not significantly different from P_d [28]. These observations are consistent with water crossing these artificial membranes by simple diffusion.

4. The Water Permeability of a Biological Membrane

Water permeability across biological membranes is completely different from the situation pertaining to an artificial lipid bilayer. By 1957, it was already apparent that the osmotic water permeability of red blood cells is larger than the diffusion water permeability [29]. The activation energy of the water transport across biological membranes is low, at values <5 kcal/mol, which fits well with values for water diffusion in aqueous solutions.

Using tritiated water (^3H_2O), it was possible to demonstrate that $t_{1/2}$ for diffusional exchange across the membrane of red blood cells is about 4 ms. This corresponds to a value of P_d of about 4×10^{-3} cm/s [30]. On the other hand, using light scattering to detect cell volume changes, a higher value for P_f of about 2.5×10^{-2} cm/s was found when an osmotic gradient was applied [31]. In addition, the osmotic water permeability of the membrane can be reduced in the presence of mercury compounds (e.g., *p*-chloromercuribenzene sulfonate, PCMBS), which reduces the ratio of P_f:P_d to 1 [32]. These findings finally led to the assumption that one or more specific water transport proteins (water channels) must exist in biological membranes.

The identity of these water channels was established in the late 1980s. Gheorghe Benga first identified a membrane protein in the red blood cell membrane responsible for water transport [33]. The molecular, three-dimensional structure and further detailed structural analysis, however, was carried out by Agre and his coworkers [34–36]. In 1988, a novel 28 kDa membrane protein with channel-like properties, termed aquaporin-1 (AQP-1), was identified in the red blood cell membrane [37, 38] and its conformation established following expression in *Xenopus laevis* oocytes [39]. Only oocytes expressing AQP1 swelled when placed in hypotonic buffer solution, consistent with its putative role as a water channel. The structure of the protein with six integral membrane domains is reminiscent of an hour-glass (hour-glass model). The functional water channel consists of a tetramer. Two positive charges are located closely together at the narrow area of the protein in the middle of the membrane, preventing the passage of protons or H_3O^+. The narrowest area has a diameter of about 0.3 nm.

To date, 11 isoforms of aquaporins have been identified in mammalian cells, with about 150 isoforms estimated to exist across living organisms (mammals, amphibians, plants, and bacteria). Generally, the aquaporins are divided in two groups: one comprises channels, which transport exclusively

water; the other comprises channels, which in addition to water, are able to transport small uncharged molecules like glycerol and urea. Other permeant molecules are postulated. For example, AQP-1 may be permeable to CO_2 and that AQP-6 to anions [40, 41]. The relationship between structure and permeability properties of the aquaporins awaits further elucidation.

Water channels clearly play an important role in cellular regulatory processes. For example, in the human kidney about 180 l/day of primary filtrate is concentrated to about 1 l/day by reabsorption of water across the nephron epithelium via the aquaporins. Interestingly, however, the role of water channels in the membrane of red blood cells, where they were first discovered, remains uncertain. The rate of water to be transported via water channels and via the lipid phase in the red blood cell membrane is controversial, from with measurements ranging from 50% using NMR [42] up to 90% [43].

5. The Permeability of a Bilayer Lipid Membrane for Solutes

Although our current understanding of the permeability of artificial lipid bilayers is not markedly different from that of Overton, the situation is far more complex when the permeability of a biological membrane is considered. Artificial lipid bilayers are cell membrane-like structures but do not contain proteins. As shown in many textbooks, the permeability of a lipid membrane for a large variety of substances or ions correlates with the distribution coefficient of these substances between the lipid- and water-phase. These results are consistent with the findings of Overton. The permeability mechanism is called ''solubility-diffusion mechanism.'' The rate limiting step is the diffusion through the hydrophobic region of the membrane. Problems do remain, however. First, to explain their permeability to cations, movement through transient water filled transient pores is postulated. A second problem relates to the permeability for protons. On the basis of the measured proton permeability coefficients, two general possibilities are proposed. One is to assume that one proton is surrounded by four water molecules and permeates the lipid bilayer as $H_9O_4^+$, according to the ''solubility-diffusion mechanism.'' Alternatively, protons are envisaged as hopping along hydrogen-bonded chains of water through water filled transient pores. The permeability coefficients of different substances through artificial lipid bilayers cover a relatively large range, with the highest values for water (10^{-2} cm/s), medium values for urea and glycerin (10^{-5}–10^{-6} cm/s) or tryptophane and glucose (10^{-7}–10^{-8} cm/s), and the lowest for ions, for example, Cl^- (10^{-10} cm/s), K^+ (10^{-11} cm/s), and Na^+ (10^{-12} cm/s) (for more detailed information, see, e.g., Ref. [44]).

6. Mechanisms of Ion Transport through Biological Membranes

Ion transport through biological membranes can be divided into four principal mechanisms (see Sections 6.1–6.4 and Fig. 1). Various techniques are available to determine transport rates. These include radioactive tracers and fluorescence-labeled dyes (flux measurements). Alternatively, electrophysiological methodology including the patch-clamp is applicable to electrogenic transport. In a simple analogy, one can visualize the energetics of different transport mechanisms as follows: pump—as a boat lift (an external active drive is essential); carrier—as a sluice (water flows passively downhill in the sluice resulting in a lifting of the water level and the boat); or channel—waterfall (can occur only downhill).

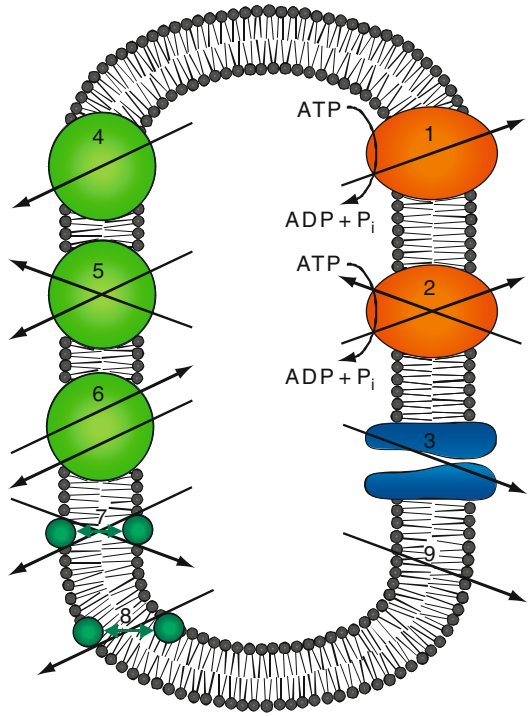

Figure 1 Schematic illustration of the mechanisms of the ion transport through biological membranes. 1, 2: Active transport; 3: transport through channels; 4–8: carrier-mediated transport (4: uniport realized by an integral membrane protein, 5: symport realized by an integral membrane protein, 6: antiport realized by an integral membrane protein, 7: ionophore acting as antiporter, 8: ionophore-mediated uniport); 9: leak transport; for detailed explanations see Sections 6.1–6.4.

6.1. Active Transport (ATPases, Ion Pumps)

Active transport (or more correctly primary active transport) is characterized by one or more ions moving against the electrochemical potential(s) through direct coupling to metabolic energy (ATP). The enzymes which hydrolyze ATP to harness energy for solute movement are termed ATPases. They often need cosubstrates, for example, Na^+ and K^+ for the Na^+, K^+-ATPase, Ca^{2+}, and H^+ for the Ca^{2+}-ATPase. In functional terminology, they are called pumps, for example, Na^+/K^+ pump or Ca^{2+} pump. During transport, there is a conformational change of the pump protein, driven by energy released from ATP hydrolysis. There are four different types in biological membranes: P-type ATPases, V-type ATPases, F-type ATPases, and ABC transporters (explained in the following paragraphs (a)–(d)).

(a) P-type ATPases (P stands for phosphorylation) have a phosphorylated aspartate residue as an intermediate product during the reaction cycle. The prototype ATPase first discovered was the P-type Na^+, K^+-ATPase. This Na^+/K^+ pump is able to maintain a 10-fold gradient for Na^+ and K^+ across the biological membrane. For each molecule of ATP hydrolyzed, three Na^+ are transported out of the cell and two K^+ inwards. Ion transport mediated by the Na^+/K^+ pump is completely and specifically inhibited by ouabain (g-strophanthin). In fact, ouabain represents one of the few truly specific transport inhibitors—an important caveat when using other reagents to define the transport characteristics of biological membranes. Nearly all cells contain a Na^+/K^+ pump in their membrane. An exception is the red blood cells of carnivore (including cats and dogs), which although lacking Na^+/K^+ pump activity are able nevertheless to realize an asymmetric distribution of Na^+ and K^+ across the membrane. In this case, active transport of Ca^{2+} is used. Outward transport of Ca^{2+} via the plasma membrane Ca^{2+} pump is followed by exchange of extracellular Ca^{2+} for intracellular Na^+ by the action of the Na^+/Ca^{2+} antiporter, thus lowering intracellular Na^+. Intracellular K^+ is then elevated by subsequent activity of the Na^+–K^+–$2Cl^-$ symporter (see the following section for carrier-mediated transport). The Na^+/Ca^{2+} antiporter of cat and dog red blood cells is absent in red blood cells of many other species including humans. Many cell membranes, however, contain a Ca^{2+}-ATPase (Ca^{2+} pump), which produces a 10,000-fold Ca^{2+} gradient over the membrane (intracellular Ca^{2+} concentration ~ 100 nM, extracellular Ca^{2+} concentration ~ 1 mM). Other important ATPases (or ion pumps) are the H^+, K^+-ATPase (H^+/K^+ pump), important in secretion of gastric acid, which can even realize a 10^6-fold H^+ gradient, and the K^+-ATPase (K^+ pump) found in bacteria.

(b) V-type ATPases (V stands for vacuole) transport exclusively H^+ and are therefore termed H^+-ATPases. They are responsible for the acidification of some intracellular compartments. They occur in vacuoles of fungi, yeast, and higher plants but are also found in the secretory vesicles of animal cells.

The V-type ATPase is much larger than the P-type ATPase and consists of many subunits. It is neither phosphorylated nor dephosphorylated. V-type ATPases contain an integral membrane domain (V_0), which acts as an H^+ channel, and a peripheral domain (V_1) with the ATP-binding site. The mechanism of the coupling of ATP hydrolysis and H^+ transport is still unknown. Through analysis of structure and transport function, it is apparent that the V-type ATPase is closely related to the F-type ATPase.

(c) F-type ATPases (F stands for factors participating in energy coupling): Like the V-type ATPases, F-type ATPases catalyze ATP hydrolysis and the transport of H^+ through the membrane against its electrochemical gradient. However, in contrast to the V-type ATPases, the F-type ATPases are able to synthesize ATP from ADP and inorganic phosphate by using dissipative H^+ movement down its electrochemical gradient (inverse reaction). In this mode, they are called ATP-synthases. F-type ATPases contain an integral membrane domain (F_0) acting as H^+ channel and a peripheral domain (F_1), which is of importance for both ATP-synthase and ATPase activity. This type of ATPases plays a central role in energy conserving reactions in mitochondria, bacteria, and chloroplasts.

(d) ABC transporter (ABC stands for *A*TP-*b*inding *c*assette) also uses a conformational change of the transport protein induced by ATP hydrolysis to transport a large variety of substances actively across the cell membrane. ABC transporters comprise a large class of transporters containing, to date, more than 100 ABC transporters, divided into seven families. Their structure consists of two transmembrane domains (6–11 α-helices) and two cytoplasmatic ATP-binding domains. Typical functions of different ABC transporters include, for example, cholesterol and phospholipid transport out of eukaryotic cells, or the uptake of nutrients (amino acids, saccharides, peptides, and vitamins) into prokaryotic cells. ABC transporters were first found in humans as underlying the multidrug-resistance phenomenon. Some proteins functioning as ion channels also belong to the ABC transporters (one family out of the seven). These channels are regulated by ATP but do not carry out active transport (see also below for ion transport via channels). An important representative is the cystic fibrosis transmembrane conductance regulator (CFTR) protein. It is an epithelial Cl^- channel, which is mutated and dysfunctional in cystic fibrosis patients, resulting in abnormalities of salt and water transport in several diverse tissues.

For different ATPases, the three-dimensional structure is known at the level of atomic resolution (for the Ca^{2+}-ATPase, see, e.g., Ref. [45]). Computer simulations of Ca^{2+} transport, showing the dynamic movement of the whole ATPase, ATP binding and hydrolysis, exist. The first three-dimensional structure of the Na^+, K^+-ATPase was based on an 11 Å resolution [46]. Recently, the crystal structure has been analyzed with 3.5 Å resolution [47]. We are still ignorant, however, of the exact mechanism by which it is able to translocate its transported species.

6.2. Carrier-Mediated Transport

Proteins acting as carriers mediate the transport of ions or other substrates by making use of a periodic repeated conformational change of the protein. By this means, it becomes possible for the transported substrate to gain access to its binding site at both the inner and outer membrane surface. An intermediate folded conformational state is sometimes seen. In this transitional stage, the bound substrate is denied access to the aqueous solutions on either side of the membrane. However, an open channel-like pore structure is never seen. Ionophore-mediated transport (e.g., valinomycin) occurs in a different way. Here, the ionophores acting as carriers, shuttling across the membrane from one side to the other. In contrast, integral membrane proteins are too big to move through the membrane. They have a more-or-less constant topology. The transport rate of an ion or a substance based on a carrier mechanism is significantly increased in comparison to the transport without such a mechanism. However, it is much less than the transport rate of ions through channels. A carrier is able to transport one or few ions (molecules) per one conformation cycle. In contrast, a channel once open can mediate transport of several thousand ions. Carrier-mediated transport can be described with Michaelis–Menten kinetics, being saturable and with defined affinity. In general, we can divide a carrier-mediated transport into two different mechanisms: uniport and cotransport. A uniport mediates transport of a single ion or other substrate. As such, transport can only occur ''downhill,'' that is, along the concentration gradient of the transported substance (or along its electrochemical gradient if it is a charged species). This is termed facilitated diffusion. This type of transport is exemplified by the glucose transporter GLUT1, which exists in the membranes of a large variety of cells (see, e.g., Ref. [48]). It is an integral membrane protein consisting of 12 membrane domains (transmembrane α-helices). When carriers mediate cotransport of several species, there is a stoichiometric coupling of the transported entities by the integral membrane protein. Cotransporters can be divided into symporters and antiporters. Terminology may vary, however. In some cases, the term cotransport is used as synonym for symport, while an antiport function may be called exchange or countertransport. A symporter binds the ions and/or substances (two or more substrates) and transports them together in one step in the same direction through the membrane. Movement of one substrate down its chemical or, in most cases, its electrochemical gradient is used to power the ''uphill'' transport of the cotransported substrate(s), that is, against their chemical or electrochemical gradients. An example is the glucose-Na^+-symporter, present in the membrane of epithelial cell, and the lactose-permease, a lactose-H^+-symporter, in the membrane of bacteria. The crystalline (three-dimensional) structure of the latter has been elucidated in 2003 [49]. Our first ideas about the molecular mechanism of

carrier-mediated transport originate from this structure. An antiporter mediates exchange of an ion (or substance) for another ion (or substance) transporting them in opposite directions. Like the symporter, the antiporter can carry out its transport process in one step. More commonly, antiporters show ping-pong kinetics, that is, after the binding of one substrate, it is transported across the membrane and only after this can the cosubstrate then bind for it to be transported in the opposite direction. Such a mechanism cannot bring about net transport as the carrier protein is unable to perform a conformational change in the absence of one of the substrates. However, like symporters, antiporters can mediate "uphill" transport, that is, against the chemical or electrochemical cosubstrate gradient.

Distinct from pumps, the "uphill" transport carried out by cotransporters is not directly coupled to metabolic energy. The only requirement is the existence of a "downhill" gradient of a cosubstrate to be energetically coupled to. This mechanism is sometimes called "secondary active transport." Examples of antiporters include the adenine-nucleotide-translocase (ADP/ATP antiporter), which catalyzes a 1:1 exchange of ADP for ATP across the inner mitochondrial membrane. The Na^+/Ca^{2+}-antiporter, by which the Na^+ gradient is used to power an exchange of 1 Ca^{2+} against three Na^+, is also present in the membrane of a number of different cell types. Some more cotransporters using Na^+ or H^+ gradients are presented in Table 1.

A classical example of an ionophore-mediated uniport is the naturally occurring cyclic antibiotic valinomycin, isolated from *Streptomyces*

Table 1 Cotransporters driven by Na^+ or H^+ gradients

Organism or tissue	Driven by the gradient of	Substance or ion to be transported	Type
Escherichia coli	H^+	Lactose	Symport
E. coli	H^+	Proline	Symport
Epithelia and red blood cells	H^+	Lactate	Symport
Small intestine and proximal tubule of vertebrates	H^+	Glucose	Symport
Small intestine and proximal tubule of vertebrates	Na^+	Amino acids	Symport
Cells of vertebrates	Na^+	Ca^{2+}	Antiport
Stomach and collecting duct of vertebrates	H^+	K^+	Antiport
Higher plants	H^+	K^+	Antiport
Fungi	H^+	K^+	Antiport

fulvissimus [50]. It is a carrier for K^+, and is highly selective for K^+ over Na^+, which moves as a valinomycin-K^+-complex through the membrane from one side to the other. This is achieved through the ring structure of the molecule. The K^+ localized in the inner part interacts with, and is held by, six oxygen atoms. The smaller Na^+ (when removed from its water shell) does not have the ability to interact with all six oxygen atoms simultaneously. The binding of K^+ is reversible. The inner part of the valinomycin-K^+-complex is hydrophilic, whereas the outer surface is hydrophobic. Therefore, valinomycin can easily penetrate into the lipid phase of the bilayer membrane as well as adsorb and dispense K^+ upon reaching the membrane surface. Valinomycin is able to mediate net transport of K^+ since it can also move across the membrane in unloaded form (without K^+). The direction of the net transport, therefore, depends on the electrochemical K^+ gradient. An ionophore acting as an antiporter is represented by the polyether-antibiotic nigericin, which exchanges K^+ for H^+. It was isolated from *Streptomyces hygroscopycus* [51]. These ionophores/carriers (valinomycin, nigericin), as well as that of channel-like agents (gramicidin A, amphotericin B), markedly increase the cation permeability of biological membranes leading to an equilibrium distribution of the cations which cannot be compensated by the ion pumps. The ensuing osmotic lysis accounts for their bacteriacidal action.

6.3. Transport through Channels

Biological membranes contain a large variety of integral transport proteins. These often consist of several transmembrane α-helices. In the inner part of the protein, several helices together can form a channel structure. Such structures allow a more-or-less specific transport of ions (or other substances—for water, see above). Ion channels are readily amenable to investigation using the patch-clamp technique. By applying a constant voltage over the membrane patch containing one or a few channels, one can measure the ionic current mediated upon channel opening. Classical Na^+ and Ca^{2+} channels are characterized by 24 transmembrane helices (in a single protein), whereas K^+ channels comprise four identical proteins each of which contains six transmembrane helices [52]. All channels exhibit two general features, they possess a mechanism for opening and closing and a selectivity filter. The high-frequency switch between the open and closed state of the channel is termed gating, and the duration of opening is called open time. The selectivity filter is responsible for the more-or-less specific transport of one or several ion species. Gating can be divided into four categories by modality:

1. Change of the electrical membrane potential, that is, change of the electrical field strength in the membrane,
2. Binding of a regulatory substance (including Ca^{2+}) or receptor ligand,

3. Mechanical forces (membrane "stretch" or cell volume changes), and
4. Light.

In the open state of a single channel a current of some pA can be measured, corresponding to a movement of about 10,000 ions through the channel during a few milliseconds. Originally it was thought that the gating process was mediated by a conformational change of a small part of the channel protein close to the channel entrance. Latterly, it has been assumed that ball-like protein structures attached to protein chains can move and close or open the gate (ball-chain model, see, e.g., Ref. [53]). Finally, it was the group of MacKinnon, which elucidated the three-dimensional structure of a K^+ channel [54]. The molecular gating mechanism of a Ca^{2+}-activated K^+ channel [55] as well as for a potential-dependent K^+ channel [56, 57] has been described. For the Ca^{2+}-activated K^+ channel, a Ca^{2+} binding to eight subunits results in a reorientation of the whole protein leading to a change of the diameter of the channel opening area. The actual model of the opening and closing mechanism of the potential-dependent K^+ channel assumes so-called paddles (paddle-like protein structure at the outer protein surface in the membrane) provided with potential sensors (positive charges), which can move through the membrane at the protein-lipid interface in response to changes in the electrical field strength. In this way they are able to modify the protein conformation.

Following the elucidation of the three-dimensional structure of a K^+ channel, our appreciation of the selectivity filter has also changed [54]. The interior of the channel is structured in such a way that the water-filled entrance area opens out into a cave. After the cave, there is a narrow channel (the length of which is approximately one-third of the whole channel diameter) where K^+ moves in dehydrated form. The stabilization of K^+ in the cave is accomplished by the steric alignment of four oxygen atoms. The smaller Na^+ can only interact with two oxygen atoms in this cave, insufficient to facilitate its transportation through the narrow channel.

From analyzing different ion channels, it has become evident that the structure of selectivity filters can vary. Channels can be specific for particular cations or anions, but also for some cations or anions. Future investigations are anticipated which will elucidate the molecular mechanisms of these selectivity filters.

The antibiotic polypeptide gramicidin represents a simple ionophore forming a cation channel. It is synthesized by the bacterium *Bacillus brevis* and consists of 15 alternating D- and L-amino acids. The primary structure of gramicidin A is: HCO-L-Val-D-Gly-L-Ala-D-Leu-L-Ala-D-Val-L-Val-D-Val-L-Trp-D-Leu-L-Trp-D-Leu-L-Trp-D-Leu-L-Trp-$NHCH_2CH_2OH$.

In a lipid bilayer or in a biological membrane, gramicidin A appears as a dimer forming a clockwise β-helix. In contrast to the channels, which are integral membrane proteins, the gating mechanism of gramicidin A channels is based on a reversible building of dimers from two single

polypeptides. An open channel is formed upon end-to-end connection of two polypeptides to produce a structure just able to span the membrane. The outer surface of the channel interacting with the surrounding membrane lipids is hydrophobic. Ions pass through hydrophilic channel interior. The three-dimensional structure of gramicidin A has already been elucidated by Prilusky and coworkers [58] using solid state NMR. Another relative simple molecule which forms a hydrophilic pore across lipid bilayer or biological membranes is the macrocyclic polyen antibiotic amphotericin B (molecular formula: $C_{47}H_{73}NO_{17}$). It was isolated from the bacterium *Streptomyces nodosus* and is used mainly as an antimycotic. The name originates from its amphoteric character [59, 60], which results from a carboxyl group at the main ring and a primary amino group at the mycosamin [61]. Amphotericin B binds to steroids (e.g., cholesterol, ergosterol) whereby some amphotericin B molecules aggregate to form a ring structure. A channel-like structure is formed, permeable for ions and small organic compounds (amino acids, sugars, nucleotides). However, the molecular mechanism of the interaction of amphotericin B within a biological membrane, the formation of its membrane pore and its selectivity mechanism remain unresolved [62].

6.4. Residual (“leak”) Transport

The residual or ‘‘leak’’ transport of an ion or other substance is defined as transport through a membrane which does not involve a specific transport pathway. Such residual transport would remain when all transport pumps, carriers, and channels are blocked. There is, of course, a particular problem. One has to be sure that all specific transport pathways are known and that they are all fully inhibited. Only then would the transport of an ion or a substance be truly residual. With the discovery of more and hitherto unknown transporters, it should be emphasized that the residual transport is smaller than previously expected. In principle, residual transport of an ion or a substance through a biological membrane should agree with the ‘‘solubility-diffusion mechanism’’ (with the exception of the cation and proton transport—see above). However, when solute transport through artificial lipid bilayer is compared with that across biological membranes, it becomes evident that residual transport in the latter is 2 orders of magnitude greater (see, e.g., Ref. [63]). This discrepancy may be due to incomplete inhibition of all specific transport pathways. There may be alternative explanations, however. Thus, insertion of nontransporting proteins into an artificial lipid bilayer membrane produces a significantly enhanced permeability for ions and uncharged substances. Should the lipid bilayer consist of a mixture of different lipids, for example, the extract of lipids from the red blood cell membrane, then this permeability increase is much smaller [64–66]. In addition, it has been shown that human red

blood cells became leaky for K^+ if the native phosphatidylcholine is partly replaced by phosphatidylcholine containing arachidonic acid [67]. Taking into account our knowledge about the structure of a biological membrane as well as the dynamics of its constituents, several possible explanations for residual transport must be considered:

1. Diffusion through imperfections in the lipid bilayer (existence of non-bilayer structures, kinks, interfaces of lipids in different states, and rafts).
2. Diffusion at protein-lipid interface.
3. Diffusion through structures formed in the interior of protein aggregates or on protein subunits.

Which one(s) of these possibilities is (are) more important remains unknown. In any case, the residual transport of ions will occur in areas of the membrane where water can enter. Here ions can pass in hydrated form. Such water-filled pores are unlikely to static entities with long lifetimes, rather they are likely to be dynamic structures with half-times set by the range of the dynamics of their components.

The classical textbook equation for the description of the passive ion diffusion through a biological membrane (equation of electrodiffusion or ion flux equation) was derived by Goldman in 1943 [68]. It is still used to characterize ion fluxes through biological membranes. However, it is important to understand the assumptions implicit in its derivation. Goldman [68] assumed "free" ion diffusion in a water filled pore, that is, without any interactions of the moving ion with its surroundings, for example, the pore structure. Such an idea may reasonably be used to characterize specific ion channels, at least to see the difference between the ion transport via the channel route and the free diffusion in a water-filled pore. Because of the problems outlined above, however, it is not readily applicable to residual ion transport. In addition to the existence of water filled dynamic structures in the membrane, the interaction of the diffusing ion with its surroundings must be considered. At the moment there is no adequate theory to describe the residual ion transport through a biological membrane quantitatively. A prerequisite for its formulation would be development of a mathematical model taking into consideration all fluctuations in the biological membrane contributing to the residual transport. In our opinion, this will be possible only through reliance on statistical thermodynamics.

7. The Ion Transport Pathways of the Red Blood Cell Membrane

The red blood cell is probably the most extensively investigated cell in the context of membrane transport pathways, being the subject of many studies over the last 100 years. Red blood cells present a number of

advantages which have encouraged their use. They are relatively stable, simple-structured (e.g., human red blood cells in contrast to red blood cells of fishes, amphibians, and birds do not contain a nucleus) and easy to handle (sterile conditions are not required). As discussed in the following sections, these cells may provide us with important clues about the nature of transport across biological membranes, and, in particular, that of the residual (''leak'') pathway.

After the discovery of the Na^+/K^+ pump, it was assumed that in addition to the active transport of Na^+ and K^+ mediated by this pump, only passive dissipative diffusion of these ions occurred down their electrochemical gradients. This concept is known as ''pump-leak'' hypothesis. However, as early as the mid-1950s, it was shown that the K^+ uptake of red blood cells of different species consists of both linear and saturation kinetics [69–71]. The kinetic component showing saturation was still observed after the inhibition of the Na^+/K^+ pump using ouabain [72]. This experiment, and two other reports, gave an important indication that other transport processes must be present, resulting finally in the discovery of a large variety of Na^+- and K^+-transport pathways in the red blood cell membrane. One fundamental investigation was carried out by Gardos [73]. He first demonstrated that the K^+ efflux of human red blood cells, which can be induced by inhibition of glycolysis, is significantly reduced in the presence of Ca^{2+} chelating agents. This finding was the basis of our knowledge of the Ca^{2+}-activated K^+ channel (or Gardos channel). The second important work was the demonstration of a stoichiometrically coupled transport of Na^+ and K^+ (cotransport) insensitive to ouabain but inhibited by the diuretic furosemide [74]. All transport pathways for Na^+ and K^+ in the human red blood cell membrane known to date are shown in Fig. 2. The situation for the Na^+ and K^+ transport in red blood cell membranes of other species is similar. Carnivore (dog, cat, bear, ferret, seal) red blood cells do not have a Na^+/K^+ pump but contain a Na^+/Ca^{2+} antiporter.

In addition to these Na^+ and K^+ transporters, red blood cells have a great variety of transport pathways for other ions, amino acids, nucleotides, saccharides, monocarboxylates, and other organic ions, as well as water. For further details, the interested reader is referred to the book ''Red Cell Membrane Transport in Health and Disease'' [75]. The situation is similar for ion transport through the membranes of other cell types, which show a great variety of pumps, carriers, channels, and the leak pathway. In contrast to the red blood cell membrane, however, most other cell types contain a broader variety of ion channels in their membranes. Extensive future investigations will reveal more and more specific (and so far unknown) ion transport pathways.

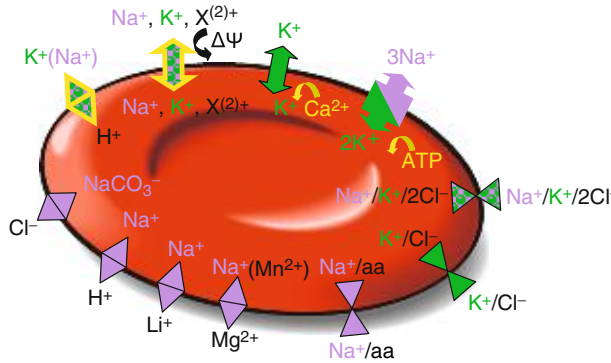

Figure 2 Overview on the ion transport pathways involving Na^+ and K^+ in the human red blood cell membrane. The following transport mechanisms are shown: Na^+/K^+ pump; Na^+–K^+–$2Cl^-$ symporter; K^+–Cl^- symporter; Na^+-dependent amino acid (aa) transport (several discrete transporters); $Na^+(Mn^+)/Mg^{2+}$ antiporter; Na^+/Li^+ antiporter; Na^+/H^+ antiporter; $NaCO_3^-/Cl^-$ exchange (via the protein band 3); $K^+(Na^+)/H^+$ antiporter; nonselective, voltage-dependent cation (NSVDC) channel; and Ca^{2+}-activated K^+ channel (Gardos channel).

8. The Effect of Low Ionic Strength Media on Transport of Na^+ and K^+ Through the Human Red Blood Cell Membrane

Under physiological conditions, that is, when suspended in salines of plasma-like composition, red blood cells are relatively impermeable to salts. Permeability is markedly altered, however, when red blood cells are suspended in isosmotic solutions of low ionic strength (LIS)—salt (especially K^+) permeability is increased. An early indication of this came from the observations of Gürber [76], that red blood cells from ox lost salt when washed in solutions of cane sugar. The significance of LIS-induced fluxes is relevant in the context of ion permeation pathways across lipid bilayers. Their importance in relation to the residual (“leak”) pathway is discussed in the following sections.

Gürber’s results were confirmed and extended by several groups [77–83]. While replacement of salts with nonelectrolytes (such as sucrose) concomitantly reduces ionic strength, a number of other changes also occur, however. These include an electrogenic Cl^- efflux which polarizes the membrane p.d. to positive potentials, imposition of a pronounced intracellular alkalinity as some of the intracellular Cl^- exchanges for extracellular base (such as OH^-) and, in addition, moderate cell shrinkage. It was important to determine whether LIS *per se* or any of these secondary effects was responsible for the altered permeability.

The effect of membrane potential was first studied by Donlon and Rothstein [84]. By analyzing K^+ loss with the simple Goldman flux equation [68], they proposed that the rates of efflux required an increase in the permeability coefficient of the red blood cell membrane. Bernhardt et al. [85], however, pointed out that the Goldman equation may not hold under LIS conditions. Using an extended form of the equation to take into account inner and outer surface potentials, they calculated that, in fact, the observed K^+ efflux did not require a change in the permeability coefficient. That changes in membrane potential were not the precipitating event was also suggested from K^+ influx experiments. These, too, increased in human red blood cells suspended in LIS solutions [86] while the polarization of the membrane (from normal − 10 to + 50 mV, as assumed earlier but see next section) would bring about a three-fold fall in influx according to the Goldman flux equation. In further experiments, using impermeant anions such as gluconate or glucoronate to replace extracellular Cl^- (instead of LIS solutions), to polarize the red blood cell to a similar extent, it was found that only a small increase in K^+ flux was observed [86]—and cf. effect of tatarate in the next section.

Later, from studying red blood cells from different species, it became apparent that changes in surface potentials *per se* did not provide the solution. Bovine red blood cells, like those of humans, have asymmetrically distributed phospholipids such that all of the negatively charged phosphatidylserine is confined to the inner surface. Their surface potentials would therefore be similar. This has been confirmed electrophoretically for the external surface potential [87]. However, bovine red blood cells do not show increased K^+ loss in LIS solutions. Comparing the effect of LIS solutions in red blood cells from a range of species, it was found that human, cat, rat, horse, LK sheep, and rabbit show increased K^+ efflux, those of pig, cattle, and HK sheep do not [88, 89]. LIS effect in cattle also shows an age-dependency. Thus, red blood cells from young cattle show a LIS effect (with maximal effects on the first day after birth) with effects declining over the next 6 weeks [90].

An effect due to elevation of intracellular pH has also been largely discounted. Thus, the normal intracellular pH of human red blood cells is 7.2 and this increased to 7.8 in LIS solutions of normal extracellular pH (7.4). However, by suspending red blood cells in acidified LIS solutions (pH 6.5), it is possible to reduce intracellular pH back to normal. This titration does not prevent the elevated K^+ fluxes observed under LIS conditions [86]. On the other hand, residual K^+ influx does show some sensitivity to intracellular pH [91, 92].

It should also be noted that K^+ fluxes in LIS conditions show little volume sensitivity [86]. The shrinkage which occurs in LIS solutions can be offset by using hypo-osmotic LIS solutions (250 mOsm/kg, cf. normal 290–300). These have little effect on K^+ fluxes.

Inhibitors of LIS-induced fluxes and the identity of a specific protein transporter responsible for them have been studied in some detail, without definitive answers. Ouabain, bumetanide, and EGTA do not prevent the fluxes, indicating the absence of involvement of the Na^+/K^+ pump, Na^+–K^+–$2Cl^-$ cotransporter (NKCC) and the Gardos channel. Fluxes are also unaffected by Cl^- substitution with methylsulphate, and are inhibited modestly on cell swelling, making the participation of the K^+–Cl^- cotransporter (KCC)—which is stimulated by swelling—unlikely [86] (cf. [93]). A role for the nonselective, voltage-dependent cation (NSVDC) channel has also been excluded since this channel occurs in both human and HK sheep red blood cells [94, 95], while only human red blood cells show the LIS effect [94, 96]. In addition, the channel does not discriminate between Na^+, K^+, and Ca^{2+} whereas the permeability induced by LIS media is impermeable to Ca^{2+} [96, 97]. DIDS, however, does significantly reduce LIS-induced fluxes [98], which may indicate participation in some way of band 3, as suggested earlier [99]. It is also possible that LIS-induced ion permeabilities do not involve a definitive transport system. Other explanations include altered protein–protein and/or protein–lipid interactions, to produce instabilities between these macromolecules leading to regions which allow transmembrane ion movements. A role for H^+-coupled electroneutral transport is discussed in the next section.

9. The $K^+(Na^+)/H^+$ Exchanger in the Human Red Blood Cell Membrane

More recent work has strengthened the postulate that the residual K^+ and Na^+ fluxes observed under LIS conditions represent fluxes mediated by a $K^+(Na^+)/H^+$ exchanger. Such a $K^+(Na^+)/H^+$ exchanger probably represents one of the nine isoforms of the Na^+/H^+ exchanger (NHE) known to date. It has been shown that NHE6-9 are able to transport K^+ in addition to Na^+ [100–102]. The cations involved in this sort of exchange function will be attracted to the membrane more strongly under LIS conditions, as reduction in ionic strength of the extracellular solution will necessarily enhance the negative outer surface membrane potential. It is also possible to analyze LIS-induced fluxes (using linearized Gouy-Chapman and Boltzman equations). Using these equations, the logarithmic value of the apparent rate constants for these ions would be proportional to the square root of the ionic strength, and this is found experimentally—see Ref. [103] for further details. In addition, for a $K^+(Na^+)/H^+$ exchange function, there should be a 1:1 stoichiometry between cation flux and that of H^+. Through careful calibration, it is possible to measure H^+ entry into red blood cells with the pH-sensitive fluorescent dye BCECF [104]. In LIS

solutions, intracellular pH increased from about 7.2 to 7.7, after which a slow reduction was observed, which is consistent with H^+ entry (i.e., in exchange for K^+). By comparing K^+ efflux with equivalent acid influx (as assessed with BCECF), a 1:1 stoichiometry was indeed present [104]. Interestingly, in agreement with the previous section, the effect of Cl^- replacement with tartarte was also tested. In these circumstances, as for gluconate and glucoronate, the red blood cell membrane potential depolarizes, accompanied by an intracellular alkaline shift of equivalent magnitude for that observed under LIS conditions. In this case, however, the slow acidification is much slower. As for K^+ efflux, therefore, H^+ influx is not elicited by the high membrane potential. Again, bovine and pig red blood cells, which show little LIS-induced K^+ loss, also show little H^+ influx but stoichiometry remained compatible with a 1:1 exchange, perhaps implying that the same function is present in the red blood cells from these species, rather that its activity is low.

The search for potential inhibitors of $K^+(Na^+)/H^+$ exchange has continued. Quinacrine, a known mitochondrial $K^+(Na^+)/H^+$ exchange blocker [105], reduces K^+ efflux by 80% and H^+ influx nearly completely in LIS solutions, while DIDS is also partially effective. Surprisingly, quinacrine activated the K^+ flux under physiological conditions [106]. In this context, it is interesting that DIDS also affects K^+/H^+ exchange in *Amphiuma* and trout red blood cells [107, 108]. A better $K^+(Na^+)/H^+$ exchange inhibitor may be represented by HOE-642 which inhibits the (ouabain + bumetanide + EGTA)-insensitive K^+ influx in physiological ionic strength and LIS solutions by 40% and 65%, respectively [106]

Of course, a functional $K^+(Na^+)/H^+$ countertransport could be explained by mechanisms other than a $K^+(Na^+)/H^+$ exchange protein *per se*. The existence of separate channels for K^+ efflux and H^+ influx (or OH^- efflux), perhaps via band 3, have been proposed. These are less likely given the lack of dependence of fluxes on the transmembrane potential (e.g., [86]). Similarly, these observations would argue against a more complex mechanism with Cl^- leaving the cells immediately after transfer to LIS media, coupled with K^+ through separate ion channels, with Cl^- then re-entering cells slowly in exchange for OH^-. Again, while a K^+–OH^- symport cannot be completely excluded, it is less likely that anions are involved given the negative surface potential (e.g., [109]). Finally, the possible participation of band 3 should be considered (see Ref. [98]). As above, the surface potential argument makes a role for band 3 less likely. In addition, inhibitor studies and other data are less persuasive for the involvement of band 3. Quinacrine (which blocks K^+/H^+ movements) does not act on band 3 while niflumic acid (which inhibits band 3) has no effect on LIS-induced fluxes [104]. Finally, pig and cattle red blood cells, lacking LIS effects on cation permeability, have normal band 3 function.

It cannot be ruled out completely, however, that both the NSVDC channel (see section before) and the $K^+(Na^+)/H^+$ exchanger are candidate pathways mediating the LIS effect since the channel is activated at membrane potentials above + 30 mV [110]. It is also possible that these pathways represent different modes of operation of a single system. To clarify this possibility, therefore, the effect on the NSVDC channel of the recently characterized inhibitor of the $K^+(Na^+)/H^+$ exchanger HOE-642 has been determined. Radioisotope flux measurements and conductance determinations showed that HOE-642 exerted differential effects on the NSVDC channel and the $K^+(Na^+)/H^+$ exchanger [111].

It is important to note that, after transferring cells from physiological ionic strength to LIS solutions, a new steady state is quickly established, associated with an increase of the internal pH from 7.2 to approximately 7.7 [104]. This results in a depolarization of the membrane from − 10 to + 18.5 mV. Although this calculation (which assumes a Nernst distribution of H^+) will be an underestimation given that there will be a significant buffer capacity in both extracellular and intracellular compartments, it would appear that the membrane potential is below the level at which significant activation of the NSVDC channel will occur [110, 112]. In this context, it is interesting to note that in the fundamental investigation of the LIS effect by Donlon and Rothstein [84], where the authors decreased the extracellular ionic strength to a very low level (close to 0), the increase of the net K^+ loss was described as a triphasic response (a curve with two inflection points). The first inflection point (estimated at a membrane potential of + 45 mV) probably reflects the transition from a situation in which $K^+(Na^+)/H^+$ exchange dominates to one in which the NSVDC channel is most important. The second reflection point at very low ionic strength (at a calculated membrane potential of around + 170 mV) may represent the beginning of an electrical break-down of the membrane.

10. Concluding Discussion: Ion Transport through Biological Membranes

Our understanding of the nature of ion permeation through membranes has undergone remarkably advancement over the last 50 or so years. We now know that a rich diversity of specific channels, pumps and carriers carry out numerous roles in different cell types and organelles. Different isoforms and interactions between these protein transport pathways, as well as with other components of the cell, have marked effects on their function. For some, their mechanism is well appreciated at a molecular level—the voltage sensor or selectivity filter of channels, for example. For others, just how transport is achieved remains to be determined. The Na^+/K^+ pump is

notable in this context. Over the ensuing years, our molecular appreciation of such active transport processes will surely be revolutionized.

A further, unsolved problem is nature of the residual (or ''leak'') transport of biological membranes. As pointed out above, the permeability coefficient of a real biological membrane is markedly higher compared to that of an artificial lipid bilayer (by about 2 orders of magnitude). This transport function may be afforded by, as yet, unidentified but specific transport proteins. A case in point is provided by the $K^+(Na^+)/H^+$ exchange function of red blood cells activated under LIS conditions—hence our discussion above. It is still arguable whether this function can be explained by a discrete transport entity (the proposed $K^+(Na^+)/H^+$ exchanger, probably one of the nine isoforms of the NHE) or whether it is in some way part of the residual (''leak'') membrane permeability. Clearly, all specific transport entities must be accounted for and inhibited before the true ground state is revealed. A caveat to the specificity of most inhibitors has been discussed above—with ouabain-inhibition of Na^+/K^+ pump representing a notable exception.

In addition, our theoretical understanding of transport under various conditions requires further development. A ''leak,'' dependent on interaction between ions and proteins or lipids, or through transient water-filled pores (which may not be manifest for sufficient time for ''free'' diffusion) is not readily amenable to analysis by the Goldman flux equation. In a similar way, the effect of the three-dimensional electric field to which a membrane is exposed remains to be fully analyzed. Given the complexity of structural components comprising the membrane, many of which have charged species, the constant field simplification underpinning the Goldman flux equation is unlikely to hold in all circumstances. We need a new mathematical description to analyze such issues quantitatively.

Finally, while ion permeation is often regarded as the prerogative of transport proteins, the effect of lipid composition is not negligible. Alterations in the lipid component of biological membranes has pronounced effects (e.g., [67, 113]), and it is not clear to what extent these are exerted on the true ''leak'' or on the function of specific transport proteins.

In these areas, the red blood cell will surely represent an invaluable model system in future work on these questions, as it has done in the past.

REFERENCES

[1] R. Hooke, Micrographia, Royal Society, London, 1665.
[2] C. Nägeli, Pflanzliche Untersuchungen von Nägeli und Cramer Heft 1, Zürich, 1855.
[3] W.F.P. Pfeffer, Osmotische Untersuchungen, W. Engelmann, Leipzig, 1877.
[4] E. Overton, Über die osmotischen Eigenschaften der lebenden Pflanzen- und Tierzelle, Vierteljahresschr. Naturforsch. Ges. Zürich 40 (1895) 159–201.

[5] E. Overton, Über die allgemeinen osmotischen Eigenschaften der Zelle, ihre vermutlichen Ursachen und ihre Bedeutung für die Physiologie, Vierteljahresschr. Naturforsch. Ges. Zürich 44 (1899) 88–114.
[6] E. Gorter, J. Grendel, On bimolecular layers of lipoids on the chromocytes of blood, J. Exp. Med. 41 (1925) 439–443.
[7] H. Dawson, J.F. Danielli, The Permeability of Natural Membranes, Cambridge University Press, Cambridge, 1943.
[8] J.D. Robertson, The occurrence of a subunit pattern in the unit membranes of club endings in mauthner cell synapses in goldfish brains, J. Cell Biol. 19 (1963) 201–221.
[9] S.J. Singer, G.L. Nicolson, The fluid mosaic model of the structure of cell membrane, Science 175 (1972) 720–731.
[10] M.S. Bretscher, Asymmetrical lipid bilayer structure for biological membranes, Nat. New Biol. 236 (1972) 11–12.
[11] P.R. Cullis, B. DeKruijff, Lipid polymorphism and the functional roles of lipids in biological membranes, Biochim. Biophys. Acta 559 (1979) 399–420.
[12] E. Abderhalden, Zur quantitativen analyse des blutes, Z. Physiol. Chem. 23 (1897) 521–531.
[13] A. Gürber, Die salze des blutes, Jahresbericht über die Fortschritte der Tierchemie oder der Physiologischen und Pathologischen Chemie 24 (1895) 172–175.
[14] D.D. Van Slyke, H. Wu, F.C. McLean, Studies of gas and electrolyte equilibria in the blood. V. Factors controlling the electrolyte and water distribution in the blood, J. Biol. Chem. 56 (1923) 765–849.
[15] W.O. Fenn, D.M. Cobb, Electrolyte changes in muscle during activity, Am. J. Physiol. 115 (1936) 345–356.
[16] R.B. Dean, Theories of electrolyte equilibrium in muscle, Biol. Symp. 3 (1941) 331–348.
[17] A. Krogh, The active and passive exchanges of inorganic ions through the surfaces of living cells and through living membranes generally, Proc. R. Soc. Lond., B, Biol. Sci 133 (1946) 140–200.
[18] J.C. Skou, The influence of cell cations on adenosine triphosphatase from peripheral nerves, Biochim. Biophys. Acta 23 (1957) 394–401.
[19] R.J. Sachs, Na^+/K^+ pump, in: I. Bernhardt, J.C. Ellory (Eds.), Red Cell Membrane Transport in Health and Disease, Springer, Berlin, 2003, pp. 111–137.
[20] A.L. Hodgkin, A.F. Huxley, A quantitative description of membrane current and ist application to conduction and excitation in nerve, J. Physiol. 117 (1952) 500–544.
[21] A.L. Hodgkin, R.D. Keynes, The potassium permeability of a giant nerve fibre, J. Physiol. 128 (1955) 61–88.
[22] B. Hille, Ionic channels in nerve membranes, Prog Biophys. Mol. Biol. 21 (1970) 1–32.
[23] C.M. Armstrong, Interaction of tetraethylammonium ion derivatives with the potassium channels of giant axons, J. Gen. Physiol. 58 (1971) 413–437.
[24] E. Neher, B. Sakmann, Single-channel currents recorded from membrane of denervated frog muscle fibres, Nature 260 (1976) 799–802.
[25] A. Cass, A. Finkelstein, Water permeability of thin lipid membranes, J. Gen. Physiol. 50 (1967) 1765–1784.
[26] A. Finkelstein, A. Cass, Effect of cholesterol on the water permeability of thin lipid membranes, Nature 18 (1967) 717–718.
[27] D.C. Petersen, Water permeation through the lipid bilayer membrane: Test of the liquid hydrocarbon model, Biochim. Biophys. Acta 600 (1980) 666–667.
[28] H. Träuble, The movement of molecules across lipid membranes: A molecular theory, J. Membr. Biol. 4 (1971) 193–208.
[29] C.V. Paganelli, A.K. Solomon, The rate of exchange of tritiated water across the human red cell membrane, J. Gen. Physiol. 41 (1957) 259–277.

[30] T. Conlon, R. Outhred, Water diffusion permeability of erythrocytes using a nuclear magnetic resonance technique, Biochim. Biophys. Acta 288 (1972) 354–361.
[31] T.C. Terwilliger, A.K. Solomon, Osmotic water permeability of human red cells, J. Gen. Physiol. 77 (1981) 549–570.
[32] R.I. Macey, R.E.L. Farmer, Inhibition of water and solute permeability in human red cells, Biochim. Biophys. Acta 211 (1970) 104–106.
[33] G. Benga, O. Popescu, V.I. Pop, R.P. Holmes, *p*-(Chloromercuri)benzenesulfonate binding by membrane proteins and the inhibition of water transport in human erythrocytes, Biochemistry 25 (1986) 1535–1538.
[34] J.S. Jung, G.M. Preston, B.L. Smith, W.B. Guggino, P. Agre, Molecular structure of the water channel through aquaporin CHIP. The hourglass model, J. Biol. Chem. 269 (1994) 14648–14654.
[35] T. Walz, T. Hirai, K. Murata, J.B. Heymann, K. Mitsuoka, Y. Fujiyoshi, B.L. Smith, P. Agre, A. Engel, The 6 Å three-dimensional structure of aquaporin-1, Nature 387 (1997) 624–627.
[36] K. Murata, K. Mitsuoka, T. Hirai, T. Walz, P. Agre, J.B. Heymann, A. Engel, Y. Fujiyoshi, Structural determinants of water permeation through aquaporin-1, Nature 407 (2000) 599–605.
[37] B.M. Denker, B.L. Smith, F.P. Kuhajda, P. Agre, Identification, purification, and partial characterization of a novel Mr 28,000 integral membrane protein from erythrocytes and renal tubules, J. Biol. Chem. 263 (1988) 15634–15642.
[38] B.L. Smith, P. Agre, Erythrocyte Mr 28,000 transmembrane protein exists as a multisubunit oligomer similar to channel proteins, J. Biol. Chem. 266 (1991) 6407–6415.
[39] G.M. Preston, T.P. Carroll, W.B. Guggino, P. Agre, Appearance of water channels in *Xenopus* oocytes expressing red cell CHIP28 protein, Science 256 (1992) 385–387.
[40] G.J. Cooper, W.F. Boron, Effect of PCMBS on CO_2 permeability of *Xenopus* oocytes expressing aquaporin 1 or its mutant, Am. J. Physiol. 275 (1998) C1481–C1486.
[41] M. Yasui, pH regulated anion-permeability of aquaporin 6, Handbook Exp. Pharmacol. 190 (2009) 299–308.
[42] G. Lahajnar, P. Macek, I. Zupancic, Suppression of red cell diffusional water permeability by lipophilic solutes, Bioelectrochemistry 52 (2000) 179–185.
[43] J. Brahm, Diffusional water permeability of human erythrocytes and their ghosts, J. Gen. Physiol. 79 (1982) 791–819.
[44] S. Paula, D.W. Deamer, Membrane permeability barriers to ionic and polar solutes, in: Membrane permeability, 100 Years since Ernest Overton, Current Topics in membranes, Vol. 48 Academic Press, San Diego, 1999, pp. 77–95.
[45] A.G. Lee, A calcium pump made visible, Curr. Opin. Struct. Biol. 12 (2002) 547–554.
[46] W.J. Rice, H.S. Young, D.W. Martin, J.R. Sachs, D.L. Stokes, Structure of Na^+, K^+-ATPase at 11-Å resolution: Comparison with Ca^{2+}-ATPase in E_1 and E_2 states, Biophys. J. 80 (2001) 2187–2197.
[47] J.P. Morth, B.P. Pedersen, M.S. Toustrup-Jensen, T.L. Sørensen, J. Petersen, J.P. Andersen, B. Vilsen, P. Nissen, Crystal structure of the sodium–potassium pump, Nature 450 (2007) 1043–1049.
[48] R.J. Naftalin, Glucose transport, in: I. Bernhardt, J.C. Ellory (Eds.), Red Cell Membrane Transport in Health and Disease, Springer, Berlin, 2003, pp. 339–372.
[49] J. Abramson, I. Smirnova, V. Kasho, G. Verner, H.R. Kaback, S. Iwata, Structure and mechanism of the lactose permease of *Escherichia coli*, Science 301 (2003) 610–615.
[50] C.H. Hassall, W.A. Thomas, Conformations of cyclic cylindrical peptides, Chem. Br. 7 (1971) 145–153.
[51] S.N. Graven, S. Estrada-O, H.A. Lardy, Alkali metal cation release and respiratory inhibition induced by nigericin in rat liver mitochondria, Proc. Natl. Acad. Sci. USA 56 (1966) 654–658.

[52] W.A. Catterall, Structure and function of voltage-sensitive ion channels, Science 242 (1988) 50–61.
[53] J. Adley, P.R. Stanfield, Molecular structures—voltage-gated channels and their relatives, in: J. Adley, P.R. Stanfield (Eds.), Ion Channels—Molecules in Action Cambridge University Press, Cambridge, 1998.
[54] D.A. Doyle, J. Morais Cabral, R.A. Pfuetzner, A. Kuo, J.M. Gulbis, S.L. Cohen, B. T. Chait, R. MacKinnon, The structure of the potassium channel: Molecular basis of K^+ conduction and selectivity, Science 280 (1998) 69–77.
[55] Y. Jiang, A. Lee, J. Chen, M. Cadene, B.T. Chait, R. MacKinnon, Crystal structure and mechanism of a calcium-gated potassium channel, Nature 417 (2002) 515–522.
[56] Y. Jiang, A. Lee, J. Chen, V. Ruta, M. Cadene, B.T. Chait, R. MacKinnon, X-ray structure of a voltage-dependent K^+ channel, Nature 423 (2003) 33–41.
[57] Y. Jiang, V. Ruta, J. Chen, A. Lee, R. MacKinnon, The principle of gating charge movement in a voltage-dependent K^+ channel, Nature 423 (2003) 42–48.
[58] J.L. Sussman, D. Lin, J. Jiang, N.O. Manning, J. Prilusky, O. Ritter, E.E. Abola, Protein data bank (PDB): Database of three-dimensional structural information of biological macromolecules, Acta Crystallogr. D Biol. Crystallogr. 1 (1998) 1078–1084.
[59] M.C. Heit, J.E. Riviere, Antifungal and antiviral drugs, in: H.R. Adams (Ed.), Veterinary Pharmacology and Therapeutics seventh ed., Iowa State University Press, Ames, USA, 1995, pp. 855–884.
[60] D.C. Plumb, Veterinary Drug Handbook, PharmaVet Publishing, White Bear Lake, USA, 1999.
[61] J.E. Bennett, Antimicrobial agents: Antifungal agents, in: J.G. Hardman, L.E. Limbird (Eds.), Goodman & Gilman's the Pharmacological Basis of Therapeutics tenth ed., McGraw-Hill, New York, 1995, pp. 1175–1190.
[62] W. Huang, Z. Zhang, X. Han, J. Tang, J. Wang, S. Dong, E. Wang, Ion channel behavior of amphotericin B in sterol-free and cholesterol- or ergosterol-containing supported phosphatidylcholine bilayer model membranes investigated by electrochemistry and spectroscopy, Biophys. J. 83 (2002) 3245–3255.
[63] W.D. Stein, Channels, Carriers, and Pumps, Academic Press, London, 1990.
[64] A.T.M. Van der Steen, B. De Kruijff, J. De Gier, Glycophorin incorporation increases the bilayer permeability of large unilamellar vesicles in a lipid-dependent manner, Biochim. Biophys. Acta 691 (1982) 13–23.
[65] P. Van Hoogevest, A.P.M. Du Maine, B. De Kruijff, Characterization of the permeability increase induced by the incorporation of glycophorin in phosphatidylcholine vesicles, FEBS Lett. 157 (1983) 41–45.
[66] P. Van Hoogevest, A.P.M. Du Maine, B. De Kruijf, J. De Gier, The influence of lipid composition on the barrier properties of band 3-containing lipid vesicles, Biochim. Biophys. Acta 777 (1984) 241–252.
[67] F.A. Kuypers, B. Roelofsen, J.A.F. Op den Kamp, L.L.M. Van Deenen, The membrane of intact human erythrocytes tolerates only limited changes in the fatty acid composition of its phosphatidylcholine, Biochim. Biophys. Acta 769 (1984) 337–347.
[68] D.E. Goldman, Potential, impedance and rectification in membranes, J. Gen. Physiol. 27 (1943) 37–60.
[69] T.I. Shaw, K movements in washed erythrocytes, J. Physiol. 129 (1955) 464–475.
[70] I.M. Glynn, Sodium and potassium movement in human red cells, J. Physiol. 134 (1956) 278–316.
[71] L.A. Beaugé, O. Ortiz, Rubidium, sodium and ouabain interactions on the influx of rubidium in red blood cells, J. Physiol. 210 (1970) 519–533.
[72] I.M. Glynn, The action of cardiac glycoside on sodium and potassium movements in human red cells, J. Physiol. 136 (1957) 148–173.

[73] G. Gardos, The function of calcium in the potassium permeability of human erythrocytes, Biochim. Biophys. Acta 30 (1958) 653–654.
[74] J.S. Wiley, R.A. Cooper, A furosemide-sensitive cotransport of sodium plus potassium in the human red cell, J. Clin. Invest. 53 (1974) 745–755.
[75] I. Bernhardt, J.C. Ellory, Red Cell Membrane Transport in Health and disease, Springer, Berlin, 2003.
[76] A. Gürber, Salze des Blutes, II. Teil: Salze der Blutkörper, Habilitationsschrift, Kgl Julius-Maximilians-Universität Würzburg, Bayer, 1904.
[77] I. Bang, Physiko-chemische Verhältnisse der Blutkörperchen, Biochem. Z. 16 (1909) 255–276.
[78] R. Mond, Umkehr der Anionenpermeabilität der roten Blutkörperchen in eine elektive Durchlässigkeit für Kationen. Ein Beitrag zur Analyse der Zellmembranen, Pflügers Arch. 217 (1927) 618–630.
[79] H. Davson, Studies on the permeability of erythrocytes, VI. The effect of reducing salt content of the medium surrounding the cell, Biochem. J. 33 (1939) 389–401.
[80] W. Wilbrandt, Die Ionenenpermeabilität der Erythrozyten in Nichtleiterlösungen, Pflügers Arch. 242 (1940) 537–556.
[81] W. Wilbrandt, H.J. Schatzmann, Changes in the passive cation permeability of erythrocytes in low electrolyte media, Ciba Found. Study Group 5 (1960) 34–52.
[82] D.A. Carolin, M. Maizels, Effect of the duration of loading lactose-treated red cells with cations on the rate of subsequent cation flux, J. Physiol. 179 (1965) 54–94.
[83] P.L. LaCelle, A. Rothstein, The passive permeability of red blood cells to cations, J. Gen. Physiol. 50 (1966) 171–188.
[84] J.A. Donlon, A. Rothstein, The cation permeability of erythrocytes in low ionic strength media of various tonicities, J. Membr. Biol. 1 (1969) 37–52.
[85] I. Bernhardt, E. Donath, R. Glaser, Influence of surface charge and transmembrane potential on Rb-86 efflux on human erythrocytes, J. Membr. Biol. 78 (1984) 249–255.
[86] I. Bernhardt, A.C. Hall, J.C. Ellory, Effects of low ionic strength media on passive human red cell monovalent cation transport, J. Physiol. 434 (1991) 489–506.
[87] I. Bernhardt, Untersuchungen zur Regulation des Ouabain-insensitiven Membrantransports monovalenter Kationen an Erythrozyten, D.Sc. thesis Humboldt University, Berlin, 1986.
[88] I. Bernhardt, A. Erdmann, R. Glaser, G. Reichmann, R. Bleiber, Influence of lipid composition on passive ion transport of erythrocytes, in: R. Klein, B. Schmitz (Eds.), Topics in Lipid Research, Royal Society of Chemistry, London, 1986, pp. 243–248.
[89] A. Erdmann, I. Bernhardt, A. Hermann, R. Glaser, Species-dependent differences in the influence of ionic strength on potassium transport of erythrocytes: The role of membrane fluidity and Ca^{2+}, Gen. Physiol. Biophys. 9 (1990) 577–588.
[90] I. Bernhardt, G. Seidler, I. Ihrig, A. Erdmann, Species-dependent differences in the influence of ionic strength on potassium transport of erythrocytes: The role of lipid composition, Gen. Physiol. Biophys. 11 (1992) 287–299.
[91] A.R. Chipperfield, D.B. Shennan, The influence of pH and membrane potential on passive Na^+ and K^+ fluxes in human red blood cells, Biochim. Biophys. Acta 886 (1986) 373–382.
[92] A.M.M. Zade-Oppen, D.C. Tosteson, N.C. Adragna, Effects of pH, potential, chloride and furosemide on Na^+ and K^+ effluxes from human red blood cells, J. Membr. Biol. 103 (1988) 217–225.
[93] J.C. Ellory, A.C. Hall, Human red cell volume regulation in hypotonic media, Comp. Biochem. Physiol. 90A (1988) 533–537.
[94] J.A. Halperin, C. Brugnara, M.T. Tosteson, T. Van Ha, D.C. Tosteson, Voltage-activated cation transport in human erythrocytes, Am. J. Physiol. 257 (1989) C986–C996.
[95] J.A. Halperin, C. Brugnara, T. Van Ha, D.C. Tosteson, Voltage-activated cation permeability in high potassium but not in low potassium red blood cells, Am. J. Physiol. 258 (1990) C1169–C1172.

[96] L. Kaestner, P. Christophersen, I. Bernhardt, P. Bennekou, The non-selective voltage-activated cation channel in the human red blood cell membrane: Reconciliation between two conflicting reports and further characterisation, J. Bioelectrochem. 52 (2000) 117–125.
[97] Y.V. Kucherenko, E. Weiss, I. Bernhardt, Effect of the ionic strength and prostaglandin E_2 on the free Ca^{2+} concentration and the Ca^{2+} influx in human red blood cells, Bioelectrochemistry 62 (2004) 127–133.
[98] G.S. Jones, P.A. Knauf, Mechanism of the increase of the cation permeability of human erythrocytes in low-chloride media. Involvement of the anion transport protein capnophorin, J. Gen. Physiol. 86 (1985) 721–738.
[99] A.K. Solomon, B. Chasan, J.A. Dix, M.F. Lukacovic, M.R. Toon, A.S. Verkman, The aqueous pore in the red cell membrane: Band 3 as a channel for anions, cations, non-electrolytes, and water, Ann. N. Y. Acad. Sci. 414 (1983) 97–124.
[100] J. Orlowski, S. Grinstein, Diversity of the mammalian sodium/proton exchanger SLC9 gene family, Pflugers Arch.—Eur. J. Physiol. 447 (2004) 549–565.
[101] J.K. Hill, C.L. Brett, A. Chyou, L.M. Kallay, M. Sakaguchi, R. Rao, P.G. Gillespie, Vestibular hair bundles control pH with (Na^+, K^+)/H^+ exchangers NHE6 and NHE9, J. Neurosci. 26 (2006) 9944–9955.
[102] N. Nakamura, S. Tanaka, Y. Teko, K. Mitsui, H. Kanazawa, Four Na^+/H^+ exchanger isoforms are distributed to Golgi and post-Golgi compartments and are involved in organelle pH regulation, J. Biol. Chem. 280 (2005) 1561–1572.
[103] S. Richter, J. Hamann, D. Kummerow, I. Bernhardt, The monovalent cation ''leak'' transport in human erythrocytes: An electroneutral exchange process, Biophys. J. 73 (1997) 733–745.
[104] D. Kummerow, J. Hamann, J.A. Browning, R. Wilkins, J.C. Ellory, I. Bernhardt, Variations of intracellular pH in human erythrocytes via $K^+(Na^+)/H^+$ exchange under low ionic strength conditions, J. Membr. Biol. 176 (2000) 207–216.
[105] K.D. Garlid, D.J. DiResta, A.D. Beavis, W.H. Martin, On the mechanism by which dicyclohexylcarbodiimide and quinine inhibit K^+ transport in rat liver mitochondria, J. Biol. Chem. 261 (1986) 1529–1535.
[106] E. Weiss, H.J. Lang, I. Bernhardt, Inhibitors of the $K^+(Na^+)/H^+$ exchanger of human red blood cells, Bioelectrochemistry 62 (2004) 135–140.
[107] J.S. Adorante, P.M. Cala, Activation of electroneutral K^+ flux in *Amphiuma* red blood cells by *N*-ethylmaleimide. Distinction between K/H exchange and KCl cotransport, J. Gen. Physiol. 90 (1987) 209–227.
[108] B. Fievet, H. Guizouarn, B. Pellissier, F. Garcia-Romeu, R. Motais, Evidence for a K^+–H^+ exchange in trout red blood cells, J. Physiol. 462 (1993) 597–607.
[109] I. Bernhardt, Alteration of cellular features after exposure to low ionic strength medium, in: J. Bauer (Ed.), Cell Electrophoresis CRC Press, Boca Raton, FL, 1994, pp. 163–179.
[110] P. Bennekou, P. Christophersen, Ion channels, in: I. Bernhardt, J.C. Ellory (Eds.), Red Cell Membrane Transport in Health and Disease Springer, Berlin, 2003, pp. 139–152.
[111] I. Bernhardt, E. Weiss, H.C. Robinson, R. Wilkins, P. Bennekou, Differential effect of HOE642 on two separate monovalent cation transporters in the human red cell membrane, Cell. Physiol. Biochem. 20 (2007) 601–606.
[112] I. Bernhardt, E. Weiss, Passive membrane permeability for ions and the membrane potential, in: I. Bernhardt, J.C. Ellory (Eds.), Red Cell Membrane Transport in Health and Disease, Springer, Berlin, 2003, pp. 84–109.
[113] J.F.S.J. Dwight, B.M. Hendry, Actions of arachidonic acid on erythrocyte membrane Rb permeability, Clin. Chim. Acta 238 (1995) 187–197.

CHAPTER THREE

Membrane Nanotubes in Urothelial Cell Line T24

Maruša Lokar,[1,*] Šárka Perutková,[1] Veronika Kralj-Iglič,[2] Aleš Iglič,[1] *and* Peter Veranič[3]

Contents

Abstract

Membrane nanotubes (also referred as tunnelling nanotubes—TNTs, nanotubules, cytonemes), that directly connect separated neighboring cells, may offer a very specific and effective way of intercellular transport and communication. Our experiments on T24 cell line show that TNTs can be divided into two types with respect to their biochemical and biophysical characteristics and the nature of their formation. As type I were characterized the nanotubes which are shorter, more dynamic and contain actin filaments. These structures remain stabile even if underlying actin cytoskeleton is disintegrated by cytochalasin D. The nanotubes of type II are much longer, appear more stable and contain cytokeratin filaments. In both types microtubules can be found, but this type of cytoskeleton is present in only a small fraction of the TNTs. On the nanotubes of

* Corresponding author. Tel.: + 386 1 4768 235;
E-mail address: marusa.lokar@fe.uni-lj.si

[1] Laboratory of Biophysics, Faculty of Electrical Engineering, University of Ljubljana, Tržaška 25, SI-1000 Ljubljana, Slovenia
[2] Laboratory of Clinical Biophysics, Institute of Biophysics, Faculty of Medicine, University of Ljubljana, Vrazov trg 2, SI-1000 Ljubljana, Slovenia
[3] Institute of Cell Biology, Faculty of Medicine, University of Ljubljana, Lipičeva 2, SI-1000 Ljubljana, Slovenia

Advances in Planar Lipid Bilayers and Liposomes, Volume 10
ISSN 1554-4516, DOI: 10.1016/S1554-4516(09)10003-0

both types small vesicular dilatations were found as an integral part of the nanotubes (i.e., dilatations of the nanotubes, gondolas). Vesicular dilatations of type I nanotubes move along the nanotubes in both directions, while the vesicular dilatations of type II nanotubes do not move along the nanotubes. Both TNTs by themselves and the transporting gondolas were proposed to be involved in intercellular communication and transport. The possible mechanisms of stabilization of membrane nanotubular protrusions and TNTs are also discussed.

Abbreviations

CMFDA	5-Chloromethylfluorescein diacetate
DiD	1,1′-Dioctadecyl-3,3,3,3′-tetramethylindodicarbocyanine
DiI	1,1′-Dioctadecyl-3,3,3′3′-tetramethylindocarbocyanine
DiO	3,3′-Dilinoleyloxacarbocyanine
EFGP	Enhanced green fluorescent protein
FITC	Fluorescein isothiocyanate
GFP	Green fluorescent protein
GPI	Glycosyl-phosphatidylinositol
HLA, -B, -C	Human leukocyte class I antigens
TNTs	Tunneling nanotubes
TRITC	Tetramethylrhodamine isothiocyanate

1. Introduction

Cell-to-cell communication is one of the fundamental processes in the development and homeostasis of multicellular organisms. For this purpose organisms have evolved diverse mechanisms to communicate on the level of connected or/and spatially separated cells. The most common mechanisms depend on secretion of diffusible signal molecules (like hormones, growth factors) that bind to specific receptors in/on target cells [1]. A few years ago a novel type of cell-to-cell connection was discovered, where two spatially separated cells are connected by a long, thin tubular membranous structures [43]. They were named tunnelling nanotubes (TNTs) and are now known as membrane nanotubes. The membrane nanotubes were found in cultures and cocultures of both permanent cell lines and primary cultures (see Tables 1 and 2), mostly between cells that are weakly connected to each

Table 1 Human and animal cell lines shown to form TNTs and their characteristics

Cell lines forming TNTs		Morphology			Transferred cellular components (markers)		
(From)	Φ (diameter) l (length)	Prevalence; form	Cytosolic continuity	Junction[a]	Cytoskeleton (filament binding proteins)	Cytoplasmic components (dyes)	Membrane components (dyes)
Rat pheochromacytoma cells (PC12) [43]	Φ = 50–200 nm l = 16–60 μm	Few; straight, rarely branched, above substratum	ND	Yes	F-actin (myosin Va)	EGFP-actin	f-EGFP
Human embionic kidney cells (Hek-293) [15]	ND	Few	ND	ND	F-actin (myosin Va)	ND	(DiI, DiO, DiD)
Normal rat kidney cells (NRK) [15]	ND	Many: form ND	ND	ND	ND	Endocytic organelles (DiD)	(DiI, DiO, DiD)
Primary human T-cells [48]	Φ = 180–380 nm[a] l = 30–50 μm, some ≤ 200 μm	Many; straight, curved in 3D environment, rarely branched, above substratum	No[b]	Yes	F-actin	ND	ND
Jurkat T-cells [48]	Φ = ND l = ∼22 μm, some ≤ 100 μm in a 3D mimic of ECM	Many: straight, curved in 3D environment, rarely branched, above substratum	No[b]	Yes	F-actin	GFP, (CFDA, calcein)	GFP-I-CAM1, GFP-HLA-Cw7, GPI-GFP (DiO, DiD), HIV-1 Gag-GFP

(*continued*)

Table 1 (*continued*)

Cell lines forming TNTs		Morphology			Transferred cellular components (markers)		
(From)	Φ (diameter) l (length)	Prevalence; form	Cytosolic continuity	Junction[a]	Cytoskeleton (filament binding proteins)	Cytoplasmic components (dyes)	Membrane components (dyes)
EBV-transformed human B cell line (721.221) [41]	ND	ND	ND	ND	ND	ND	GPI-GFP, HLA-Cw6 in coculture with human peripheral blood NK cells
Transitional cell carcinoma of urinary bladder cells (T24) [51]	Φ = 60–200 nm l = most < 30 μm, some ≤ 120 μm	Many: multiple, straight, on the substratum, rare above substratum	Yes[b]	Yes	Only F-actin cytokeratin 7, F-actin + microtubules (α-tubulin)	Actin-GFP, (CMFDA)	Choleratoxin-GFP (DiI, DiO)
Transitional cell papillomaa of urinary bladder cells (RT4) (Lokar *et al.*, unpublished)	ND	Few, on the substratum	ND	ND	F-actin	ND	ND
DU 145 human prostate cancer cells [52]	Φ: thinner 100–200 nm, thicker (≥ 1 μm) l = few μm – 100 μm)		Yes	ND	Microtubules	Mitochondria (MitoTracker) lysosomes	ND
Human glioblastoma cells (U-87 MG) [42]	Φ = 42–54 nm l = tens of μm	Straight	ND	ND	F-actin	Vesicle trafficking under stress conditions	ND

THP-1 monocytes [40]	Φ = ~35–250 nm l = <100 μm	Many	Yes[b]	ND	F-actin	Ca^{2+} (Lucifer Yellow)	HLA-A,B, C class I MHC
Human hepatic cells (Hep G2) [54]	ND	Few	ND	ND	ND	ND	ND
Dendritic cells from peripheral blood monocytes [53]	Φ = ~35–250 nm l = <100 μm	Many	Yes[b]	ND	ND	Ca^{2+} (Lucifer Yellow)	HLA-A,B, C class I MHC
Human monocyte-derived macrophages [40, 41]	thin (<0.7 μm) thick (>0.7 μm)	Many: thick prevalent, most are connecting apical parts of the cells, some are branched	ND	No	F-actin, F-actin + microtubules	Endosomes (DiD) mitochondria Φ = (Mito Tracker) lysosomes (LysoTracker), EB1-GFP	ND
Primary rat astrocytes [17]	Φ = ~100 nm l = several μm l = <1 μm l = >100 μm	Many, branched	ND	ND	F-actin	ND	ND
Hematopoetic stem and progenitor cells [14]		No data				No data	
Bovine mammary gland epithelial cells (BMGE) [54]		No data				No data	
Primary cultures of mouse medulla [15]		No data				No data	
Murine macrophage J477 cells [40]		No data				No data	

ND — not determined.
[a] Was assessed by transmission electron microscopy.
[b] Was proved indirectly by measuring calcium fluxes.

Table 2 Cocultures of cell lines shown to form TNTs between different cell types

Coculture (from)	Transferred cellular component (dye)
PC12 and NRK cells [15]	Endosome related cell organelle (DiI, DiO, DiD)
PC12 and Hek-293 cells [15]	Endosome related cell organelle (DiI, DiO, DiD)
Hek-293 and NRK cells [15]	Endosome related cell organelle (DiI, DiO, DiD)
722.221 and NK cells cells [40]	Surface receptor HLA-Cw6-GFP
macrophages and NK cells [40]	ND, seen upon separation
Neonatal rat cardiomycites and adult human endothelial progenitor (EPC) cells [29]	Mitochondria (MytoTracker), GFP
Dendritic and THP-1 cells [40]	Ca^{2+}

other or in those which are actively migrating and seeking for bacteria or attachment to neighboring eukaryotic cells. Nanotubes exist also in cells with limited ability of movement and strong intercellular connections like epithelial cells. The diameter of these membrane nanostructures ranges from 30 to 400 nm, in some cases up to 1 μm, and their length can span for more cell diameters, depending on the cell type. They are versatile in ultrastructure and formation, and consequently also in function (reviewed by Refs. [9, 15]). Although TNTs are versatile, they share some common features like the presence of cytoskeleton and cytoskeleton-associated proteins. Through them different cellular material is being transported—from signaling molecules, soluble cytoplasmic proteins, membrane proteins and cell organelles [15, 16, 20, 21, 43, 51], to viruses [46, 47, 49] and bacteria. Viruses and bacteria are being transported only upon nanotube surfaces [41].

There is a considerable heterogeneity present between membrane nanotubes. They differ in their cytoskeletal composition, diameter, length, proposed function, ability to form cytoplasmic continuity. Ongoing studies of relatively young field in different cellular models are focused primarily on morphology, transported material and their frequency, but little is known about their biophysical properties, what factors influence their formation, what is the driving force of their formation, which protein complexes are involved in their dynamics and initiation of cell-to-cell contacts.

Considering their heterogeneity it is not an easy task to subdivide them ubiquitously into distinct types, since membrane nanotubes differ much from one cell type to another and their properties sometimes overlap between designated forms. Our classification of membrane nanotubes, in accordance with other authors, is presented in Fig. 1.

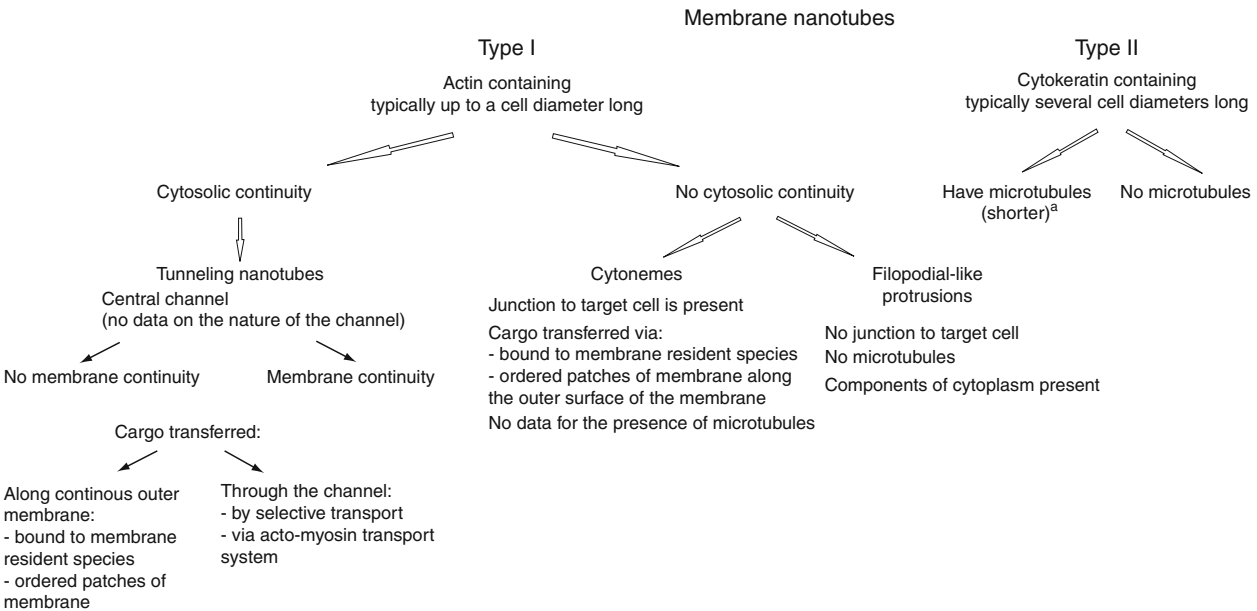

Figure 1 *Classification and forms of membrane nanotubes*. Criteria used for classification and their main properties are briefly described. Additional remarks are described in brackets. [a]Unpublished observation.

The focus of this chapter will be on the properties and formation of nanotubes found in urothelial cell line T24. In our studies phase contrast, fluorescence, time-lapse and electron microscopy were employed to study structural characteristics, formation, stability and dynamics of nanotubes that bridge two neighboring urinary bladder epithelial cells T24. Theoretical models of mechanical stabilization of membrane nanotubes are suggested.

2. T24 Cell Line and Membrane Nanotubes

Cells in a permanent cell line isolated from transitional cell carcinoma of urinary bladder epithelia are heterogenous, consisting of at least two morphologically distinct types [4]. Cells grow in a disorderly manner, forming a monolayer of cells, where individual cells are lying partly over one other. Cell population consists of two main types of cells: (i) large cells with large, round, light nuclei with scarce chromatin and numerous nucleoli, abundant and slightly pyronin-positive cytoplasm (pyronin is a ribonucleic acid dye) which is rather poor in organelles, with a few mitochondria and ribosomes; (ii) elongated cells with oval, darker nuclei, with many protrusions, abundant in chromatin and several nucleoli, more strongly pyroninphylic cytoplasm with numerous mitochondria and abundant endoplasmic reticulum. Cells contain numerous vacuoles of different sizes with inclusion bodies sometimes present. Cell membrane has many protrusions, especially at the basal edges of the cells, with nanotubes connecting cells close together (Fig. 2).

Membrane nanotubes are readily formed only between closely positioned cells of a subconfluent culture, where cells have a certain degree of freedom to move around on the substratum. The most appropriate conditions for studying their properties were found to be 70–80% confluent overnight cultures grown on glass coverslips, where cells were not yet mitotic and have enough space to form membrane protrusions.

2.1. Types of Membrane Nanotubes, Their Structural and Functional Properties

In subconfluent culture of T24 cells two distinct types of membrane nanotubes were identified and classified with respect to their cytoskeletal content, origin, stability and consequently their proposed function (Fig. 3).

2.1.1. Type I nanotubes

Type I nanotubes are shorter, usually not longer than 30 μm, dynamic structures and contain actin filaments. Actin filaments give them their dynamic properties. The protruding type I nanotubes are formed when a

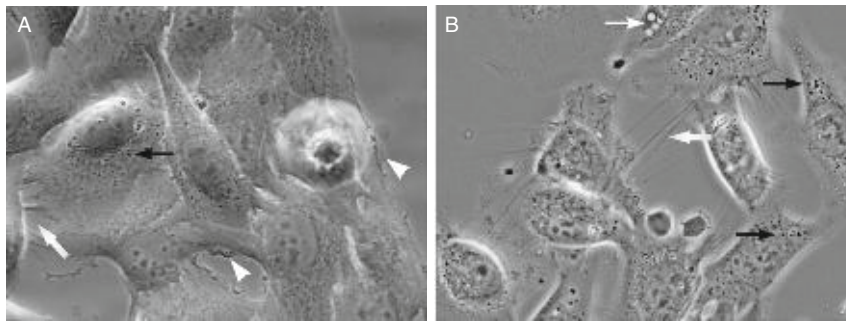

Figure 2 *T24 cell line, grown in normal conditions*. Cells are growing partly one over other. Note that the membrane of the cells on the edge of the cell island (indicated by arrowhead in (A) are not and firmly attached to the substratum along entire edge of the cell body, but at some places rather undulating with the cell membrane floating in the medium. Cells in the middle of the cell island are tightly connected with tubular connection forming between separating cells. Cells have numerous vacuoles (gray-white circular structures in cells, marked by white arrow in (B) and inclusion bodies (black circular structures in cells, marked by black arrows). Individual cells are connected by membranous nanotubes (wider white arrow).

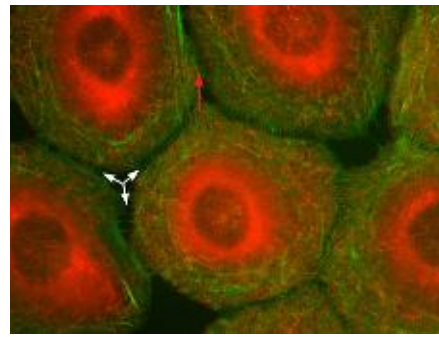

Figure 3 *T24 cell stained for actin (gray) and cytokeratin (white) filaments*. White arrows are pointing at multiple, acting containing type I nanotubes, whereas gray arrow is pointing at longer, cytokeratin containing type II nanotube (see also Fig. 11).

cell explores its surroundings, through a thin filopodial-like tubular membrane protrusion extending from basal part of the cell body in order to make contact with another cell (Figs. 4 and 5). This type of actin-containing nanotubes can also bridge cells at distances of less than 30 μm and is most likely derived from the adherence cell–cell contacts of cells that move apart as they appear higher on the cell body (Fig. 6). Type I nanotubes have no cytokeratin filaments (Fig. 5). Microtubules are present in some of type I nanotubes (Figs. 6B and 7). The primary function of these nanotubes seems to be intercellular communication by initiation of cell-to-cell contacts and

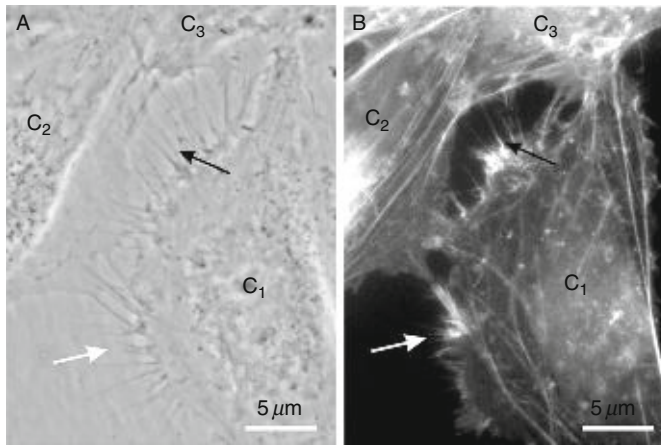

Figure 4 Type I nanotubes. (A) is a phase contrast image of live T24 cells while (B) is a fluorescence micrograph showing actin-TRITC labeling of the same cells as in A, after 15 min of paraformaldehyde fixation. Cell C1 is approaching the cells C2 and C3 (for animation see Supplementary material I in Ref. [51]). The white arrows in (A) and (B) indicate short and dynamic membrane protrusion with which the approaching cell explores its surroundings. Black arrow in (A) points at protrusions that have already connected to the target cell. In all these multiple tubular connections actin filaments are present (arrow in B). Adapted from Veranič *et al.* [51].

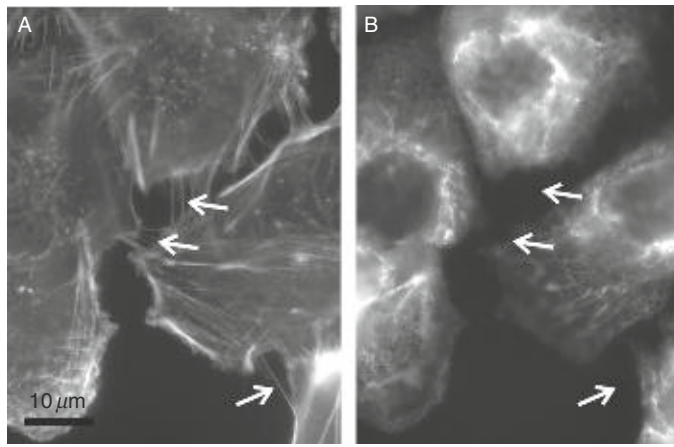

Figure 5 T24 cells stained for actin filaments with phalloidin-FITC (A) and cytokeratin filaments with anti-cytokeratin 7 antibodies (B). Arrows (in A and B) are indicating type I containing nanotubes that bridge two cells. These structures have no cytokeratin filaments.

subsequent transport of cellular components from one cell to another once a contact has been made. Their formation and stability is discussed in Section 3.

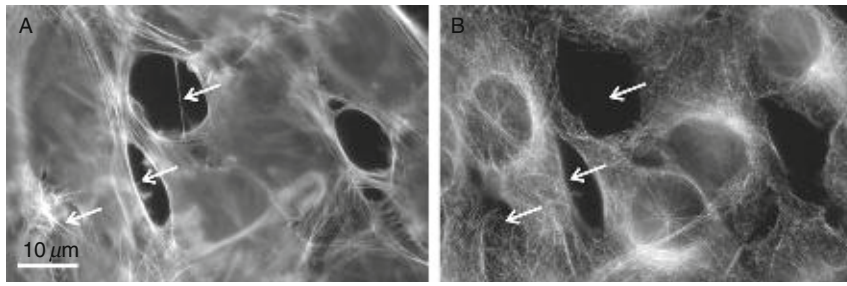

Figure 6 T24 cells stained for actin filaments with phalloidin (A) and microtubules with anti-alpha-tubulin antibodies (B). White arrows are pointing at actin containing nanotube connecting two separated cells. Dashed arrows are pointing at dynamic acting containing nanotubes with which cell is exploring its surroundings. These structures have no microtubules. Arrows in (B) are pointing at the same parts as in (A).

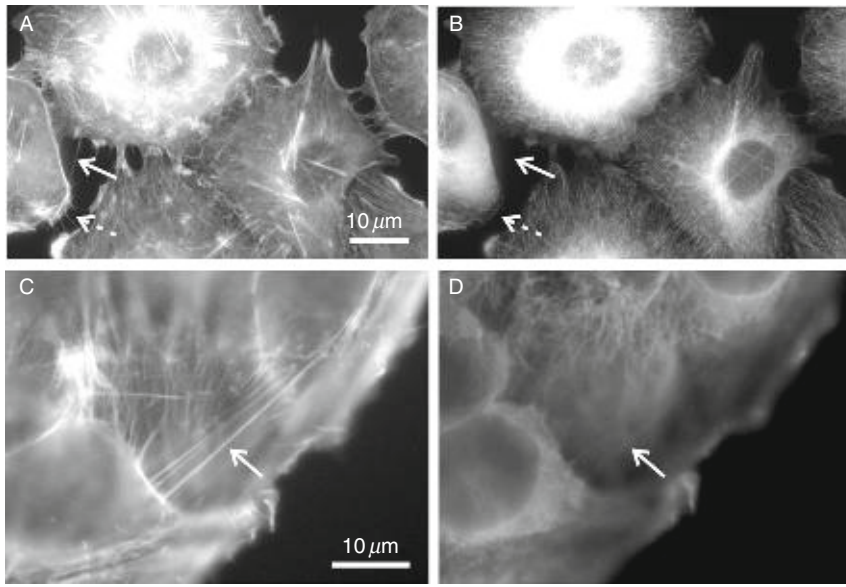

Figure 7 T24 cells stained for actin filaments with phalloidin (A and C) and microtubules with anti-alpha-tubulin antibodies (B and D). In type I nanotubules, that search the surroundings (indicated with dashed arrows in (A) and corresponding places in (B)) or connecting two neighboring cells (indicated with arrows in (A) and corresponding places in (B)), there is no microtubules. Microtubules can be found in intercellular connections of cells that are separating (arrows in (C) and corresponding places in (D)). See also Fig. 12A and B.

The protruding type I nanotubes start growing as filopodia at the basal level of the cell surface and continue to grow until they reach the target cell (Fig. 5), where the nanotube can attach by an anchoring type of intercellular

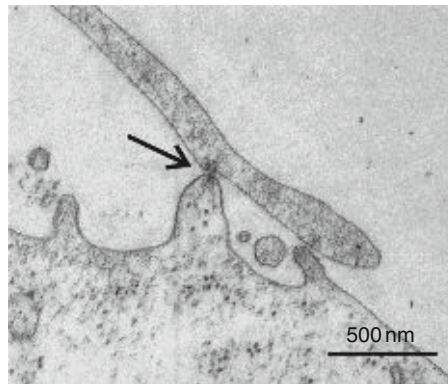

Figure 8 A TEM micrograph showing an anchoring type of intercellular junction (arrow) connecting a nanotubule to the protrusion of a neighboring cell. Adapted form Veranič *et al.* [51].

junction [43, 51] (Fig. 8). However, it is not much known about the nature of these contacts. The connection via nanotubules may not be initiated directly by contact of the tip of the membrane nanotube with the target membrane, but may require a nanotube first to slide along target cell membrane and connect to the cell via several adherens junctions at the lateral region of nanotube (Fig. 8) before the cytosolic continuity can be established via communication junction at the nanotube tip. These adhesion contacts might also be necessary for the nanotube to stabilize the contact with the target cell when it is ''searching'' for appropriate docking site for the communication junction to be formed.

Proteins responsible for formation of lateral connection of the nanotubes to the target cell most likely belongs to cadherin family, since these proteins were found at both tips and tubular regions of type I nanotubular protrusions (Fig. 9).

Nanotubes in T24 cell line can mediate cytosolic continuity [16, 51] even though no exchange of membrane labels could be found between cells [51] (Fig. 10).

2.1.2. Type II nanotubes

In comparison to abundant type I nanotubes, type II nanotubes are quite scarce. They are much longer, up to several 100 μm and appear to be more stable (Fig. 11). They are usually located more apically on the cell body. Type II nanotubes differ from all previously described nanotubes (which can be determined as type I nanotubes) by having no actin filaments but only cytokeratin filaments, which are probably responsible for their stability [37] and longer life span. Actin network is still present at both ends of the

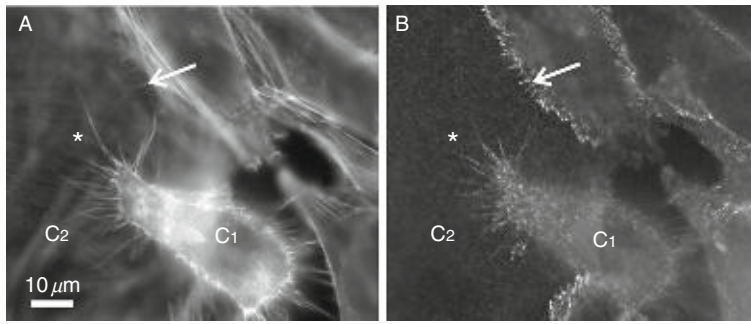

Figure 9 T24 cells stained for actin filaments with phalloidin-FITC (A) and anti-pan-cadherin antibodies (B). Cell C_1 is crawling upon cell C_2. Cadherins are present at cell–cell contacts (arrow) and actin containing nanotubes (asterix), even though not at all tips of the nanotubes.

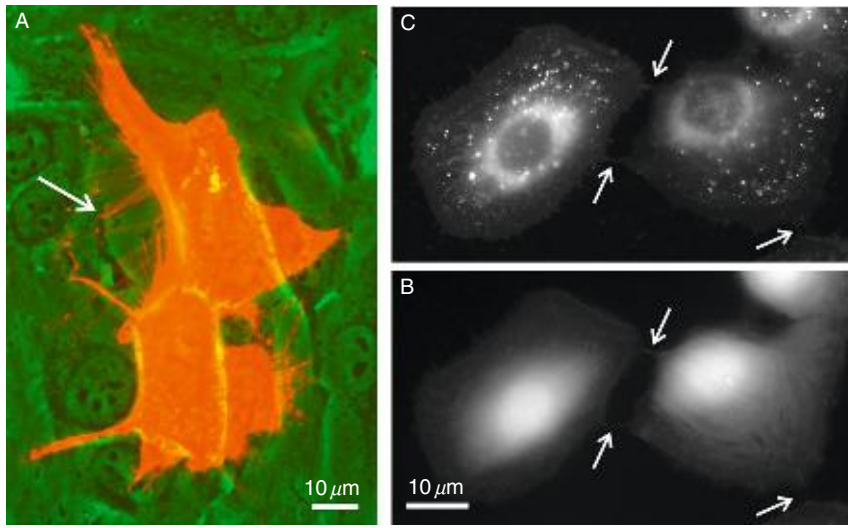

Figure 10 (A) Urothelial cells T24 labeled with lipophilic stain DiI were cocultured with unlabelled T24 cells. The nanotubes (arrow) of stained cells (white) became protruded and attached to unstained cells (gray) in 3 h. However, even after 24 h DiI stain did not spread to the connected cells. (B) and (C) Live urothelial cells T24 colabeled with lipophilic membrane stain DiI (B) and cytoplasmic dye CMFDA (C). Nanotubes are mediating cytoplasmic connection between two neighboring cells (arrows). Adapted from Veranič *et al.* [51].

nanotube, but as the nanotube narrows actin disappears. They may be formed when two already connected cells start to move apart (Fig. 12A and B). As is the case of type I nanotubes, microtubules are present in only some of type II nanotubes, mainly those which connect separating cells (Fig. 12C).

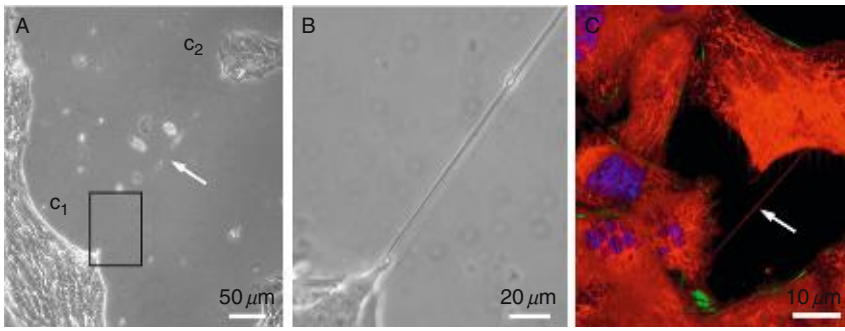

Figure 11 In urothelial line T24 a long tubular structure connects cells of the two cell clusters C_1 and C_2 (A). (B) is a magnified region of the area in the black frame in (A). Such long singular tubes of type II contain thin cytokeratin filaments (arrow in (C)). In C cytokeratin 7 is labeled in white, and actin in gray. From Veranič *et al.* [51].

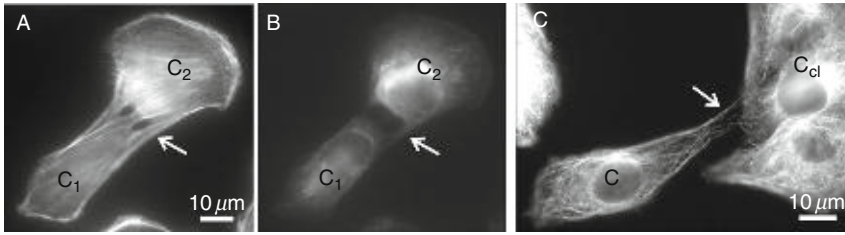

Figure 12 (A) and (B) Two separating T24 cells (C1 and C2) having actin (A) and cytokeratin (B) filaments present in the forming nanotubules. (C) Cells stained for alpha-tubulin. Cell (C) is migrating away from a cluster of cells (C_{cl}). Membranes of the two cells detach at certain sites forming tail-like protrusions between the membranes. The membranes gradually separate as the cells move apart, pulling and dividing their cytoskeletal content. Note that actin (A), cytokeratin (B) filaments, and microtubules (C) are still present in growing tubular connections (arrows in (A)–(C)). From Veranič *et al.* [51].

Type II nanotubes do not seem to be involved in transport between cells, but they rather provide a positional effect to connected cells by sensing their direction of migration and enabling reverted movement along the intercellular tether [51]. Since they are rare, their dynamics is still to be elucidated.

2.2. Vesicular Dilatations on Membrane Nanotubes

Many nanotubes have vesicular dilatations as an integral part of their membrane. Vesicular dilatations or gondolas, as we named them, can be seen in both types of nanotubes (Fig. 13), but they differ in size and dynamics.

Type I nanotubes frequently have smaller vesicular dilatations that can move along the tubes in both directions. These vesicular dilatations

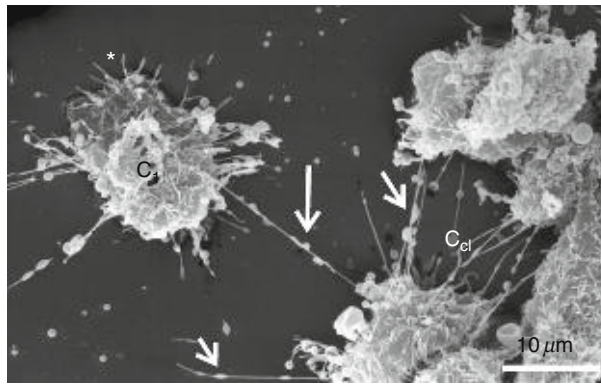

Figure 13 *A scanning electron micrograph of T24 cell line.* Nanotubular structures connect adjacent cells between cell cluster (C_{cl}) and cell C_1. Cell C_1 radially extends many thin filopodial-like tubular protrusions upon the substratum in the leading part of cell (asterix). It is connected to cell cluster by a longer nanotube, located higher on the cell body. On all nanotubes vesicular dilatations are present (arrows).

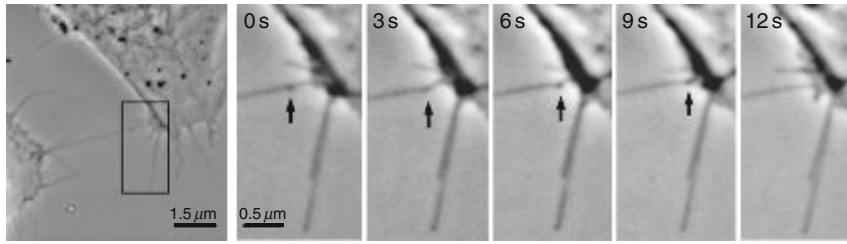

Figure 14 *Vesicular dilatation (gondola) on type I membrane nanotube (arrow).* Fusion of a gondola (black arrow) with a cell body is seen after a time-lapse sequence showing directional movement of the gondola along a nanotube. The time sequence in seconds is indicated on the upper left side of each micrograph. Adapted from Veranič *et al.* [53].

(gondolas) move for 5–15 μm in certain direction with an average speed of 40 nm/s [51]. They sometimes appear in the middle of the nanotube and travel along the nanotube until they fuse with the cell body (Fig. 14).

On the other hand, the dilatations on type II nanotubes are larger, usually placed in the middle of the nanotube and do not move along the nanotube (Fig. 15).

2.2.1. Possible origins of vesicular dilatations and mechanisms of their propagation along nanotubes

The observed vesicular dilatations of the nanotubes (gondolas) moving along the type I nanotubes (Fig. 16) may be formed in different ways. In some cases the formation of gondolas, corresponding to transient excited states, may be induced by a sudden tension (caused, e.g., by diverging or

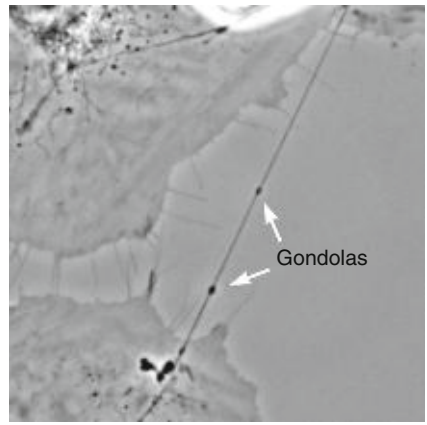

Figure 15 Vesicular dilatations (gondolas) on type II membrane nanotubes.

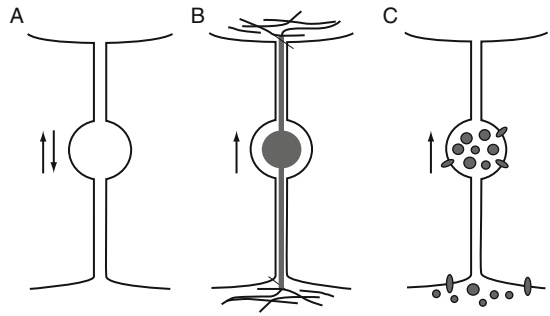

Figure 16 *Possible origins of gondola formation and its movement along a nanotube*. The direction of its movement is indicated by arrows. The distention of the nanotubule (gondola) may be formed in different ways. In illustration (A) the distention is formed because of sudden tension (caused by diverging cells) in the membrane at specific sites on the nanotube, where local constituents enable and favor the formation of this structure. This kind of distention may appear anywhere along the nanotube and travels in the direction that is energetically favorable. In illustrations (B) the distention is formed because material inside the gondola is actively transported along the filaments by motor proteins ([41, 43]). The total volume of the enclosed material (an organelle or a vesicle) is larger than the inner diameter of the nanotube. Transported material (multiple small particles moving synchronously within the distension) may be enclosed within gondola or may be a part of the gondola membrane. Illustration C schematically indicates nanotubule-directed movement of the gondola, formed in the budding process.

approaching cells) in the membrane nanotubes at specific sites where the local membrane constituents of the nanotubes enable and favor the formation of such dilatations. The tension-induced dilatation of the nanotubes may appear anywhere along the nanotube and then travels as a wave along

the nanotube in the direction that is energetically favorable. The tension might be the most probable reason of gondolas that suddenly appear in the middle of the nanotube [51]. These tension-induced dilatations are as any other excited states of the membrane relaxed after a certain time. It has been reported that slight undulations are relaxed in seconds while sphere-like blobs are relaxed in minutes [2].

The vesicular dilatations of the nanotubes may also be formed because of a small organelle, vesicle or supramolecular assembly (multiple small particles moving synchronously within the distension) is being transported inside the nanotubes, if their effective diameter is larger than the inner diameter of the nanotube [15, 27, 51]. The material inside the nanotubes may be actively transported by different actomyosin-dependent mechanisms ([15, 40], reviewed by Ref. [8]). These dilatations are forming at the beginning of the nanotube of one cell as a vesicle-like structures, are transported along the nanotube and are then released into the cytoplasm of the second cell (see Fig. 17).

The observed vesicular dilatations of the nanotubes moving along the membrane nanotubes of type I show striking similarity to the dilatations of phospholipid nanotubes, which move along these nanotubes [24]. Therefore it is also possible that the initiation of gondola formation (Fig. 17A) may be based on similar physical mechanisms as those governing the formation of free membrane daughter vesicles, which are created in the processes of budding. In contrast to the latter process however, in gondolas, the connection to the parent membrane, from which they originate is not disrupted when the dilatation is detached from the parent cell (Fig. 17B). Once the gondola is formed, its movement along the nanotube (Fig. 17C) requires no additional bending energy. Nevertheless, a mechanism is still needed to provide the energy for the dilatation to travel along the nanotube. It is possible that the gondola movement is driven by the difference in chemical potentials between the molecules packed inside the gondola and the

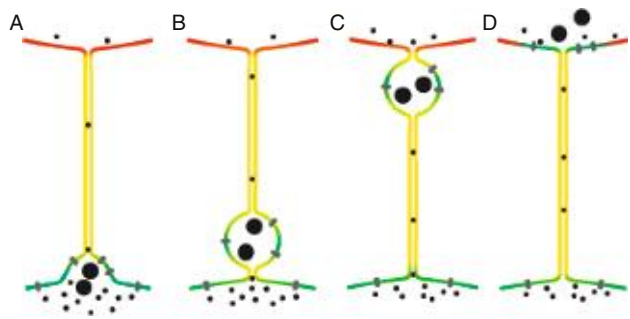

Figure 17 Schematic illustration of nanotubule-directed transport of small vesicular dilatations (gondolas) transporting granular content and membrane particles.

molecules in the interior of the target cell, or the difference in chemical potential between the molecules composing the membrane of the gondola and the molecules in the membrane of the target cell. The final event of the transport is the fusion of the gondola with the target membrane [24]. In this process, molecules of the gondola's membrane which originate from the parent, nearly flat membrane, redistribute again in an almost flat target membrane (Fig. 17D). This may be energetically favorable and therefore also part of a driving mechanism to facilitate fusion of the gondola with the membrane. Prior to fusion of the gondola with the target cell membrane, no neck formation is needed (Fig. 17C) since the neck is already part of the nanotube connecting the gondola to the membrane of the target cell. This is contrary to the case of a free transport vesicle. It can therefore be concluded that the transport of material in dilatations (or the transport of molecules composing the membrane of dilatations) may be more efficient, since it is guided either by actomyosin transport system or passive diffusion along the nanotube, and therefore energetically advantageous over free vesicle transport.

3. Formation and Stability of Type I Membrane Nanotubes

Membrane nanotubes are thin, dynamic structures, but nevertheless at least transiently stable structures. We presume they are formed on (and between) specific surface regions on the cell membrane where the local environment favors their molding and stabilization (or attachment). There are several factors that influence their dynamics and stability, the major players being cytoskeleton and membrane constituents.

Although the underlying cytoskeleton greatly influences their shape, molding and mechanical stability, its primary role may not be in formation of very first steps of nanotubules but rather in strengthening the already formed membrane protrusions (nanotubular buds), to provide the core which pushes the membrane outward and on which transport of material is being conduced once the nanotube is connecting two cells. The protruding type I nanotubes in the beginning of their formation resemble the growth of flilopodia (for review see Ref. [36]). Therefore it is likely that an actin cross-linker, like facsin [57], may be involved in the growth of type I membrane nanotube, by helping to organize actin filaments into parallel and nearly aligned filamentous bundles which push the membrane outward and in the stabilization of the nanotubes by increasing the stiffness of these bundles, therefore giving the tubular part of the nanotube the necessary mechanical support ([15, 40, 53, 57]). However, protrusions of this kind remain stable even after disintegration of the actin filaments with cytochalasin D (Fig. 18), that is, without the force of cytoskeleton

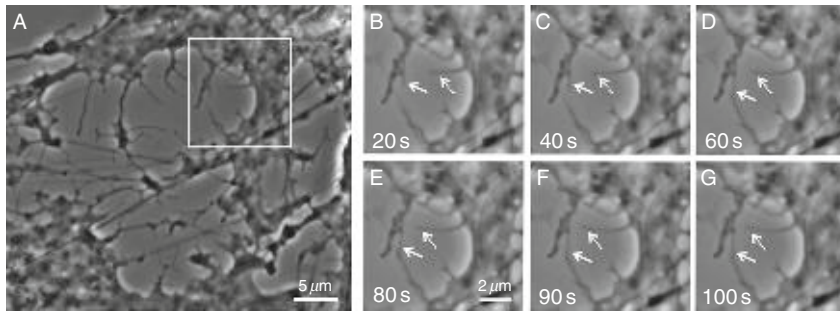

Figure 18 *T24 cells after cytochalasin D treatment (A).* **After incubation in cytochalasin D for 30 min, a time-lapse sequence was recorded. The flexible stability of type I membrane protrusions of T24 cells can be seen by time-lapse sequence in frames B–G (magnified region of squared area in (A)). The white arrows in these frames point to the tip of two nanotubes that passively move in the solution. Times indicated is the time passed from the beginning of the time-lapse sequence. From Veranič *et al.* [51].**

elements which would push the membrane tubular protrusion outward, leaving protrusions freely diffusing in solution. These results indicate that there must also be other factors stabilizing the nanotube in addition to cytoskeleton.

Possible candidates for the stabilization of nanotubular structures are membrane nanodomains. Their membrane constituents: phospholipids, cholesterol and proteins, and their interactions with each other, may have primary role in the formation of nanotubes by forming flexible membrane nanodomains [27] (including membrane rafts) that selfaggregate at sites of the forming nanotube and thus enable the formation of nanotubular tips (see Fig. 25). They stabilize the structure in the tubular region, once the nanotube is already protruding from the membrane. This process depends on the local curvature of the membrane, which is—in turn—determined by the local composition of its constituents, their intrinsic shape and interactions with the neighboring molecules (see also Section 3, Fig. 25). In favor of this assumption is that the tips of the nanotubes tend to accumulate ganglioside GM1 (Fig. 19) as one of the characteristic components of membrane nanodomains referred to as membrane rafts. Membrane rafts are small (10–200 nm), heterogeneous, highly dynamic, sterol- and sphingolipid-enriched domains that compartmentalize cellular processes. Small rafts can sometimes be stabilized to form larger platforms through protein–protein and protein–lipid interactions [58]. The appearance of membrane rafts in vesicular protrusions at the tip of the nanotubes might also be crucial for the attachment of the nanotube to the target cell, because among proteins included in lipid raft domains N-cadherins were also found [6]. These cadherins are responsible for making intercellular connections between mesenchymal cells and are also found in urothelial T24 cells (Fig. 9).

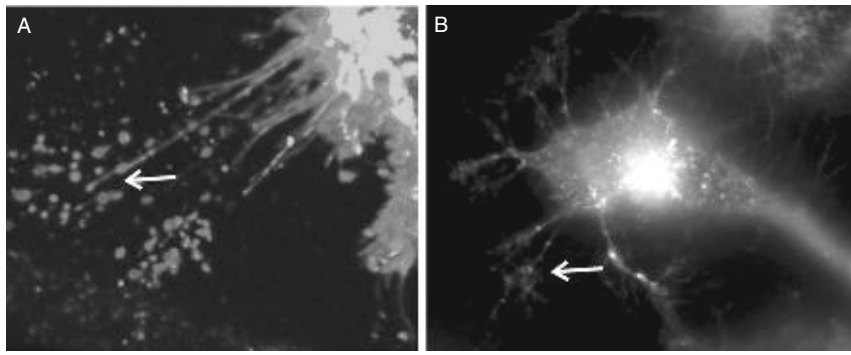

Figure 19 Membrane rafts are present at the tips and entire length of the nanotubes as well as on cell body. Cells were stained with a membrane raft marker choleratoxin B (arrows) that binds G_{M1}, a membrane raft resident ganglioside.

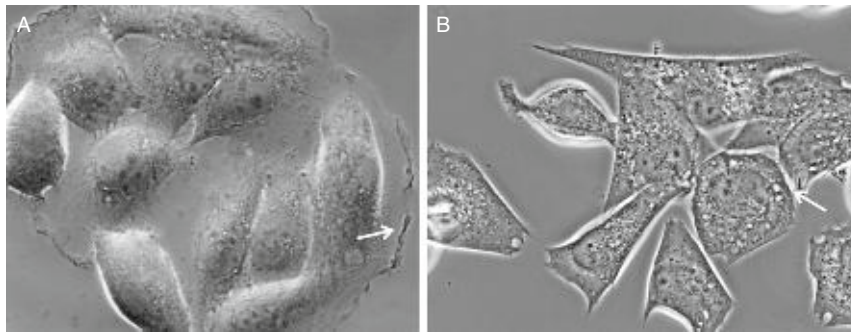

Figure 20 *Control (A) and cholesterol depleted cells (B) and their morphology*. In cholesterol depleted cells the cells round and their membrane appears more rigid with no dynamically fluctuating protrusions at the cell edges like in control (arrow in (A)). Their shape is rather determined by the underlying cytoskeleton. Cells do not appear firmly attached to each other anymore, although they still preserve some connections (arrow in (B)).

Since nanodomains are thought to be important in both formation and stability of nanotubes and these nanostuctures are shown to be enriched in cholesterol (Pike *et al.*, 2006) it is expected that content of cholesterol in the membrane will influence also the dynamic of nanotubes. Cholesterol decreases membrane fluidity, locally increases membrane thickness and can directly modulate the dynamics of membrane rafts-associated proteins (reviewed in Ref. [39]) as well as cell-to-cell junctions [10, 38].

Our preliminary results show that depletion of cholesterol by β-methyl cyclodextin changes morphology of T24 cells as well as almost totally inhibits formation of type I membrane nanotubes, whereas the effect on type II nanotubes is not known (no experimental data) (Fig. 20).

3.1. On the Role of Small Anisotropic Protein–Lipid Nanodomains in Formation and Stabilization of Membrane Nanotubes

The observed stability of tubular membrane protrusions after disintegration of the actin filaments within tubular protrusions (Fig. 18) can be explained by coupling between the nonhomogeneous lateral distribution of the membrane nanodomains and the specific membrane curvatures [5, 22, 25, 45, 50]. The proposed mechanism of mechanical stabilization of tubular membrane protrusions is a part of the general mechanism of stabilization of highly curved membrane structures (spherical buds, necks, tubular protrusions) [5, 18, 23, 26, 28, 49, 50]. For example, it was suggested that due to its specific molecular shape the prominin molecules [56] may form small anisotropic protein–lipid nanodomains [26, 27] which may associate into larger two-dimensional aggregates accumulated in tubular membrane protrusions (Lubrol rafts) [23, 26, 28, 59]. Lubrol rafts, formed by clustering of prominin nanodomains, are considered to be a novel type of membrane rafts (microdomains) that are distinct from the cholesterol-sphingolipid (Triton resistant) rafts in the planar parts of the membrane [23, 28, 59].

The prevalent force of the origin of membrane protrusion is usually the force exerted by the cytoskeleton elements [3]. However, also in this case, the accumulation of anisotropic membrane nanodomains in tubular membrane protrusions may offer an additional physical mechanism for stabilization of tubular membrane protrusions [26, 32, 55]. The observed stability of thin tubular membrane protrusions without the inner supporting rod-like skeleton (Fig. 18) is in line with the assumption that prominin nanodomains (and other anisotropic membrane inclusions) have an important role in generation and stabilization of plasma membrane protrusions and TNTs; [26, 28] (Fig. 21).

In accordance with above proposed mechanism of stabilization of tubular membrane protrusions we proposed [51] that membrane nanodomains (Fig. 21) which compose the membrane of bridging nanotubes energetically prefer highly curved cylindrical geometry ($C_1 > 0$ and $C_2 = 0$) (for definition of the principal membrane curvatures C_1 and C_2 see Fig. 22).

In our model [12, 27] we divide the flexible membrane nanodomains in two groups. In the first are small molecular complexes composed of proteins and lipids where the proteins are often chain-like biopolymers that cross the membrane bilayer a few times (Fig. 21A) [22, 26]. Membrane nanodomains and raft elements of biological membranes usually fall into this category. The second group of flexible membrane inclusions are induced by a single rigid globular membrane protein, which can be described in the first approximation as a rigid object of a simple geometrical shape (Fig. 21B) [7, 8, 11, 12, 19, 30, 31].

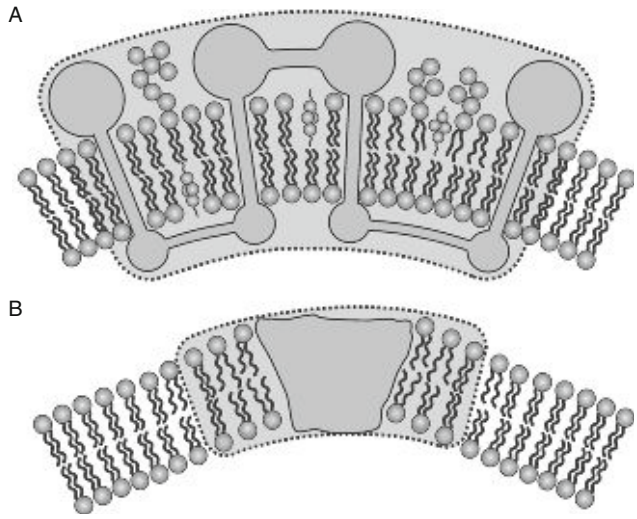

Figure 21 *Schematic illustration of membrane nanodomains (shaded area)*: A flexible lipid-protein membrane nanodomain containing transmembrane proteins (A) and a flexible membrane nanodomain induced by single membrane-embedded rigid (globular) protein (B) [12].

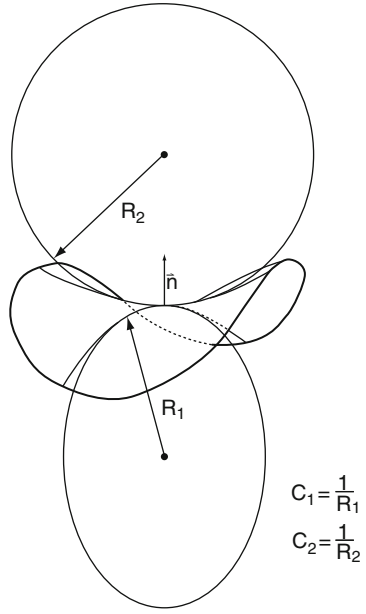

Figure 22 Schematic presentation of the two principal membrane curvatures C_1 and C_2 (for the case of saddle-like membrane shape) defined in the origin of the membrane normal n. The principal curvatures C_1 and C_2 are inversely proportional to principal radii of curvatures R_1 and R_2, respectively.

In the following we assume that membrane nanodomains (Fig. 21), as a result of their structure and local interactions energetically prefer a local geometry that is described by the two intrinsic principal curvatures (C_{1m} and C_{2m}) [13, 31, 36]. The intrinsic principal curvatures (spontaneous curvatures) (C_{1m} and C_{2m}) are in general different ($C_{1m} \neq C_{2m}$) (Fig. 23). If they are identical ($C_{1m} = C_{2m}$), the nanodomain is called isotropic. If $C_{1m} \neq C_{2m}$ the nanodomain is called anisotropic. The location and orientation of the anisotropic nanodomain are important for its energy. An anisotropic nanodomain (Fig. 24) will therefore prefer to accumulate in the membrane region with the principal curvatures C_1 and C_2 close to the values of its intrinsic principal curvatures C_{1m} and C_{2m} [22, 26] and on the average also spend more time in the orientation that is energetically more favorable than in any other orientation. A coupling between the membrane shape (i.e., curvature) and the nonhomogeneous lateral distribution of membrane nanodomains has been predicted [5, 18, 22, 25, 27, 45, 50].

The elastic energy of a small anisotropic membrane nanodomain derives from the mismatch between the actual local curvature of the membrane (Fig. 22) and the intrinsic (spontaneous) curvature of the constituents (Fig. 23) which can be characterized by the mismatch tensor $\underline{M} = \underline{R}\underline{C}_m\underline{R}^{-1} - \underline{C}$ [27]. Here the tensor $\underline{C}$ describes the actual curvature (see Fig. 22), while the tensor $\underline{C}_m$ describes the intrinsic curvature of the constituents:

$$\underline{C} = \begin{bmatrix} C_1 & 0 \\ 0 & C_2 \end{bmatrix}, \quad \underline{C}_m = \begin{bmatrix} C_{1m} & 0 \\ 0 & C_{2m} \end{bmatrix}, \tag{1}$$

where

$$\underline{R} = \begin{bmatrix} \cos\omega & -\sin\omega \\ \sin\omega & \cos\omega \end{bmatrix}, \tag{2}$$

is the rotation matrix. The angle ω describes the orientation of the principal axes system of a single membrane nanodomain with respect to the local principal axes system of the membrane [28, 32]. In the respective principal

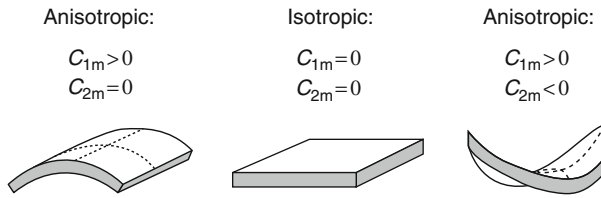

Figure 23 Schematic representation of different intrinsic shapes of larger of membrane nanodomains described by the two intrinsic principal (spontaneous) curvatures C_{1m} and C_{2m}.

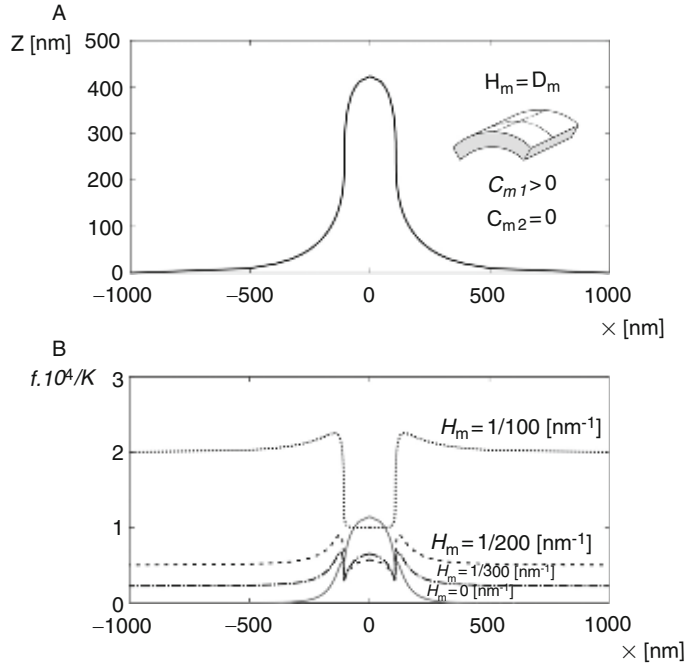

Figure 24 Normalized free energy of single membrane nanodomain (f_i/K) in different regions of tubular membrane protrusion and its surroundings calculated for three different shapes of membrane nanodomain characterized by $H_m = D_m$: 1/100 nm^{-1}, 1/200 nm^{-1}, 1/300 nm^{-1} and $K = -\overline{K} = 5000kT\,nm^2$ (B). The planar shape when $H_m = D_m = 0$ nm^{-1} was added for comparison ((B) gray line). We assume the axis-symmetric shape of spiculum as presented in (A).

systems the matrices that represent curvature tensors $\underline{C}$ and $\underline{C}_m$ include only the diagonal elements (for tensor $\underline{C}$ the principal curvatures C_1 and C_2 (Fig. 22) and for tensor $\underline{C}_m$ the intrinsic principal curvatures C_{1m} and C_{2m}).

The elastic energy of the membrane nanodomain (f_i) should be a scalar quantity. Therefore, each term in the expansion of f_i must also be scalar, that is, invariant with respect to all transformations of the local coordinate system. In this work, the energy of nanodomain is approximated by an expansion in powers of invariants of the tensor $\underline{M}$ up to the second order in the components of $\underline{M}$. The trace and the determinant of the tensor are taken as the set of invariants [27]:

$$f_i = \frac{K}{2}(\mathrm{Tr}\,\underline{M})^2 + \overline{K}(\mathrm{Det}\,\underline{M}), \tag{3}$$

Where K and $\overline{K}$ are constants. Taking into account the definition of the tensor $\underline{M}$ it follows from Eq. (3) that the elastic energy of the single membrane nanodomain can be written as [27]:

$$f_i = [(2K + \overline{K})(H - H_m)^2 - \overline{K}(D^2 - 2DD_m\cos 2\omega + D_m^2)], \tag{4}$$

where $H=(C_1+C_2)/2$ and $D=|C_1-C_2|/2$ are the mean curvature and the curvature deviator of the membrane (see also Fig. 22), $H_m=(C_{1m}+C_{2m})/2$ is the intrinsic (spontaneous) mean curvature and $D_m=|C_{1m}-C_{2m}|/2$ is the intrinsic (spontaneous) curvature deviator. The constants K and $\overline{K}$ are proportional to the area of the single membrane nanodomain [12, 27]. In the case of a simple flexible membrane nanodomain composed of a rigid core (protein) and the surrounding lipids which are distorted in order to fit with the rigid core (Fig. 21), the constants K and $\overline{K}$ were estimated using a microscopic model [12] while in the case lipid molecules they were estimated from the bending constant [34, 35]. The optimal values of the membrane mean curvature H, the curvature deviator D and the membrane constituent orientation angle ω corresponding to the minimum of the function f_i can be calculated from the necessary and sufficient conditions for the extremum of f_i [27]: $H=H_m$, $D=D_m$, $\omega=0,\ \pi,\ 2\pi$ where $\omega=0$ and $\omega=2\pi$ describe the same orientation and where $K>-\overline{K}/2$, $\overline{K}<0$.

The partition function of a single anisotropic membrane nanodomain:

$$Q=\frac{1}{\omega_o}\int_0^{2\pi}\exp\left(-\frac{f_i(\omega)}{kT}\right)d\omega, \tag{5}$$

The free energy of the single anisotropic nanodomain is then obtained by considering that $f_i=-kT\ln Q$ [27]:

$$f_i=(2K+\overline{K})(H-H_m)^2-\overline{K}(D^2+D_m^2)-kT\ln\left(I_0\left(\frac{2\overline{K}DD_m}{kT}\right)\right), \tag{6}$$

where I_0 is the modified Bessel function. In the limit $|2\overline{K}DD_m/kT|>1$, Eq. (6) becomes:

$$f_i=(2K+\overline{K})(H-H_m)^2-\overline{K}(D-D_m)^2, \tag{7}$$

where we took into account that $\ln I_0(x)\approx|x|$ for $x>1$ and $\overline{K}<0$. In the limit of small $|2\overline{K}DD_m/kT|$, Eq. (6) transforms into:

$$f_i=\left(2K-\frac{\overline{K}^2D_m^2}{kT}\right)(H-H_0)^2+\left(\overline{K}+\frac{\overline{K}^2D_m^2}{kT}\right)C_1C_2, \tag{8}$$

$$H_0=\frac{H_m(2K+\overline{K})}{\left(2K-\frac{\overline{K}^2D_m^2}{kT}\right)}, \tag{9}$$

where we took into account $\ln I_0(x)\approx x^2/4$ for $x<<1$, $D^2=H^2-C_1C_2$ and omitted the constant term.

Figure 24 shows the influence of the anisotropy of the intrinsic shape of the membrane nanodomain (described by intrinsic mean curvature

$H_m = (C_{1m} + C_{2m})/2$ and intrinsic curvature deviator $D_m = (C_{1m} - C_{2m})/2$) on the energy of the nanodomain f_i (Eq. (6)) in the different parts of the tubular membrane protrusions and the surrounding membrane. It can be seen in Fig. 24 that the energy of anisotropic nanodomains (f_i) with the intrinsic shape characterized by $H_m = D_m$ (or equivalently $C_{1m} > 0$ and $C_{1m} = 0$, see Fig. 23) may be strongly decreased in the region of tubular protrusion which leads to accumulation of such nanodomains in the tubular membrane protrusion and consequently to mechanical stabilization of tubular membrane protrusions as shown elsewhere [26, 27, 32, 33, 51].

Based on the results presented in Fig. 24 and our previous theoretical consideration of the stability of tubular membrane protrusions [26, 27, 32, 33] we suggest that nanotubular membrane protrusions and membrane nanotubes are in addition to stabilization forces of cytoskeleton elements mechanically stabilized also by energetically favorable clustering of anisotropic (flexible) membrane nanodomains in nanotubes [17, 26, 27, 51] (Fig. 25).

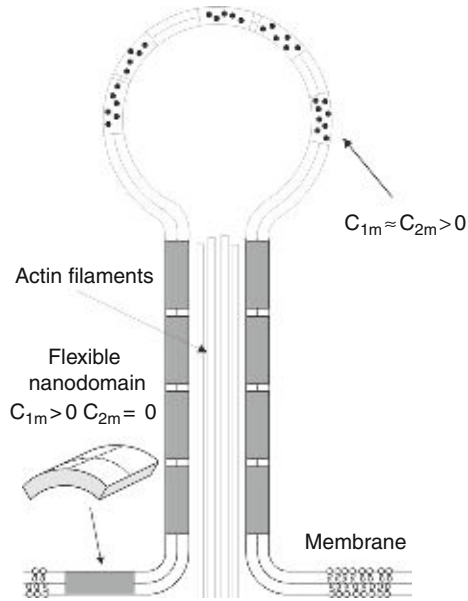

Figure 25 Schematic illustration of stabilization of type I nanotubular membrane protrusions by accumulation of anisotropic membrane nanodomains in the tubular region. Bending deformation and rotation of the nanodomain allow the nanodomain to adapt its shape and orientation to the actual membrane curvature, which in turn is influenced by the nanodomains [23,28]. Growing actin filaments push the membrane outward. The protrusion is additionally stabilized by accumulated anisotropic nanodomains with membrane curvatures that favor anisotropic cylindrical geometry of the membrane. The cylindrical-shaped anisotropic membrane domains, once assembled in the membrane region of a nanotubular membrane protrusion, keeps the protrusion mechanically stable even if the cytoskeletal components (actin filaments) are disintegrated. Adaped from [46].

4. Concluding Remarks

In urothelial T24 cell line at least two different kinds of membrane nanotubes exist. These two types differ in their structural components (type I having actin cytoskeleton and type II having cytokeratins) stability, dynamics and consequently also in function. Type II nanotubes do provide cytosolic and membrane continuity between two cells, at least in the beginning, since they are presumably formed in nonmitotic separation of two cells. As for type I nanotubes cytosolic continuity can be established after an adherens and communication junctions between a protruding nanotube and acceptor cell is assembled even though their protein components have not been undoubtedly determined. Which proteins make this possible need to be further defined. Also the stability of these nanotubules is not well understood, but ongoing studies are suggesting that both cholesterol and lipid constituents that determine the local geometry of the membrane are important in this process.

REFERENCES

[1] B. Alberts, A. Johnson, J. Lewis, M. Raff, K. Roberts, P. Walter, Molecular Biology of the Cell, 4th ed., Garland Science, New York, 2002.
[2] R. Bar-Ziv, E. Moses, Instability and "pearling" states produced in tubular membranes by competition of curvature and tension, Phys. Rev. Lett. 73 (1994) 1392–1395.
[3] A.A. Boulbitch, Deflection of a cell membrane under application of local force, Phys. Rev. E 57 (1998) 1–5.
[4] J. Bubeník, M. Baresová, V. Viklický, J. Jakoubková, H. Sainerová, J. Donner, Established cell line of urinary bladder carcinoma (T24) containing tumour-specific antigen, Int. J. Cancer 11 (1973) 765–773.
[5] L. Cantu', M. Corti, P. Brocca, E. del Favero, Structural aspects of ganglioside-containing membranes, Biochim. Biophy. Acta 1788 (2009) 202–208.
[6] M. Causeret, N. Taulet, F. Comunale, C. Favard, C. Gauthier-Rouvière, N-cadherin association with lipid rafts regulates its dynamic assembly at cell-cell junctions in C2C12 myoblasts, Mol. Biol. Cell. 16 (2005) 2168–2180.
[7] N. Dan, P. Pincus, S.A. Safran, Membrane-induced interactions between inclusions, Langmuir 9 (1993) 2768–2771.
[8] N. Dan, S.A. Safran, Effect of lipid characteristics on the structure of transmembrane proteins, Biophys. J. 75 (1998) 1410–1414.
[9] D.M. Davies, S. Sowinski, Membrane nanotubes: dynamic long-distance connections between animal cells, Nat. Rev. Mol. Cell Biol. 9 (2008) 431–436.
[10] S.A. Francis, J.M. Kelly, J. McCormack, R.A. Rogers, J. Lai, E.E. Schneeberger, R.D. Lynch, Rapid reduction of MDCK cell cholesterol by methyl-beta-cyclodextrin alters steady state transepithelial electrical resistance, Eur. J. Cell Biol. 78 (1999) 473–484.
[11] M. Fošnarič, A. Iglič, S. May, Influence of rigid inclusions on the bending elasticity of a lipid membrane, Phys. Rev. E 174 (2006) 051503.

[12] M. Fošnarič, A. Iglič, T. Slivnik, V. Kralj-Iglič, Flexible membrane inclusions and membrane inclusions induced by rigid globular proteins, Advances in planar lipid bilayers and liposomes, Elsevier, (2008) 143–168.
[13] J.B. Fournier, P. Galatola, Bilayer membranes with 2-D nematic order of the surfactant polar heads, Braz. J. Phys. 28 (1998) 329–338.
[14] D. Freund, N. Bauer, S. Boxberger, S. Feldmann, U. Streller, G. Ehninger, C. Werner, M. Bornhäuser, J. Oswald, D. Corbeil, Polarization of human hematopoietic progenitors during contact with multipotent mesenchymal stromal cells: effects on proliferation and clonogenicity, Stem Cells Dev. 15 (2006) 815–829.
[15] H.H. Gerdes, N.V. Bukoreshtliev, J.F. Barroso, Tunneling nanotubes: a new route for the exchange of components between animal cells, FEBS Lett. 581 (2007) 2194–2201.
[16] H.H. Gerdes, R.N. Carvalho, Intercellular transfer mediated by tunneling nanotubes, Curr. Opin. Cell Biol. 20 (2008) 470–475.
[17] U. Gimsa, A. Iglič, S. Fiedler, M. Zwanzig, V. Kralj-Iglič, L. Jonas, J. Gimsa, Actin is not required for nanotubular protrusions of primary astroctes grown on metal nanolawn, Mol. Membr. Biol. 24 (2007) 243–255.
[18] W.T. Góźdź, Diffusion of macromolecules on lipid vesicles, Langmuir 24 (2008) 12458–12468.
[19] H. Gruler, Chemoelastic effect of membranes, Z. Naturforsch. [C] 30 (1975) 608–614.
[20] S. Gürke, J.F. Barroso, E. Hodneland, N.V. Bukoreshtliev, O. Schlicker, H.H. Gerdes, Tunneling nanotube (TNT)-like structures facilitate a constitutive, actomyosin-dependent exchange of endocytic organelles between normal rat kidney cells, Exp. Cell Res. 314 (2008) 3669–3683.
[21] S. Gürke, J.F. Barroso, H.H. Gerdes, The art of cellular communication: tunneling nanotubes bridge the divide, Histochem. Cell Biol. 129 (2008) 539–550.
[22] H. Hägerstrand, L. Mrówczyńska, U. Salzer, R. Prohaska, K. Michelsen, V. Kralj-Iglič, A. Iglič, Curvature-dependent lateral distribution of raft markers in the human erythrocyte membrane, Mol. Membr. Biol. 23 (2006) 277–288.
[23] J.C. Holthius, G. van Meer, K. d'Huitema, Lipid microdomains, lipid translocation and the organization of intracellular membrane transport (review), Mol. Membr. Biol. 20 (2003) 231–241.
[24] A. Iglič, H. Hägerstrand, M. Bobrowska-Hägerstrand, V. Arrigler, V. Kralj-Iglič, Possible role of phospholipid nanotubes in directed transport of membrane vesicles, Phys. Lett. 310 (2003) 493–497.
[25] A. Iglič, M. Fošnarič, H. Hagerstrand, V. Kralj-Iglič, Coupling between vesicle shape and the non-homogeneous lateral distribution of membrane constituents in Golgi bodies, FEBS Lett. 574/1–3 (2004) 9–12.
[26] A. Iglič, H. Hägerstrand, P. Veranič, A. Plemenitaš, V. Kralj-Iglič, Curvature induced accumulation of anisotropic membrane components and raft formation in cylindrical membrane protrusions, J. Theor. Biol. 240 (2006) 368–373.
[27] A. Iglič, M. Lokar, B. Babnik, T. Slivnik, P. Veranič, H. Hägerstrand, V. Kralj-Iglič, Possible role of flexible red blood cell membrane nanodomains in the growth and stability of membrane nanotubes, Blood Cells Mol. Dis. 39 (2007) 14–23.
[28] P. Janich, D. Corbeil, GM_1 and GM_3 gangliosides highlight distinct lipid microdomains with the apical domain of epithelial cells, FEBS Lett. 581 (2007) 1783–1787.
[29] M. Koyanagi, R.P. Brandes, J. Haendeler, A.M. Zeiher, S. Dimmeler, Cell-to-cell 31. connection of endothelial progenitor cells with cardiac myocytes by nanotubes: A novel mechanism for cell fate changes? Circ. Res. 96 (2005) 1039–1041.
[30] V. Kralj-Iglič, S. Svetina, B. Žekš, Shapes of bilayer vesicles with membrane embedded molecules, Eur. Biophy. J. 24 (1996) 311–321.
[31] V. Kralj-Iglič, V. Heinrich, S. Svetina, B. Žekš, Free energy of closed membrane with anisotropic inclusions, Eur. Phys. J. B 10 (1999) 5–8.

[32] V. Kralj-Iglič, A. Iglič, H. Hägerstrand, P. Peterlin, Stable tubular microexovesicles of the erythrocyte membrane induced by dimeric amphiphiles, Phys. Rev. E 61 (2000) 4230–4234.
[33] V. Kralj-Iglič, H. Hägerstrand, P. Veranič, K. Jezernik, B. Babnik, D.R. Gauger, A. Iglič, Amphiphile-induced tubular budding of the bilayer membrane, Eur. Biophys. J. 34 (2005) 1066–1070.
[34] V. Kralj-Iglič, B. Babnik, R.D. Gauger, S. May, A. Iglič, Quadrupolar ordering of phospholipid molecules in narrow necks of phospholipid vesicles, J. Stat. Phys. 125 (2006) 727–752.
[35] T. Mareš, M. Daniel, Š. Perutkova, A. Perne, G. Dolinar, A. Iglič, M. Rappolt, V. Kralj-Iglič, Role of phospholipid asymmetry in the stability of inverted hexagonal mesoscopic phases, J. Phys. Chem. B 112 (2008) 16575–16584.
[36] P.K. Mattila, P. Lappalainen, Filopodia: Molecular architecture and cellular functions, Nat. Rev. Mol. Cell Biol. 9 (2008) 446–454.
[37] T.J. Mitcinson, Actin based motility on retraction fibers in mitotic PtK2 cells, Cell Motil. Cytoskeleton 22 (1992) 135–151.
[38] A. Nusrat, C.A. Parkos, P. Verkade, C.S. Foley, T.W. Liang, W. Innis-Whitehouse, K.K. Eastburn, J.L. Madara, Tight junctions are membrane microdomains, J. Cell Sci. 113 (2000) 1771–1781.
[39] H. Ohvo-Rekilä, B. Ramstedt, P. Leppimäki, J.P. Slotte, Cholesterol interactions with phospholipids in membranes, Prog. Lipid Res. 41 (2002) 66–97.
[40] B. Önfelt, S. Nedvetzki, K. Yanagi, D.M. Davis, Cutting edge: Membrane nanotubes connect immune cells, J. Immunol. 173 (2004) 1511–1513.
[41] B. Önfelt, S. Nedvetzki, R.K. Benninger, M.A. Purbhoo, S. Sowinski, A.N. Hume, M.C. Seabra, M.A. Neil, P.M. French, D.M. Davis, Structurally distinct membrane nanotubes between human macrophages support long-distance vesicular traffic or surfing of bacteria, J Immunol. 177 (2006) 8476–8483.
[42] B. Pontes, N.B. Viana, L. Campanti, M. Farina, V.M. Neto, H.M. Nussenzveig, Structure and elastic properties of tunneling nanotubes, Eur. Biophys. J. 37 (2008) 121–129.
[43] A. Rustom, R. Saffrich, I. Marković, P. Walther, H.H. Gerdes, Nanotubular highways for intercellular organelle transport, Science 303 (2004) 1007–1010.
[44] K. Schara, V. Janša, V. Šuštar, D. Dolinar, J.I Pavlič, M. Lokar, V. Kralj-Iglič, P. Veranič, A. Iglič, Mechanisms for the formation of membranous nanostructures in cell-to-cell communication, Cell. Mol. Biol. Lett. 2009.
[45] P. Sens, M.S. Turner, The forces that shape caveolae, In: Lipid Rafts and Caveolae, (C.J. Fielding, Ed.), 2006, pp. 25–44. Wiley-VCH Verlag, Weinheim.
[46] N.M. Sherer, M.J. Lehmann, L.F. Jimenez-Soto, C. Horensavitz, M. Pypaert, W. Mothes, Retroviruses can establish filopodial bridges for efficient cell-to-cell transmission, Nat. Cell Biol. 9 (2007) 310–315.
[47] N.M. Sherer, W. Mothes, Cytonemes and tunneling nanotubules in cell-cell-communication and viral pathogenesis, Trends Cell Biol. 18 (2008) 414–420.
[48] S. Sowinski, C. Jolly, O. Berninghausen, M.A. Purbhoo, A. Chauveau, K. Köhler, S. Oddos, P. Eissmann, F.M. Brodsky, C. Hopkins, B. Önfelt, Q. Sattentau, D.M. Davis, Membrane nanotubes physically connect T cells over long distances presenting a novel route for HIV-1 transmission, Nat. Cell Biol. 10 (2008) 211–219.
[49] C. Thiele, M.J. Hannah, F. Fahrenholz, W.B. Huttner, Cholesterol binds to synaptophysin and is required for biogenesis of synaptic vesicles, Nat. Cell Biol. 2 (2000) 42–49.
[50] A. Tian, T. Baumgart, Sorting of lipids and proteins in membrane curvature gradients, Bipohys. J. 96 (2009) 2676–2688.

[51] P. Veranič, M. Lokar, G.J. Schütz, J. Weghuber, S. Wieser, H. Hägerstrand, V. Kralj-Iglič, A. Iglič, Different types of cell-to-cell connections mediated by nanotubular structures, Biophys. J. 95 (2008) 4416–4425.
[52] C. Vidulescu, S. Clejan, K.C. O'connor, Vesicle traffic through intercellular bridges in DU 145 human prostate cancer cells, J. Cell. Mol. Med. 8 (2004) 388–396.
[53] S.C. Watkins, R.D. Salter, Functional connectivity between immune cells mediated by tunneling nanotubes, Immunity 23 (2005) 309–318.
[54] D. Wüstner, Plasma membrane sterol distribution resembles the surface topography of living cells, Mol. Biol. Cell. 18 (2007) 211–228.
[55] Y. Yamashita, S.M. Masum, T. Tanaka, Y. Tamba, M. Yamazaki, Shape changes of giant unilamellar vesicles of phosphatidiylcholine induced by a de novo designed peptide interacting with their membrane interface, Langmuir 18 (2002) 9638–9641.
[56] S. Zacchigna, H. Oh, M. Wilsch-Brauninger, E. Missol-Kolka, J. Jaszai, S. Jansen, N. Tanimoto, F. Tonagel, M. Seeliger, W.B. Huttner, D. Corbeil, M. Dewerchin, *et al.* Loss of the cholesterol-binding protein prominin-1/CD133 causes disk dysmorphogenesis and photoreceptor degeneration, J. Neurosci. 29 (2009) 2297–2308.
[57] D. Vignjevic, S. Kojima, Y. Aratyn, O. Danciu, T. Svitkina, G.G. Borisy, Role of fascin in filopodial protrusion, J. Cell Biol. 11 (2006) 863–875.
[58] L.J. Pike, Rafts defined: a report on the Keystone Symposium on Lipid Rafts and Cell Function, J. Lipid Res. 47 (2006) 1597–1598.
[59] W.B. Huttner, J. Zimmerberg, Implications of lipid microdomains for membrane curvature, budding and fission, Curr. Opin. Cell Biol. 13 (2001) 478–484.

CHAPTER FOUR

Cytoskeletal Control of Red Blood Cell Shape: Theory and Practice of Vesicle Formation

N. Gov,[1,*] J. Cluitmans,[2] P. Sens,[3] *and* G.J.C.G.M. Bosman[2]

Contents

Abstract

The erythrocyte cytoskeleton is composed of a two-dimensional network of flexible proteins that is anchored to the cell membrane, and determines cell shape. The cytoskeleton also affects the diffusion and distribution of membrane proteins and lipids through direct interactions and steric effects. Here, we present a unified model which describes how the coupling of the local

* Corresponding author: Tel.: +972 8 934 3323; Fax: +972 8 934 4123
E-mail address: nirgov@wisemail.weizmann.ac.il

[1] Department of Chemical Physics, The Weizmann Institute of Science, P.O. Box 26, Rehovot 76100, Israel
[2] Department of Biochemistry, Radboud University Medical Center Nijmegen, P.O. Box 9101, 6500 HB Nijmegen, The Netherlands
[3] Physico-Chimie Théorique (CNRS UMR 7083), ESPCI, 10 rue Vauquelin, 75231 Paris Cedex 05, France

Advances in Planar Lipid Bilayers and Liposomes, Volume 10
ISSN 1554-4516, DOI: 10.1016/S1554-4516(09)10004-2

interactions of the cytoskeleton with the bilayer exerts control over the process of membrane vesiculation. In this model, a disturbance of the band 3-ankyrin anchoring complexes leads to increased compression and rigidity of the spectrin cytoskeleton, leading to buckling of the phospholipid bilayer, resulting in vesicle formation. The predictions of this model on size and protein composition of vesicles are confirmed by the available data, especially data of vesicles that are generated during aging *in vivo* and in blood bank storage conditions. Finally, we suggest some future theoretical elaborations of this model, as well as the experimental approaches for testing it.

1. Introduction

Microvesicles, also referred to as microparticles, are fragments that are shed from the plasma membrane of stimulated or apoptotic cells. They are associated with various physiological processes involving intercellular communication, hemostasis, and immunity. Variations in their number and/or characteristics are observed in pathophysiological circumstances. High shear stress, oxidative stress, inflammatory or procoagulant stimulation, and apoptosis all stimulate vesicle generation [1–3]. Stimulation leads to a redistribution of lipids and proteins in and associated with the cell membrane, leading to changes in (the kinetics of) microdomain organization, changes in phospholipid asymmetry, cytoskeleton reorganization, and vesicle release. Controlled inclusion or exclusion of specific molecule species into these microdomains results in vesicles with a particular membrane composition and content [2]. This explains how microvesicles of the same cellular origin may have different protein and lipid compositions, be involved in the maintenance of homeostasis under physiological conditions, or initiate a deleterious process in case of excess or when carrying pathogenic constituents [1, 2].

Thus, vesicles constitute a disseminated storage pool of bioactive effectors. For example, antigen-presenting cells secrete MHC-carrying vesicles that stimulate proliferation of T cells [2, 4]. Microvesicles that are shed from activated platelets expose phosphatidylserine (PS), thereby providing a catalytic surface promoting the assembly of the enzyme complexes of the coagulation cascade. Furthermore, vesiculation is thought to represent a mechanism to eliminate cell waste products. This plays an important role in the problems around the immunity of cancer cells, as vesicles may be instrumental in the elimination of membrane proteins that are recognized by the immune system, and thereby facilitate escape and promote survival. Also, cancer cells may use vesicles to get rid of toxic drugs, accounting in part for the resistance to chemotherapy [2].

Classically, the erythrocyte has always been an important subject in research on the structure/function relationship of the plasma membrane,

including vesicle formation [5]. In the last few years, the interest in the ins and outs of erythrocyte vesiculation has increased, since vesiculation plays a role in all stages of the erythrocyte life. During erythropoiesis, iron is transported into the erythroblast for hemoglobin synthesis by receptor-mediated endocytosis of vesicles containing complexes of transferrin receptor, transferrin, and iron. At a later point in erythroid terminal differentiation, vesiculation plays a crucial role in remodeling of the reticulocyte membrane, when a number of integral membrane proteins, including the transferrin receptor, are removed from the cell surface by exocytosis. Finally, vesiculation of the mature erythrocyte plasma membrane is not only an integral part of the physiological erythrocyte aging process but also constitutes one of the erythrocyte storage lesions in the blood bank, and also plays a role in the pathology of hemoglobinopathies and erythrocyte membranopathies [6].

In this chapter, we will present the recent data on erythrocyte microvesicle composition, and discuss these in the light of the mechanisms that have been postulated on the vesicle generation process. We will try to combine these into a new model, and will propose some experimental approaches that could falsify and/or refine this theory. In this model, we propose that a crucial role in the process of membrane vesiculation is played by the erythrocyte cytoskeleton. The erythrocyte cytoskeleton is composed of a two-dimensional network of flexible proteins that is anchored to the cell membrane, and determines the overall mechanical properties of the cell [7–9]. On the cell level, this network plays a crucial role in determining the overall cell shape [10], by modifying the force balance (tension) at the membrane [11, 12]. On a more local level, the cytoskeleton affects the diffusion and distribution of membrane proteins and lipids through direct interactions and steric effects ('membrane corrals') [11–16]. Here, we present a unified model which describes how the coupling of the local interactions of the cytoskeleton with the bilayer can drive and exert some control over the process of membrane vesiculation.

2. The Membrane/Cytoskeleton Model of the Erythrocyte

During its life, the erythrocyte is squeezed through capillaries that are roughly one-third of its diameter, for approximately 100,000 times [17]. Therefore, the erythrocyte must have a highly deformable as well as stable membrane. Membrane deformability gives the erythrocyte the capacity to deal with the shear forces in the circulation, and membrane stability provides the capacity to circulate without fragmentation. The ability of the erythrocyte membrane to store energy during brief periods of deformation

and to return to its original shape is associated with the maximal duration of its lifespan of 120 days in the human circulation [7, 8].

The well-described biochemical characteristics of the erythrocyte membrane underlying these unique functional requirements have long been instrumental for the development of models of the generic cell membrane.

Phosphatidylcholine (PC) and sphingomyelin (SM) are the dominant lipid components of the outer leaflet of the lipid bilayer, and PS and phosphatidylethanolamine (PE) are mainly found in the inner leaflet. This asymmetry is under control of a flippase, an inward-directed pump specific for PS and PE, an outward-directed pump referred to as floppase, and a lipid scramblase, which catalyzes unspecific, bidirectional redistribution of phospholipids across the bilayer. The asymmetry may be involved in erythrocyte homeostasis, as PS binds to the cytoskeletal components spectrin and protein 4.1 [17]. Also, erythrocyte stimulation accompanied by a significant, sustained increase in the cytosolic Ca^{2+} concentration may lead to a collapse of the membrane asymmetry, with the most prominent change being the surface exposure of PS. PS is a recognition signal for macrophages, thereby promoting erythrocyte removal [18].

It was thought for a long time that the plasma membrane is a two-dimensional 'fluid mosaic', and that the membrane proteins are uniformly dispersed in the lipid solvent [19]. However, in recent years, the existence of other lipid bilayer organization states, 'liquid-ordered' membranes, became clear [20, 21]. These regions, also called rafts, are enriched in cholesterol and sphingolipids, making them more ordered, less fluid, and more resistant to solubilization by detergents than the bulk plasma membrane [21]. Rafts are also distinguished by a specific assortment of proteins that are anchored by a glycosylphosphatidylinositol (GPI) anchor to the outer leaflet, such as acetylcholinesterase [22]. Also, at the cytosolic side, the proteins stomatin, flotillin-1, and flotillin-2 are concentrated in rafts [23]. Rafts of different sizes are formed continuously, and their stability is a function of size, capture by raft-stabilizing protein, and protein–protein interactions [24, 25].

The main integral membrane protein is band 3, which constitutes 15–20% of the total membrane protein, and is present in a monomer/dimer/tetramer equilibrium [26]. The band 3 molecule consists of three dissimilar, functionally distinct domains. The N-terminal, cytoplasmic domain binds with a variety of peripheral membrane and cytoplasmic proteins including some key glycolytic enzymes, peripheral proteins ankyrin, protein 4.2, and hemoglobin. The hydrophobic transmembrane domain functions as the chloride/bicarbonate exchanger, and forms a complex with other integral membrane proteins such as the Rhesus and Rhesus-associated proteins, and the glucose transporter. The C-terminal domain has a binding site for carbonic anhydrase II. Band 3 is crucial for a proper linking of the lipid bilayer to the membrane skeleton, through its interaction with ankyrin and binding to protein 4.2. Also, glycophorin C

(GPC) functions as a bilayer–skeleton tethering point via its interaction with protein 4.1 within the junctional complex (see below), while glycophorin A (GPA) is partially associated with band 3 [26, 27].

The cytoskeleton is a filamentous network of peripheral proteins that is composed of three principal components: spectrin, actin, and protein 4.1. The cytoskeleton consists mainly of polymeric spectrin molecules which are tied together by actin, protein 4.1 at nodes called junctional complexes. The skeleton is highly flexible and compressible [27].

Spectrin, the main component of the skeleton, is a flexible, filamentous molecule and constitutes 20–25% of the mass of proteins that can be extracted from the membrane. Spectrin is composed of two nonidentical subunits (α and β) intertwined side by side to form a heterodimer. Spectrin heterodimers self-associate at one end of the molecule to form tetramers. These self-associating heterodimers dominate in the cytoskeleton. At opposite ends, the tails of the dimers are associated with short oligomers of actin. The spectrin–actin interactions are stabilized by the formation of a ternary complex with protein 4.1. Each actin oligomer can bind to six spectrin tetramer ends, thereby creating an approximately hexagonal lattice [27].

The structural model of a hexagonal lattice is supported by high-resolution electron micrographs of isolated membranes [28]. In order for the membrane to deform in the microcirculation, the skeletal network must be able to undergo rearrangement. In one model, deformation occurs with a change in geometric shape, but at a constant surface area. In the nondeformed state, the spectrin molecules exist in a folded confirmation, but with increased shear stress the membrane becomes increasingly extended as some spectrin molecules become uncoiled while others assume a more compressed and folded form. When the spectrin molecules attain their maximal extension, the limit of reversible deformality is obtained. Further extension would result in an increase in surface area and the breaking of junction points and of the tetramers [29], at which stage membrane fragmentation is thought to occur [28].

3. The Mechanical Properties of the Membrane/Cytoskeleton of the Erythrocyte

The filamentous spectrin proteins that compose the cytoskeletal network each have elastic spring-like properties [30–33]. Under moderate extension, these molecules behave as soft elastic spring (their elasticity is controlled by thermal fluctuations), giving the cytoskeleton network an elastic shear modulus: $\mu \sim k_B T/4r_g^2 \sim 2 \times 10^{-6}$ J m^{-2}, where $k_B T$ is thermal energy and $r_g \sim 13$ nm is the estimated radius of gyration of a spectrin

tetramer filament in water [31]. This shear modulus of the erythrocyte depends on the entropic spring constant of each filament, and the average connectivity of the whole network. The entropic spring constant of each filament is given by: $k \sim 3\ k_B T/4r_g^2$. Under normal conditions, the spectrin filaments have their ends anchored to the membrane at a distance of $2r \sim 80$ nm on average. This distance is larger than $2r_g$, and the filaments are under extension, experiencing a tensile force: $F_{cyto} \sim (k_B T/r_g)(r/r_g - 1)$. This force of the individual filaments, which acts to stretch the spectrin filaments, is acting equally to compress the membrane bilayer, until the two components globally balance each other [11, 34]. Note that there may be also an overall osmotic pressure difference across the cell membrane, which stretches both the bilayer and spectrin network.

On a local scale, the membrane may slightly bend to balance the compression force applied on it by the cytoskeleton. Over the whole cell, this compression means that the cytoskeleton is pulling the membrane inwards, while the finite membrane area counteracts this inward-directed force [11]. The overall compression applied by the cytoskeleton on the membrane is, therefore, a function of the proportion of connected filaments, and their average spring constant. The bending of the membrane caused by this inward compression can be described on the level of the whole cell as an induced spontaneous curvature, or equivalently an area difference between the inner and outer leaflets [10]. We have shown, for example, that the calculated increase in cytoskeletal compression of the bilayer when adenosine triphosphate (ATP) is depleted, is indeed large enough to drive the discocyte–echinocyte shape transition [11] observed under these conditions [11, 30]. The effects of the cytoskeleton-induced compression of the bilayer on the local scale, where it may affect the vesiculation process, are discussed in the following sections.

Various factors can modify the entropic elasticity (spring constant) of the individual spectrin filaments: (i) adding or removing a band 3-ankyrin binding complex at the filament midpoints results in lowering or, respectively, increasing the entropic spring constant [14]; (ii) unfolding of the spectrin protein under stretching of the cell (such as in shear flow) results in an increase of the molecular length (increase of r_g) and, therefore, lower tension [28, 35, 36]; (iii) complete breakup of the spectrin tetramer into two dimers [29], or dissociation of the bound spectrin filament ends from the attachments at the actin–band 4.1 anchor complex, both result in a vanishing of the elasticity for that filament, since the mechanical linkage is broken. In addition to the main anchoring points at the filament ends (actin–band 4.1 complex) and midpoints (band 3-ankyrin complex), the spectrin filaments have interactions with a variety of membrane components, that may give rise to further attachment points of the filament to the bilayer, of various strength. Examples of such interactions are between spectrin and PS, and a variety of raft components such as stomatin [23].

Furthermore, the close association of lipids with band 3 and spectrin suggests that the lipid composition may also affect the stability of the anchoring complexes.

4. Vesiculation

4.1. *In Vivo*

During the lifespan of the mature erythrocyte, volume and hemoglobin content decrease by 30% and 20%, respectively [37]. Also, the surface area and lipid content decrease by 20%, mainly by the release of hemoglobin-containing vesicles. This process occurs throughout the lifespan, but is accelerated in the second half, if a functional spleen is present [38]. Vesicles are rapidly removed by the mononuclear phagocyte system, especially by Kupffer cells in the liver. This removal, which occurs very rapidly, is mediated by PS-binding scavenger receptors, and probably by autoantibodies as well [39]. The presence of the latter on vesicles has been postulated to be caused by binding of autologous IgG to band 3-derived senescent cell antigens [40]. Vesicle formation may serve as a means to dispose of 'bad' membrane patches, thereby getting rid of nonfunctional proteins and potentially damaging autoantigens, and simultaneously saving an otherwise functional erythrocyte from an untimely death [40]. From data obtained from patients who had undergone splenectomy, it is clear that the spleen plays an important role in vesicle formation, but the mechanism of this process is obscure [38].

4.2. In Transfusion Units

Also, vesiculation takes place during storage, resulting in the accumulation of vesicles in erythrocyte concentrates for transfusion, and contributing to irreversible cell shape change and membrane changes. The resulting dense, poorly deformable spherocytes are presumed to be quickly removed from the circulation after transfusion [41]. The lipid component of vesicles might be the stimulus for the activation of inflammatory genes in leukocytes in the recipient, possibly contributing to transfusion-related multiple organ failure [42]. Also, removal signals on the most damaged erythrocytes and on storage vesicles may lead to an overload of the reticulo-endothelial system, and thereby to a depression of the immune defenses [43]. In addition, a concentration of structurally altered membrane proteins such as band 3 on the vesicles in transfusion units could generate nonphysiological neoantigens that may activate the recipient's immune system to generate alloantibodies and/or autoantibodies, and thereby lead to autoimmune hemolytic anemia, especially in transfusion-dependent patients [6].

4.3. *In Vitro*

Shedding of vesicles is also observed under other conditions that trigger the transition from a discocyte into an echinocyte shape *in vitro*, such as ATP depletion and Ca^{2+} loading [44–46]. In these conditions, shedding of vesicles has been described to occur at the tip of membrane spicules [47]. Also, numerous membrane-active compounds, such as detergents, that disturb the lipid organization of the membrane or agents that affect ion transport across the membrane induce vesicle formation [48].

4.4. In Patients

Altered vesicle formation has been associated with various abnormal erythrocyte morphologies. Spherocytosis is one of the inherited erythrocyte disorders that result from mutations in various membrane and cytoskeletal proteins. The affected proteins are mainly ankyrin, spectrin, and band 3, and occasionally protein 4.2 and the Rh protein. These proteins are all part of one of the complexes by which the cytoskeleton is anchored to the lipid bilayer [27].

Hereditary elliptocytosis is caused mainly by mutations in the spectrins and protein 4.1, leading to decreased spectrin self-association and/or weakened junctional complexes, thereby decreasing the mechanical stability.

Ovalocytosis is caused by a deletion in band 3, and is associated with increased membrane rigidity [49]. One form of acanthocytosis has been linked with a mutation in band 3 [50]. Finally, stomatocytosis has been thought to result from defects in cell volume regulation, probably by mutations in as yet unidentified cation transport systems [51]. A decrease in the capacity to regulate erythrocyte water content and thereby volume and morphology has also been implicated in the pathophysiology of hemoglobinopathies such as sickle cell disease and thalassemia. In these patients, the blood content of erythrocyte-derived vesicles was found to be increased, and related to the plasma hemoglobin concentrations [52]. Electron micrographs show that vesicles are formed during spherocyte formation in patients with hereditary spherocytosis [53]. Also, the erythrocytes of transgenic mice lacking band 3 have a spherocyte morphology, and show prominent vesicle production [54]. Similarly, mutations leading to defects in the band 4.2 protein also lead to breakage of the band 3-ankyrin anchors of the spectrin filaments, and give rise to hereditary spherocytosis and vesicle shedding [51, 53]. It has been suggested that, in patients with spherocytosis, an acceleration of vesicle formation leads to a membrane loss that cannot be compensated for by uptake of lipids from plasma proteins. The erythrocytes become more and more microspherocytic, and are thought to be hemolysed principally by the spleen, a serious anemia being the consequence [6, 37]. A special case is constituted by patients with neuroacanthocytosis. In all

manifestations of this syndrome of basal ganglia degeneration, structural changes in band 3 are central in acanthocyte formation [55].

5. Vesicle Composition

5.1. *In Vivo*

Erythrocyte-derived (i.e., GPA-positive) vesicles obtained from the freshly drawn plasma of healthy donors are variable in size (200–800 nm), predominantly right-side-out, and contain all hemoglobin components in a pattern similar to that of old erythrocytes, that is, enriched in modified hemoglobins such as HbA1c [38]. All the vesicles are positive for the complement-regulating, GPI-anchored proteins CD55 and CD59, approximately 40% contain IgG, and 50–70% expose PS [38–40]. Based on immunoblot analysis suggesting altered band 3 structures in these vesicles, it was speculated that the IgG is bound to band 3-derived senescent cell-specific antigens [40]. These data are all confirmed by proteomic analysis (Bosman *et al.*, in preparation). Thus, vesicles contain aged cytoplasmic hemoglobin as well as aged membrane band 3. The presence of removal signals such as senescent cell antigens and PS are likely to be responsible for their very fast removal [40, 41]. As yet, no data are available on the lipid composition of these vesicles.

5.2. In Transfusion Units

In contrast to the scarcity of information on erythrocyte-derived vesicles *in vivo*, many data are available on vesicles that are generated during storage [48]. Very recently, a combination of proteomic and immunochemical investigations have provided an updated structural and functional inventory of the vesicles that originate during processing and storage of erythrocyte concentrates under blood bank conditions [56–59]. These analyses partially confirm earlier data, such as a storage-associated increase in (aggregated) hemoglobin in the vesicles, and in aggregated and degraded band 3 in vesicle membranes. The size of the vesicles may vary with storage time and storage medium, but most vesicles have a diameter of 80–200 nm [57, 58]. Vesicles contain hardly any of the major integral membrane proteins and cytoskeletal proteins, with the exception of band 3 and protein 4.1 [56]. The concentration of carbonyl groups in vesicles increases with storage time relative to that in erythrocyte membrane fractions, indicating the accumulation of oxidized proteins, some of which could be identified as band 3, actin, and stomatin [56, 57]. Storage vesicles have also been described to contain proteins that are part of an apoptosis signaling cascade, such as Fas and caspase 3 [60]. Storage vesicles are enriched in the raft protein stomatin, but contain less of the other raft proteins flotillin-1 and

flotillin-2 [56, 58]. Storage vesicles expose PS, and contain IgG. Reliable, detailed data on the phospholipid composition of vesicles generated in transfusion units are lacking [48], but the available data suggest that the phospholipid organization of the vesicle membrane is different from that of the erythrocyte, and that it varies depending on storage medium and storage time [60] (Bosman *et al.*, unpublished observations). Immunoblot analysis of the vesicular proteins that are resistant to solubilization by Triton X-100 shows that most of the stomatin and almost all of the flotillins are associated with rafts. Also, the GPI-linked proteins acetylcholinesterase and CD55 in vesicles are associated with the vesicle rafts. Band 3 and the Duffy antigen, previously shown to be present in rafts from erythrocyte membranes, were absent from the vesicle rafts [58, 59].

5.3. *In Vitro*

Upon an increase of the intracellular calcium concentration by treatment with the cation ionophore A23187, a shape change from discocyte to echinocyte occurs. Furthermore, microvesicles bud off from the microvillous-like projections of the echinocytes. Calcium-induced vesicles are depleted of PC, spectrin, actin, and glycophorin, while band 3 and acetylcholinesterase are retained [48]. Vesicle formation is associated with activation of a calcium-dependent phospholipase C producing 1,2-diacylglycerol, and with translocation to the membrane and activation of the protease calpain. There is a significant negative correlation between erythrocyte ATP content and vesicle amount [58]. ATP depletion induces the same morphological changes as calcium loading, but the protein compositions of the vesicles induced by ATP depletion, calcium loading, and storage differ [48]. The spectrin-free vesicles induced by nutrient deprivation bind IgG in much higher quantities than the erythrocytes they are derived from, suggesting a selective enrichment of autoantigens in vesicles [61]. The raft proteins stomatin, acetylcholinesterase, and CD55 are enriched in calcium-induced vesicles, but other raft proteins such as flotillin-1 and flotillin-2 are absent [58, 62]. Together with the differences in protein and phospholipid composition as well as in size and shape of vesicles induced by various membrane-active compounds such as amphiphiles or lysophosphatidic acid [63, 64], these *in vitro* data emphasize an earlier conclusion that the composition of vesicles differs depending on the manner by which they were produced [48]. These data also support and highlight the theory that multiple pathways are likely to be involved in the mechanism of vesicle generation.

5.4. In Patients

Many data are available on the differences in membrane protein composition and/or organization between pathological and healthy erythrocytes, but only scarce data are available on the composition of erythrocyte-derived

vesicles from the blood of inpatients with membranopathies and hemoglobinopathies described earlier. These vesicles contain hemoglobin and 50% of these vesicles express PS at their surface as do the vesicles in healthy controls. PS exposure is associated with a promotion of thrombin generation [58]. Erythrocytes with sickle cell hemoglobin shed vesicles upon unsickling *in vitro*. Such vesicles are devoid of spectrin, ankyrin, and protein 4.1, and their membranes contain extensive regions of nonbilayer phase regions [65, 66].

6. Mechanism(s)

A summary of the presently available data on the composition of vesicles as compiled above may serve as the framework for our present theory on the mechanism by which erythrocytes generate vesicles in health and (erythrocyte) disease, and during storage under blood bank conditions. The main characteristic of all vesicles is the virtual absence of spectrin and ankyrin, the main components of the erythrocyte cytoskeleton, and of an intact cytoskeletal spectrin–actin network. The observation that vesicle membranes are highly enriched in a variety of proteins, compared to their concentration in the intact erythrocyte membrane, suggests that there is a relationship between their protein composition and the vesiculation process.

Generically, membrane vesiculation can be achieved either by an asymmetry in the membrane leaflet composition that favor membrane curvature, or by the generation of forces (e.g. from the cytoskeleton). While the lipid composition of the plasma membrane of cells is always asymmetric, the increase of this asymmetry, for instance under the action of proteins such as flippase, can increase steric torques within the bilayer and trigger the formation of vesicles [67, 68].

The cytoskeleton is likely to play an important role in erythrocyte vesiculation. By segregating the erythrocyte membrane into ''corrals,'' the cytoskeleton affects both the rate of diffusion of the membrane components, and the physical extent of free membrane patches. The spectrin filaments affect membrane proteins by steric repulsion which tends to segregate some proteins away from the filaments, and by attractive interactions with other membrane components which therefore aggregate near the filaments. The result is a mosaic of membrane compositions [69], which reflects the network geometry of the cytoskeleton, and the chemical affinities of the membrane components (Fig. 1A).

The most obvious process driving vesicle formation is the aggregation of membrane proteins of specific types that have mutual affinity, forming membrane domains. Membrane domains of a large enough size will

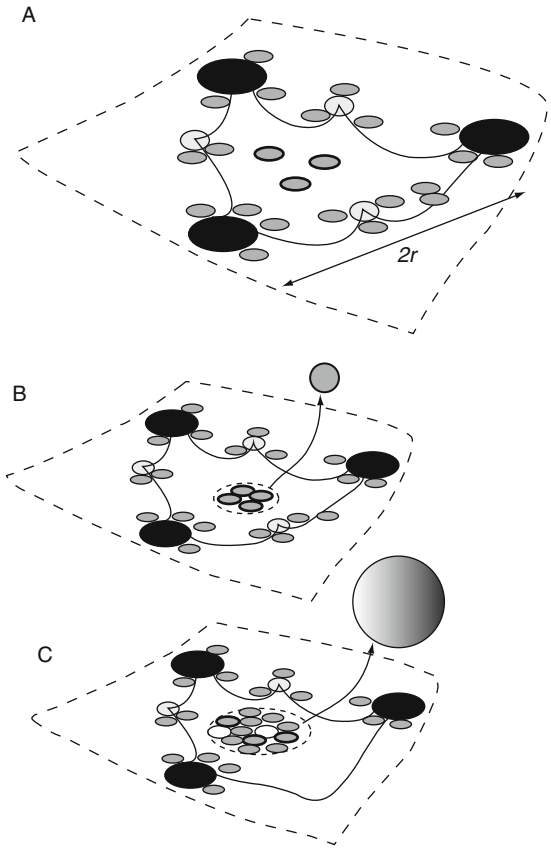

Figure 1 Vesicle formation. (A) Schematic illustration of the erythrocyte cytoskeleton and membrane. Black ovals: spectrin end-points anchoring complex of actin-band 4; light-gray ovals: midpoint anchoring complex of band 3-ankyrin; black solid lines: spectrin filaments (intact tetramers); gray ovals: various membrane proteins and charged lipids that are attracted to the cytoskeleton; gray ovals with thick rim: membrane proteins that are repelled from the cytoskeleton. (B) Mobile components may aggregate and form domains which leave as nanovesicles of uniform composition and radius, determined by their spontaneous curvature. (C) Breakage of the midpoint band 3-ankyrin anchors releases mobile proteins to form an aggregate, which together with the increased tension leads to budding and eventual vesicle detachment (driven by the aggregate line tension) of vesicles that are larger and more heterogeneous compared to (B). White ovals: degraded band-3 proteins from the broken anchor point, which are mobile and free to aggregate.

spontaneously bud and detach as a vesicle when above some critical size, driven by the minimization of the line tension along the domain perimeter. The radius of the formed vesicles is roughly equal to the spontaneous curvature of the domain components. For domains and vesicles of sizes that are very small compared to the typical size of the cytoskeleton units,

that is, for diameters $d \ll 2r \sim 60 - 100\,\text{nm}$, the aggregation-driven vesiculation process can proceed without being necessarily affected by the cytoskeleton. This process may result in nanovesicles of a diameter of order ~ 25 nm [70–72]. In this case, we expect that the domains (and resulting vesicles) will have compositions which differ according to the vesicle size, corresponding to the spontaneous curvature of each membrane component that tends to form domains. This would explain why vesicles of different sizes have very different membrane compositions [56, 62] (Fig. 1B).

The formation of larger (micro)vesicles, with diameters in the range of 60–300 nm, most likely involves a local deformation of the spectrin cytoskeleton. The challenge is to provide a unified model for the interplay between the process of membrane domains aggregation and the bilayer interaction with the erythrocyte cytoskeleton. The effects of the cytoskeleton on the bilayer can be divided into two types: the chemical binding of the spectrin filaments to the integral membrane components and the compressive force that the cytoskeletal network exerts on the bilayer. These two effects are coupled to each other, as we discuss below.

All vesicles contain band 3, but apparently in a condition that makes it incapable of functioning as an anchorage site for the cytoskeleton. Thus, the central event in vesicle formation seems to be the breakage of the link between band 3 and the spectrin network, the so-called vertical linkage, rather than in the horizontal interactions in the spectrin–actin–protein 4.1 ternary complex. The processes that lead to a disruption of this linkage may differ, for example, the breakdown of band 3 and/or ankyrin by the calcium-activated proteases calpain or caspases, triggered by aging-related, apoptosis-like processes [73, 74], or mutation-related, specific alterations in the structure of band 3, ankyrin, spectrin, or other components of the band 3 complex [75]. Since the cytoplasmic domain of band 3 has high-affinity binding sites not only for ankyrin but also for denatured hemoglobin and for key enzymes of the glycolysis, the oxidation status as well as the energy content of the erythrocyte may also affect binding of ankyrin to band 3. Binding and activity of glycolytic enzymes is regulated by phosphatases and kinases [76], indicating that signal transduction by intracellular as well as extracellular triggers may influence lipid bilayer–cytoskeleton interaction.

Whatever the cause of the decrease in interaction may be, it has been proposed that the degradation of band 3-ankyrin anchoring complexes leads to increased compression and rigidity of the cytoskeleton, leading to buckling of the bilayer and resulting in vesicle formation [33, 34]. These vesicles will bud from the free membrane patches that are constrained by the cytoskeletal network (Fig. 1C), and therefore have a more heterogeneous composition compared to the nanovesicles that form due to a pure aggregation process (Fig. 1B). Release of the spectrin–bilayer anchoring also diminishes the direct chemical interaction between the spectrin filaments

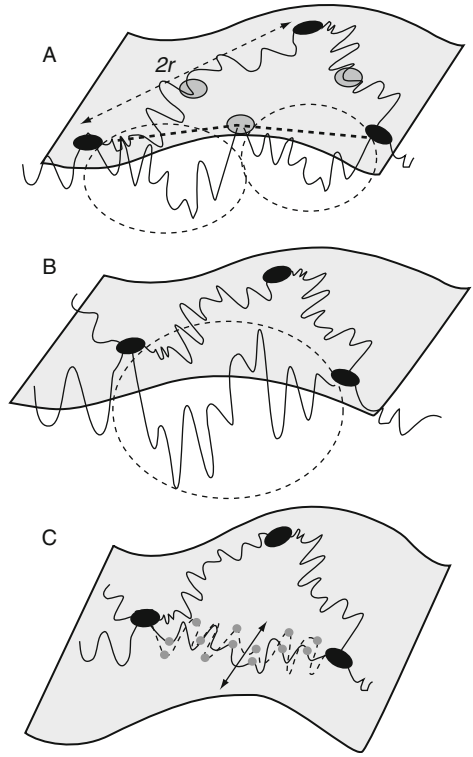

Figure 2 Vesicle formation and spectrin–bilayer anchorage. (A) Schematic illustration of the erythrocyte cytoskeleton and membrane. Black ovals: spectrin end-points anchoring complex of actin–band 4; gray ovals: midpoint anchoring complex of band 3-ankyrin; black solid lines: spectrin filaments (intact tetramers). The dashed circles denote the configurations of the spectrin filament that contribute to the entropic elasticity. (B) When the midpoint band 3-ankyrin anchors are degraded, the configurational entropy of the spectrin filaments increases, leading to stiffer entropic spring constant. (C) In the limit of many spectrin–bilayer attachments (grey circles), the filament can only have 2D conformations inside the plane of the membrane (black arrow and dashed line), and a low entropic elasticity.

and the membrane components, making them more mobile and free to aggregate (Fig. 1C). We therefore propose that both an increased cytoskeleton rigidity and the release of mobile membrane components drive the formation of microvesicles in response to degradation of the spectrin–bilayer anchoring through the band 3-ankyrin complex.

We start with the relationship between the elastic rigidity of the spectrin filaments and the removal of the midpoint anchoring (Figs. 1C and 2). The effect of the latter can be understood as a direct manifestation of the entropic nature of the elasticity of the spectrin filaments; the larger the configurational entropy of the flexible proteins, the larger the spring constant of

this filament, and therefore decreasing this configurational entropy by the addition of midpoint anchoring leads to a lower elasticity. The increased cytoskeleton-induced tension when the midpoint anchoring is removed can be demonstrated by the following estimate of this force; $F_{cyto} \sim (k_B T/r_g)(r/r_g - 1)$. When the midpoint anchor is present, the effective r becomes half that of the end-points, and similarly r_g is reduced by a factor of $\sim\sqrt{2}$ (for pure Gaussian chains). If we use the values for r and r_g given above for the spectrin network of the erythrocyte, the reduction in the tension can be estimated to be of order 2. Another demonstration of the effect of anchoring on the spring constant of the filament is by considering the theoretical limit of many anchoring points, such that the filament becomes effectively two-dimensional, moving only in the plane of the bilayer (Fig. 2C). Using the description of a Gaussian chain in 2D, we find that the effective spring constant is smaller compared to 3D (no midpoint anchors) by a factor of $k_{2D} = (2/3)k_{3D}$. This is the maximal softening that we can get, and this is a weaker effect than for fixed attachment points, since the conformational entropy of the anchor points inside the bilayer plane is maintained.

It is important to note the opposite effects on the cytoskeleton stiffness of the band 3–ankyrin and actin–band 4 anchoring complexes; the removal of the first kind increases the stiffness of the spectrin bond, while removal of the second kind results in a vanishing of the stiffness of the bond, since the mechanical linkage is broken. Some agents may affect both types of complexes, in opposite manners; calcium loading seems to lead to band 3-ankyrin breakage as described earlier, while it strengthens the spectrin–actin–band 4 anchoring complexes [77]. Both these modifications result in a stiffer cytoskeleton, which we propose to play a role in the overall shape transitions of the cell (discocyte to echinocyte) and in increased vesiculation.

Next, we describe how the local compressive forces applied by the cytoskeleton on the fluid membrane can drive a local bilayer buckling and budding of a membrane blister, which afterwards detaches as a free vesicle. This process occurs when the local compressive force increases beyond a critical threshold where the barrier for membrane budding becomes small enough (or even vanishes). The mathematical details of this analysis have been presented before [34], and we will here give a description of the basic physical mechanisms.

The local force balance between the compressed bilayer and the stretched cytoskeleton is schematically shown in Fig. 3. There are three energies in this system which we considered, all depending on the local shape and area of the membrane. (i) First, there is the membrane tension energy, which arises from the thermal fluctuations of the bilayer. This energy is minimized when the bilayer area is larger than the projected local area, such that there is excess area ''stored'' in the thermal undulations of the bilayer. The cytoskeleton anchoring introduces a constraint on the bilayer undulations, and the simplest way to analyze this local coupling of

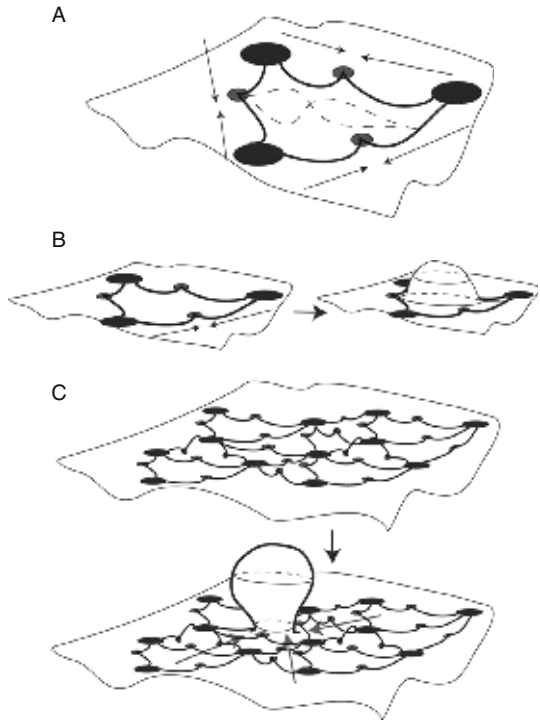

Figure 3 Schematic description of the force balance at the erythrocyte membrane. (A) The cytoskeleton units apply a compressive pressure on the bilayer (thin black arrows), which is balanced by the bilayer thermal fluctuations, undulations modes within each cytoskeleton units (dashed lines). Large black circles represent the actin–band 4.1 complex anchoring the ends of the spectrin filaments (thick black lines), while the small gray circles represent the ankyrin–band 3 anchoring complex. (B) Beyond a critical compression in the cytoskeleton (thin black arrows, left image), the bilayer within the cytoskeleton unit buckles to form a curved bud, which can then form a vesicle, and releases the tension in the cytoskeleton unit (right image). (C) In an array of stretched cytoskeleton units, the system can overcome the energy barrier to form a growing vesicle at one of the units, which then grows due to flow of bilayer from the surrounding units (gray arrows). When the vesicle detaches the whole array is relaxed slightly, until the next event of vesicle nucleation.

the bilayer and cytoskeleton is to assume that the bilayer within each membrane patch that is defined by a closed cytoskeletal unit has independent thermal fluctuations (Fig. 3A). Using this assumption, the bilayer tension energy, therefore, acts to keep the bilayer area within each cytoskeleton unit at the optimal value determined by the local thermal fluctuations. (ii) Second, there is the curvature energy of the bilayer. We assume for simplicity that the bilayer has an average of zero spontaneous curvature, so that this energy is zero when the membrane is flat. As the membrane buckles and forms a curved bud, this energy increases. Note that if the bud

contains membrane components that have a convex spontaneous curvature, then the curvature energy cost of forming the bud (and vesicle) is reduced. (iii) Finally, there is the elastic stretching energy of the cytoskeleton unit which defines the perimeter of the membrane unit.

Minimizing these energies, we find the following behavior as a function of the bilayer area (Fig. 3B): as the bilayer area within the cytoskeleton unit increases, the cytoskeleton is at first stretched, but eventually the system prefers to release the cytoskeleton tension at the cost of membrane bending energy, and the membrane buckles. The instability from flat to buckled bilayer occurs as the area mismatch between the bilayer and unstretched cytoskeleton unit is increased, or as the cytoskeleton stiffness increases. Alternatively, decreasing the bilayer bending modulus or increasing its spontaneous curvature, also gives rise to a buckling instability.

The behavior we have just described can now be implemented for an array of identical units, where we consider a transition from all units being flat, to one unit that buckles and relieves the tension throughout the array (Fig. 3C). The fluid bilayer can easily flow between the cytoskeleton units, so that the entire excess area can be (theoretically) concentrated at one unit which buds and vesiculates. This picture allows us to calculate the equilibrium configuration of such a system, and find the critical area mismatch leading to vesiculation.

In reality, this process of membrane flow and vesicle growth leads to formation of vesicles with some size distribution, with typical diameters 80–300 nm, and of both spherical and cylindrical shapes. This observation indicates that as the vesicles grow there are various forces that destabilize the growing vesicle, leading to its detachment. The most dominant force leading to vesicle pinching and detachment arises from line tension due to the different composition of the bilayer at the growing bud as compared to the surrounding membrane (Fig. 1C) [78]. Note that the bending modulus of the bilayer in the growing bud is lowered due to the aggregation of membrane proteins [79], further lowering the energy cost of vesicle formation. *In vivo*, the vesicles may furthermore be detached from the cell due to the forces of the shear flow.

The location of the growing vesicle in the array may be random, as nucleation is driven by thermal fluctuation over an energy barrier. The local shape of the membrane does play a role, as there is evidence that vesicle is shed preferentially from highly curved regions such as the tips of spicules [64, 79–82]. The high curvature of the membrane at the tips of spicules lowers the energy cost to form a vesicle, making these regions have a lower energy barrier and increased vesicle nucleation rate.

The rate of vesicle formation depends on the slowest process which drives their formation. The two processes that determine the vesicle growth when it is driven by the cytoskeleton compression are (i) the rate of increase of stiffness which determines the rate of vesicle nucleation and (ii) the rate of

vesicle growth which is limited by the flow of membrane to the budded unit from the surrounding units. For example, during the natural aging process of the cell, the observed rate of membrane shedding is 20% of the area in 100 days, which translates to about one 100-nm-sized vesicle an hour. We can give a rough estimate of the rate at which membrane can flow in order to concentrate enough material at the budded unit to form a vesicle of this size; the number of units needed to be ''drained'' in order to form a vesicle of diameter of 100 nm is $N_v \sim S_v/\delta s$, where $S_v \sim 5S_0$ is the area of the vesicle and $\delta s \sim S_0/10$ is the excess area per unit cytoskeleton–membrane (S_0 is the equilibrium area of the unstretched cytoskeleton units). The time it takes to concentrate the bilayer at the growing bud can therefore be estimated as: $t_v \sim \sqrt{N_v}/v$, where the flow velocity of the bilayer can be estimated as: $v \sim \Delta F/\gamma\sqrt{S_0}$, where $\Delta F \sim 10k_BT$ is the energy barrier for the vesicle formation and γ is an effective friction coefficient of the bilayer as it flows past the cytoskeleton anchors (proportional to the membrane viscosity). Putting all these numbers together we get that the flow time-scale is $t_v \sim \sqrt{N_v}S_0^{3/2}\eta_m/\Delta F \sim 0.1 - 1\,\mathrm{s}$, where η_m is the membrane viscosity. The slowest time-scale giving rise to one vesicle per hour during normal aging is therefore the rate of stiffness increase. Note that this estimation, based on dimensional analysis, only gives the approximate time-scale for the vesicle rate of formation.

In experiments where the stiffness increases more rapidly, for example, due to calcium loading, or by changing the membrane fluidity of the whole erythrocyte (e.g., through the cholesterol content) so that the flow time-scale increases, the two timescales may be closer and both affect the rate of vesiculation.

The model we present here predicts that membrane vesicles are effectively ''extruded'' in between the filaments of the cytoskeletal network, and are therefore free of any spectrin cytoskeleton components. The sizes of such vesicles are also predicted to be of order 80–200 nm, corresponding to the range of sizes of network compartments in the erythrocyte cytoskeleton. Both these predictions are in agreement with the observed properties of these vesicles, as described earlier.

Integrating the models presented earlier we now suggest the following chain of events that lead to the shedding of membrane vesicles when components of the band 3-ankyrin anchors are modified and/or degraded in the erythrocyte:

(i) Degraded or otherwise aging-modified proteins of the anchor complex, such as band 3 and band 4.2, loose the ability to bind ankyrin and spectrin, which releases the midpoint anchoring of the spectrin filament.
(ii) The increased tension lowers the energy barrier for local membrane budding. Note that the estimated increase in local stiffness of an

individual spectrin filament is by a factor of 1.5–2, which is much larger than the overall 50% increase in stiffness of the whole network observed in the senescent erythrocyte. This indicates that the overall network connectivity also decreases, through dissociation of the spectrin tetramers.

(iii) The modified, released band 3 molecules are free to diffuse in the membrane, and to aggregate at regions that are far from the spectrin filaments, that is, at the middle of the membrane patch. The degraded band 3 can be linked by oxidatively damaged hemoglobin; denatured hemoglobin has a high affinity for the cytoplasmic domain of band 3, and aggregation of damaged hemoglobin leads to aggregation of band 3. This leads to conformational changes in band 3 that are antigenic. Binding of damaged hemoglobin to band 3 further leads to conformational changes in both the cytoplasmic and membrane domains, leading to increased sensitivity to proteases and thereby to aggregation and senescent cell antigen activity.

(iv) Furthermore, the degraded proteins aggregated at the free membrane patch in the budding unit may further drive the vesicle formation due to an emergent convex spontaneous curvature. This may arise from the formation of an aggregate with strong asymmetry between the proteins at the inner and outer bilayer leaflets (see step iii). Molecules such as IgG, found in high concentrations on vesicles, may also induce spontaneous curvature due to their asymmetric form. A convex spontaneous curvature further lowers the energy barrier toward local budding and vesicle growth.

(v) Finally, the aggregated proteins and lipids at the growing bud drive the pinching of the bud and its detachment as a free vesicle, due to the line tension that forms along the perimeter of the domain aggregate.

Thus, we have described an interesting self-regulating system in which the process of aging-related modification and/or degradation of some key proteins such as band 3 initiates the physical process of membrane vesiculation, which allows the cell to shed defective components.

Also, the asymmetric lipid composition of the erythrocyte bilayer may play an additional role in vesicle formation. In the normal cell, PS is biased toward the inner leaflet of the plasma membrane due to the activity of various enzymes and to their attractive interactions with the spectrin filaments. Similar to the role played by the band 3-ankyrin anchors, the negatively charged PS on the inner leaflet of the bilayer increases the attraction between the spectrin filaments and the bilayer. Releasing these attractive interactions through the flip-flop of PS will have an effect that is similar to the breakage of the band 3-ankyrin anchors, that is, an increase in cytoskeleton stiffness and compression. Furthermore, as the spectrin anchors break and the filaments become, on average, more distant from the bilayer,

their interaction with the charged lipids weakens, lowering the local asymmetry between the leaflets further. Indeed, the lipid asymmetry in vesicles is lower than in the membrane of the healthy, intact erythrocyte. The distinct protein and lipid composition of the bilayer at the growing bud and consequent vesicle may be instrumental in driving the vesicle detachment, as discussed earlier.

7. Conclusions

The model described above has several biological implications: (i) vesicle formation is a relevant biomarker for erythrocyte homeostasis, both *in vivo* and *in vitro*; (ii) manipulation of the lipid composition of the erythrocyte membrane may be instrumental in improving erythrocyte quality, for example, in blood bank conditions; (iii) manipulation of protein modification, including but possibly not restricted to prevention of oxidation and/or proteolysis, may result in a more robust erythrocyte; (iv) more detailed, molecular elucidation of the vesicle composition is necessary to falsify our hypotheses.

The physicochemical mechanisms that we have proposed to drive the vesiculation process in the eythrocyte can be tested experimentally. For example, to test our proposal that the compressive force of the cytoskeleton on the bilayer can drive the vesicle formation, one could apply calcium loading which drives vesiculation, while balancing it by swelling the cell through osmotic pressure. If there is an osmotic swelling that cancels the effect of the increased calcium concentration, this will show that indeed the force balance at the membrane plays a crucial role in driving the vesicle formation. The relationship between the rate of compression increase at the membrane and the rate of vesicle shedding has not been well studied so far, and can also be compared to the theoretical calculations.

From a theoretical point of view, the challenges that remain for a complete description of the complex dynamics of the erythrocyte membrane are numerous. Regarding the vesiculation processes we discussed here, we can chart the following tentative directions for future theoretical progress. On a microscopic scale, future numerical simulations that describe the individual spectrin filaments as worm-like chains can be extended to include the fluid and flexible nature of the bilayer. These simulations will then allow a detailed testing of the coarse-grained models we presented here for the cytoskeleton-induced budding and vesicle formation. These models can then be further elaborated by including the complex composition of the bilayer, allowing for the segregation and aggregation of membrane domains, and the consequences these have on the vesiculation process.

At the coarse-grained level, one could combine the models that we presented into a single model that describes the stiffness of the spectrin

filaments by their anchoring state, together with the bilayer deformation. The local membrane composition is then added using standard Ginzburg–Landau formalism to capture the phase separation of the bilayer components into domains, and to describe how these domains are coupled to the local bilayer shape. These combined models can then be used to chart the equilibrium states of the system, or dynamically using a linear stability analysis, and using simulations for the full nonlinear evolution. As one elaborates the theoretical models of this system, either through detailed molecular-scale simulations or using coarse-grained descriptions, there will be a need for detailed experimental data to supply the necessary values for the parameters appearing in the models. The validity of such models will have to be tested experimentally, and they will hopefully provide us with a comprehensive understanding of the key mechanisms that dominate the evolution of this complex biological system.

REFERENCES

[1] J.M. Freyssinet, Cellular microparticles: What are they bad or good for? J. Thromb. Haemost. 1 (2003) 1655–1662.
[2] B. Hugel, M.H. Martínez, C. Kunzelmann, J.M. Freyssinet, Membrane particles: Two sides of the coin, Physiology 20 (2005) 22–27.
[3] M.H. Martínez, A. Tesse, F. Zobairi, R. Andriantsitohaina, Shed membrane particles from circulating and vascular cells in regulating vascular function, Am. J. Physiol. Heart Circ. Physiol. 288 (2005) H1004–H1009.
[4] K. Denzer, M.J. Kleijmeer, H.F. Heijnen, W. Stoorvogel, H.J. Geuze, Exosome: From internal vesicle of the multivesicular body to intercellular signaling device, J. Cell Sci. 113 (2000) 3365–3374.
[5] D.W. Knowles, L. Tilley, N. Mohandas, J.A. Chasis, Erythrocyte membrane vesiculation: Model for the molecular mechanism of protein sorting, Proc. Natl. Acad. Sci. USA 94 (1997) 12969–12974.
[6] G.J.C.G.M. Bosman, J.M. Werre, F.L.A. Willekens, V.M.J. Novotný, Erythrocyte ageing *in vivo* and *in vitro*: Structural aspects and implications for transfusion, Transfus. Med. 18 (2008) 335–347.
[7] V. Bennet, The membrane skeleton of human erythrocytes and its implications for more complex cells, Ann. Rev. Biochem. 54 (1985) 273–304.
[8] J.A. Chasis, N. Mohandas, Erythrocyte membrane deformability and stability: Two distinct membrane properties that are independently regulated by skeletal protein associations, J. Cell Biol. 103 (1986) 343–350.
[9] N. Mohandas, E. Evans, Mechanical properties of the red cell membrane in relation to molecular structure and genetic defects, Annu. Rev. Biophys. Biomol. Struct. 23 (1994) 787–818.
[10] H.W.G. Lim, M. Wortis, R. Mukhopadhyay, Stomatocyte–discocyte–echinocyte sequence of the human red blood cell: Evidence for the bilayer-couple hypothesis from membrane mechanics, Proc. Natl. Acad. Sci. USA 99 (2002) 16766–16769.
[11] N.S. Gov, S.A. Safran, Red blood cell membrane fluctuations and shape controlled by ATP-induced cytoskeletal defects, Biophys. J. 88 (2005) 1859–1874.
[12] N.S. Gov, Active elastic network: Cytoskeleton of the red blood cell, Phys. Rev. E 75 (2007) 011921.

[13] L.C.L. Lin, F.L.H. Brown, Dynamics of pinned membranes with application to protein diffusion on the surface of red blood cells, Biophys. J. 86 (2004) 764–780.
[14] F.L.H. Brown, Regulation of protein mobility via thermal membrane undulations, Biophys. J. 84 (2003) 842–853.
[15] T. Auth, N.S. Gov, Diffusion in a fluid membrane with a flexible cortical cytoskeleton, Biophys. J. 96 (2009) 818–830.
[16] M.A. De Matteis, J.S. Morrow, Spectrin tethers and mesh in the biosynthetic pathway, J. Cell Sci. 113 (2000) 2331–2343.
[17] S. Manno, T. Takakuwa, N. Mohandas, Identification of a functional role for lipid asymmetry in biological membranes: Phosphatidylserine-skeletal protein interactions modulate membrane stability, Proc. Natl. Acad. Sci. USA 99 (2002) 1943–1948.
[18] F.A. Kuijpers, K. de Jong, The role of phosphatidylserine in recognition and removal of erythrocytes, Mol. Cell. Biol. 50 (2004) 147–158.
[19] S.J. Singer, G.L. Nicolson, The fluid mosaic model of the structure of cell membranes, Science 175 (1972) 720–731.
[20] D.A. Brown, E. London, Structure of detergent-resistant membrane domains: Does phase separation occur in biological membranes? Biochem. Biophys. Res. Commun. 240 (1997) 1–7.
[21] M. Edidin, The state of lipid rafts: From model membranes to cells, Annu. Rev. Biophys. Biomol. Struct. 32 (2003) 257–283.
[22] F.J. Sharom, M.T. Lehto, Glycosylphosphatidylinositol-anchored proteins: structure, function, and cleavage by phosphatidylinositol-specific phospholipase C, Biochem. Cell Biol. 80 (2002) 535–549.
[23] U. Salzer, R. Prohaska, Stomatin, flotillin-1, flotillin-2 are major integral proteins of erythrocyte lipid rafts, Blood 97 (2001) 1141–1143.
[24] M.A. Alonso, J. Millán, The role of lipid rafts in signalling and membrane trafficking in T lymphocytes, J. Cell Sci. 114 (2001) 3957–3965.
[25] J.F. Hancock, Lipid rafts: Contentious only from simplistic standpoints, Nat. Rev. Mol. Cell Biol. 7 (2006) 456–462.
[26] S.L. Alper, Molecular physiology of SLC4 anion exchangers, Exp. Physiol. 911 (2006) 153–161.
[27] N. Mohandas, E. Evans, Mechanical properties of the red cell membrane in relation to molecular structure and genetic defects, Annu. Rev. Biophys. Biomol. Struct. 23 (1994) 787–818.
[28] D.E. Discher, P. Carl, New insights into red cell network structure, elasticity, and spectrin unfolding—A current review, Cell. Mol. Biol. Lett. 6 (2001) 593–606.
[29] X. An, M.C. Lecomte, J.A. Chasis, N. Mohandas, W. Gratzer, Shear-response of the spectrin dimer-tetramer equilibrium in the red blood cell membrane, J. Biol. Chem. 277 (2002) 31796–31800.
[30] S.K. Boey, D.H. Boal, D.E. Discher, Simulations of the erythrocyte cytoskeleton at large deformation I. Microscopic models, Biophys. J. 75 (1998) 1573–1583.
[31] D.E. Discher, D.H. Boal, S.K. Boey, Simulations of the erythrocyte cytoskeleton at large deformation II. Micropipette aspiration, Biophys. J. 75 (1988) 1584–1597.
[32] D.H. Boal, Computer-simulation of a model network for the erythrocyte cytoskeleton, Biophys. J. 67 (1994) 521–529.
[33] N.S. Gov, Less is more: Removing membrane attachments *stiffens* the RBC cytoskeleton, New J. Phys. 9 (2007) 429.
[34] P. Sens, N. Gov, Force balance and membrane shedding at the red-blood-cell surface, Phys. Rev. Lett. 98 (2007) 018102.
[35] J.C.M. Lee, D.E. Discher, Deformation-enhanced fluctuations in the red cell skeleton with theoretical relations to elasticity, connectivity, and spectrin unfolding, Biophys. J. 81 (2001) 3178–3192.

[36] C.P. Johnson, H.-Y. Tang, C. Carag, D.W. Speicher, D.E. Discher, Forced unfolding of proteins within cells, Science 317 (2007) 663–666.
[37] J.M. Werre, F.L.A. Willekens, F.H. Bosch, L.D. de Haan, S.G. van der Vegt, A.G. van den Bos, G.J.C.G.M. Bosman, The red cell revisited—Matters of life and death, Cell. Mol. Biochem. 50 (2004) 139–146.
[38] F.L.A. Willekens, B. Roerdinkholder-Stoelwinder, Y.A. Groenen-Döpp, H.J. Bos, G. J.C.G.M. Bosman, A.G. van den Bos, A.J. Verkleij, J.M. Werre, Hemoglobin loss from erythrocytes *in vivo* results from spleen-facilitated vesiculation, Blood 101 (2003) 747–751.
[39] F.L.A. Willekens, J.M. Werre, J.K. Kruijt, B. Roerdinkholder-Stoelwinder, Y. A. Groenen-Döpp, A.G. van den Bos, G.J.C.G.M. Bosman, T.J. Van Berkel, Liver Kupffer cells rapidly remove red blood cell-derived vesicles from the circulation by scavenger receptors, Blood 105 (2005) 2141–2145.
[40] F.L.A. Willekens, J.M. Werre, J.K. Kruijt, Y.A. Groenen-Döpp, B. Roerdinkholder-Stoelwinder, B. De Pauw, G.J.C.G.M. Bosman, Erythrocyte vesiculation: A self-protective mechanism, Br. J. Haematol. 141 (2008) 549–556.
[41] L. Mitrofan-Oprea, C. Palii, J.-P. Tissier, A. Héron, T. Verpoort, M. Behague, E. Smagghe, F. Schooneman, J.-J. Huart, F. Goudaliez, J. Montreuil, D. Bratosin, Novel criteria for assessing red blood cell viability in blood banks, Transfus. Clin. Biol. 14 (2007) 393–401.
[42] G.A. Escobar, A.M. Cheng, E.E. Moore, J.L. Johnson, C. Tannahill, H.V. Baker, L. L. Moldawer, A. Banerjee, Stored packed red blood cell transfusion up-regulates inflammatory gene expression in circulating leukocytes, Ann. Surg. 246 (2007) 129–134.
[43] C.F. Högman, H.T. Meryman, Storage parameters affecting red blood cell survival and function after transfusion, Transfus. Med. Rev. 13 (1999) 275–296.
[44] D. Allan, R.H. Michell, Accumulation of 1, 2-diacylglycerol in the plasma membrane may lead to echinocyte transformation of erythrocytes, Nature 258 (1975) 348–349.
[45] D. Allan, M.M. Billah, J.B. Finean, R.H. Michell, Release of diacylglycerol-enriched vesicles from erythrocytes with increased intracellular Ca^{2+}, Nature 261 (1976) 58–60.
[46] H. Müller, U. Schmidt, H.U. Lutz, On the mechanism of vesicles release from ATP-depleted human red blood cells, Biochim. Biophys. Acta 649 (1981) 462–470.
[47] H. Hägerstrand, M. Danieluk, M. Bobrowska-Hägerstrand, A. Iglic, A. Wrobel, B. Isomaa, M. Nikinmaa, Influence of band 3 protein absence and skeletal structures on amphiphile- and Ca^{2+}-induced shape alterations in erythrocytes: A study with lamprey (Lampetra fluviatilis), trout (onchorhynchus mykiss) and human erythrocytes, Biochim. Biophys. Acta 1466 (2000) 125–138.
[48] T.J. Greenwalt, The how and why of exocytic vesiculation, Transfusion 46 (2006) 143–152.
[49] P. Jarolim, J. Palek, D. Amato, K. Hassan, P. Sapak, G.T. Nurse, H.L. Rubin, S. Zhai, K.E. Sahr, S.C. Liu, Deletion in erythrocyte band 3 gene in malaria-resistant Southeast Asian ovalocytosis, Proc. Natl. Acad. Sci. USA 88 (1991) 11022–11026.
[50] M.M.B. Kay, G.J.C.G.M. Bosman, C. Lawrence, Functional topography of band 3: Specific structural alteration linked to functional aberrations in human erythrocytes, Proc. Natl. Acad. Sci. USA 85 (1988) 492–496.
[51] N. Mohandas, P.G. Gallagher, Red cell membrane: Past, present and future, Blood 112 (2008) 3939–3948.
[52] M. Westerman, A. Pizzey, J. Hirschman, M. Cerino, Y. Weil-Weiner, P. Ramotar, A. Eze, A. Lawrie, G. Purdy, I. Mackie, J. Porter, Microvesicles in haemoglobinopathies offer insights into mechanisms of hypercoagulability, haemolysis and the effects of therapy, Br. J. Haematol. 142 (2008) 126–135.

[53] S. Eber, S.E. Lux, Hereditary spherocytosis—Defects in proteins that connect the membrane skeleton to the lipid bilayer, Semin. Hematol. 41 (2004) 118–124.
[54] L.L. Peters, R.A. Shivdasani, S.C. Liu, M. Hanspal, K.M. John, J.M. Gonzalez, C. Brugnara, B. Gwynn, N. Mohandas, S.L. Alper, S.H. Orkin, S.E. Lux, Anion exchanger 1 (band 3) is required to prevent erythrocyte membrane surface loss but not to form the membrane skeleton, Cell 86 (1996) 917–927.
[55] G.J.C.G.M. Bosman, L. DeFranceschi, Neuroacanthocytosis-related changes in erythrocyte membrane organization and function, in: R.H. Walker, S. Saiki, A. Danek (Eds.), Neurocanthocytosis Syndromes, Springer-Verlag, Berlin, pp. 133–142.
[56] G.J.C.G.M. Bosman, E. Lasonder, M. Luten, M.B. Roerdinkholder-Stoelwinder, V. M.J. Novotný, H.J. Bos, W.J. DeGrip, The proteome of red cell membranes and vesicles during storage in blood bank conditions, Transfusion 48 (2008) 827–835.
[57] A.G. Kriebardis, M.H. Antonelou, K.E. Stamoulis, E. Economou-Petersen, L. H. Margaritis, I.S. Papassideri, Storage-dependent remodeling of the red blood cell membrane is associated with increased immunoglobulin G binding, lipid raft rearrangement, and caspase activation, Transfusion 47 (2007) 1212–1220.
[58] U. Salzer, R. Zhu, M. Luten, H. Isobe, V. Pastushenko, T. Perkmann, P. Hinterdorfer, G.J.C.G.M. Bosman, Vesicles generated during storage of red cells are rich in the lipid raft marker stomatin, Transfusion 48 (2008) 451–462.
[59] O. Rubin, D. Crettaz, G. Canellini, J.D. Tissot, N. Lion, Microparticles in stored red blood cells: An approach using flow cytometry and proteomic tools, Vox Sang. 95 (2008) 288–297.
[60] C. Hagelberg, D. Allan, Restricted diffusion of integral membrane proteins and polyphosphoinositides leads to their depletion in microvesicles from human erythrocytes, Biochem. J. 271 (1990) 831–834.
[61] H. Müller, H.U. Lutz, Binding of autologous IgG to human red blood cells before and after ATP-depletion. Selective exposure of binding sites (autoantigens) on spectrin-free vesicles, Biochim. Biophys. Acta 729 (1983) 249–257.
[62] U. Salzer, P. Hinterdorfer, U. Hunger, C. Borken, R. Prohaska, Ca^{++}-dependent vesicle release from erythrocytes involves stomatin-specific lipid rafts, synexin (annexin VII), and sorcin, Blood 99 (2002) 2569–2577.
[63] H. Hägerstrand, B. Isomaa, Lipid and protein composition of exovesicles released from human erythrocytes following treatment with amphiphiles, Biochim. Biophys. Acta 1190 (1994) 409–415.
[64] A. Iglic, P. Veranic, K. Jezernik, M. Fosnaric, B. Kamin, H. Hägerstrand, V. Kralj-Iglic, Spherocyte shape transformation and release of tubular nanovesicles in human erythrocytes, Bioelectrochemistry 62 (2004) 159–161.
[65] D. Allan, A.R. Limbrick, P. Thomas, M.P. Westerman, Microvesicles from sickle erythrocytes and their relation to irreversible sickling, Br. J. Haematol. 47 (1983) 383–390.
[66] M.P. Westerman, L. Unger, O. Kucuk, P. Quinn, L.J. Lis, Phase changes in membrane lipids in sickle red cell-shed vesicles and sickle red cells, Am. J. Hematol. 58 (1998) 177–182.
[67] P.F. Devaux, Is lipid translocation involved during endo- and exocytosis? Biochimie 82 (2000) 1–13.
[68] P. Sens, Dynamics of membrane budding driven by lipid translocation, Phys. Rev. Lett. 93 (2004) 108103.
[69] B.F. Lillemeier, J.R. Pfeiffer, Z. Surviladze, B.S. Wilson, M.M. Davis, Plasma membrane-associated proteins are clustered into islands attached to the cytoskeleton, Proc. Natl. Acad. Sci. USA 103 (2006) 18992–18997.
[70] P. Sens, M. Turner, Budded membrane microdomains as tension regulators, Phys. Rev. E Stat. Nonlin. Soft Matter Phys. 73 (2006) 031918.

[71] A. Roux, D. Cuvelier, P. Nassoy, J. Prost, P. Bassereau, B. Goud, Role of curvature and phase transition in lipid sorting and fission of membrane tubules, EMBO J. 24 (2005) 1537.
[72] F.-C. Tsai, H.-Y. Chen, Adsorption-induced vesicle fission, Phys. Rev. E Stat. Nonlin. Soft Matter Phys. 78 (2008) 051906.
[73] G.J.C.G.M. Bosman, F.L.A. Willekens, J.M. Were, Erythrocyte aging: A more than superficial resemblance to apoptosis? Cell. Physiol. Biochem. 16 (2005) 1–8.
[74] F. Lang, K.S. Lang, P.A. Lang, S.M. Huber, T. Wieder, Mechanisms and significance of eryptosis, Antiox. Redox Sig. 8 (2006) 1183–1192.
[75] D.K. Wilkinson, E.J. Turner, E.T. Parkin, A.E. Garner, P.J. Harrison, M. Crawford, G.W. Stewart, N.M. Hooper, Membrane raft actin deficiency and altered Ca^{2+}-induced vesiculation in stomatin-deficient overhydrated hereditary stomatocytosis, Biochim. Biophys. Acta—Biomembranes 1778 (2008) 125–132.
[76] M.E. Campanella, H. Chu, P.S. Low, Assembly and regulation of a glycolytic enzyme complex on the human erythrocyte membrane, Proc. Natl. Acad. Sci. USA 102 (2005) 2402–2407.
[77] F. Liu, H. Mizukami, S. Sarnaik, A. Ostafin, Calcium-dependent human erythrocyte cytoskeleton stability analysis through atomic force microscopy, J. Struct. Biol. 150 (2005) 200–210.
[78] A. Iglic, H. Hägerstrand, P. Veranic, A. Plemenitas, V. Kralj-Iglic, Curvature-induced accumulation of anisotropic membrane components and raft formation in cylindrical membrane protrusions, J. Theor. Biol. 240 (2006) 368–373.
[79] M. Fosnaric, A. Iglic, S. May, Influence of rigid inclusions on the bending elasticity of a lipid membrane, Phys. Rev. E Stat. Nonlin. Soft Matter Phys. 74 (2006) 051503.
[80] S.-C. Liu, L.H. Derick, M.A. Duquette, J. Palek, Separation of the lipid bilayer from the membrane skeleton during discocyte–echinocyte transformation of human erythrocyte ghosts, Eur. J. Cell Biol. 49 (1989) 358.
[81] W.H. Reinhart, S. Chien, Echinocyte–stomatocyte transformation and shape control of human red blood cells: Morphological aspects, Am. J. Hematol. 24 (1987) 1–14.
[82] J. Li, G. Lykotrafitis, M. Dao, S. Suresh, Cytoskeletal dynamics of human erythrocyte, Proc. Natl. Acad. Sci. USA 104 (2007) 4937–4942.

CHAPTER FIVE

Lipid Membranes as Tools in Nanotoxicity Studies

Damjana Drobne[1,*] *and* Veronika Kralj-Iglič[2]

Contents

Abstract

The uniqueness of nanoparticles/nanomaterials requires a new experimental methodology for nanotoxicity studies to complement the conventional techniques of traditional toxicology. Manufactured nanoparticles are potentially capable of inducing defects in lipid membranes such as physical disruptions, formation of holes, thinned regions, etc. The effects of nanoparticles on cell membranes are one of the key issues we are concerned about. Many methods may be employed to directly or indirectly explore this issue. Our aim is to show and discuss possibilities where nanoparticle–cell membrane or nanoparticle–vesicle interactions can be demonstrated. The aim of such studies is twofold. First, they help to characterize the membrane disruption potential of nanoparticles as their intrinsic property and second, they provide evidence to link the biological activity of nanoparticles to their toxic potential. The effects of nanoparticles were observed on lipid vesicles which are simplified biological membranes. Interactions between nanoparticles (C_{60}) and lipid vesicles (POPC) were demonstrated. Nanoparticles caused differences in size distribution of the population of vesicles incubated with nanoparticles when compared to the control population of vesicles.

* Corresponding author. Tel.: +386 1 42 33 388; Fax: +386 1 25 73 390;
E-mail address: damjana.drobne@bf.uni-lj.si

[1] Department of Biology, Biotechnical Faculty, University of Ljubljana, SI-1000 Ljubljana, Slovenia
[2] Laboratory of Clinical Biophysics, Institute of Biophysics, Faculty of Medicine, University of Ljubljana, Vrazov trg 2, SI-1000 Ljubljana, Slovenia

Advances in Planar Lipid Bilayers and Liposomes, Volume 10
ISSN 1554-4516, DOI: 10.1016/S1554-4516(09)10005-4

We also present and discuss interactions of nanoparticles with cell membrane in *in vivo* model system. Model invertebrate organism was orally exposed to a suspension of nanoparticles (nanosized TiO_2, nanosized ZnO, and C_{60}). After the exposure, destabilization of digestive gland cell membrane was assessed by acridine orange and ethidium bromide (AO/EB) differential fluorescent staining.

Results of studies on unintentional interactions of nanoparticles with biological membranes could benefit to the safe use of nanoparticles that are already available in medical, pharmaceutical, or food application. Understanding the nanoparticle-induced defects in biological membranes is among the major challenges of nanotoxicology. In the future, research on nanoparticle–membrane interactions needs to go toward understanding the mechanism of interaction which could lead to less hazardous nanotechnologies.

1. Introduction

Nanoparticles differ substantially from bulk materials having the same composition. Novel properties distinguishing nanoparticles from the bulk material typically become apparent at critical particle lengths below 100 nm. Particles of this size have numerous potential technological applications [1] but maybe hazardous as a result of a variety of interactions with biological systems possibly leading to harmful effects. Evaluating the potential hazards related to exposures to nanoscale materials and its products has become an emerging area in toxicology and health risk assessment.

Particle surface area and particle number determinations have been postulated to play significant roles in the development of nanoparticle-related effects. As the particle size is reduced, the proportion of atoms found at the surface is enhanced relative to the proportion inside its volume. This results in nanoscale particles, which are likely to be more reactive, thus generating more effective catalysts from an applications standpoint. However, from a health implications perspective, reactive groups on a particle surface are likely to modify the biological (potentially toxicological) effects. Therefore, changes in surface chemistry forming the ''shell'' on a (core) nanoparticle-type may be important and relevant for their biological potential. In addition, surface coatings can be utilized to alter surface properties of nanoparticles to prevent aggregation or agglomeration with different particle-types, and/or can serve to ''passivate'' the particle-type to mitigate the effects. It is interesting to note that surface coatings, functioning to reduce aggregation and to facilitate particle dispersion, enhance the efficacy of the particle-type in its *designed application*, but may also accelerate translocation of the nanoparticle throughout the body [2, 3]

Recent studies indicate that the toxicity of some nanoparticulates may be related, in large part, to the surface reactivity of the particles, indicating

that the particle surface–cellular interactions may take precedence over the core particle or particle size/surface area *per se* in influencing the development of (cyto)toxic responses [4]. It was shown that nanoparticles can strongly interact with cell membranes, either adsorbing onto it or compromising the membrane integrity to result in the formation of holes, membrane thinning and lipid peroxidation [5–9]. Recent papers report *in vivo* and *in vitro* [7] effects of nanoparticles on membrane stability and pore forming. The term hole or pore can refer to a wide range of structural changes that could lead to enhanced permeability ranging from the formation of an actual hole in the membrane to more subtle changes in content of the membrane leading to enhanced diffusion. Different mechanisms of permeabilization of cell membrane by nanoparticles have been proposed [10]. Membrane permeability could arise from a reduction in density of the plasma membrane. In this case, a hole or pore corresponds to a region of reduced material (lipid, protein, cholesterol, etc.). Furthermore, it is well-known that the phase transition of membrane lipids from the liquid crystalline state to the gel is followed by the ion permeability increase [11, 12]. To what extent nanoparticles affect phase transition of membrane lipids and subsequently increased ion permeability is of high importance in all bio–nano interaction studies.

Until recently, the biophysical behavior of lipid membranes was not of fundamental importance in toxicological studies. This is rapidly changing with the emergence of nanoparticles and questions regarding their safety. Concerns about cell plasma membrane disruption resulting in toxic effects are also paramount in the minds of nanoparticle designers focused on nanoparticle applications.

A convenient system for the study of the effect of various substances on membranes is artificial phospholipid membranes, which can be readily obtained by forming phospholipid vesicles in water solution. As the phospholipid bilayer being the basic constituent of the cell membrane, it is believed that the cell membranes and phospholipid membranes share some important features. Phospholipid vesicles are suitable since the composition of the membrane bilayer can be controlled to some extent. As artificial membranes are much less heterogeneous than cell membranes, it is easier to focus on a particular mechanism of interest. Also, giant phospholipid vesicles are large enough to be clearly observed live under the phase contrast optical microscope, so some processes such as shape transformations can be directly followed. Vesicles can be made of different lipid compositions while the surrounding solution can be manipulated by adding substances and changing the temperature.

It was previously found that some substances can have strong effect on giant phospholipid vesicles, so it would be possible that we would observe such features also due to the presence of nanoparticles. To show examples of such effects on the giant phospholipid vesicles, Fig. 1 shows that upon

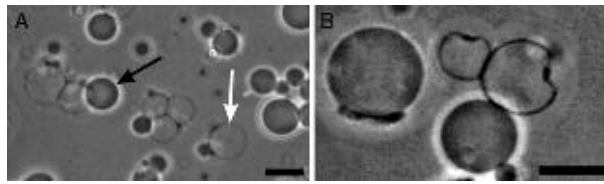

Figure 1 (A, B) Lipid vesicles incubated with buffer solution of plasma apolipoprotein H. Vesicles were created by electroformation in saccharose solution and rinsed with equiosmolar glucose solution. Due to difference in sugar composition the inside of the vesicle is darker than the surrounding solution if the membrane is intact and thus impermeable to sugar molecules (A, black arrow). After addition of apolipoprotein H adhesion between vesicles took place (A). Also, the membrane of some vesicles became permeable to sugar so the inside and the outside solutions mixed (A, white arrow). Lateral segregation of membrane material was also observed (B). Bar = 10 μm. Adapted from Ref. [13].

addition of a certain plasma protein, which also interacts with phospholipids on the microtitter plate (apolipoprotein H), causes adhesion between vesicles (A). Vesicles were created by electroformation in saccharose solution and rinsed with equiosmolar glucose solution. Since the intact membrane is impermeable to sugar molecules, the sugar composition inside (saccharose) differed from the composition outside (saccharose and glucose) and the inside of the vesicle is darker than the surrounding solution (A, black arrow). After the addition of apolipoprotein H, the membrane of some vesicles became permeable to sugar so the inside and the outside solutions mixed (A, white arrow). Furthermore, it can be seen in Fig. 1B that lateral segregation of membrane material took place, concomitant with the local curvature of the membrane.

Vesicles can adhere to each other due to the mediating effect of the surrounding solution. Figure 2 shows a population of giant phospholipid vesicles before (A) and after (B), the addition of the low-molecular-weight heparin dissolved in blood plasma into the suspension of vesicles. A strong effect of the mediated interaction can be observed.

Constituents of the outer solution can affect the shape of the entire vesicle. Figure 3 shows a pronounced transformation of shape of a vesicle with a long protrusion after the addition of the phosphate buffer saline to the outer solution. Although the membrane seems to stay intact, it can be seen that the shape of the protrusion changes from a tube-like to a bead-like. The shape changes can take place due to electrostatic properties of the membrane–solution interface, due to entropic effects and also due to difference of the osmotic pressure between the outer and the inner solution. The vesicles shown in Figs. 1–3 were created by electroformation method as described in Refs. [13, 14] and are mostly (over 90%) unilamellar [15].

As mentioned above, nanoparticles have also a potential to interact with biological membranes, so similar effects on vesicles could be expected also

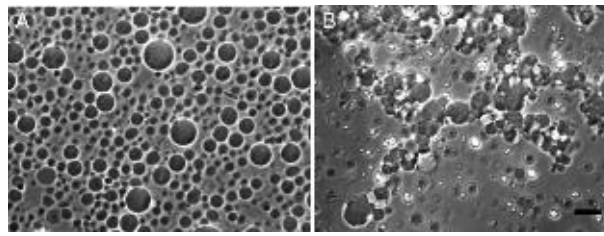

Figure 2 (A, B) Giant lipid vesicles before (A) and after (B) the addition of sugar solution of low molecular weight heparine. Adhesion of vesicles and permeabilization of membranes can be observed due to the presence of heparine (B). Bar = 20 μm.

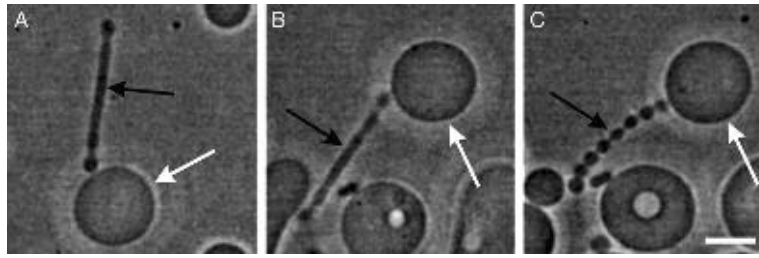

Figure 3 (A–C) Transformation of shape of a lipid vesicle after the addition of phosphate buffer saline to the sugar solution containing vesicles. A pronounced transformation of the protrusion shape can be observed. Time intervals between images are of the order of minutes. White arrows point to the mother vesicle while black arrows point to the protrusion. Bar = 10 μm. Adapted from Ref. [14].

due to the presence of nanoparticles. Giant phospholipid vesicles appeared to be an ideal system to study these interactions. An example is presented below. In addition, an *in vivo* system is presented too which can complete and upgrade the results obtained in *in vitro* system with lipid vesicles. The combination of *in vivo* and *in vitro* methods could significantly improve the relevance of results in nanotoxicology.

2. Effects of Engineered Nanoparticles on Lipid Membranes

2.1. Vesicle Shape Transformation Study

To a large extent, morphology of biological membranes is due to the ability of the molecules within them to move laterally along the membranes. Freely suspended membranes form closed vesicles which exhibit a variety of different shapes and shape transformations.

Phospholipid vesicles (also called liposomes) are under investigation both as models for biological membranes and as carriers for various bioactive agents such as drugs, diagnostic and genetic materials, and vaccines [16–19]. An essential parameter that describes the quality of liposome suspensions is the mean size, respectively the size distribution. A rigorous control of vesicle size and lamellarity within the vesicle population is stringent for achieving the desired behavior and thus the performance of vesicles for these purposes. In most laboratories routine liposome size analysis is carried out by photon correlation spectroscopy (PCS) using commercial instruments. This technique gives a measure for the mean size of the vesicles. Although PCS allows in principle the determination of particle size distributions, the reproducibility and reliability of the method for calculation is insufficient. Quantitative determination of the liposome size distribution, thus, is still difficult [20]. Although a number of powerful approaches like electron microscopy, ultracentrifugation, analytical size exclusion chromatography, and field-flow fractionation have been suggested, none of these approaches has found widespread use due to various limitations.

Recently, Zupanc *et al.* [21] studied the shape transformations of lipid vesicles by machine learning methods taking advantage of a possibility of direct observation of the vesicles within a population comparing to the above methods which are based on indirect measurements. They developed automated image segmentation and analyses for assessing population differences among vesicles incubated in different media.

In the study conducted by Zupanc *et al.* [21], differences in shapes between a population of nanoparticle-incubated vesicles and a control population were sought. Although the two populations did not show differences at a first sight (Figs. 4A, B and 5), subtle changes in size and shape could be revealed by quantitative analysis of the images. The authors discuss the imaging technologies which generate a wealth of images but require also quantitative image analysis as a prerequisite to turning qualitative data into quantitative values. Such quantitative data are expected to

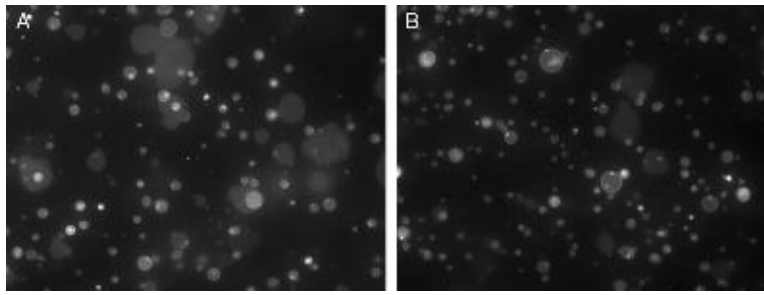

Figure 4 (A, B) Lipid vesicles incubated without (A) or with nanoparticles C_{60} (B). There are no differences in the shape transformation that could be observed by eye.

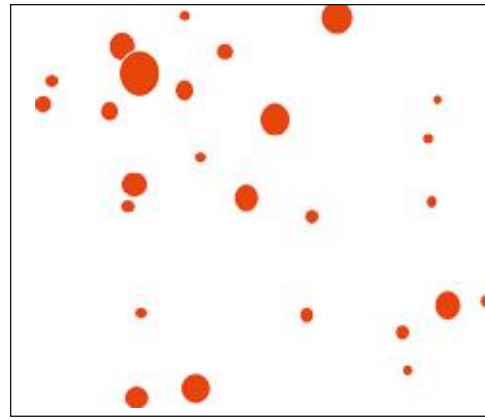

Figure 5 The circles represent segmented lipid vesicles. Their properties are evaluated by statistical image analysis approach [21]. Here the segmentation was done by an expert. In the future, it is strived that segmentation will be computer assisted.

open the way toward a detailed view of interactions between nanoparticles and biological membranes. The method based on computer aided analysis of lipid vesicles shape transformations holds many promises for future investigation of morphological characteristics of lipid vesicles.

We believe that the giant phospholipid vesicles are a promising system for the study of complex interactions of nanoparticles with biological membranes. A significant advantage of the system is that nanoparticles–giant phospholipid vesicles interactions could be studied under highly controlled conditions.

2.2. Membrane Destabilization as a Base for *In Vivo* Studies on Effect of Nanoparticles on Cell Membranes

Different mechanisms of permeabilization of cell membrane by nanoparticles have been proposed [10]. For example, membrane permeability could arise from a reduction in density of the plasma membrane. In this case, a hole or pore corresponds to a region of reduced material (lipid, protein, cholesterol, etc.). Another possibility for the hole or pore formation involves a change in plasma membrane content. For example, the formation of dendrimer/lipid vesicles could create a localized region that was lipid poor and protein and cholesterol rich. In addition, nanoparticles can provoke oxidative stress which in turn leads to lipid peroxidation and cell membrane permeabilization [22, 23].

Studies on juvenile largemouth bass brain cells confirmed that fullerenes do in fact induce oxidative stress [24]. Another possible mechanism

of nanoparticle membrane destabilization involves direct oxidation of the lipid membranes. For example, in the case of nanosized TiO_2, efficient destruction of bacteria has been ascribed to ultra-structural alterations of membranes, especially when irradiated with visible light [25]. In the case of nanosized ZnO, external generation of hydrogen peroxide has been considered to be one of the primary factors of antibacterial activity [26]. In the case of C_{60} [27], it has been suggested that induction of lipid peroxidation by C_{60} can result from direct physical contact with biological membranes.

An appealing method for assessing cell membrane permeabilistion employs acridine orange/ethidium bromide (AO/EB) staining and is widely conducted in *in vitro* studies with different types of cells. Recently, Valant *et al.* [28] modified this method to be applicable for cell membrane stability assessment of entire organ where a model animal is exposed *in vivo*.

The AO/EB assay is based on the assumption that changes in cell membrane integrity result in differences in permeability of cells to AO and EB dyes. Different permeability by the two dyes result in differentially stained nuclei as follows. Acridine orange is taken up by cells with membranes that are intact or destabilized, and in the cell, emits green fluorescence, as a result of its intercalation into double-stranded nucleic acids. Ethidium bromide, on the other hand, is taken up only by cells with destabilized cell membranes, and it emits orange fluorescence, after intercalation into DNA [29]. The assay has been applied to a variety of medical [30], pharmacological [31], biotechnological [32], and cell biology [33] studies.

In the modified AO/EB assay, the digestive glands (hepatopancreas) of a well-known group of terrestrial invertebrates, terrestrial isopods (*Porcellio scaber*, Isopoda, Crustacea) were taken as a model test system (Fig. 6A–F). Animals were orally exposed to a suspension of nanoparticles (nanosized TiO_2, nanosized ZnO, and C_{60}). Digestive gland cells came in direct contact with nanoparticles. The deferential staining showed that all tested nanoparticles, that is, nanosized TiO_2, fullerenes (C_{60}), and nanosized ZnO (Fig. 7), have cell membrane destabilization potential (Fig. 8A and B). Among them, C_{60} is the most biologically potent. Differently pretreated particles differ in their biological activity as well. Sonicated nanoparticles are more biologically aggressive than nonsonicated nanoparticles. As expected, bulk material failed to cause any membrane destabilization.

The AO/EB assay is applicable for ranging chemicals and nanoparticles according to their cell membrane destabilization potential. The advantage of the modified AO/EB method is its applicability to *in vivo* study under a realistic exposure scenario, which is via mouth to the digestive gland epithelium.

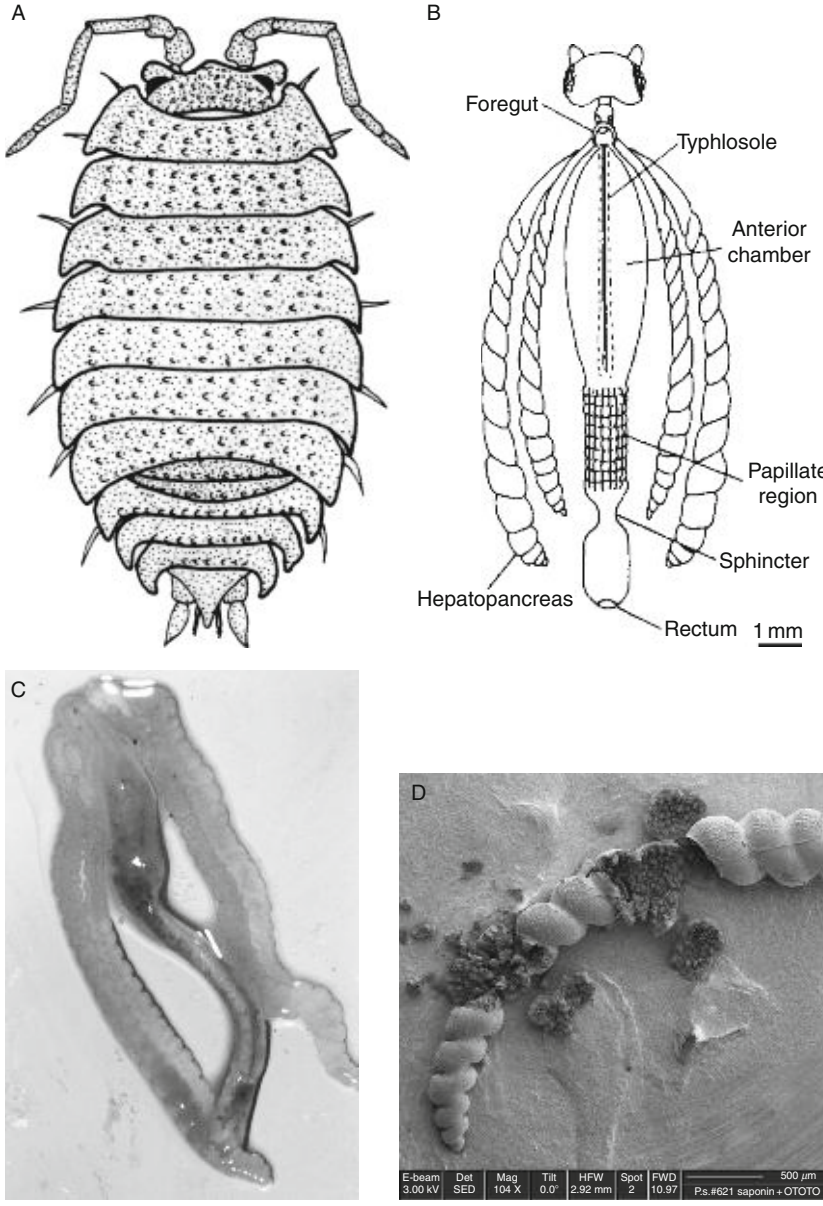

Figure 6 (Continued)

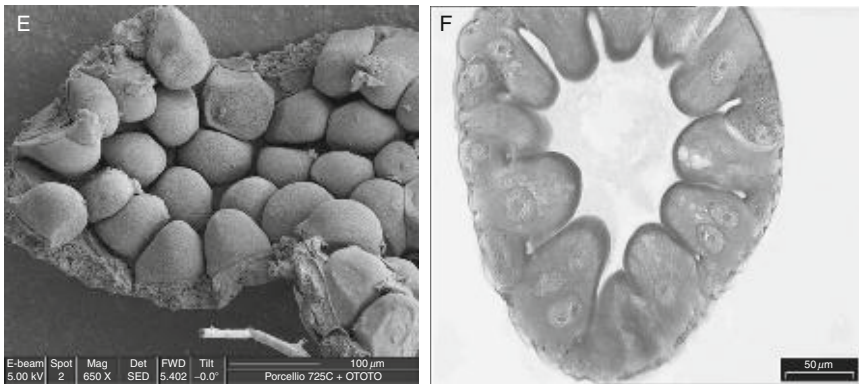

Figure 6 (A) A sketch of a model organism, terrestrial isopod *P. scaber* (Isopoda, Crustacea). (B) A sketch of a digestive system, the main route of particle uptake. (C) Light micrograph of isolated digestive system which is composed of four digestive gland tubes (hepatopancreas) and a gut. (D) Scanning electron micrograph of one digestive gland tube. Two parts of the tube are mechanically opened to expose the internal surface of the gland epithelium, see detail (F). (E) Scanning electron micrograph of apical surfaces of digestive gland cells which come in direct contact with suspension of nanoparticles applied orally. (Scanning electron micrographs taken by F. Tatti). (F) Light micrograph of a histological section of one digestive gland tube. Dom-shaped cells have one or two nuclei. (photos D and Ephotos taken by F. Tatti, CNR-INFM, University Modena, Modena, Italy)

3. Lipid Membranes in Nanotoxicity Studies

The lack of metrology for nanotoxicological evaluation contributes much of the confusion in the current exposure/risk assessment framework, causes uncertainty in the prediction of toxicity of nanoparticulate material and adds to the challenge of bio–nano interaction research. The lack of assessment technology is a critical issue for regulators and investors, agencies who fund the research or industries that expect to profit from nanotechnology.

At the moment, the use of existing toxicity tests for chemicals is recommended also for assessing the hazards of nanoparticles. A major reason for that is the familiarity and interpretability of these tests. However, in the future new tests are need which would include specific characteristics of nanoparticles.

On the basis of present knowledge, it appears that lipid vesicles fulfill many of requirements to be used in assessment of biological potential of nanoparticles *in vitro*. They are simple models for biological membranes and provide highly controllable and repeatable experimental conditions. In addition, such *in vitro* system is cost effective mean for toxicological and pharmaceutical studies.

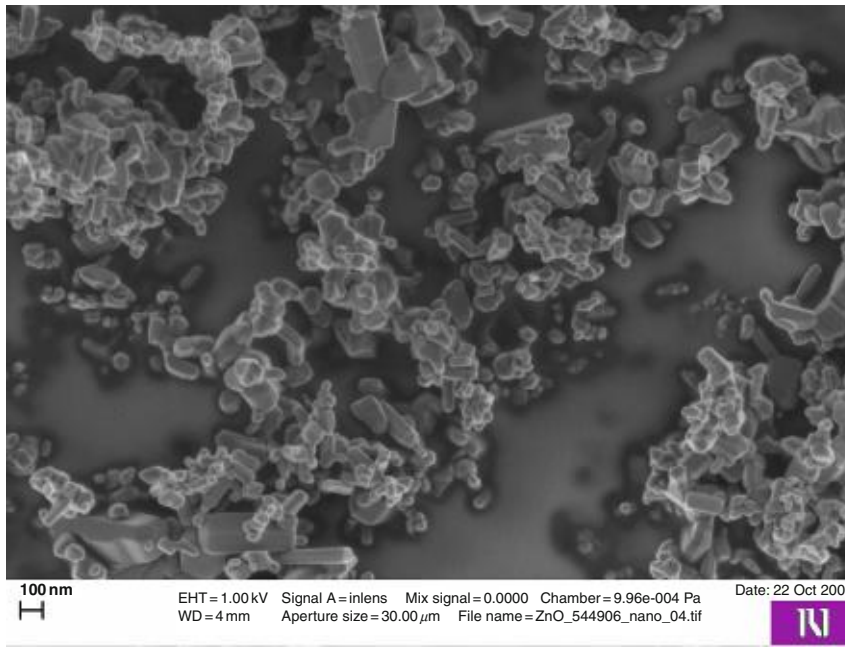

Figure 7 Scanning electron micrograph shows nanosized ZnO which membrane destabilization potential was tested in *in vivo* test system with *P. scaber.* The suspension of nanoparticles was orally applied and came in direct contact with the surface of gland epithelium cells (see Fig. 6E and F). After application digestive gland cells are stained with AO/EB (see Fig. 8A and B). (photo taken by M. Bele, National Institute of Chemistry, Ljubljana, Slovenia)

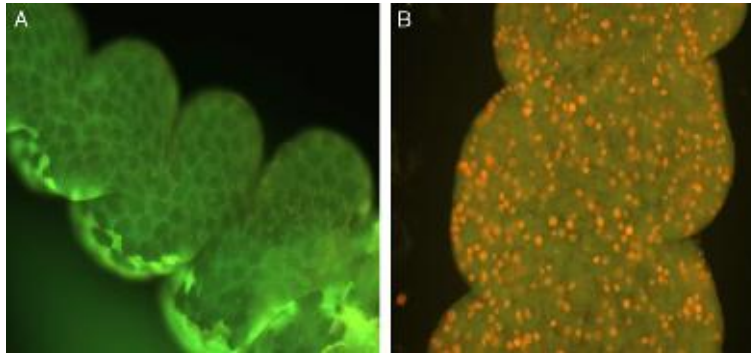

Figure 8 Micrographs of hepatopancreatic tissue of *P. scaber* taken by fluorescent microscope. (A) A control, untreated animal. No nuclei are stained with EB; (B) severely affected cell membranes. Cells with destabilized membranes have nuclei stained with EB (gray-white). (photos taken by J. Valant, Department of Biology, Biotechnical faculty, University of Ljubljana, Ljubljana, Slovenia)

In the future, studies on lipid vesicles could provide basic understanding of nanoparticle–membrane interactions and, second, the information on biological reactivity of nanoparticles could be used as an additional biological characteristic of nanoparticles apart from their physicochemical properties.

It is very important that biological effects of nanoparticles be tested also under realistic *in vivo* conditions because nanoparticles can be subject to a variety of alterations before they interact with cells. This could not be predicted in *in vitro* cell culture tests.

In vivo test with *P. scaber*, which is presented here, assures realistic exposure conditions which could reveal specific and unique interactions of the nanostructures with biological components inside the organism.

The same as in toxicity testing with chemicals most probably also in testing effects of nanoparticles a multilevel approach will be proposed. Such approach could involve more levels of testing that utilize both *in vitro* and *in vivo* methods. Perhaps, it will be visible that tier 1 evaluates nanoparticle–membrane interactions in a simplified *in vitro* system. Positive results at this level can be used either to direct further testing or just to rank-order the nanoparticles in terms of their membrane-destabilization potency.

4. Conclusions

A lot of knowledge already exists on interactions between nanoparticles and lipid membranes. This knowledge might significantly contribute to emerging field of nanotoxicology and support determination of safe doses of nanoparticles for humans and environment.

We presented here two different approaches for studying nanoparticle-membrane interactions. The application of machine-learning approach in studying shape transformations of vesicles illustrates the potential of computational imaging in understanding of the dynamics of nanoparticle–vesicle interactions. The other AO/EB staining allows assessing the nanoparticle–cell membrane interactions under realistic *in vivo* conditions.

Nanoparticles will have several beneficial applications in the future, but they should be applied at safe doses. However, at the same time, they have the potential to act as dangerous toxic compounds. This behavior is not surprising. The natural nanoparticles, oligonucleotides, and proteins, as well as more complex functional nanoparticles such as viruses have always presented humanity with a bipolar, Janus face.

REFERENCES

[1] R. Paull, J. Wolfe, P. Herbert, M. Sinkula, Investing in nanotechnology, Nat. Biotechnol. 21 (2003) 1144–1147.

[2] P.J.A. Borm, D. Robbins, S. Haubold, T. Kuhlbusch, H. Fissan, K. Donaldson, R. Schins, V. Stone, W. Kreyling, J. Lademann, J. Krutmann, D. Warheit, E. Oberdorster, The potential risks of nanomaterials: A review carried out for ECETOC, Particle Fibre Toxicol. 3 (2006) 1–35.
[3] G. Oberdörster, V. Stone, K. Donaldson, Toxicology of nanoparticles: A historical perspective, Nanotoxicology 1 (2007) 2–25.
[4] D.B. Warheit, R.A. Hoke, C. Finlay, E.M. Donner, K.L. Reed, C.M. Sayes, Development of a base set toxicity tests using ultrafine TiO_2 particles as a component of nanoparticle risk management, Toxicol. Lett. 171 (2007) 99–110.
[5] A. Mecke, IstvánJ. Majoros, AnilK. Patri, JamesR. Baker , MarkM. Banaszak Holl, BradfordG. Orr, Lipid bilayer disruption by polycationic polymers: The roles of size and chemical, Langmuir 21(23) (2005) 10348–10354.
[6] S. Hong, P.R. Leroueil, E.K. Janus, J.L. Peters, M.M. Kober, M.T. Islam, B.G. Orr, J.R. Baker, M.M. Banaszak Holl, Interaction of polycationic polymers with supported lipid bilayers and cells: Nanoscale hole formation and enhanced membrane permeability, Bioconjug. Chem. 17(3) (2006) 728–734.
[7] P.R. Leroueil, S. Hong, A. Mecke, J.R. Baker , B.G. Orr, M.M. Banaszak Holl, Nanoparticle interaction with biological membranes: Does nanotechnology present a Janus face? Acc. Chem. Res. 40(5) (2007) 335–342.
[8] L. Zhang, S. Granick, How to stabilize phospholipid liposomes (using nanoparticles), Nano Lett. 6(4) (2006) 694–698.
[9] V.V. Ginzburg, S. Balijepalli, Modeling the thermodynamics of the interaction of nanoparticles with cell membranes, Nano Lett. 7(12) (2007) 3716–3722.
[10] K. Unfried, C. Albrecht, L.O. Klotz, A. Von Mikecz, A. Grether, P.F. Beck, R. Schins, Cellular responses to nanoparticles: Target structures and mechanisms, Nanotoxicology 1 (2007) 52–71.
[11] V.F. Antonov, V.V. Petrov, A.A. Molnar, D.A. Predvoditelev, A.S. Ivanov, The appearance of single-ion channels in unmodified lipid bilayer membranes at the phase transition temperature, Nature 283 (1980) 585–586.
[12] V.F. Antonov, A.A. Anosov, O. You Nemchenko, E.Yu. Smirnova, in: A. Ottova-Leitmannova, H.T. Tein (Eds.), Advances in Planar Lipid Bilayers and Liposomes fifth ed., Elsevier, Amsterdam, 2007, pp. 151–172.
[13] A. Ambrožič, S. Čučnik, N. Tomšič, J. Urbanija, M. Lokar, B. Babnik, B. Rozman, A. Iglič, V. Kralj-Iglič, Interaction of giant phospholipid vesicles containing cardiolipin and cholesterol with β2-glycoprotein-I and anti-β2-glycoprotein-I antibodies, Autoimmun. Rev. 6 (2006) 10–15.
[14] J. Urbanija, N. Tomšič, M. Lokar, A. Ambrožič, S. Čučnik, B. Rozman, M. Kandušer, A. Iglič, V. Kralj-Iglič, Coalescence of phospholipid membranes as a possible origin of anticoagulant effect of serum proteins, Chem. Phys. Lipids 150 (2007) 49–57.
[15] L.A. Bagatolli, T. Parasassi, E. Gratton, Giant phospholipid vesicles: Comparison among the whole lipid sample characteristics using different preparation methods: A two photon fluorescence microscopy study, Chem. Phys. Lipids 105 (2000) 135–147.
[16] A. Imparato, J.C. Shillcock, R.T. Lipowsky, Shape fluctuations and elastic properties of two-component bilayer membranes, Europhys. Lett. 69(4) (2005) 50–656.
[17] G.T. Linke, R. Lipowsky, T. Gruhn, Free fluid vesicles are not exactly spherical, Phys. Rev. E 71(5) (2005) 051602-1–051602-7.
[18] R. Lipowsky, The morphology of lipid membranes, Curr. Opin. Struct. Biol. 5(4) (1995) 531–540.
[19] R. Lipowsky, M. Brinkmann, R. Dimova, C. Haluska, J. Kierfeld, J. Shillcock, Wetting, budding, and fusion-morphological transitions of soft surfaces, J. Phys.-Condens. Matter 17(31) (2005) S2885–S2902.

[20] M.H. Moona, I. Parka, Y. Kimb, Size characterization of liposomes by flow field-flow fractionation and photon correlation spectroscopy: Effect of ionic strength and pH of carrier solutions, J. Chromatogr. A 813(1) (1998) 91–100.
[21] J. Zupanc, J. Valant, A. Dobnikar, V. Kralj Iglič, A. Iglč, D. Drobne, Interactions of nanoparticles with lipid vesicles: a population based computer aided image analyisis approach, IEEE EMBS (in press).
[22] M. Heinlaan, A. Ivask, I. Blinova, H.C. Dubourguier, A. Kahru, Toxicity of nanosized and bulk ZnO, CuO and TiO_2 to bacteria *Vibro fischeri* and crustacea *Daphnia magna* and *Thamnocephalus platyurus*, Chemosphere 71 (2008) 1308–1316.
[23] K.L. Adams, D.Y. Lyon, P.J.J. Alvarez, Comparative eco-toxicity of nanoscale TiO_2, SiO_2 and ZnO water suspension, Water Res. 40 (2006) 3527–3532.
[24] E. Oberdörster, Manufactured nanomaterials (fullerenes, C_{60}) induce oxidative stress in brain of juvenile largemouth bass, Environ. Health Persp. 112 (2004) 1058–1062.
[25] P.C. Maness, S. Smolinski, D.M. Blake, Z. Huang, E.J. Wolfrum, W.A. Jackoby, Bactericidal activity of photocatalytic TiO_2: Toward an understanding of its killing mechanism, Appl. Environ. Microb. 65 (1999) 4094–4098.
[26] L. Zhang, Y. Jiang, Y. Ding, M. Povey, D. York, Investigation into the antibacterial behaviour of suspensions of ZnO nanoparticles (ZnO nanofluids), J. Nanoparticle Res. 9 (2007) 479–489.
[27] C.M. Sayes, A.M. Gobin, K.D. Ausman, J. Mendez, J.L. West, V.L. Colvin, Nano-C60 cytotoxicity is due to lipid peroxidation, Biomaterials 26 (2005) 7587–7595.
[28] J. Valant, D. Drobne, K. Sepčić, A. Jemec, K. Kogej, R. Kostanjšek, Hazardous potential of manufactured nanoparticles identified by *in vivo* assay, J. Hazard. Matr. (in press).
[29] A.J. McGahon, S.J. Martin, R.P. Bissonnette, A. Mahboubi, Y. Shi, R.J. Mogil, W. K. Nishioka, D.R. Green, The end of the (cell) line: Methods for the study of apoptosis, Method Cell Biol. 46 (1995) 153–185.
[30] L.M. Ellerby, A.S. Hackam, S.S. Propp, H.M. Ellerby, S. Rabizadeh, N.R. Cashman, M.A. Trifiro, L. Pinsky, C.L. Wellington, G.S. Salvesen, M.R. Hayden, D.E. Bredesen, Kennedy's disease. Caspase cleavage of the androgen receptor is a crucial event in cytotoxicity, J. Neurochem. 72 (1999) 185–195.
[31] D. Hreniuk, M. Garay, W. Gaarde, B.P. Monia, R.A. Mckay, C.L. Cioffi, Inhibition of c-Jun N-terminal kinase 1, but not c-Jun N-terminal kinase 2, suppresses apoptosis induced by ischemia/reoxygenation in rat cardiac myocytes, Mol. Pharmacol. 59 (2001) 867–874.
[32] S. Mercille, B. Massie, Induction of apoptosis in nutrient-deprived cultures of hybridoma and myeloma cells, Biotech. Bioeng. 44 (1994) 1140–1154.
[33] P.X. Petit, H. Lecoeur, E. Zorn, C. Dauguet, B. Mignotte, M.L. Gougeon, Alterations in mitochondrial structure and function are early events of dexamethasone-induced thymocyte apoptosis, J. Cell Biol. 130 (1995) 157–167.

CHAPTER SIX

Structure and Function of Biomembranes and Membrane Phospholipids of Rat Salivary Glands: Properties of Liposome- and Plasma Membrane-Induced Membrane Fusion and Consequent Amylase Release from Isolated Secretory Granules

Yasunaga Kameyama[1,*]

Contents

* Corresponding author. Tel.: +81 58 329 1417; Fax: +81 58 329 1417;
E-mail address: kameyama@dent.asahi-u.ac.jp

[1] Department of Oral Biochemistry, Asahi University School of Dentistry, 1851 Hozumi, Mizuho, Gifu 501-0296, Japan

Advances in Planar Lipid Bilayers and Liposomes, Volume 10
ISSN 1554-4516, DOI: 10.1016/S1554-4516(09)10006-6

Abstract

Exocytosis is phenomena of the membrane fusion between the plasma membranes and the secretory granular membranes and finally, the components of granule are secreted. Recently, the molecular mechanisms of the exocytosis are focused to clarify the interactions and organizations of cells. The membrane physical properties, which are mainly affected by the membrane phospholipids, play a very important role for the process of membrane fusion. We extensively investigated about the mechanisms of saliva secretion as a model cell for exocytosis. To clarify the characteristics of membranes which are not only from whole cells but also from secretory granule, their phospholipids and fatty acids compositions were analyzed. Among the many steps of enzyme reaction for the biosynthesis of phosphatidylcholine, which is a major phospholipid present in mammalian cell membranes, the reacylation enzyme activity is very important to estimate the phospholipid fatty acyl composition. Physicochemical properties, membrane fluidity, of various types of biomembrane isolated from the cells, and their phospholipid liposomes were measured by the electron spin resonance method using various types of spin probes. Under the reconstitution system for membrane fusion and amylase secretion consisted by isolated secretory granules and phospholipids liposomes or isolated plasma membranes, many modulation effectors in exocytosis are clarified.

1. Introduction

In higher animals, cells and organs exchange information and maintain a balance and harmony to perpetuate life. Ligands for information exchange: neurotransmitters, hormones, and cytokines, are mostly proteins. Protein synthesized in cells is extracellularly released via the Golgi apparatus and secretory vesicles. Elucidation of the molecular control system of exocytosis has recently been progressing with regard to the maintenance of homeostasis of the body, memory formation, and neurotransmission. The final step of exocytosis is the docking of secretory vesicles to the plasma membrane and subsequent membrane fusion. The involvement of a series of soluble-*N*-ethylmaleimide-sensitive factor attachment protein receptor (SNARE) proteins has been reported, and studies on membrane fusion using an artificial membrane reconstruction system have been progressing [1–6]. High-molecular-weight organic components of saliva including protein are present in the storage organ of acinar cells: secretory granules. Secretory granules fuse with the plasma membrane in response to appropriate stimulation, and saliva is extracellularly released by exocytosis [7]. Membrane fusion involves a dynamic alternation of the state of biomembranes, in which the physicochemical properties of the membrane, consisting of phospholipids as the main component, play an important role in the

initiation and progression of fusion. For our group, who selected the salivary glands as the study subject, clarification of the molecular mechanism of salivary protein exocytosis may lead to analysis of the secretory control of physiologically active proteinaceous substances in higher animals. Since the involvement of proteins, represented by SNARE, in salivary exocytosis has been reported [8, 9], and its elucidation has been progressing, we focused on the essential component of membrane fusion, the biomembrane, as a clue to the study approach.

The physicochemical properties of biomembranes are markedly influenced by the composition and structure of their lipid components [10]. An index of a membrane's physical properties, membrane fluidity, is closely related to the exertion and control of membrane function, and controlled by the amphipathic phospholipid structure in a complex way [11]. In addition, intracellular organelles have characteristic lipid compositions [12]. The presence of functional domains with partially different lipid compositions, rafts and caveolae, has recently been clarified [13–16].

Based on the above viewpoints, we investigated salivary gland function represented by salivary exocytosis and its correlation with the phospholipid structure, physical properties, biosynthesis, and salivary secretory function using rat salivary acinar cells as a secretory cell model [17–19]. Herein, we report the results of the series of studies.

2. Membrane Phospholipids and their Fatty Acid Composition

2.1. Phospholipid Composition

Regarding the phospholipid composition of the salivary acinar cell membrane, the main components, phosphatidylcholine (PC) and phosphatidylethanolamine (PE), account for 60–70%, followed by sphingomyelin (SM), phosphatidylinositol (PI), phosphatidylserine (PS), and phosphatidic acid (PA) (Table 1) [20]. In higher animals, phospholipid compositions characteristic of organs and tissues are present [21], but the phospholipid composition ratio in salivary acinar cells is similar to that in the liver, and mostly the same among the three major salivary glands. The development of the saliva secretory function completes with maturation after birth. On comparison of the salivary gland between immature (3 weeks of age) and adult (9 weeks of age) rats, the PC content increased with growth.

Since salivary exocytosis occurs through fusion of the secretory granule and plasma membranes, we analyzed the phospholipid composition of secretory granules of parotid acinar cells isolated by density gradient centrifugation. There was no marked difference determining the characteristics of the secretory granule membrane, but the PE content was high, and

Table 1 Membrane phospholipid compositions of the three major salivary glands of 3- and 9-week (W)-old rats [20]

	Parotid gland		Submandibular gland		Sublingual gland	
	3 W (3–9)	9 W (7)	3 W (3–9)	9 W (7)	3 W (3–9)	9 W (7)
Total phospholipids (μmol/g of wet tissue wt)	17.6 ± 3.8	17.0 ± 1.9	18.7 ± 1.4	20.2 ± 2.5	22.6 ± 1.4	22.1 ± 1.5
Each phospholipid (%)						
Phosphatidylcholine (PC)	39.0 ± 1.4	45.9 ± 4.0	37.9 ± 2.8	44.4 ± 1.3	35.3 ± 2.9	45.3 ± 1.2
Phosphatidylethanolamine (PE)	27.2 ± 2.4	27.3 ± 1.8	24.0 ± 1.2	25.9 ± 1.6	22.9 ± 0.8	24.7 ± 0.9
Sphingomyelin (SM)	8.2 ± 0.7	7.1 ± 1.4	7.6 ± 0.9	7.6 ± 0.7	7.3 ± 0.6	7.7 ± 1.6
Phosphatidylinositol (PI)	3.9 ± 1.0	3.4 ± 0.7	5.4 ± 0.8	3.4 ± 0.5	5.7 ± 0.4	4.9 ± 1.4
Phosphatidylserine (PS)	3.4 ± 0.7	3.6 ± 0.9	5.4 ± 1.1	3.9 ± 1.0	5.5 ± 0.8	4.5 ± 1.8
Phosphatidic acid (PA)	2.1 ± 0.7	1.7 ± 0.3	3.2 ± 0.7	2.2 ± 0.9	3.3 ± 0.7	2.0 ± 0.8
Others	16.2	11.0	16.5	12.6	20.0	10.9

Values are means ± S.E. of independent experiments shown in parenthese.

Table 2 Membrane phospholipid compositions of cell organelles isolated from the rat parotid acinar cell fraction [23]

	Homogenate (3)	Microsomes (4)	Secretory granules (3)
Each phospholipid (%)			
Phosphatidylcholine (PC)	46.5 ± 3.6	51.1 ± 1.2	40.3 ± 0.7**
Phosphatidylethanolamine (PE)	25.7 ± 1.2	24.8 ± 0.8	30.5 ± 1.0*
Sphingomyelin (SM)	7.3 ± 0.1	7.8 ± 0.3	7.0 ± 0.2*
Phosphatidylinositol (PI)	6.5 ± 0.9	5.1 ± 0.8	3.6 ± 0.4
Phosphatidylserine (PS)	4.8 ± 0.8	4.2 ± 0.3	2.4 ± 0.1**
Caldiolipin (CL)	1.9 ± 0.4	0.3 ± 0.1	3.9 ± 0.2**
Phosphatidic acid (PA)	1.1 ± 0.6	0.2 ± 0.1	0.5 ± 0.3
Lysophospholipids (LPLs)	3.1 ± 0.6	3.1 ± 0.5	8.3 ± 0.8**
Others	3.1	3.4	3.5
PC/PE ratio	1.8 ± 0.1	2.1 ± 0.1	1.4 ± 0.0

* $p < 0.05$
** $p < 0.01$; significance of difference between secretory granular fraction and microsomal fraction judged by Student's *t*-test.
Values are means ± S.E. of independent experiments shown in parenthese.

lysophospholipids were abundant (Table 2) [22, 23]. Physicochemically, both components promote membrane fusion [24, 25], suggesting that these affect the promotion of salivary secretion.

The hydrophobic region of membrane phospholipids is bound by long-chain carbohydrates, represented by fatty acids. These long-chain carbohydrates are classified into three types based on the pattern of bonding to the phospholipid glycerol backbone: acyl (ester bond), alkyl (ether bond), and alkenyl (vinyl ether bond) types, and the structural characteristics are reflected in the physicochemical properties of the biomembrane. When the acyl-, alkyl-, and alkenyl-type composition ratios were investigated in the parotid gland PC and PE, the acyl-type accounted for the highest ratio in both phospholipids, followed by the acyl type in PC and the alkenyl type in PE (Table 3) [26].

2.2. Fatty Acid Composition of Each Phospholipid

A characteristic of membrane phospholipids is marked variation of the fatty acid composition among phospholipids. The fatty acid compositions of PC, PE, and PI in parotid acinar cells are shown in Table 4 [20]. In PC, palmitic acid (16:0) accounted for about 40%, and linolenic acid (18:2), oleic acid (18:1), and arachidonic acid (20:4) for 10–20%. In PE, 20:4 accounted for 20–30%, followed by 18:1 and stearic acid (18:0). These findings suggested

Table 3 Compositions of choline- and ethanolamine-containing glycerophospholipids isolated from the rat parotid gland membrane [26]

	Major glycerophospholipid	
Type	Choline-containing (%)	Ethanolamine-containing (%)
1-Acyl-2-acyl	72.7	42.6
1-Alkyl-2-acyl	23.8	25.4
1-Alkenyl-2-acyl	3.5	32.0

that fatty acids are selectively incorporated in biosyntheses of the two main phospholipids. In phospholipids of higher animal cells, generally, saturated and unsaturated fatty acids are ester-bonded at the *sn*-1 and *sn*-2 sites of the glycerol backbone, respectively. The high 20:4 content of phospholipids suggests that the *sn*-2 sites of PC and PE serve as important storage sites of eicosanoid precursors. The fatty acid composition of PI was also different from those of PC and PE: 18:0 and 16:0 were bonded to the *sn*-1 site, and 20:4, 18:2, and eicosapentaenoic acid (20:5) to the *sn*-2 site, showing that the *sn*-2 site is also the eicosanoid precursor storage site, despite the composition ratio being different. Table 4 reveals that the composition did not change for any phospholipid during maturation of the parotid gland after birth. These analytical findings observed in the parotid gland were similarly noted in the submandibular and sublingual glands.

Among phospholipids isolated from the secretory granule membrane, the fatty acid compositions of PC and PE were similar to those in the homogenates and microsomes (Table 5) [23].

3. Fatty Acid-Related Phospholipid-Metabolizing Enzyme

3.1. 1-Acyl-*sn*-Glycero-3-Phosphocholine (1-Acyl GPC) Acyltransferase

Polyunsaturated fatty acids (20:4: 26%, 18:2: 24%, 20:3: 4.6%), which are eicosanoid precursors, are ester-bonded to the *sn*-2 site of PC in the parotid gland [27]. The enzyme introducing these is 1-acyl-glycerophosphocholine (1-acyl GPC) acyltransferase. The substrate specificities of salivary gland and liver 1-acyl GPC acyltransferase for acyl-CoA are shown in Table 6 [28]. The activity level for unsaturated acyl-CoA was high in all salivary glands measured. In addition, the activity levels for 20:5, 20:4, and 20:3 were high in the parotid gland [28, 29], strongly suggesting that 1-acyl GPC acyltransferase plays an important role in the establishment of the fatty acid composition at the *sn*-2 site of PC.

Table 4 Fatty acid compositions of phospholipids isolated from the parotid acinar cell membranes of 3- and 9-week (W)-old rats [20]

	Phosphatidylcholine (PC) (%)		Phosphatidylethanolamine (PE) (%)		Phosphatidylinositol (PI) (%)	
Fatty acid (%)	3 W (3)	9 W (3)	3 W (3)	9 W (3)	3 W (3)	9 W (3)
Myristic acid (14:0)	0.9 ± 0.1	1.0 ± 0.3	0.9 ± 0.7	2.6 ± 1.0	1.1 ± 0.7	1.7 ± 1.0
Palmitic acid (16:0) alkenyl	0.3 ± 0.1	0.2 ± 0.1	6.5 ± 1.4	5.9 ± 0.4	0.6 ± 0.2	0.6 ± 0.2
Palmitic acid (16:0)	43.5 ± 1.7	40.4 ± 1.4	8.4 ± 0.9	10.1 ± 0.1	16.2 ± 1.6	15.6 ± 1.0
Palmitoleic acid (16:1)	1.6 ± 0.1	1.3 ± 0.2	1.3 ± 0.3	2.3 ± 0.2	1.9 ± 0.4	2.6 ± 1.3
Stearic acid (18:0)	8.1 ± 0.3	8.7 ± 0.3	15.3 ± 1.4	14.4 ± 0.6	36.6 ± 1.2	29.5 ± 1.3
Oleic acid (18:1)	13.3 ± 0.6	10.8 ± 0.7	18.2 ± 0.7	15.3 ± 0.1	11.7 ± 1.8	10.1 ± 0.6
Linoleic acid (18:2)	15.9 ± 0.4	17.4 ± 0.4	9.0 ± 0.4	9.5 ± 0.5	4.2 ± 0.1	4.0 ± 0.9
Eicosatrienoic acid (20:3)	1.9 ± 0.3	1.6 ± 0.2	1.9 ± 0.1	1.7 ± 0.2	1.8 ± 0.4	1.5 ± 0.2
Arachidonic acid (20:4)	9.9 ± 1.2	12.3 ± 1.3	22.9 ± 2.5	23.7 ± 0.6	11.3 ± 1.4	11.8 ± 1.0
Eicosapentaenoic acid (20:5)	0.2 ± 0.1	0.8 ± 0.1	0.2 ± 0.1	1.5 ± 0.2	1.9 ± 0.2	9.9 ± 0.8
Docosapentaenoic acid (22:5)	0.3 ± 0.0	0.3 ± 0.1	1.3 ± 0.1	1.1 ± 0.1	0.6 ± 0.1	0.5 ± 0.2
Docosahexaenoyl (22:6)	0.5 ± 0.1	0.7 ± 0.2	5.3 ± 0.6	4.6 ± 0.1	1.2 ± 0.1	1.5 ± 0.5
Others	3.6	4.5	8.8	7.3	10.9	10.7

Values are means ± S.E. of independent experiments shown in parenthese.

Table 5 Fatty acid compositions of cell organelle membrane phospholipids isolated from the rat parotid acinar cell fraction [23]

	Phosphatidylcholine (PC) (%)			Phosphatidylethanolamine (PE) (%)		
Fatty acid	Homogenate (3)	Microsomes (4)	Secretory granules (3)	Homogenate (3)	Microsomes (4)	Secretory granules (3)
Myristic acid (14:0)	0.40 ± 0.06	0.45 ± 0.02	0.42 ± 0.06	0.17 ± 0.06	0.23 ± 0.06	0.23 ± 0.13
Palmitic acid (16:0) alkenyl	0.84 ± 0.22	0.71 ± 0.12	0.80 ± 0.15	9.62 ± 0.48	10.87 ± 0.89	7.01 ± 1.16
Palmitic acid (16:0)	39.99 ± 0.37	40.93 ± 0.37	40.29 ± 0.86	7.75 ± 0.33	7.78 ± 0.32	7.52 ± 0.41
Palmitoleic acid (16:1)	0.89 ± 0.36	1.19 ± 0.19	0.88 ± 0.35	0.95 ± 0.14	1.01 ± 0.10	1.06 ± 0.32
Stearic acid (18:0) alkenyl	0.13 ± 0.01	0.12 ± 0.01	0.13 ± 0.02	4.62 ± 0.58	5.91 ± 0.34	3.37 ± 0.26**
Stearic acid (18:0)	7.83 ± 0.29	7.80 ± 0.25	8.17 ± 0.36	14.83 ± 1.94	13.90 ± 1.60	20.80 ± 1.65*
Oleic acid (18:1)	10.51 ± 0.28	10.46 ± 0.32	10.74 ± 0.08	15.65 ± 0.15	16.16 ± 0.58	16.08 ± 0.63
Linoleic acid (18:2)	18.47 ± 1.01	18.36 ± 0.74	18.44 ± 0.66	8.19 ± 0.58	7.53 ± 0.49	9.12 ± 0.73
Eicosatrienoic acid (20:3)	1.66 ± 0.07	1.54 ± 0.11	1.61 ± 0.20	1.48 ± 0.04	1.32 ± 0.06	1.32 ± 0.11
Arachidonic acid (20:4)	14.55 ± 0.42	14.27 ± 0.37	13.87 ± 0.85	26.20 ± 1.52	25.12 ± 2.09	23.73 ± 1.19
Eicosapentaenoic acid (20:5)	0.26 ± 0.06	0.19 ± 0.03	0.54 ± 0.13	0.16 ± 0.05	0.36 ± 0.20	0.62 ± 0.35
Docosapentaenoic acid (22:5)	0.20 ± 0.04	0.20 ± 0.02	0.11 ± 0.05	0.92 ± 0.04	1.02 ± 0.12	0.67 ± 0.02
Docosahexaenoyl (22:6)	0.68 ± 0.03	0.63 ± 0.04	0.60 ± 0.12	5.23 ± 0.28	4.98 ± 0.52	4.44 ± 0.15
Tetracosanoic acid (24:0)	0.84 ± 0.08	0.84 ± 0.06	0.80 ± 0.10	1.30 ± 0.16	1.23 ± 0.13	1.16 ± 0.11
Others	2.75	2.31	2.60	2.93	2.58	2.87

* $p < 0.05$
** $p < 0.01$; significance of difference between secretory granular fractionand microsomal fraction judged by Student's *t*-test.
Values are means ± S.E. of independent experiments shown in parenthese.

Table 6 Substrate specificity of rat salivary acinar cell 1-acyl-glycerophosphocholine acyltransferase [28]

Acyl-CoA	Specific activity (nmol/min per mg of protein)			Ratio of specific activity		
	Submandibular gland (A)	Parotid gland (B)	Liver (C)	A/B	A/C	B/C
Myristoyl[14:0]-CoA	10.5	2.3	6.9	4.6	1.5	0.3
13-Methyltetradecanoyl[*iso*15:0]-CoA	25.3	4.8	14.5	5.3	1.7	0.3
Palmitoyl[16:0]-CoA	14.8	4.4	6.5	3.4	2.3	0.7
Palmitoleoyl[16:1(*n*-7)]-CoA	12.9	3.9	10.8	3.3	1.2	0.4
Stearoyl[18:0]-CoA	9.7	–*	–	–	–	–
Oleoyl[18:1(*n*-9)]-CoA	50.1	11.6	37.1	4.3	1.4	0.3
Elaidoyl [*trans*18:1(*n*-9)]-CoA	46.9	12.0	22.8	3.9	2.1	0.5
Linoleoyl[18:2(*n*-6)]-CoA	32.5	10.9	25.3	3.0	1.3	0.4
Linoelaidoyl[*trans*18:2(*n*-6)]-CoA	32.9	9.5	23.8	3.5	1.4	0.4
α-Linolenoyl[18:3(*n*-3)]-CoA	10.5	4.0	6.6	2.6	1.6	0.6
γ-Linolenoyl[18:3(*n*-6)]-CoA	40.0	14.0	33.9	2.9	1.2	0.4
11,14,17-Eicosatrienoyl[20:3(*n*-3)]-CoA	63.9	19.4	40.6	3.3	1.6	0.5
Bishomo-γ-linolenoyl[20:3(*n*-6)]-CoA	37.2	8.1	–	4.6	–	–
Arachidonoyl[20:4(*n*-6)]-CoA	55.6	13.8	33.1	4.0	1.7	0.4
5,8,11,14,17-Eicosapentaenoyl[20:5(*n*-3)]-CoA	99.4	33.6	54.7	3.0	1.8	0.6
4,7,10,13,16,19-Docosahexaenoyl[22:6(*n*-3)]-CoA	20.1	5.0	15.7	4.0	1.3	0.3

* Not determined.

Specific activities represent the averages of duplicate assays. Acyl chains are designated as the number of carbon atoms:the number of double bonds followed by the position of double bonds.

3.2. 1-Acyl-*sn*-Glycero-3-Phosphoinositol (1-Acyl GPI) Acyltransferase

PI has a high amount of 20:4 at the *sn*-2 position. The tendency, observed in the acyl-CoA specificities of 1-acyl GPC acyltransferase activity, was also marked with regard to the specificity of 1-acyl glycerophosphoinositol (1-acyl GPI) acyltransferase, the enzyme incorporating a fatty acid at the *sn*-2 site of PI in the submandibular gland (Fig. 1) [30], indicating that 1-acyl GPI acyltransferase actively incorporates 20:4 at the *sn*-2 site in PI biosynthesis, forming the characteristic functional lipid. This high characteristic activity of 1-acyl GPI acyltransferase was also observed in mammalian tissues [31].

3.3. Possible Induction of Acyltransferases

As shown in Table 7, the enzyme activity levels of both 1-acyl GPC and GPI acyltransferases in the submandibular gland increased by two to three times with growth without changes in the substrate specificity for various acyl-CoA including polyunsaturated acyl-CoA and Km values [32, 33], suggesting the specific contribution of the deacylation–acylation enzyme system to the maturation process after birth. Recently, there are many reports on cloning and characterization of those lysophospholipid

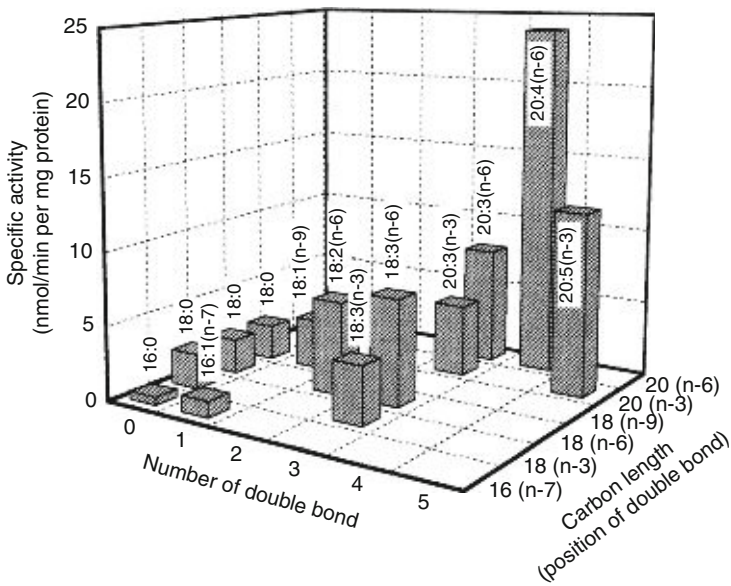

Figure 1 Fatty acid chain length- and double bonding site-specific substrate specificity of rat submandibular gland 1-acyl glycerophosphoinositol (1-acyl GPI) acyltransferase for acyl-CoA [30].

Table 7 Substrate specificities and activity levels of acyltransferases of 3- and 10-week (W)-old rat submandibular acinar cells [33]

	Specific activity (nmol/min per mg of protein)		Ratio of specific activity
Acyltransferase Acyl-CoA	3 W (A)	10 W (B)	B/A
1-Acyl-*sn*-glycero-3-phosphocholine(1-acyl GPC)			
Linoleoyl[18:2(*n*-6)]-CoA	11.2	32.5	2.9
Arachidonoyl[20:4(*n*-6)]-CoA	13.2	55.6	4.2
5,8,11,14,17-Eicosapentaenoyl [20:5(*n*-3)]-CoA	27.5	99.4	3.6
1-Acyl-*sn*-glycero-3-phosphoinositol(1-acyl GPI)			
Arachidonoyl[20:4(*n*-6)]-CoA	5.5	13.9	2.5
5,8,11,14,17-Eicosapentaenoyl [20:5(*n*-3)]-CoA	3.1	8.4	2.7

acyltransferases which propose the biological significance of membrane diversity and asymmetry [34–36], and their specific functions in the salivary glands should become clear.

4. Biomembrane Phospholipid Composition and Membrane Fluidity

As observed in exocytosis-associated membrane fusion, biomembranes are in a dynamic state, and their physicochemical properties are markedly affected by the composition and structure of the component phospholipids. The physical properties of membranes determine and maintain important conditions to exert their dynamic function, through which the optimum site for membrane proteins including SNARE to exert their functions may be provided.

An index of a membrane's physical properties, membrane fluidity, can be observed using the electron spin resonance (ESR) method with two stearic acid spin probes, 5-doxyl-stearic acid (5-SAL) and 12-doxyl-stearic acid (12-SAL) (Fig. 2). As shown in Fig. 3, the parallel (T_{II}') and perpendicular (T_{L}') principal values of the hyperfine tensor of an axially symmetrical spin Hamiltonian were estimated from the ESR spectra. The order parameter (S) was calculated using the following relation:

$$S = \frac{a \times (T_{\mathrm{II}}{}' - T_{\mathrm{L}}{}')}{a' \times [Tzz - (Txx + Tyy)/2]}$$

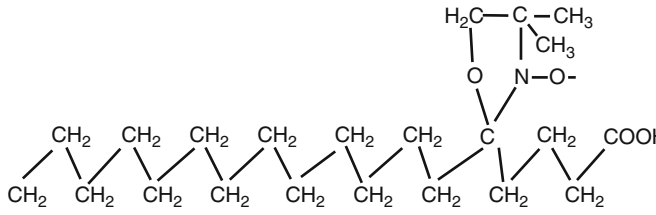

5-doxyl-stearic acid (5-SAL)

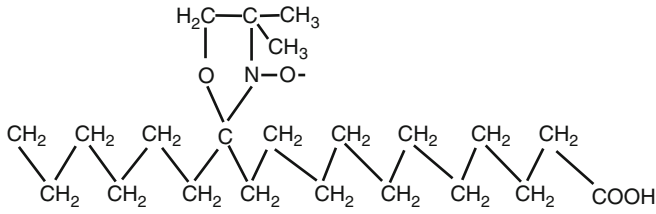

12-doxyl-stearic acid (12-SAL)

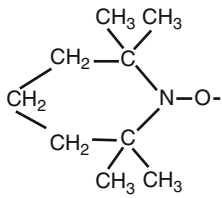

2,2,6,6-tetramethylpiperidine *N*-oxyl(TEMPO)

Figure 2 Chemical structure of spin probes. 5-Doxyl-stearic acid (5-SAL) and 12-doxyl-stearic acid (12-SAL), and 2,2,6,6-tetramethylpiridine *N*-oxyl (TEMPO) were used to obtain the order parameter (S) and the spectral parameter (f), respectively, calculated from electron spin resonance (ESR) spectra.

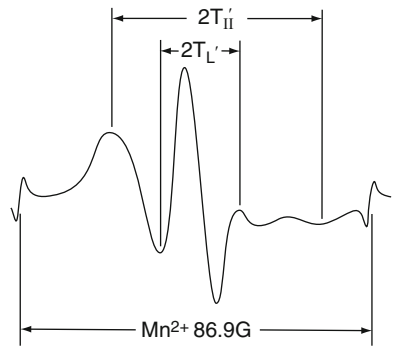

Figure 3 Electron spin resonance (ESR) spectrum of 12-SAL spin probe at 25 °C. The T_{II}' and T_L' show the parallel and perpendicular principal values of the hyperfine tensor of an axially symmetrical spin Hamiltonian, respectively [10].

where $Txx = Tyy = 5.9$ G and $Tzz = 32.9$ G are the hyperfine principal values of the nitroxide radical. a/a' is the polarity correction factor, where $a = (Txx + Tyy + Tzz)/3 = 14.9$ G and $a' = (T_{II}' + 2T_{L}')/3$ [10]. A smaller value of the order parameter (S) means a more 'fluid' membrane.

Figure 4 shows the membrane fluidities of total phospholipids isolated from the three major salivary glands observed using two types of spin probe, 5-SAL and 12-SAL [37]. In the deep region of the membrane lipid bilayer (close to the center of the hydrophobic region, a 12-SAL spin probe was used), the order parameter (S) value was low, indicating more fluid membrane. In contrast, the S value was high in the shallow region (close to the hydrophilic region, a 5-SAL spin probe was used), indicating more rigid membrane. The membrane fluidity of the two regions was similar among the three major salivary glands.

In secretory granules of the parotid gland, significant characteristics were noted in the biomembrane phospholipid composition (Table 2) and in the acyl-, alkyl-, and alkenyl-type composition in the main components, PC and PE (Table 5) [52]. To clarify the effects of acyl(ester)- and alkyl(ether)-bonds, the membrane fluidity of liposomes made by simplified PCs was measured using 5-SAL (Fig. 5). The changes of the order parameter as a function of temperature were similar between acyl- and alkyl-type PCs.

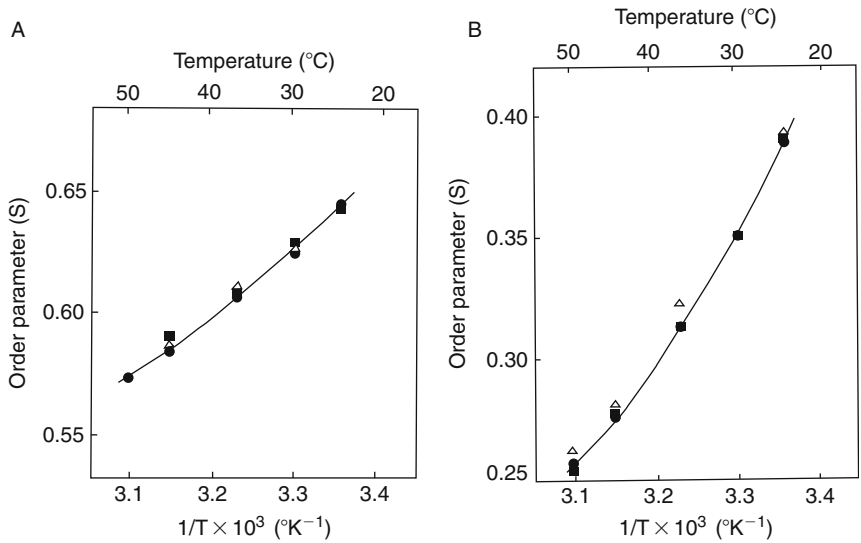

Figure 4 Membrane fluidity of total phospholipid liposomes prepared from the rat 3 major salivary glands [37]. The data obtained using 5-SAL and 12-SAL spin probes represent the fluidity of the shallow and deep regions of the liposomal phospholipid membrane bilayer. As the value of S becomes smaller, the membrane becomes more fluid. (A) Measured using 5-SAL; (B) measured using 12-SAL: (●) parotid, (Δ) submandibular, (■) sublingual.

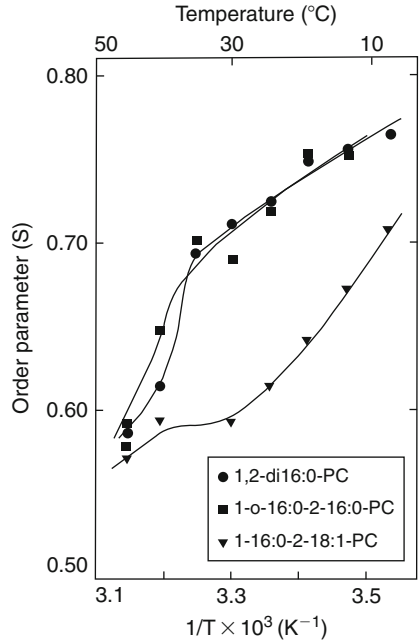

Figure 5 Membrane fluidity of various types of phosphatidylcholine liposomes as a function of temperature [26]. The data were obtained using 5-SAL spin probe. A small *S* value indicates high-level membrane fluidity.

When the saturated fatty acid was replaced by the monounsaturated fatty acid, oleic acid, in ester bond, the order parameter was drastically decreased.

As another approach to observing the physicochemical properties of the membrane, the membrane lateral phase separation was observed by the measuring of transition temperatures using 2,2,6,6-tetramethylpiperidine *N*-oxyl (TEMPO) spin probe (Fig. 2). As shown in Fig. 6, the spectrum is a superimposition of two spectra: one due to TEMPO dissolved in the fluid, hydrophobic region of the lipid; the other due to TEMPO in the aqueous phase. From the measurement of the two amplitudes, H (proportional to the amount of spin probe dissolved in the membrane bilayer) and P (proportional to the amount dissolved in the aqueous region) of the high-field nitroxide hyperfine signals (Fig. 6). Figure 7 shows that the phase transition of alkyl-type PC liposomes was not as drastic as that of acyl-type PC ones.

As shown in Fig. 8, the order parameter was lower in the total phospholipid liposomes prepared from the secretory granule membrane than in those prepared from the homogenate and microsomes, showing that the fluidity of the secretory granule membrane was high [23]. This difference was marked in the shallow region (measured using 5-SAL spin probe) of the

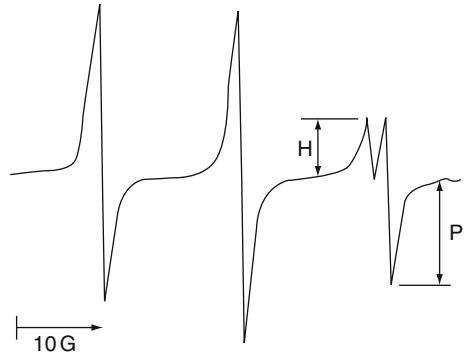

Figure 6 Typical electron spin resonance (ESR) spectrum from TEMPO spin probe measured in aqueous dispersion of phospholipids [26]. H, proportional to the amount of spin probe dissolved in the membrane bilayer; P, proportional to the amount dissolved in the aqueous region.

membrane lipid bilayer. When the membrane fluidity was investigated in cell organelles involved in membrane fusion in parotid gland salivary secretion (secretory granules and the apical plasma membrane) and endoplasmic reticulum, the fluidity increased in the order of secretory granules > endoplasmic reticulum > apical plasma membrane (Fig. 9) [38]. The physical properties of these may reflect not only the biomembrane component lipids characteristic of the cell organelles but also the physicochemical properties of membrane proteins facilitating the specific functions of each organelle. In addition, the presence of a raft-like structure in the apical plasma membrane of secretory cells with polarity, such as parotid acinar cells, has been reported [14]. These findings suggested that secretory granules with high-level membrane fluidity fuse with the apical plasma membrane showing low-level fluidity, making the plasma membrane partially vulnerable, and induces exocrine secretion following membrane fusion on salivary secretion from the parotid gland.

In addition to phospholipids, the cholesterol content of animal cell biomembranes is high. The composition varies among organelles, and its influence on the physical properties of membranes shows a biphasic pattern depending on the content [39]. About 30% (300 mmol/total phospholipid mol) of the parotid gland membrane lipids comprises cholesterol [39]. The coexistence of 30% cholesterol reduced the membrane fluidity of phospholipid liposomes, which consequently reduced membrane fluidity and phase transition (Fig. 10). This is considered to occur particularly in raft regions with a high cholesterol content. SNARE protein-rich regions to which the secretory granule membrane docks also contain abundant cholesterol [40, 41], suggesting that cholesterol controls membrane fusion by partially solidifying the membrane.

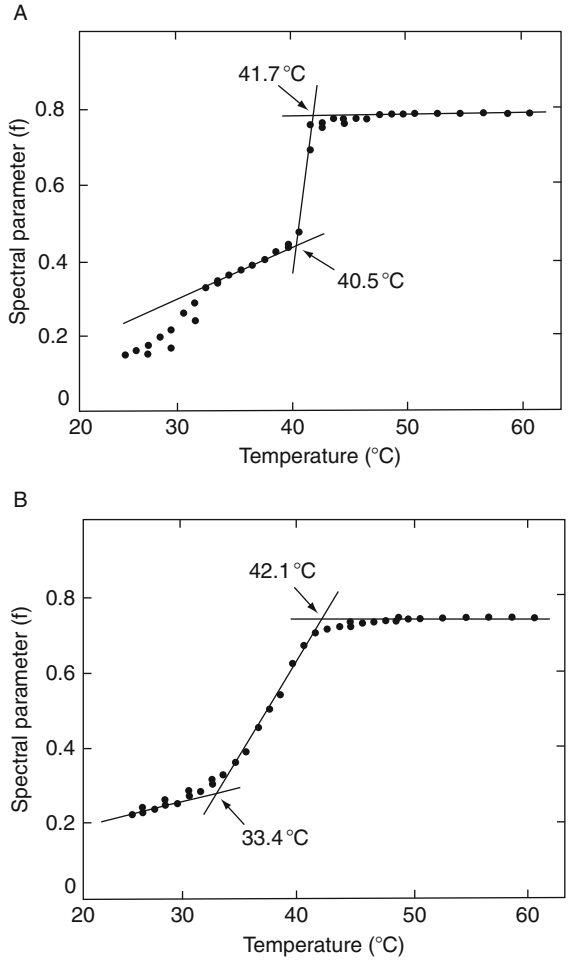

Figure 7 Changes in the TEMPO spectral parameter (f) in phospholipid liposomes as a function of temperature [26]. The temperatures shown at arrows represent the transition temperature: (A) 1,2-dipalmitoyl phosphatidylcholine (1-acyl-type phosphatidylcholine); (B) 1-*O*-hexadecyl-2-palmitoyl phosphatidylcholine (1-alkyl-type phosphatidylcholine).

5. Membrane Fusion and Salivary Secretion Model

The series of SNARE membrane proteins are considered to regulate the docking of exocytosis-induced secretory granule membranes to the plasma membrane and subsequent initial membrane fusion. To investigate

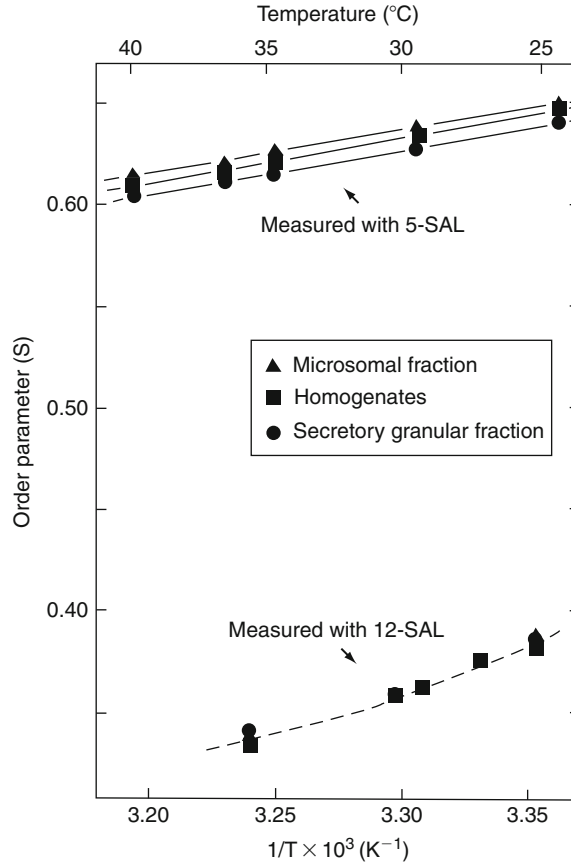

Figure 8 Membrane fluidity of secretory granule membrane phospholipid liposomes prepared from the rat parotid acinar cell fraction as a function of temperature [23]. The data obtained using 5-SAL and 12-SAL spin probes represent the fluidity of the shallow and deep regions of the liposomal phospholipid membrane bilayer. A small *S* value indicates high-level membrane fluidity.

factors influencing this exocytosis accompanied by membrane fusion, we have been using an *in vitro* membrane fusion model system reconstructed with a secretory granule fraction separated from the rat parotid gland and model or apical plasma membrane. The secretory granule membrane of this model system was labeled with the fluorescent probe R18, and the recovery of fluorescence photobleaching by coexistence with the plasma membrane was observed as an increase in the fluorescence intensity, through which the progression of membrane fusion can be monitored [42]. As shown in Fig. 11, incubation of the labeled secretory granules with PC liposomes promoted membrane fusion in a PC concentration-dependent manner [43].

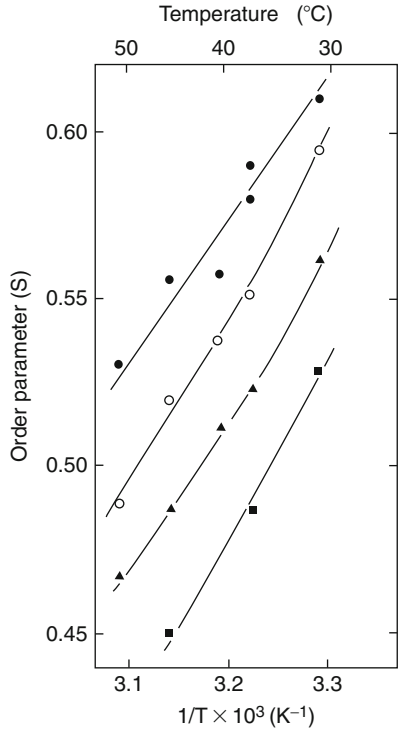

Figure 9 Membrane fluidity of the secretory granule and plasma membranes prepared from the rat parotid acinar cell fraction as a function of temperature [38]. The data were obtained using 5-SAL spin probe. A small *S* value indicates high-level membrane fluidity. (●) Apical plasma membrane-rich fraction, (○) apical and basolateral plasma membrane-rich fraction, (▲) endplasmic reticulum-rich fraction, (■) secretory granule-rich fraction.

As a high lysophospholipid content is a characteristic of the secretory granule membrane (Table 2), this model system clarified that lysophospholipids promote membrane fusion [25].

To investigate the role of the cytoskeleton during secretion using the apical plasma membrane and secretory granules isolated from the rat parotid gland, the localization of cytoskeletal proteins (tubulin and actin) was investigated. Both proteins were present in the apical plasma membrane. When the apical plasma membrane isolated by multistep centrifugal fractionation was used instead of the artificial membrane, membrane fusion also progressed (Fig. 12) [44]. The addition of F-actin suppressed membrane fusion (Fig. 13) [44], suggesting that F-actin present directly below the apical plasma membrane as microfilaments serves as a barrier and directly inhibits membrane fusion [45–48]. Actually, the addition of F-actin to an *in vitro* secretion model inhibited amylase release by almost 100% [49]. Actin

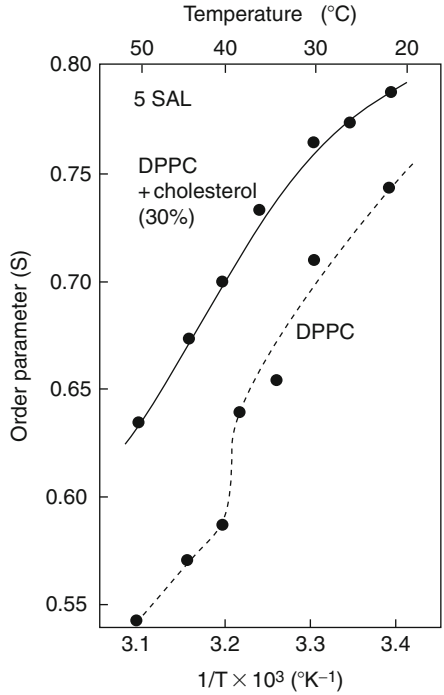

Figure 10 Influence of cholesterol on the membrane fluidity of phospholipid liposomes. The data obtained using 5-SAL spin probe represent the effects of cholesterol on the fluidity of phospholipid liposomes as a function of temperature. DPPC, dipalmitoylphosphatidylcholine.

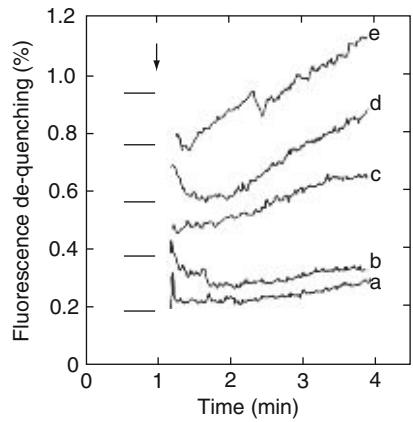

Figure 11 Phosphatidylcholine liposome-induced membrane fusion with secretory granules [43]. Fluorescence probe R18-loaded secretory granules were combined with unlabeled liposomes at arrow, and fluorescence photobleaching recovery by membrane fusion was measured. The concentration of phospholipids added was 0 (a), 10 (b), 50 (c), 100 (d), and 150 (e) nmol/2 ml.

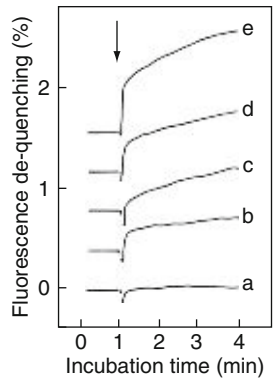

Figure 12 Plasma membrane-induced membrane fusion with secretory granules [44]. Fluorescence probe R18-loaded secretory granules were combined with unlabeled plasma membrane, and fluorescence photobleaching recovery by membrane fusion was measured. The concentration of plasma membrane added was 0 (a), 4 (b), 9 (c), 19 (d), and 38 (e) μg of protein/2 ml.

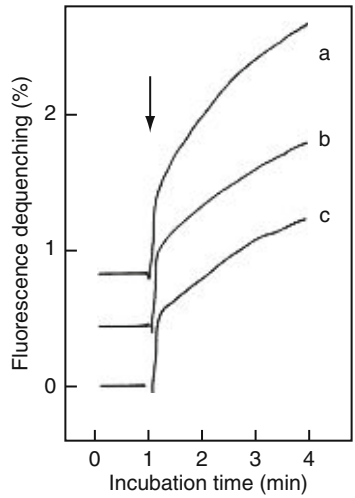

Figure 13 Inhibition of membrane fusion with secretory granules by F-actin [44]. Fluorescence probe R18-loaded secretory granules were combined with unlabeled plasma membrane at arrow, and fluorescence photobleaching recovery by membrane fusion was measured. The concentration of F-action added was 0 (a), 20 (b), and 200 (c) μg/2 ml.

polymerization to microfilaments is also regulated by calcium ions [50, 51] and phosphoinositide [52]. Calcium-dependent phospholipase D [53] reacting with phosphoinositide as the substrate is present in the apical plasma membrane [25] and deacylation enzyme are also in the apical plasma

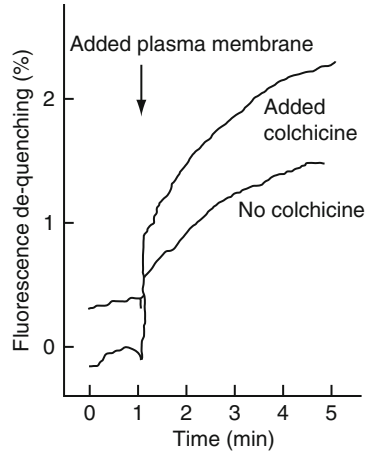

Figure 14 Effect of colchicine on apical plasma membrane-induced fluorescence dequenching caused by membrane fusion [49]. Fluorescence probe R18-loaded secretory granules were combined with unlabeled plasma membrane at arrow, and fluorescence photobleaching recovery by membrane fusion was measured. The concentration of colchicine was 10 μM.

membrane and secretory guranule membrane [25, 54, 55], and degradation products of these enzymes also promote membrane fusion [53]. The direct involvement of lysophosphatidic acid [56] and phosphatidic acid [57] in the regulation of exocytosis accompanied by membrane fusion has been reported. When a structural inhibitor of microtubules, colchicine, was added to an *in vitro* secretion model, the amylase-releasing activity was about two-fold enhanced, and this was consistent with membrane fusion measurement employing the fluorescence photobleaching recovery method (Fig. 14) [49]. The interaction between secretory vesicles and microtubules via kinesin in nerve cells [58] has been clarified, and the presence of this interaction in parotid acinar cells may be clarified in the future.

6. Conclusion

Exocytosis is a common process in the secretion of salivary protein, neurotransmitters, and hormones. Many proteins including SNARE have been identified as regulatory factors, and the details of their action mechanisms have been clarified. Since exocytosis is a dynamic phenomenon of biomembranes involving fusion and reconstruction of the lipid bilayer making up the membrane, the characteristics and variation in membrane phospholipid components and the phospholipid-metabolizing enzyme

system causing the variation are important regulatory factors. The comprehensive molecular regulatory system of exocytosis may be clarified by basic analyses utilizing the advantages of salivary acinar cells. Further progress in the elucidation of the secretory function of salivary acinar cells, including recovery of the fused membrane for secretion, is expected.

ACKNOWLEDGMENTS

I thank my research colleagues, Drs. Koji Yashiro and Masako Mizuno-Kamiya, who contributed to the research described here. I am grateful to Prof. Angelica Leitmannova Liu for reading the manuscript and for helpful comments. This research was supported in part by a Grant-in-Aid for Scientific Research (C) from the Japan Society for the promotion of Science, Japan and by a Miyata Grant for Scientific Research (A) from Asahi University.

REFERENCES

[1] R. Jahn, T.C. Südhof, Membrane fusion and exocytosis, Annu. Rev. Biochem. 68 (1999) 863–911.
[2] T.C. Südhof, The synaptic vesicle cycle, Annu. Rev. Neurosci. 27 (2004) 509–547.
[3] C.G. Giraudo, W.S. Eng, T.J. Melia, J.E. Rothman, A clamping mechanism involved in SNARE-dependent exocytosis, Science 313 (2006) 676–680.
[4] S. Takamori, R. Jahn, Progress in molecular mechanisms of exocytosis, Seikagaku (Japanese) 79 (2007) 879–882.
[5] E.R. Chapman, How does synaptotagmin trigger neurotransmitter release? Annu. Rev. Biochem. 77 (2008) 615–641.
[6] S.R. Pfeffer, Unsolved mysteries in membrane traffic, Annu. Rev. Biochem. 76 (2007) 629–645.
[7] F. Dowd, E. Watson, R.P. Suddick, Salivary gland metabolism, in: E.P. Lazzari (Ed.), Handbook of Experimental Aspects of Oral Biochemistry CRC Press, Boca Raton, FL, 1983, pp. 285–306.
[8] T. Takuma, T. Arakawa, Y. Tajima, Interaction of SNARE proteins in rat parotid acinar cells, Arch. Oral Biol. 45 (2000) 369–375.
[9] J. Fujita-Yoshigaki, O. Katsumata, M. Matsuki, T. Yoshigaki, S. Furuyama, H. Sugiya, Difference in distribution of membrane proteins between low- and high-density secretory granules in parotid acinar cells, Biochem. Biophys. Res. Commun. 344 (2006) 283–292.
[10] Y. Kameyama, K. Ohki, Y. Nozawa, Thermally induced heterogeneity in microsomal membranes of fatty acid-supplemented Tetrahymena: Lipid composition, fluidity and enzyme activity, J. Biochem. 88 (1980) 1291–1303.
[11] T.-C. Lee, Biosynthesis and possible biological functions of plasmalogens, Biochim. Biophys. Acta 1394 (1998) 129–145.
[12] W.C. McMurray, Phospholipids in subcellular organelles and membranes, in: G.B. Ansell, J.N. Hawthorne, R.M.C. Dawson (Eds.), Form and Function of Phospholipids Elsevier Inc., Amsterdam, 1973, pp. 205–251.
[13] D.A. Brown, E. London, Structure and function of sphingolipid- and cholesterol-rich membrane rafts, J. Biol. Chem. 275 (2000) 17221–17224.
[14] L.J. Pike, Lipid rafts: Bringing order to chaos, J. Lipid Res. 44 (2003) 655–667.
[15] K. Simons, E. Ikonen, Functional rafts in cell membranes, Nature 387 (1997) 569–572.

[16] E. Ikonen, Roles of lipid rafts in membrane transport, Curr. Opin. Cell Biol. 13 (2001) 470–477.
[17] Y. Kameyama, K. Yashiro, M. Mizuno-Kamiya, A. Fujita, Form and function of phospholipids in rat salivary glands (Japanese), J. Gifu Dent. Soc. 30 (2004) 290–306.
[18] Y. Yokota, Y. Kameyama, K. Yashiro, M. Mizuno-Kamiya, S.-O. Shin, Regulation of phospholipids metabolism and its functions to secretory exocytosis in rat salivary glands, Dent. Jpn. 30 (1993) 56–62.
[19] Y. Kameyama, K.-I. Nagata, M. Mizuno-Kamiya, Y. Yokota, A. Fujita, Y. Nozawa, Localization of a low *Mr* GTP-binding protein, *rap1* protein, in plasma membranes and secretory granule membranes of rat parotid gland, Life Sci. 55 (1994) 213–219.
[20] Y. Kameyama, K. Yashiro, M. Mizuno, A. Okada, K. Takahashi, Y. Yokota, Comparison of membrane phospholipid and its fatty acid compositions in developing rat salivary glands, Comp. Biochem. Physiol. 87B (1987) 741–746.
[21] D.A. White, The phospholipids composition of mammalian tissues, in: G.B. Ansell, J.N. Hawthorne, R.M.C. Dawson (Eds.), Form and Function of Phospholipids Elsevier Inc., Amsterdam, 1973, pp. 441–482.
[22] M. Mizuno, Y. Kameyama, K. Yashiro, Y. Yokota, Properties of membrane phospholipids and their fatty acyl composition of secretory granules from rat parotid gland, Cell Biol. Intern. Rep. 11 (1987) 629–636.
[23] M. Mizuno, Y. Kameyama, K. Yashiro, Y. Yokota, Characterization of secretory granular membranes from rat parotid gland: Analysis of membrane lipid composition and fluidity, Jpn. J. Oral Biol. 32 (1990) 563–573.
[24] P.R. Cullis, M.J. Hope, Effects of fusogenic agent on membrane structure and erythrocyte ghosts and the mechanism of membrane fusion, Nature 271 (1978) 627–674.
[25] M. Mizuno-Kamiya, H. Inokuchi, Y. Kameyama, K. Yashiro, A. Fujita, Ca^{2+}-independent phospholipaseA_2 activity in apical membranes from the rat parotid gland, Arch. Oral Biol. 46 (2001) 789–799.
[26] A. Shinkai, Y. Kameyama, K. Yashiro, M. Mizuno-Kamiya, A. Fujita, Analyses of membrane phospholipid compositions and their physical properties in rat parotid gland, J. Gifu Dent. Soc. 25 (1998) 247–253.
[27] K. Yashiro, Y. Kameyama, M. Mizuno, Y. Yokota, Inducing effects of chronic administration of isoproterenol on 1-acyl-*sn*-glycero-3-phosphocholine acyltransferases in rat parotid salivary gland, Comp. Biochem. Physiol. 90C (1988) 397–402.
[28] Y. Kameyama, M. Mizuno-Kamiya, K. Yashiro, F. Atsushi, Substrate specificity of microsomal 1-acyl-*sn*-glycero-3-phosphocholine acyltransferase in rat salivary glands for polyunsaturated long-chain acyl-CoAs, J. Gifu Dent. Soc. 34 (2008) 105–109.
[29] Y. Kameyama, A. Shinkai, Characterization of 1-alkenyl-*sn*-glycero-3-phosphorylcholine acyltransferase activity in the microsomes from rat parotid gland, Jpn. J. Oral Biol. 42 (2000) 319–325.
[30] K. Yashiro, Y. Kameyama, M. Mizuno-Kamiya, S.-O. Shin, A. Fujita, Substrate specificity of microsomal 1-acyl-*sn*-glycero-3-phosphoinositol acyltransferase in rat submandibular gland for polyunsaturated long-chain acyl-CoAs, Biochim. Biophys. Acta 1258 (1995) 288–296.
[31] Y. Kameyama, S. Yoshioka, A. Imai, Y. Nozawa, Possible involvement of 1-acylglycerophosphorylinositol acyltransferase in arachidonate enrichment of phosphatidylinositol in human platelets, Biochim. Biophys. Acta 752 (1983) 244–250.
[32] Y. Kameyama, K. Kitamura, K. Yashiro, M. Mizuno-Kamiya, A. Fujita, Enhancement of acyl-CoA:1-acyl-*sn*-glycero-3-phosphocholine acyltransferase activity in the microsomes from rat submandibular gland during growth, J. Gifu Dent. Soc. 34 (2007) 1–4.
[33] Y. Kameyama, A. Fujita, The increase of reacylation enzyme activities which synthesize phosphatidylcholine and phosphatidylinositol in microsomes from rat submandibular gland during growth, Med. Biol. 152 (2008) 14–19.

[34] H. Shindou, T. Shimizu, Acyl-CoA:lysophospholipid acyltransferases, J. Biol. Chem. 284 (2009) 1–5.
[35] J. Cao, D. Shan, T. Revett, D. Li, L. Wu, W. Liu, J.F. Tobin, R.E. Gimeno, Molecular identification of a novel mammalian brain isoform of acyl-CoA:lysophospholipid acyltransferase with prominent ethanolamine lysophospholipid acylation activity, LPEAT2, J. Biol. Chem. 283 (2008) 19049–19057.
[36] H.-C. Lee, T. Inoue, R. Imae, N. Kono, S. Shirae, S. Matsuda, K. Gengyo-Ando, S. Mitani, H. Arai, Caenorhabditis elegans mboa-7, a member of the MBOAT family, is required for selective incorporation of polyunsaturated fatty acids into phosphatidylinositol, Mol. Biol. Cell 19 (2008) 1174–1184.
[37] Y. Kameyama, A. Okada, K. Yashiro, M. Mizuno, S. Hayashi, A. Mori, Y. Yokota, Comparison of physical properties of membrane phospholipid liposomes in rat salivary glands, Jpn. J. Oral Biol. 28 (1986) 766–769.
[38] Y. Kameyama, K. Kitamura, K. Yashiro, M. Mizuno-Kamiya, A. Fujita, Physical properties of subcellular membrane fractions isolated from rat salivary glands, J. Gifu Dent. Soc. 34 (2008) 93–98.
[39] Y. Kameyama, K. Yashiro, M. Mizuno, K. Takahashi, Y. Sakashita, T. Takenaka, Y. Yokota, Physical properties of membrane lipids in rat salivary glands: Involvement of cholesterol, Jpn. J. Oral Biol. 30 (1988) 841–847.
[40] T. Lang, D. Bruns, D. Wenzel, D. Riedel, P. Holroyd, C. Thiele, R. Jahn, SNAREs are concentrated in cholesterol-dependent clusters that define docking and fusion sites for exocytosis, EMBO J. 20 (2001) 2202–2213.
[41] E. Ikonen, Roles of lipid rafts in membrane transport, Curr. Opin. Cell Biol. 13 (2001) 170–177.
[42] C.M. Maclean, J.M. Edwardson, Fusion between rat pancreatic zymogen granules and plasma membranes. Modulation by a GTP-binding protein, Biochem. J. 286 (1992) 747–753.
[43] M. Mizuno-Kamiya, H. Inokuchi, Y. Kameyama, K. Yashiro, S.-O. Shin, A. Fujita, The significance of membrane lipids in exocytosis: Control of liposome-evoked amylase release from secretory granules isolated from the rat parotid gland, J. Biochem. 118 (1995) 693–699.
[44] Y. Kameyama, A. Fujita, The regulatory effect of microfilaments in exocytosis: Direct fusion assay by fluorescence dequenching in an *in vitro* interaction system using purified secretory granules and apical plasma membranes from the rat parotid gland, Med. Biol. 152 (2008) 9–13.
[45] T. Nashida, S. Yoshie, A. Imai, H. Shinomura, Presence of cytoskeleton proteins in parotid glands and their roles during secretion, Arch. Oral Biol. 49 (2004) 975–982.
[46] T. Kanamori, The control system of actin, cytoskeleton, in the parotid gland tissues: The involvement of destrin and cofilin, J. Jpn. Salivary Gland Soc. (Japanese) 48 (2007) 55–65.
[47] B.L. Goode, M.J. Eck, Mechanisms and function of Formins in the control of actin assembly, Annu. Rev. Biochem. 76 (2007) 593–627.
[48] L. Lanzetti, Actin in membrane trafficking, Curr. Opin. Cell Biol. 19 (2007) 453–458.
[49] Y. Kameyama, K. Kitamura, M. Mizuno-Kamiya, K. Yashiro, A. Fujita, The significance of cytoskeleton in exocytosis: Control of apical plasma membrane-evoked amylase release from secretory granules isolated from the rat parotid gland, J. Gifu Dent. Soc. 34 (2008) 99–104.
[50] M. Malacombe, M.F. Bader, S. Gasman, Exocytosis in neuroendocrine cell: New tasks for actin, Biochim. Biophys. Acta 1763 (2006) 1175–1183.
[51] M. Mizuno, Y. Kameyama, K. Yashiro, S.O. Shin, Y. Yokota, Properties of plasma membrane-induced amylase release from rat parotid secretory granules: Effects of Ca^{2+} and Mg-ATP, Biochim. Biophys. Acta 1116 (1992) 104–111.

[52] T. Takenawa, T. Itoh, Phosphoinositides, key molecules for regulation of actin cytoskeletal organization and membrane traffic from the plasma membrane, Biochim. Biophys. Acta 1533 (2001) 190–206.
[53] A. Fujita, M. Mizuno-Kamiya, K. Yashiro, Y. Kameyama, The role of phospholipase D associated with apical plasma membranes in post-docking steps of exocytosis, Dent. Jpn. 42 (2006) 43–47.
[54] M. Mizuno, Y. Kameyama, Y.Y. Yokota, Ca^{2+}-independent phospholipase A_2 activity associated with secretory granular membranes in rat parotid gland, Biochim. Biophys. Acta 1084 (1991) 21–28.
[55] M. Mizuno-Kamiya, Y. Kameyama, K. Yashiro, A. Fujita, ATP-Mediated activation of Ca^{2+}-independent phospholipase A2 in secretory granular membranes from rat parotid gland, J. Biochem. 123 (1998) 205–212.
[56] A. Schmidt, M. Wolde, C. Thiele, W. Fest, H. Kratzin, A.V. Podtelejnikov, W. Witke, W.B. Huttner, H.-D. Söling, Endophilin I mediates synaptic vesicle formation by transfer of arachidonate to lysophosphatidic acid, Nature 401 (1999) 133–141.
[57] M. Zeniou-Meyer, N. Zabari, U. Ashery, S. Chasserot-Golaz, A.M. Haeberlé, V. Demais, Y. Bailly, I. Gottfried, H. Nakanishi, A.M. Neiman, G. Du, M. A. Frohman, M.F. Bader, N. Vitale, Phospholipase D1 production of phosphatidic acid at the plasma membrane promotes exocytosis of large dense-core granules at a late stage, J. Biol. Chem. 282 (2007) 21746–21757.
[58] N. Hirokawa, R. Takemura, Kinesin superfamily proteins and their various functions and dynamics, Exp. Cell Res. 301 (2004) 50–59.

CHAPTER SEVEN

Influenza A M2: Channel or Transporter?

David D. Busath*

Contents

Abstract

Influenza M2 is one of the membrane proteins in the viral envelope that is necessary for cell infection by the virus. In epithelial cells, M2 responds to endosome acidification by transporting protons into the virus to release M1 in preparation for extrusion of the viral RNA into the cytoplasm, while hemagglutinin undergoes a change in conformation that initiates fusion of the viral membrane with the endosome membrane. In some cases, M2 also prevents normal acidification of the Golgi apparatus in infected cells to prevent premature conformational change in developing hemagglutinin. It is expressed in the apical membrane of infected cells and a few copies each are found in the virions budding from such cells. Its function in the virus has been inferred primarily

* Corresponding author. Tel.: +1 801 422-8753; Fax: +1 801 422-0700;
E-mail address: david_busath@byu.edu

Department of Physiology and Developmental Biology, Brigham Young University, Provo, UT 84602, USA

Advances in Planar Lipid Bilayers and Liposomes, Volume 10
ISSN 1554-4516, DOI: 10.1016/S1554-4516(09)10007-8

from its function in infected or transfected cells expressing the protein in the plasmalemma, which are accessible for electrophysiology. Then, to evaluate the structural quality and relevance of the purified protein reconstituted into lipid bilayers for structural determination (e.g., solid state NMR), the same functions are assayed for the purified protein reconstituted as nearly identically as possible into planar bilayers and liposomes. The assumption in this strategy is that if function has not been perturbed by the purification and reconstitution, neither has structure. In the past 17 years, M2 has been referred to as a proton channel, and has been shown to be activated by acidification, blocked by amantadine and related compounds, to have a linear current–voltage relationship when gated open, and to have nearly perfect selectivity for proton transport over Na^+ or Cl^- transport. In the past year, however, structural progress has begun to inspire a reinterpretation of the functional data in terms of a transporter model. Although there is a fine line between channels and transporters, the designation of transporter very much facilitates understanding and description of the available functional data. Here the functional characteristics of M2, as deduced from transfected cell expression systems, are reviewed and compared to functional characteristics of reconstituted protein in suspended planar bilayers and liposomes, where the liposome assay has been found to have the definite advantage. Classic figures from the literature are reproduced, which illustrate the main functional features.

1. Introduction

Pumps, whether primary or secondary active transporters, must never or rarely present a patent path through the membrane or they would drain, rather than build concentration gradients. Passive transporters do not concentrate solutes against electrochemical gradients, but are slow like pumps. One way to distinguish them from channels would be to define them as never having a patent water-filled pore. Channels, on the other hand, are aqueous pores with gates that all open simultaneously, on a fairly common basis (Fig. 1A). When the gates are open, their conductance [1] and water permeability [2–4] are high. Although there are no fixed limits on transport rates, channels generally pass millions of ions per second when open, whereas transporters and pumps typically transport between a few and 50,000 ions or molecules per second. The border between these three classes of molecules can be fuzzy. In particular, slow channels may be indistinguishable from fast transporters. It has recently been suggested that channels and passive transporters be grouped together as ''channels,'' because it is easy to make a distinction between active and passive transport based on function (uphill vs. downhill transport), whereas the difference between fast transport in channels and slow transport in passive transporters

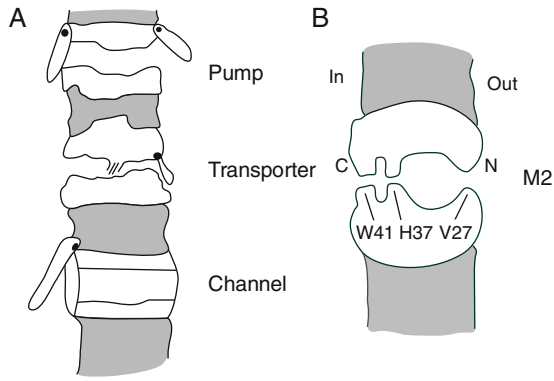

Figure 1 (A) Diagram of presumed structural differences underlying functional distinctions between pumps that alternate gate opening but are never fully patent, transporters that may behave like pumps without coupling to an energy source or perpetually occluded pores, and gated, frequently patent channels. (B) Diagram of major topographical features of M2, pointing out the Val27 sphincter, the His37 selectivity filter, and the Trp41 shutter.

is hard to delimit [5]. It is difficult to tell whether a channel is never open or sometimes open once conductance falls below 1 pS.

Here, however, we will resist this modernization long enough to demonstrate how different mindsets associated with single channel current measurements in planar bilayers and transporter activity measured with liposome uptake assays can influence one's understanding of the correlation of structure, function, and simulations. Namely, we will refer to channels as molecules that can be detected by periods of fast ion flow (millions/s) in planar bilayer assays [1], whereas transporters have no high speed flow detectable by planar bilayer or patch clamp assay, but do transport substrate molecules at a high enough rate for activity to be assessed with a cell [6–10] or liposome uptake [11–18] assay, traditionally using radioactive tracer substrate molecules. Transporters may have multiple gates that are never all jointly open, or may just be channels with narrow spots in the permeation pathway that never allow the mobility of substrate to reach levels similar to that in bulk electrolyte. Narrow, single-file channels have many of the same properties as transporters [1] (tracer flux coupling, saturation of flux at high substrate concentrations). Whereas transporter function can be assessed with neutral and charged species, channels are detected at the single-molecule level with patch clamp or planar bilayer measurements based on single channel currents due to transport of charged species.

Influenza M2 has been termed a channel because, in reports of initial planar bilayer studies early last decade, it exhibited single channel conductance behaviors [19,20], because it was studied by electrophysiologists with standard electrophysiological techniques (whole cell clamping and

two-electrode voltage clamping) [21–25], because of its linear current–voltage (I–V) relationship [26], because it was identified pharmacologically [19, 22, 27] by intra-channel blockers, including amantadine [28] and Cu^{2+} [29], both of which enter from the N terminus (i.e., the extracellular end), because it is gated open by extracellular acid [21] with efflux blocked by external base [30], and because transfected cell membranes are highly permeable to protons, typically conducting 0.7 μA with -130 mV membrane potential, pH_o 6.2 when transfected into the *Xenopus* oocyte [24].

In truth, all of the ''channel'' features could occur with an electrogenic transporter, whether it is an active transporter that generates current at the expense of ATP or a passive transporter with unbalanced charge transport stoichiometry. A channel that has a conductance of 10 pS with a driving force of 0.1 V and an open probability of 0.01 transports 1 pA when open, but the time average is only 10 fA, 62,500 monovalent cations per second. This may be near the lower limit for what should be called a channel. The upper limit for transporters may be well exemplified by Band 3, the obligate exchange anion transporter that carries 50,000 anions/s [1].

Influenza M2 seems to be at the boundary between channel and transporter: a rarely open channel or a fast transporter. Channels commonly flicker between open and closed states, forming a random boxcar (stochastic) signal that can be easily discerned in both the current versus time and in the power spectrum. Electrogenic transporters are expected to produce small, steady current, which, although noisy [31], lacks the random boxcar oscillations between open and closed states. When searched for evidence of random boxcar channel behavior, the current–time relationship and current power spectrum for M2 expressed in mouse erythroleukemia cells was so low that it could not be deduced from the voltage-clamp currents [26]. Initial estimates of the M2 specific activity based on quantitative immunoblotting [32] to measure tetramer quantities in transfected ooctyes of known amantadine-sensitive proton conductance suggest a time-average molecular conductance for M2 of 0.5 fA [33]. Two functional behaviors particularly argue for M2 to be categorized as a transporter: saturation at a very low H^+ concentration [26] and exquisite H^+ selectivity [26], both of which would be unlikely to occur with a water-filled pore. In addition, currents in deuterated water are reduced about twofold [33], much more than expected for a water-filled pore (discussed further below).

An early report of amantadine-blocked single channel currents for the transmembrane domain in suspended planar bilayers (BLMs) [19] has not been confirmed in spite of considerable effort in multiple labs, frustrating the goal of getting a temporal fix on the molecular duty cycle. Although single channel proton currents induced by M2 expressed in *E. coli* inclusion bodies and reconstituted into planar bilayers [34] suggested that M2 may function as a rarely opened channel, subsequent work indicates that such channels probably represent a rare configuration [35].

Meanwhile, usage of the liposome assay, commonly used for studies of the slower flux rates of transporters, has been found to be effective [36] for displaying the amantadine sensitivity of M2. Given its therapeutic [37], tissue culture plaque prevention [38], and transfected cell proton current blockage [22, 39] efficacies, amantadine sensitivity is the primary *sine qua non* for functional M2 reconstitution. In addition, proton transport selectivity, which is also likely to be very sensitive to structural integrity, has been demonstrated with the liposome assay [40 ,41]. Acid-gating has not yet been demonstrated using the liposome assay and is required to complete the demonstration of functional activity, and the transport rate appears to be much lower in the liposome assay than that predicted by the *Xenopus* oocyte assessment. Nevertheless, it appears that the liposome assay is quickly becoming the assay of choice for evaluating reconstituted M2 functionality [42, 43].

Starting abruptly in 2008, there has been a flurry of fresh progress on M2 structure and function, adding on the solid steady foundation laid over the prior 16 years. The structures of M2 fragments were confirmed and elaborated using crystallography [44], solution state NMR [45], magic angle spinning solid state NMR [46–49], oriented membrane solid state NMR [50–54], and infrared FTIR spectroscopy [55]. New molecular dynamics simulations [56–66] have explored the implications of the structural results. The conclusions are summarized in the diagram of M2 in Fig. 1B, which highlights the main topological features suggested by solid state NMR [52, 67], crystal [44], and solution state NMR [45] structures: the entry sphincter produced by Val27 [61], the selectivity filter comprised of His37 [68], and the exit shutter formed by Trp41 [54, 69]. The central cavity between the V27 sphincter and the H37 filter, similar to the central cavity of the K^+ channel [70], is the proposed amantadine binding site [47, 49, 51, 52, 64, 71–74]. The pore is lined by four transmembrane domain helices, one from each of four identical subunits, forming a parallel coiled bundle, each with their N terminus out in cells and virions, and randomly oriented in liposomes [40].

This review will focus on the *functional characteristics* of M2, reviewing the foundational results (for additional reviews, see Pinto and Lamb [75–77]), important recent papers that address significant controversies in the field [42, 43, 72], and the search for these characteristics using M2 reconstituted into planar bilayers and liposomes. The goal is to explore whether the liposome assay, given its inability to reveal single channel conductance, has sufficient analytical power in the case of M2 to quantitatively demonstrate the level of functional activity of the proteins, its amantadine sensitivity, and its complex functions of proton selectivity and acid-gating. For these more complex purposes related specifically to M2, a few novel experimental paradigms with liposome assays will be suggested. This review will only touch briefly on the exciting debates about the mechanisms, *per se*,

of amantadine block, acid activation, selective proton transport, and the utilization of site-directed mutagenesis to test the mechanistic hypotheses, all of which are under discussion in a plethora of papers on M2 structure, simulations, and function published in the past several years, including a few recent papers with particular significance [43, 63, 66, 72, 78]. The main objective will be to show how the liposome assay has been used to demonstrate the proton selective and amantadine-sensitive functions of reconstituted M2, and to mention recent difficulties with efforts to obtain these functions in planar bilayers. Because of this, together with the flux saturation and isotope effect observations, we think it is best to tentatively shift M2's classification from channel to transporter [63]. However, it is too soon to fully resolve the issue of whether M2 is best called a transporter or a channel, and in this review we will use both terms to describe M2, depending on what is most suitable at the moment.

2. Specific Activity: Quantitative Immunoblotting

The specific activity of the transporter (molecular conductance, current, or proton transport rate) has been assessed [23, 24, 32] by dividing the current from one transfected cell, under standard conditions (typically -130 mV applied potential with a Nernst potential for protons of $+58$ mV for a net driving force of ~ 0.2 V), by the number of tetramers measured quantitatively, for example, by immunoblotting horseradish peroxidase–densitometry calibrated with purified protein. Mould et al. [33] reassessed the initial results, correcting for the fraction of protein located in the plasmalemma, $\sim 50\%$, and estimated the specific activity of Udorn/72 M2 expressed in *Xenopus* oocytes to be 0.5 fA/tetramer or 3125 protons/s. For a driving force of 0.2 V, this molecular current corresponds to a conductance of 2.5 fS. The current measurement is accurate to within a few percent for each cell, but the protein assay accuracy is less certain. For the assay, oocyte lysate is run on an SDS–PAGE, transferred to polyvinylidene difluoride membrane, and then quantitated by binding a primary anti-M2 antibody and a horseradish–peroxidase conjugated secondary antibody. Quantitation is carried out by X-ray film with laser scanning densitometry, using immunoaffinity chromatography-purified M2 to form a standard curve. Variance could arise from the blotting, but the fraction transferred would hopefully be similar for the lysate as for the purified protein. The fraction of protein that would be functional in the plasmalemma could be overestimated if the fraction in development in the endoplasmic reticulum, trans-Golgi, vesicles, and (if any) in the plasmalemma is more than 50%, in which case the estimated specific activity would be underestimated. On the other hand, if

antibodies bind better to the protein after it is purified by column chromatography than they do when it is embedded and functional in the plasmalemma, the quantity of membrane protein in a cell would be overestimated. These uncertainties have not been addressed in the literature, but it seems reasonably likely that experiments could be designed to better characterize the M2 content in the plasmalemma. The fraction of protein in the plasmalemma that is functional will be harder to assess. Early gel electrophoresis studies reached the conclusion that it was largely tetrameric, but partly dimeric in cell membranes, and that disulfide linkages between either Cys17 residues or Cys19 residues facilitated tetramer stability, but were not necessary for assembly [79–81].

The functional form was determined to be tetrameric in transfected cells by introducing a mixture of 85% wild-type M2 RNA and 15% V27S amantadine insensitive mutant RNA [82]. The channels that were formed were 50% inhibited by amantadine, consistent with the assumption that one mutant peptide in a tetramer can knock out amantadine block, and that the monomers were freely mixing (as was confirmed by antibody staining). Furthermore, 71% wild-type M2 RNA yielded 20% amantadine sensitivity, also consistent with a tetramer as the functional unit. Likewise, structural studies indicate that M2 readily forms tetramers in various media [44, 45, 83–85], but these tests did not address what fraction of the protein was in the functional state. It would be valuable to have an accurate assay of the fraction in the tetrameric state in cell membranes so that the functional activity can be better assessed and compared to that in reconstituted systems.

3. Functional Characteristics of M2

3.1. Drug Sensitivity

The block of influenza A virus reproduction by amantadine was observed first in 1964, following which it was rapidly shown to be efficacious in man (see citations in Whitney et al. [86]). The prophylaxis against viral infection in mice was tested for a large series of bicyclohexane [86] and tricyclohexane (adamantane) [87] analogs, showing that the amantadine binding site in the virus accommodates a large number of appendages, with fair tolerance of polar functional groups. Rimantadine (in which the amine is attached to the adamantane by a methylated methylene) and α-methyl 4-methylbicyclo [2.2.2]octane methylamine were stronger antiviral agents than amantadine. Numerous amantadine analogs have been tested for antiviral activity before (cited in footnote 12 of Aldrich et al. [87]) and subsequently. For instance, a series of cycloalkylamines was compared to amantadine in their abilities to block plaque formation in chick fibroblasts [27], demonstrating cyclooctylamine to be more effective than amantadine, with much lower or no effects of

cycloheptyl-, cyclohexyl-, or cyclopentyl-amine, nor of cyclooctanol or octylamine. Especially noteworthy is a long-standing project to examine amantadine analogs by DeClerq and colleagues [71, 73, 88–104]. An azas-piro(5,5)undecano compound, BL-1743, consisting of two cyclohexanes sharing a single carbon atom, with an imidazoline residue on the opposite end of one cyclohexane, was found to block as well as amantadine, but to be more readily reversible by washout [105–107].

Extracellular amantadine blocks the M2 channel [21, 22, 39, 108], is slow to block (0.2–0.9 $M^{-1}s^{-1}$) and almost undetectably slow to leave ($\sim 10^{-4}s^{-1}$) [22], blocks at a rate proportionate to bath concentration and with an exponential time course [22] (as would be expected for the situation where only one drug molecule is required to block one channel), blocks with an inhibition constant of 10–80 μM [22], and appears to bind inside the channel [28, 29], probably just inside the V27 sphincter (Fig. 1B). BL-1743 [29, 107] probably blocks in the same site, given that mutations that prevent amantadine block also generally prevent BL-1743 block. An example of *Xenopus* oocyte currents blocked by addition of 100 μM amantadine, shown in Fig. 2, demonstrates that the time course of block is fairly slow and that it is irreversible on the minutes timescale.

Mutations of L26, V27, A30, S31, or G34 eliminate amantadine efficacy against spread of the illness [109], plaque formation in viral growth assays [27, 72], and block of the M2 channel current in oocytes [21, 22, 24, 107, 110] and cultured cells [72, 105].

In addition, extracellular Cu^{2+} blocks the channel [29] from two sites, a weak site outside the channel and a stronger site inside. For the stronger of the sites, Cu^{2+} block is eliminated by mutation of H37, is highly voltage-dependent indicating that the blocking site is toward the intracellular end, has a slow on-rate suggesting site access limitations, and has high affinity, $K_{diss} \sim 2$ μM. Ni^{2+}, Pt^{2+}, and Zn^{2+} also block, but with lower efficacy. Access to the site is prevented by prior application of BL-1763.

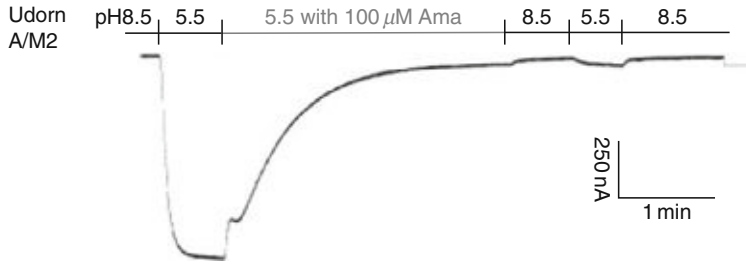

Figure 2 Inward current is produced by acidification outside of the voltage-clamped M2-transfected oocyte. Addition of 100 μM amantadine blocks most of the inward current. Washout of amantadine at either pH does not relieve the block. Reproduced with permission by *Proc Natl Acad Sci USA* from Jing et al. [72]. Copyright (2008) National Academy of Sciences, USA.

Two interesting, controversial and contradictory findings regarding amantadine block have appeared recently. Using surface plasmon resonance, Arkin and colleagues found that amantadine binds to supported planar bilayers containing the transmembrane domain of wild-type influenza A M2 [111]. However, the apparent dissociation constant was higher than the inhibition constant by 2–3 orders of magnitude, consistent with binding to the headgroups of the lipid membrane [52, 60, 112]. It was interesting that binding was disrupted for membranes containing two mutants of the transmembrane domain that, in the full-length protein, are insensitive to amantadine, namely A30T and S31N, whereas four other mutants of V27, which forms a tight region near the entry of the channel, showed the same low affinity binding as the wild-type peptide. This was interpreted to imply that the smaller side chains in the mutations of V27 region might allow binding without block, as if the opening at the mouth of the channel were enlarged in such a way as to allow protons to flow past the bound amantadine. However, given the high concentrations of amantadine used, this result should be viewed with skepticism.

Using solution state NMR for truncated M2 (18–60) in detergent micelles, Chou and colleagues found that amantadine interacted with D44, which was outside the channel on the surface of the bilayer, but could not be detected inside the channel [45]. This, too, appears at first to be an example of a lipid binding effect, because high concentrations of amantadine were required and the proposed site is exposed to the headgroup layer, a reservoir for amantadine. However, the authors argue that it indicates that amantadine block is allosteric. The corollary is that residues 26, 27, 30, 31, and 34 must mediate the conformational effects of binding at D44 in a way that can be disrupted by their mutation.

The allosteric block hypothesis was introduced early by Pinto and Lamb [113], but has not received much attention in the literature. Four arguments against an intrachannel block mechanism were presented briefly based on functional observations from transfected oocytes: 1. More drug is needed when at low pH (i.e., when the channel is opened) than at high pH; 2. Drug can block the channel during the presoak at high pH, when the channel is presumably gated closed; 3. There is no evidence of flicker block noise; 4. Inward and outward currents are equally well blocked. All of these concerns can be dismissed, once the slow on and off rates [107], the roles of channel narrowing at the entry and exit, and the pH dependence of binding seen in analytical centrifugation [85] are taken into account, and the intrachannel blocker hypothesis has been dramatically strengthened, particularly with the observations of interactions between amantadine, BL-1743 and Cu^{2+} mentioned above [29].

Returning then, to Chou's observation: although simulations have been proffered to support the argument that amantadine binding in the pocket formed by D44 and its neighbors would be stronger than intrachannel

binding [58, 62], the claim has been disputed by Pinto and colleagues based on the fact that when the full-length protein is expressed in oocytes with the D44A mutation, the M2-induced currents remain amantadine sensitive [72]. Subsequently, Chou and colleagues utilized the liposome assay (which will be discussed in more detail below) and showed that, for the truncated protein (M2 18–60), the D44A mutation rendered the proton uptake insensitive to amantadine [43]. This leaves the question open: perhaps amantadine binds externally to D44 and not internally in the truncate but *vice versa* in the full-length protein.

3.2. Proton Selectivity

Intimations of M2's permeation selectivity appeared in the reversal potentials of amantadine-sensitive currents observed with oocytes [114]. Reversal potentials were sensitive to external pH, were ~+30 mV at pH_o 6.2 for Udorn, Rostock, and Weybridge strains, and were insensitive to replacements of external Na^+ by Li^+, K^+, Rb^+, Cs^+, *N*-methyl-D-glucosamine$^+$, or tetrabutylammonium$^+$. They were increased to +50 mV by NH_4^+ replacement. The main physiological candidates for a positive reversal potential are Na^+, which typically has a Nernst potential above 50 mV, H^+, with a Nernst potential of 57 mV for each change of external pH away from the internal value (~7.4) by one pH unit, and Ca^{2+}, which, judging from cardiac action potentials, can drive the membrane potential above 0 mV as well. There have been no tests of Ca^{2+} permeability for M2, except with the H37E mutant [32], which displayed sensitivity to external [Ca^{2+}] and DIDS, a Cl^- channel blocker, but had aberrant selectivity in other ways as well. In theory, Cl^- conductance could have a positive reversal potential, but wild-type M2 is insensitive to external [Cl^-] [21].

The case for nearly perfect proton selectivity was made with small mouse erythroleukemia cells, whole cell clamped with electrodes and bath containing high concentration of buffer (180 mM internally) so that intracellular and extracellular pH could be effectively clamped [26]. Figure 3 shows the dependence of reversal potential on the H^+ gradient, in spite of Na^+ gradient changes. The estimated permeability ratio is $>1.6 \times 10^6$. Physiological changes of K^+ or Cl^- had no effect on current–voltage relationships or saturation curves, indicating proton transport is not coupled to transport of these ions. High proton selectivity was subsequently confirmed in the oocyte by study of the acidification of the cytoplasm and reversal potentials [30, 114], although there were indications in the reversal potentials, current amplitudes, and Rb^+ tracer flux that Rb^+, NH_4^+, and Li^+ affect H^+ transport or, in the case of Rb^+ and NH_4^+, are themselves transported through M2.

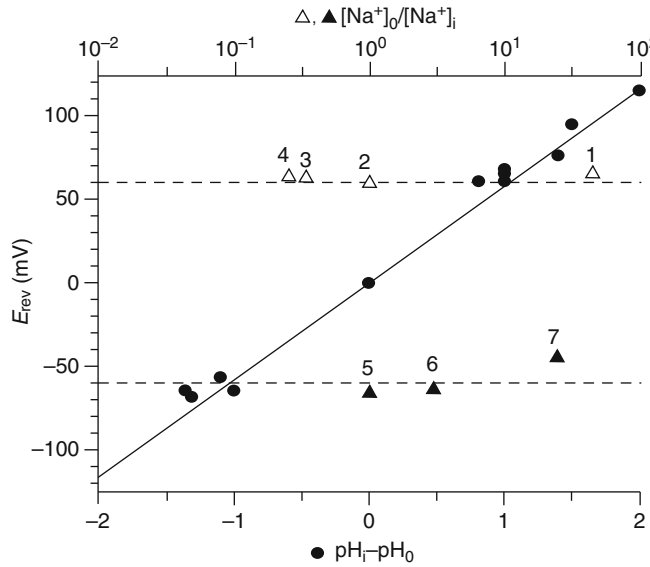

Figure 3 Voltage clamped, M2-transfected mouse erythroleukemia cell reversal potential (after rimantadine insensitive current subtraction) is plotted against Na^+ gradient (triangles) or H^+ gradient (circles). Na^+ gradient experiments were done at either of two unit pH gradient values. The Nernst potentials for H^+ are drawn as dashed horizontal lines. The fact that the triangles fall on these lines indicates that M2 is insensitive to the Na^+ gradient, but very sensitive to the H^+ gradient. This is confirmed by experiments in which pH gradients are changed at constant Na^+ gradient, where the reversal potential follows the Nernstian diagonal (57 mV/decade) prediction for a proton selective channel. Reproduced with permission by *Wiley Publishing* from Chizhmakov et al. [26].

3.2.1. Comparison to Gramicidin Channels: Selectivity, Isotope Effect, and Buffer Enhancement

It is interesting to compare the permeation properties of M2 to the simplest ion channel, gramicidin A, which is known to be an open pore with a single file of water molecules filling the lumen. Based on reversal potentials, gramicidin is selective for H^+ over Na^+ with a permeability ratio of 38–344, depending on pH and lipid composition [115]. The high level of proton permeability was attributed to Grotthus conductance, as it appears consistent with bulk H^+ mobility rather than the expected stronger binding based on the observed selectivity sequence.

In gramicidin channels, the proton conductance in H_2O is 1.3-fold higher than in D_2O [116, 117] similar to the ratio of hydrogen and deuterium mobilities in bulk solution, 1.4 [118], where Grotthus conductance is thought to be prominent, albeit complex [119, 120]. In M2 expressed in oocytes, the isotope effect on conductance is considerably higher: 1.8–2.5 and it also shifts reversal potentials upward by 10–20 mV

[33]. The decreased conductance and increased selectivity are consistent with tighter binding of deuterium to a binding site during passage through the M2 channel [121, 122].

The propensity for a buffer to deliver permeant protons to the channels and thus to speed up transport can also be compared with gramicidin. In gramicidin, the addition of 2 M formic acid to the bath increases single channel conductance 12-fold [123]. In oocytes, inward M2 current produced by hyperpolarization at constant pH (5.8) is increased by a factor of 2.5 when external buffer (4-morpholineethanesulfonic acid) is increased from 0.15 to 15 mM. In both cases, it appears that external buffer acts as a reservoir of protons to prevent diffusion limitations at the entrance, and hence that entry can be somewhat rate limiting.

Although it is possible that the carbonyl-lined walls of the gramicidin channel are unusually hospitable to Na^+ coordination compared, for instance, to side-chain lined walls in M2, it otherwise seems unlikely that the exquisite selectivity for protons over Na^+ observed with M2 could be obtained with any water-filled pore. Nevertheless, recent molecular dynamic simulations of the triply protonated tetrameric M2 transmembrane domain using the empirical valence-bond theory to represent proton motions in water (but not bonded to protein) yields a permeability ratio of 6000 [56], in spite of the observed opening of the H37 filter to a diameter sufficient to accommodate complete hydration. In this simulation, the calculated free energy profiles and diffusion coefficients for H^+ implied a maximum conductance of 53 pS and, for the triply protonated channel, a p*K*a for titration of the first H37 of 6.6. Factors that tighten up the H37 filter, such as inclusion of anions, quantum mechanical interactions of imidazoles, different tilt, kink, or helix rotation parameters, could increase the selectivity to $>6 \times 10^6$ [26], bring the open-state conductance down to <100 fS [26], and raise the imidazole–imidazolium interactions to increase the first p*K*a to >8.0 [68] to become more in line with experimental results. Some of these modeling efforts are underway but so far have not done much to achieve the goal of tightening the triply charged H37 filter [61, 78, 124].

3.3. Acid Activation and Saturation of Inward Current

There are two ways in which acid activation are manifested. The first [26, 114] is illustrated by Fig. 4, which is taken from Chizhmakov et al. [26]. Inward current at constant holding potential increases with increasing bath acidity, as if a gate on the N terminus senses the pH and opens the channel. Similar results occur with the transfected oocyte assay (Fig. 5). Although we will continue the tradition of referring to this phenomenon as acid activation, interpretation is complicated. Namely, the effects of mass action and driving force have to be deconvolved. Whether viewed kinetically or

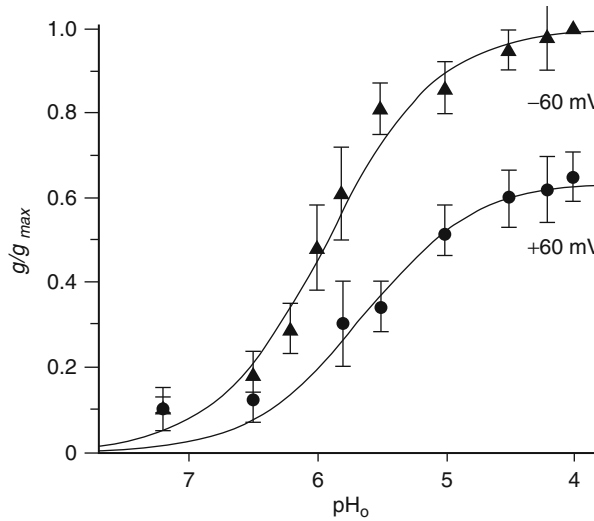

Figure 4 Whole cell chord conductance, $g = I_H/(V_m - V_H)$, normalized to pH_o 4.0, $V_m = -60$ mV, for M2-transfected mouse erythroleukemia cells voltage clamped at -60 mV (triangles) or $+60$ mV (circles). The sigmoidal increase with decreasing pH_o suggests a saturable binding site that limits flux at low pH. At high pH, flux does not increase as rapidly as $[H^+]$, suggesting that rate is limited primarily by the transport process rather than by collisions of protons with open channels. Reproduced with permission by *Wiley Publishing* from Chizhmakov et al. [26].

thermodynamically, the rates of proton collision with channels and V_H are increasing in this experimental paradigm and, either way, would cause an increase, in fact, a steeper increase. The rising inward current in the range of pH 7–8 seems remarkable because mass action would predict a low collision rate of protons with channel openings, perhaps 10^2 or $10^3\,s^{-1}$ assuming a pseudo-first-order rate constant of $10^{10}\,M^{-1}\,s^{-1}$, which would limit molecular current to the sub-fA range. The saturation would not be expected for an open channel. H^+ currents do not saturate in gramicidin channels until $pH < -0.6$ [125], presumably for lack of a saturable serial site in the transport path. Therefore, not only does the activation curve suggest acid-gating, but it also suggests that the channel is really a transporter with access to a reservoir of protons when the bath is pH 7–8, with a constricted transport pathway containing a rate-limiting saturable binding site with a pK in the range of 5–6 [26, 32].

3.4. Base Block of Backflux

The second manifestation of acid activation is less ambiguous and deserves a name of its own both because of the experimental paradigm it represents and because it may derive from a distinct mechanism, but it appears to be

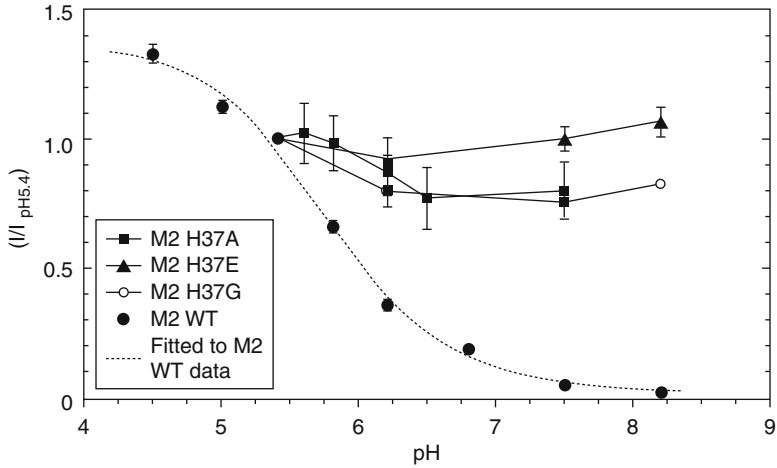

Figure 5 Similar to Fig. 4, but without normalization for changing driving force ($V_m - V_H$), the plateaued inward whole cell current for M2-transfected *Xenopus* oocytes, voltage clamped at −130 mV is plotted against pH_o. Internal pH is not regulated, but is assumed to stay constant for the short exposures to external acidification. The H37 mutations tested were interpreted to show reduced acid activation, but in fact they better show the loss of selectivity. Namely, at such low pH (7–8), one would expect entrance to become rate limiting so that little current would flow through a proton selective channel, yet these mutants have ~10-fold more than WT (before normalization), and thus must be transporting other ions. Reproduced with permission by *Biophysical Journal/Elsevier* from Wang et al. [32].

only the converse of the first, so it, too, is usually referred to as acid activation. Here, we will dignify it with a unique name. "External base block of outward current" would be an accurate name, but for the sake of alliteration, we will simplify this to "base block of backflux." This describes the experimental paradigm, which is to acidify the cell interior and hold the membrane at a positive potential, then vary the external pH and examine the effect on outward current flow. Figures 6 and 7 show results of such experiments with mouse erythroleukemia and *Xenopus* oocyte cells. In both cases, high pH_o blocks outward current, even though mass action and thermodynamics would cause an increased proton efflux. The activation curves determined with this paradigm are a convolution of gating and permeation phenomena, but conclusively demonstrate gating.

Trp41 appears to be an important factor in base block of backflux and allows us to identify a possibly telling distinction between acid activation and base block of backflux [126]. Mutations of W41 to C, A, Y or F retain acid activation, but cause an 0.8-unit upshift in the pK_i of (i.e., weaken) base block of backflux, and C, A, or F cause a six- to eightfold increase in outward current after cytoplasmic acidification. W41Y does not cause an

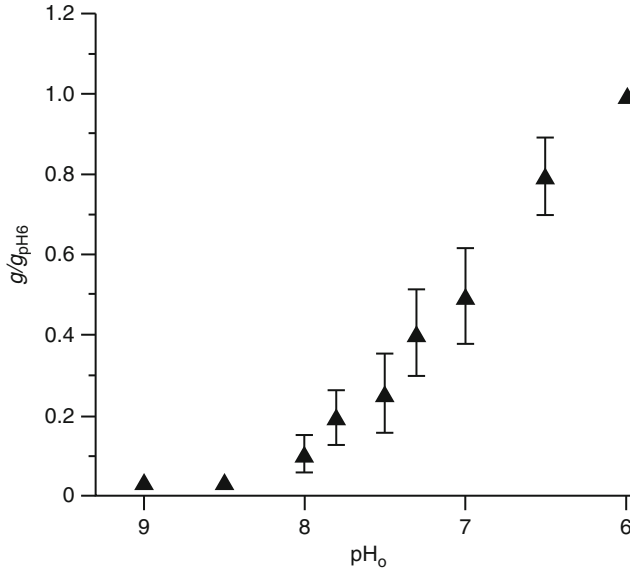

Figure 6 Increase of the bath pH eliminates outward currents when the cell interior is acidified to pH 6.0 and the mouse erythroleukemia cell is voltage clamped at + 60 mV, producing an outward electrochemical driving force that increases as pH is increased (leftward along the plot). Clearly, external base blocks H^+ efflux, giving unambiguous evidence of acid-gating by the solvent around the N terminus. Increasing the internal pH did not have the same blocking effect on inward currents. Reproduced with permission by *Wiley Publishing* from Chizhmakov et al. [26].

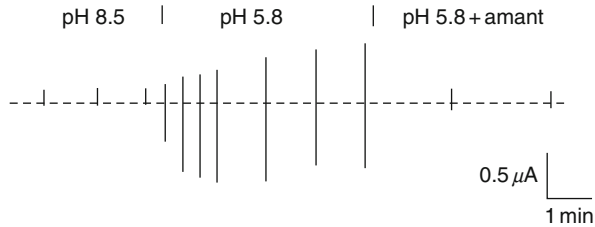

Figure 7 Brief (2 s): intermittent ramps in membrane potential (approximately − 20 to + 70 mV) in the voltage-clamped M2-transfected *Xenopus* oocyte give rise to membrane current ramps, represented by the vertical bars. The dashed horizontal represents zero current. The bottoms of the bars show the usual inward current response to external acidification and block by amantadine, while the tops demonstrate the transporters ability to reverse the direction of current flow. Current flows into the cell when the net driving force on protons in the M2 pore is reversed. Base block of efflux is demonstrated by the fact that the peak outward currents (bar tops) are smaller at pH_o of 8.5 than at pH_o of 5.8, even though the driving force is larger because of the reduction in V_H. Fashioned after Fig. 1A in Mould et al. [30].

increase in proton efflux and hydroxybenzyl methanethiosulfonate addition to W41C blocked the increased influx found with W41C, strongly suggesting that the hydroxybenzyl of tyrosine can interact, perhaps with H37, as well as tryptophan does to block efflux. The conclusion is that W41 plays a key role in producing base block of backflux, but not acid activation. However, it is not the only player. Rostock M2 was found to be unusual, compared to Weybridge (and Udorn), in that it causes sevenfold higher membrane conductance in transfected mouse erythroleukemia cells and lacks base block of backflux [127]. Any of three mutations can restore the low conductance, base block of backflux phenotype: V27I, F38L, and D44N. This strongly suggests that these three residues cooperate with W41 to produce base block of backflux. They are all emerging as key players from other perspectives. V27 forms the N-terminal sphincter (Fig. 1B) and controls amantadine binding. F38 has been involved in a dispute over the mechanism of amantadine block [43, 72]. D44 forms a salt bridge with R45 of the neighboring subunit in the crystal structure [44] and has been suggested as a candidate for a role in acid activation [63]. Because Weybridge M2 is still highly selective and its conductance saturates around pH 4, its selectivity filter and primary inline rate-limiting transport step are intact, consistent with its conservation of the structure and role of the H37 filter (Fig. 1B). Base block of backflux produces additional inhibition of transport over and above the rate limitation imposed by H37 binding, and represents cooperative behavior involving interactions between residues on both sides of H37. One could expect this cooperation to be evident in some change in helix tilt, kink, or rotation in the transmembrane domain.

3.4.1. Gating: Further Implications

It is important to point out that, like a channel, M2 transport does not rectify. It can carry outward current just as well as inward current when V_m is varied about the reversal potential [26, 30]. This implies that the rate-limiting steps in transport are voltage-sensitive and that the direction of proton transport is affected by chemical potential, that is, the H^+ concentration gradient. When thinking in terms of channels, the explanation of this concept [128] lies in the thermodynamic driving force that governs the flow of ions in the channel (analogous to fluid flow in a pipe), namely the difference between the membrane potential, V_m, and (because M2 is proton selective) the Nernst potential for H^+, V_H. The chemical potential effect is due to mass action effects at the channel entry when entry is rate limiting (i.e., the probability of a transported solute entering the channel increases proportionate to the concentration in the bath), and to Fick's first law of diffusion when transfer through the channel is rate limiting, that is, protons flow down their concentration or occupancy-probability gradient.

With M2, acid-gating complicates the channel view of transport through a water-filled pore. Until recently, however, there has been a

strong tendency to rationalize M2 transport in terms of a gated channel, and given the reversibility of the direction of proton current flow, which appears to be driven by the thermodynamic driving forces operational in channels, any revision of the view of the transport mechanism would have to accommodate these facts. Inward current through M2 appears to saturate at pH_o 4 [26], suggesting that at this pH transport through the channel is rate limiting and that at higher pH_o entrance of protons into the channel is rate limiting. This is consistent with either a channel or a transporter, but the fact that saturation occurs at such a low free $[H^+]_o$ (0.1 mM) is probably not consistent with an open channel. On the other hand, if M2 is a transporter, that is, if the conductance path is always clogged by inward pointing side chains that obligatorily rotate to pass protons through a dehydrated region of the pore, one would expect the drop in membrane potential to be highly focused on that region, particularly if the rest of the transport pathway is water filled [129, 130]. The focus of the membrane potential would still lead, thermodynamically, to the linearity in the current–voltage relationship near the reversal potential according to the small signal theory, but would, in this case, be affecting quantum mechanical processes.

At this level, as we try to explain and understand transport, it is very important, though, to avoid the comparison to irreversible unidirectional transporters. It is tempting to think of M2 as a unidirectional (N-to-C) proton transporter because the usual experimental paradigms [72] utilize inward (N-to-C) transport, because its viral functions are primarily to transport protons into the virus (N-to-C) [25] or out of the trans Golgi (N-to-C) [131, 132], and because its toxic function when expressed heterologously [133] is to shunt physiologically crucial proton gradients by carrying protons into the cell (N-to-C). Because of this, it seems natural to describe the transporter as blocked for outward current by the presence of Trp side chains forming a shutter that is closed to proton passage from C to N, but open to passage from N to C [63, 126], but this would lead to inaccurate expectations: the reversibility must be kept in mind. Although, the acid-gating of M2 does give the ''feeling'' of unidirectionality, care must be taken to avoid the trap of trying to explain rectifying transport. Specifically, explanations of acid activation that invoke protonation of residues at the N terminus, such as D22 [55, 66], seem to be required. However, it may be possible that deprotonation of the H37 residues due to efflux stimulates H37–W41 interactions that close the W41 shutter.

In the future, determination of acid activation and base deactivation rates might lead to understanding about the protein components involved in acid activation, provided perfusion delays can be deconvolved. The rates are quite fast, $\sim$250 ms, judging from the data in tissue culture preparations with very small mouse erythroleukemia cells [26, 127]. In the large oocytes, bath turnover takes longer, perhaps a few seconds. Because the oocytes are treated with collagenase, there does not appear to be a significant diffusion

limitation from the vitelline membrane, judging from the rapid access of buffer to the channels [33]. In some mutants (S31N, W41F), the activation appears markedly slower [22, 72, 126] than inactivation, which demonstrates that slow bath exchange is not the cause of the appearance of slow acid activation for those mutants. Exploration of the structural changes that occur in these mutants over the course of several seconds during acid activation is likely to shed light on the mechanism of acid activation in the wild type. It may become possible, using stopped-flow spectroscopy for instance, to improve the resolution of the acid-activation event in the wild-type M2.

4. Reconstitution of M2

4.1. Bilayer Channels

BLMs are often used to reconstitute ion channels, either by direct addition of channel protein to the lipid in folded or painted bilayers, or by spontaneous or osmotically induced fusion of channel-containing liposomes. BLMs have the advantage of demonstrating individual molecular currents whose oscillation between fully closed and open states is related, directly or indirectly, with gating modulation.

Early in the search for M2 as a channel, there were two reports of M2 reconstitutions into BLMs. The first was with M2 transmembrane domain, prepared by peptide synthesis, purified by HPLC, sequenced, and added (1 μg peptide in 6 μl methanol) to the *cis* chamber outside a cup with a 300 μm aperture containing a painted BLM (POPE/POPS 1:1 in decane) in symmetrical 50 mM glycine buffer solution titrated to pH 2.3 (free $[H^+]$ = 5 mM) [19]. Single channel currents were boxcar-shaped (distinguishing molecular activity from generic deterioration of membrane resistance), had an open-state conductance of $\sim$10 pS and average lifetime of 20 ms, and disappeared upon the addition of 20 μM amantadine. A pH gradient yielded Goldman–Hodgkin–Katz rectification with reversal potentials near V_H, indicating good (but not exquisite) selectivity for protons over Cl^-, K^+, and Na^+. This result was reported in 1992, which could be called the birth year for M2 channel studies [21, 134], and was heralded as a strong demonstration of the channel forming potential of M2. However, in spite of repeated efforts in our lab, the results have not been reproduced. We tried on several occasions between 2001 and 2005 to obtain single channels with the M2 transmembrane domain, using various similar conditions, with sporadic appearances of channels but no reproducible success. Between 2005 and 2006, one student in my lab performed over 100 experiments using experimental conditions identical to those of Duff and Ashley, assuring membrane thinning by capacitance or *post hoc* gramicidin addition, and

sometimes increasing the peptide concentration by up to a factor of 100, but rarely saw channels [135], and was unable to demonstrate amantadine sensitivity (S. Leathen Madson, personal communication). We do not currently have an explanation for this difficulty in reproducing the initial results. But it is frustrating because the information gained about activity, gating, drug block mechanism and permeation selectivity from single channel results can be very informative about mechanisms. Meanwhile, we did observe proton uptake by liposomes containing M2 transmembrane domain [68], which has now been confirmed using a similar method [43]. In our initial experiments, the transmembrane domain transport was not blocked by acute exposure to 1 mM amantadine (Craig Moffatt, personal communication). However, in the more recent report, overnight soaking of liposomes in 100 μM amantadine blocked 80% of the M2 transmembrane domain induced proton uptake [42]. The liposome assay, developed for M2 by Cornelia Schroeder and colleagues in the Hay lab [36], and results obtained with larger truncated and intact protein, will be described further below.

Secondly, in 1994 successful reconstitution into BLMs of full-length M2 protein was reported [20]. The M2 was isolated by IgG affinity chromatography from the Nonidet P-40 stabilized membrane fraction of lysate from CV-1 cells infected by the influenza A virus or from *Spodoptera frugiperda* (*Sf9*) cells infected with a recombinant-MN2 baculovirus. After dialysis against phosphate buffered saline with 1% octylglucoside, the detergent-micelle packed M2 was added directly to the *cis* chamber containing a bilayer folded over a 50–80 μm aperture in a Teflon partition from pentane-based monolayers of soybean azolectin or PE:PS (1:1). The single channel currents were not persuasive, with considerable irregular, non-boxcar shapes, low selectivity, and moderate reduction of conductance by 100 μM amantadine. At neutral pH, high and low conductance channels were observed and the high conductance channels were preferentially terminated by amantadine, while the conductance of the low conductance channels was reduced. Reducing the pH symmetrically to 5.4 appeared to convert low conductance channels to high conductance channels.

These results with the full-length protein were also difficult to reproduce. In collaboration with Prof. Larry Pinto, Prof. Carl S. Helrich spent a sabbatical year (1996–1997) on painted-bilayer experiments, initially with transfected oocyte extract, but primarily with purified influenza A M2 protein preparations. Boxcar-shaped channels were routinely observed with the purified protein, but were insensitive to amantadine or to boiling (Carl S. Helrich, personal communication). In 2004 our group reported the results of 4 years effort to reproduce the results [34] using C17S,C50S Udorn A with C-terminal His tag reconstituted into liposomes (DMPC: DMPG 4:1) from *E. coli* inclusion bodies after purification with a Nickel column and incorporation by dialysis. We used painted, decane-containing

bilayers, generally comprised of a mixture of brain lipids (4 PE, 1 PC, 1 PS, 2 cholesterol) to which vesicles were fused spontaneously. At pH 3, we routinely observed boxcar-like 6 pS channels (Fig. 8). They occurred with the same frequency but 50% of the conductance in 300 μM amantadine. Addition of Na^+, Cl^-, or tetramethylammonium to the bath did not increase single channel conductance, leading to the suggestion that they were proton selective. But changes in $[H^+]$ showed single channel currents to increase between pH 4 and pH 3 before saturating. There was no hint of the high conductance (25–500 pS) events reported previously [20], nor of reduction in channel frequency by amantadine addition. Channels occurred regularly, generally within 5–10 min of stirring in the proteoliposomes. Although we calculated that 200-nm vesicles would have 200–600 M2 tetramers, based on the weight of protein added, we never saw more than a few channels conducting simultaneously. At that time, we did not know whether this was because the channels had a very low open-state probability or the protein had a low activity level. The differences with the original report might be ascribed to folded versus painted bilayers, or to differences between eukaryotic and prokaryotic expression, as the former allows for posttrational modifications, which include disulfide linkages at C17 and/or C19, palmitoylation of C50, and N-terminal phosphorylation and glycosylation [79, 136]. However, preliminary experiments with folded bilayers in our lab yielded no differences (Chris Larson, unpublished results), and the posttranslational modifications have been shown not to affect channel behavior in cellular expression systems [136, 137]. The incomplete block by amantadine and the saturation of conductance increase at a pH 3 rather than pH 5 (Figs. 4 and 5) deviated from the established cell expression behaviors.

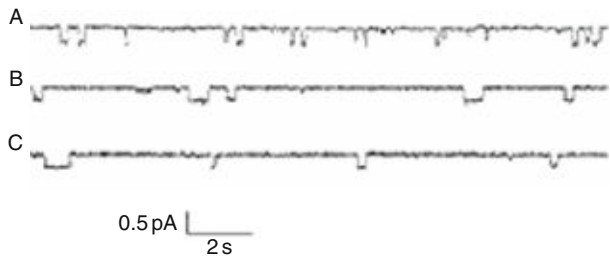

Figure 8 Single channel proton currents through full-length M2 in BLM at pH 3. Current trace in (A) 1 mM HCl, (B) 150 mM NaCl, 1 mM HCl, (C) 150 mM tetraethylammonium chloride, 1 mM HCl. All three are of similar single channel conductance, suggesting good H^+ selectivity. Random boxcar shape is encouraging, but amantadine block was through conductance reduction rather than elimination of activity, as with previous reports. Reproduced with permission by *Biophysical Journal/ Elsevier* from Vijayvergiya et al. [34].

Our lab also carried out extensive experiments over the subsequent four years at neutral pH, also in painted bilayers, which have been reported at meetings [138–140] and are being readied for publication [35]. In brief, the channels continued to be clean and boxcar like, proved to be nonselective among cations when reversal potentials were measured, insensitive to heat, amantadine, or boiling with amantadine, unaffected by several mutations (including revised placement or removal of the His tag), unaffected by detergents utilized in lysis and reconstitution or by whether the protein was taken from the inclusion body fraction or the membrane fraction of the bacteria, and found to represent <1% of the nominal tetramer content of a vesicle. We searched for, but did not see amantadine-sensitive shifts in baseline upon fusion of vesicles containing sufficient protein under acidic conditions where transport should be optimized. Reduction of pH did not affect the opening and closing rates of the channels, nor enhance the channel conductance. The channel behavior in BLMs does not appear to represent the majority of the protein or to display the characteristic functions observed in cell expression systems. Meanwhile, the same preparations yielded amantadine-sensitive proton-selective uptake in liposome assays [41].

4.2. Liposome Assays

As alluded to above, Schroeder and colleagues first demonstrated, using trapped pyranine (a pH sensitive dye), that liposomes (with a K^+ gradient, symmetric pH of 7.4, and containing reconstituted M2 and valinomycin in the membrane) are acidified unless exposed to 0.1–1.0 μM rimantadine or *N*-ethyl-rimantadine [36]. This was the first demonstration that M2 (extracted from lysed *Sf9* cells into octylglucoside, purified by antibody-based affinity column chromatography, and reconstituted into DMPC: DMPS (85:15) vesicles containing valinomycin by dialysis) could transport protons in a rimantadine sensitive way *in vitro*.

This finding was extended (Fig. 9) to demonstrate that reconstituted M2 has very low H^+ transport rates. The computed molecular time-averaged conductance for the ectodomain-out tetramers was 1.2×10^{-18} A (1.2 aA) at pH 7.4, which corresponds to 7.5 protons/tetramer/s. At pH 5.7, the conductance increased to 2.7 or 4.1 aA, depending on whether purified or complex liposomes were used, which corresponds to 17 or 27 protons/tetramer/s. Transport is selective for protons by a factor of 3×10^6 over Na^+ or K^+, is essentially completely blocked by 1 μM rimantadine, and H^+ transport rate drops abruptly by a factor of ~ 10 between 19 and 11 °C at pH 7.4, but only slightly at pH 5.7 [40]. The response to acidic conditions is encouraging, but not as great as expected from cell-clamp results. The rimantadine sensitivity in the 1 μM range indicates that the active protein in the vesicles is conformationally sound, considering that amantadine block

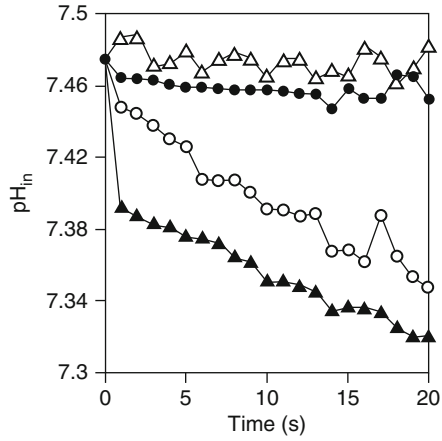

Figure 9 The liposome assay shows good acidification of pyranine trapped in vesicles (filled triangles). Rimantadine injected 5 min beforehand eliminates proton uptake (open triangles), like that seen when there is no K^+ gradient (filled circles), while rimantadine exposure at time 0 causes a reduction in uptake rate (open circles). Reproduced with permission by the *American Society for Microbiology* from Lin and Schroeder [39].

is vulnerable to very small changes in amino acid side chains in the channel. Likewise, extreme selectivity probably requires conformational accuracy, especially a tight H37 filter, because recent molecular dynamics simulations in our lab indicate that very small openings in the M2 channel lumen would allow high-speed channel-like transport of anions and cations [124].

It should be noted that the disparity between the time-averaged single channel current in the transfected oocyte system, ~ 0.5 fA at pH 6.2 and $V_m = -130$ mV [33], is ~ 100 times higher than the current calculated from the liposome assay. This might be unveiling an error in the specific activity assay that leads to an overestimate, such as an underestimate of the number of functional M2 molecules in the membrane. More likely, it indicates that the reconstituted protein is not all functional. This could be for lack of conformational quality, but might have more to do with vesicle quality. If a large fraction of the protein is incorporated into lipid structures that do not encapsulate accessible dye, such as micelles, multilamellar vesicles, or leaky vesicles, the nominal value for the number of functional channels is a large overestimate and the molecular transport rate is highly underestimated.

Returning briefly to the BLM assay, it is interesting to explore whether the single channel conductance levels observed there would be consistent with the time-average single channel conductance taken from the oocyte or liposome assays. In the most recent BLM study [34], the open channel conductance was 6 pS, but it was calculated that if all of the ~ 400 channels

per vesicle were active, the time-average single channel conductance is lower by a factor of 7.5×10^{-5}, the estimated probability of being in the open state, that is 0.45 fA at pH 3. We now believe that only a few (for the sake of round numbers, let us say 4) out of the 400 tetramers in a vesicle were causing the single channel current, so the BLM assay yields a time-average current of 45 fA, which, considering the acidic conditions, might be reasonably comparable to the 0.5 fA estimated from oocytes at pH 6.2. But, as noted above, the BLM channels do not otherwise function like cell-expressed M2, including the fact that cell expressed M2 saturates at low pH, so it is not reasonable to extrapolate its conductance to higher pH levels by assuming mass action. In any event, determination of the molecular transport rate in any of the three systems, cell expression, BLM, or liposome, will require identification and analysis of the challenges mentioned.

In the past few years, the liposome assay has become the assay of choice to assure that reconstituted protein is functional. With M2 extracted from *E. coli*, purified by nickel column, and reconstituted by dialysis into vesicles, amantadine-sensitive proton-selective uptake was reported last year [41]. The average channel conductance was lower than for that from the *Sf9* cells by a factor of ~ 10, and did not increase when the pH was reduced. Several successful studies showing good uptake rates and amantadine sensitivity were subsequently carried out by Joshua M. Rausch in the Pinto lab using encapsulated pH sensitive dyes, and were reported at the Biophysical Society meetings [141]. This year, M2 (18–60), the truncated tetramer used for the solution state NMR structure [45], was found to transport 6.5 ± 0.5 protons/s (pH_o /pH_i = 6.05/7.70, $V_m = 0$ mV) (Fig. 10), a specific activity similar to that seen with the *Sf9* protein [40] and to be amantadine selective [43]. Two mutations in the truncate [43] expected to

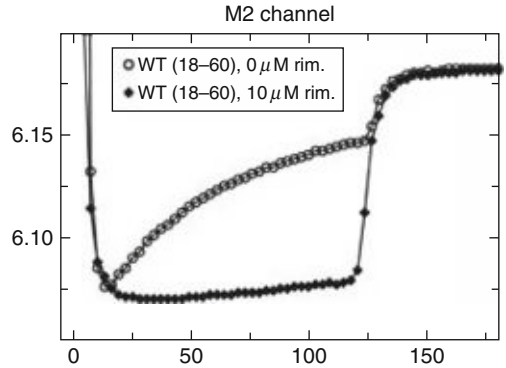

Figure 10 The liposome assay shows a strong upstroke in external pH with M2 (18–60) and valinomycin mixed initially in the membrane, but not with 10 μM rimantadine present (filled diamonds). Reproduced with permission by *Proc Natl Acad Sci USA* from Pielak et al. [42].

confer amantadine resistance, V27A and S31N, did so, whereas another that, as far as we can tell, was previously untested, S31A, did not. The homologous M2 peptide from influenza B, known to conduct protons but to be amantadine insensitive, displayed specific activity like influenza A M2 and amantadine insensitivity as expected. Most striking was the finding mentioned earlier that D44A eliminated amantadine sensitivity (Fig. 11), and that amantadine sensitivity was reduced by simultaneous mutations of external binding pocket neighbors L40, I42, and L43. Although an early oocyte study had suggested that the D44A mutation reduced amantadine sensitivity, debate over whether amantadine blocks allosterically by binding externally to D44 [45] led to reevaluation of the oocyte result [72] with negative results. Namely, D44A does not render M2 insensitive in the oocyte (Fig. 12), nor does D44N in Rostock or Weybridge [142].

Additionally, the DeGrado lab developed the liposome assay during the past year and has shown [42] that the transmembrane domain, the M2 (19–62) truncate, and the full-length protein all give similar specific activities and amantadine sensitivities in the liposome assay (Fig. 13), as well as, for the latter two, in the oocyte assay (Fig. 14).

4.3. Why are Liposomes Better for M2 Functional Assays?

So why does the protein function reproduce amantadine sensitivity and selectivity in the liposome assay, but not in the (current) BLM assays? We have mentioned several possibilities, which we summarize and expand on next. Firstly, there are biases built into the assays in this situation. Proton

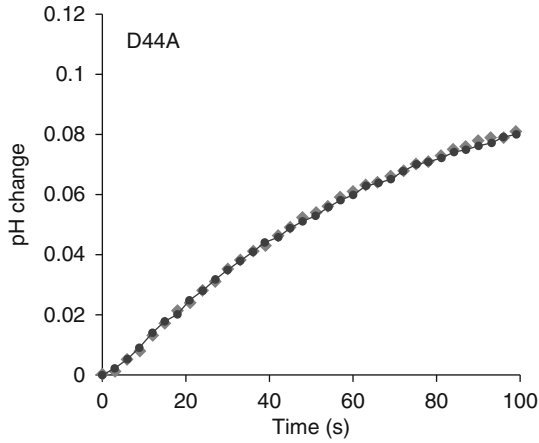

Figure 11 There is no block by amantadine in the proton uptake of the M2 (18–60) D44A mutant in the liposome assay (circles) compared to no amantadine (diamonds). Reproduced with permission by *Proc Natl Acad Sci USA* from Pielak et al. [43].

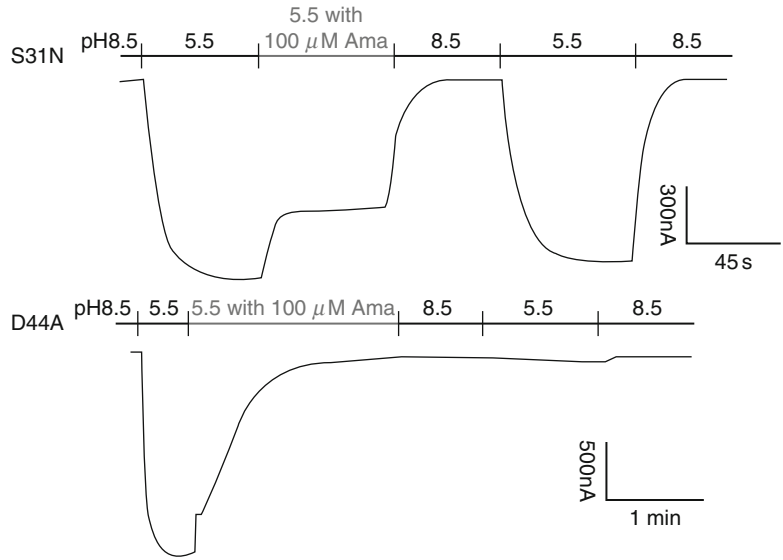

Figure 12 In the oocyte assay, M2 D44A is sensitive to amantadine. S31N is partially blocked by amantadine, but quickly recovers during washout, unlike D44A or the wild type (Fig. 2). Reproduced with permission by *Proc Natl Acad Sci USA* from Jing et al. [72]. Copyright (2008) National Academy of Sciences, USA.

uptake by a large population of channels liposomes, speaking qualitatively and with respect to amantadine sensitivity and selectivity, is insensitive to aberrant channels, because vesicles with nonfunctional protein only show reduced uptake and vesicles with dysfunctional, channel-like protein will be rapidly depolarized. On the other hand, the BLM assay, with its ultrahigh resolution of membrane conductance, highlights channel-like proteins. With osmotic gradients, BLMs selectively fuse with vesicles containing osmolyte-permeable channels [143], such that vesicles containing relatively impermeable transporters may not be very fusigenic.

The membrane thickness or direct effects of alkane solvent on membrane protein structure and function may affect protein structure and dynamics in BLM studies. The vesicle delivery method is particularly susceptible if conditions favor M2 tetramer disassembly, because once dissociated, monomers are unlikely to find new partners in the large area of the BLM. Liposomes have no solvent and have a small surface area, which should encourage subunit assembly by confinement.

There may be a difference between the surface tensions of liposomes and BLMs. For the BLM, the difference between the bilayer and the bulk phase (lens or Plateau–Gibbs border) is 0.00 dyn/cm in decane inflated monolein bilayers and up to 0.84 dyn/cm in monolein–triolein bilayers based on

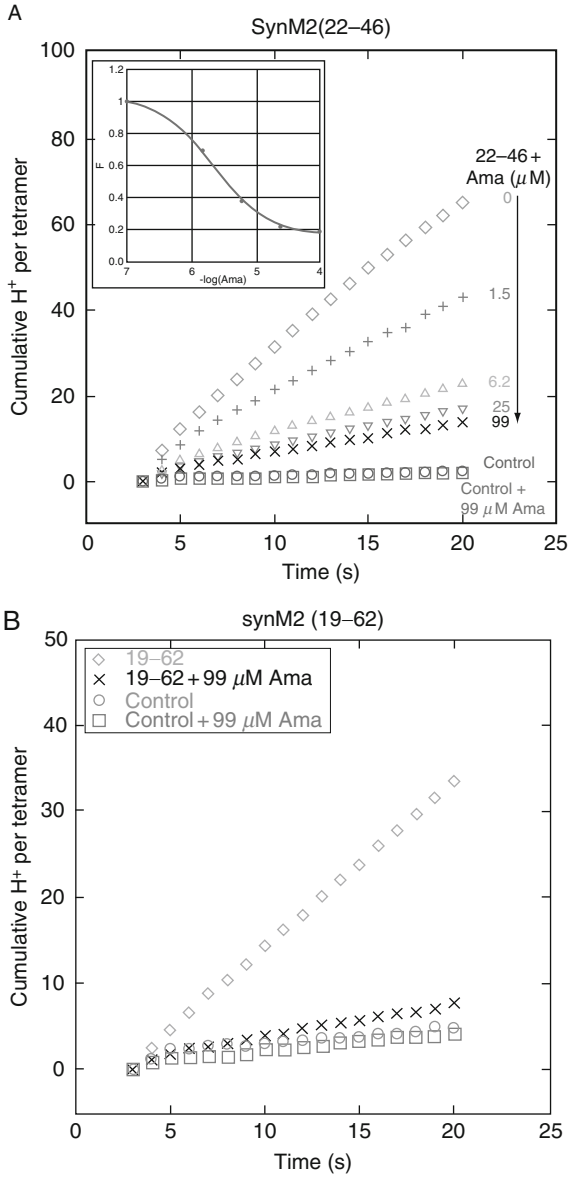

Figure 13 (Continued)

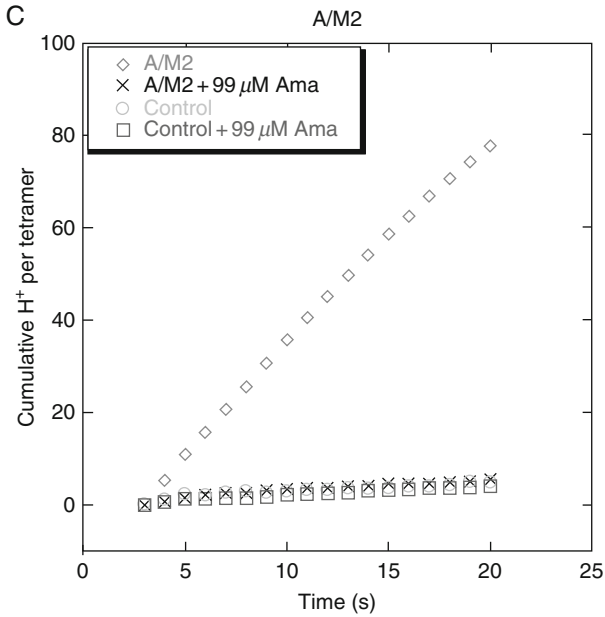

Figure 13 In the liposome assay (as in Fig. 10), (A) the synthetic transmembrane domain (22–46), (B) the synthetic truncated M2 (19–62), and (C) the reconstituted wild-type M2 all show similar proton uptake and block by amantadine. Reproduced with permission by *Proc Natl Acad Sci USA* from Ma et al. [41].

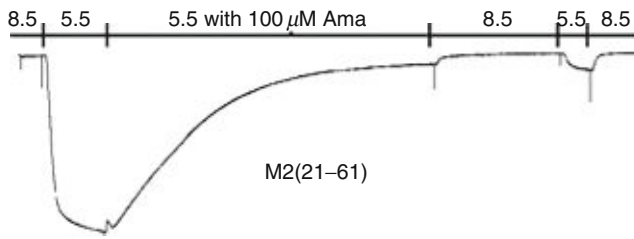

Figure 14 When expressed in transfected Xenopus oocytes, the truncated M2 (21–61) shows the same acid activation and amantadine sensitivity as the wild-type M2. Reproduced with permission by *Proc Natl Acad Sci USA* from Ma et al. [41].

measured contact angles [144]. From the drop volume method [145], the maximum surface tension in the bulk phase before lysis due to buoyancy is 3.84 dyn/cm for the monoolein/decane mixture, and 1.82 dyn/cm for the "solvent free" monoolein/triolein mixture [144]. Thus the surface tension

of the (entire) bilayer is 3.84 or 2.66 dyn/cm, respectively. Similarly, the radius of curvature of a pressure-bulged egg lecithin/decane bilayer indicates, according to the Young–Laplace equation, a surface tension of 1.62 dyn/cm [146]. Similar results have subsequently been obtained with various diglyceride bilayers using this type of measurement [147–151], complementing earlier measurements made by Tien showing ranges of 1–5 [152] and 0.2–6 dyn/cm [153] and an early calculation based on measurement of the energy of bilayer formation, which yielded an apparent surface tension of 3.4 ± 0.6 dyn/cm [154].

Relaxed vesicles with no osmotic pressure are expected, based on the Young–Laplace equation, to have zero surface tension [155] because any hydrostatic pressure gradient across the membrane should be readily relieved by water permeation. Thinning effects or other chemical factors might result in a higher equilibrium surface tension [156], but tether extension experiments suggest a very low surface tension in relaxed vesicles and cells, as low as 0.003 dyn/cm in the growth cone [157], for instance.

For molecular dynamics simulations, proper spacing of the lipid molecules surrounding the M2 transmembrane domain requires application of a surface tension of 40 dyn/cm [124]. This compensates the fact that undulations of the flaccid (presumably zero surface tension) vesicle membrane may stretch lipid molecules apart without increasing surface tension [158], but it is not clear that this compensation does not inappropriately affect protein structure and dynamics in the small simulation cell. In fact, the majority of molecular dynamics simulations with M2 transmembrane domain utilize isotropic constant pressure (zero surface tension), one effect being that the V27 sphincter is more prone to complete closure [61].

It is not known whether living cells and virions are flaccid, that is, lack osmotic strain or other chemical factors that might induce surface tension [159]. For instance, the ribonuclear proteins in the virion may attract water and strain the membrane. There is still considerable debate [158–161] and disparity of opinion about the surface tension in cells [162, 163] and the surface tension of lipid monolayers that best represent cells [164] (also see background discussion and citations in Feller and Pastor [158]) or liposomes [165, 166]. But the measurements discussed above suggest that the surface tension of planar bilayers is generally a few dynes/cm, whereas liposomes, in which osmotic strain is easily controlled, would have zero or even negative surface tension in isotonic or hypertonic solution. For instance, measurements of tether radius and tether force in DOPC/cholesterol vesicles permeabilized by streptolysin O [167] were analyzed by a mechanical model that takes surface undulations into account indicating initial surface tensions of 82 and 72 μdyn/cm, respectively [168]. It is tempting to speculate that M2 has behaved differently in BLMs than in vesicles because of higher surface tension in BLMs.

4.4. Advanced Liposome Techniques for Selectivity, Acid-Gating, and Liposome Activity

The proton uptake and amantadine sensitivity assays are straightforward. But what about the other aspects of M2 behavior which are expected to be sensitive to protein structure and dynamics? First, we clarify the two methods used so far to examine proton selectivity. Then, we suggest methods to search for indications of acid activation and base block of backflux. Finally, we suggest a method for assessing the fraction of lipid forming polarized liposomes based upon the predictions of the electrochemical compartmental analysis suggested by Moffat and colleagues [41].

Liposomes can take up (or release) neutral molecules until the concentration gradient is eliminated, but when charged particles are taken up, electrochemical equilibrium is achieved very rapidly through the formation of the membrane potential. When a semipermeable membrane, permeable only to one cation (such as H^+), becomes permeable to a second ion (such as K^+), and for one or both ions there is a concentration gradient, the system behaves like a Donnan system [169, 170], which refers to a system of impermeable ions such as proteins (or, in our case, Cl^-) dissolved in electrolyte within one compartment (e.g., intracellular, intravascular, or in our case intravesicular) and isolated from other compartments (e.g., extracellular or extravesicular fluid) by a semipermeable membrane. Perturbations from equilibrium will lead to relaxations back to the equilibrium, but because of the principle of electroneutrality, the equilibrium will be a joint Nernst equilibrium, rather than equalization of concentrations for the two species inside and out. Such a system can be modeled with compartmental analysis, taking buffers, ion concentrations, permeabilities or conductances, and membrane potential into account [41]. This type of model has been used to analyze equilibrium conditions in two-compartment systems [171–173], Na^+ equilibration between two sets of liposomes using a three compartment analysis [174], and for two-compartment analysis of transport in the cornea endothelium with eleven transport mechanisms under steady state conditions [175]. With the semipermeable membrane, the membrane potential quickly becomes the Nernst potential for the permeable ion, because it takes the transport of very few ions to produce a membrane potential gradient equal but opposite to the chemical potential gradient. The entry of 196 cations is required to charge up the membrane of a 100-nm diameter vesicle, capacitance of 1 $\mu F/cm^2$, to $+100$ mV, which is a small perturbation of the original number of cations inside the vesicle under physiological conditions (150 mM monovalent electrolyte): 4.7×10^5. With a Donnan system, where the membrane is permeable to two ions, both can flow through the membrane down their electrochemical gradients until the Nernst potential for each ion is equal to the membrane potential. At that point, Donnan equilibrium is reached. There is no driving force on

both ions, and the net fluxes of both ions stop. It could occur at any intermediate membrane potential, depending on the quantities (chemical capacities) of the two ions, and any associated buffers, on the two sides of the membranes. The assays are designed so that one ion (Na^+ or K^+) has much higher permeability, through a high concentration of ionophore (generally valinomycin for K^+ or monensin for Na^+) than the ion of interest (H^+). The proton influx will be rate limiting, and the initial rate of proton uptake will depend only on the M2 transport rate and the total number of functioning M2 tetramers in the system.

Lin and Schroeder [40] used Na^+ gradients and K^+ gradients to prove proton selectivity. They first put vesicles containing monensin into an outward K^+ gradient (symmetrical pH). Any leakage of K^+ through the M2 transporter would then allow K^+–H^+ exchange without a buildup of membrane potential, but they saw none. Then they did the converse experiment and put vesicles containing valinomycin into an outward Na^+ gradient, and again found no H^+ flux. Moffat et al. [41] used a different approach and came to the same conclusion. Vesicles were incubated in the inward Na^+ and outward K^+ gradient for variable lengths of time and the size of the peak attained after permeabilizing the membranes was measured. Any leakage of K^+ or Na^+ through M2 should cause a rundown in ionic gradients, reducing the driving force for proton uptake. Moffat did not observe rundown on the 30 min timescale, from which the M2 preference for H^+ was estimated to be $>10^7$.

So far, liposome studies with M2 have all used symmetrical solutions. Acid activation is asymmetrical, requiring the N-termini of the parallel four-helix bundle to be on the acidic side. Tetramers are randomly oriented in liposomes [40]. External acidification should activate the N-out half of the transporters, but leave the other half inactive, which should be factored into the estimates of transport rate. Prolonged acidification may cause protein activity run down, which would help explain the low activities found under acidic conditions in these assays so far [40, 41]. It should be feasible, however to pulse the pH to low values for a brief assessment of uptake. The main precaution is that buffer strengths will vary, so that care must be taken to assure that the buffer strength is assessed in each experiment. This is usually done with a back-titration that encompasses the pH range covered during vesicle uptake.

Design for a base block of backflux experiment would best utilize a variable external pH, an acidic internal pH, and an interior positive membrane potential to drive proton efflux via M2. This can be accomplished by encapsulating Na^+ buffer at low pH (e.g., 5.5), immersing the valinomycin-doped vesicles in external K^+ solutions varying from pH 6 to 8, and measuring the acidification of the external solution. When pH electrodes are used, it is valuable to have low buffer concentrations externally, and high buffer internally, which would still be the case for the base block of backflux experiment.

Finally, to assess the fraction of protein localized in a productive environment, that is, polarized, accessible vesicles, one might determine the fraction of lipid in the micellar (as opposed to vesicle) state, examine the vesicle population with electron microscopy [176, 177], assess the polarization of membrane voltage-sensitive dyes like Di-4-ANEPPS [178], or assess the quality of dye trapping and the degree of dye leakage from vesicles using the calcein [179] or the terbium/dipicolinic acid assay [180, 181], for instance. We propose another simple way that might be useful. The total external pH change that occurs before a set of vesicles encapsulating a certain fraction of trapped volume reaches Donnan equilibrium depends on buffer contents inside and out, and the quantities of the highly permeant ion inside and out. It is possible to predict the total external pH change using a simulation and compare it to the measured pH change. The measured change will be approximately proportionate to the fraction of vesicles that are productive, that is, to the effective trapped volume (Fig. 7E in Moffat et al. [41]). The contributing protein can then be taken as the fraction of the total protein that would be distributed in that fraction of lipid.

5. Summary

In summary, M2 transports protons 1.5–10 million times better than other ions in cell expression systems and liposome assays. Molecular transport rates are between 0.5 and 5 protons/s according to liposome assays and about 3000 protons/s in transfected oocytes. Proton uptake rates saturate when external $[H^+]$ exceeds $\sim 0.1\ \mu M$. The high selectivity, low conductance, and saturation of flux at low substrate concentration all suggest that M2 behaves as a transporter in cell expression systems. High selectivity and low transport rate indicate that M2 functions as a transporter in liposomes. Amantadine and rimantadine block M2 transport completely in liposomes and cell expression systems, and eliminated channel activity in planar lipid bilayers in initial reports, but these have not proved to be reproducible. Although bilayer studies do show channel activity reproducibly, unpublished results indicate that they are a minority component and do not have amantadine elimination, exclusive proton selectivity, or acid-gating. We conclude that influenza A M2 functions as a transporter in cell expression and liposome systems and a channel in planar bilayer systems, but that the liposome results match cell expression results better, as far as they have been tested. Improved analysis of specific activity and new studies of acid activation and base block of backflux are needed to complete the search for functional characteristics of the intact protein in the liposome assay.

ACKNOWLEDGMENT

This work was funded by NIH AI 23007. Dixon Woodbury, Viksita Vijayvergiya, and Emily Peterson provided helpful comments.

REFERENCES

[1] B. Hille, Ionic Channels of Excitable Membranes, Sinauer Associates Sunderland, Massachusetts, 1984.
[2] S.M. Saparov, Y.N. Antonenko, R.E. Koeppe 2nd, P. Pohl, Desformylgramicidin: A model channel with an extremely high water permeability, Biophys. J. 79 (2000) 2526–2534.
[3] S.M. Saparov, P. Pohl, Beyond the diffusion limit: Water flow through the empty bacterial potassium channel, Proc. Natl. Acad. Sci. USA 101 (2004) 4805–4809.
[4] S.M. Saparov, D. Kozono, U. Rothe, P. Agre, P. Pohl, Water and ion permeation of Aquaporin-1 in planar lipid bilayers. Major differences in structural determinants and stoichiometry, J. Biol. Chem. 276 (2001) 31515–31520.
[5] D.C. Gadsby, Ion channels versus ion pumps: The principal difference, in principle, Nat. Rev. Mol. Cell Biol. 10 (2009) 344–352.
[6] R.B. Gunn, O. Frohlich, Methods and analysis of erythrocyte anion fluxes, Methods Enzymol. 173 (1989) 54–80.
[7] O. Frohlich, J.D. Klein, P.M. Smith, J.M. Sands, R.B. Gunn, Regulation of UT-A1-mediated transepithelial urea flux in MDCK cells, Am. J. Physiol. Cell Physiol. 291 (2006) C600–C606.
[8] M.L. Jennings, J.S. Smith, Anion-proton cotransport through the human red blood cell band 3 protein. Role of glutamate 681, J. Biol. Chem. 267 (1992) 13964–13971.
[9] M.L. Jennings, M.F. Adame, Direct estimate of 1:1 stoichiometry of K(+)-Cl(-) cotransport in rabbit erythrocytes, Am. J. Physiol. Cell Physiol. 281 (2001) C825–C832.
[10] M.L. Jennings, Evidence for a second binding/transport site for chloride in erythrocyte anion transporter AE1 modified at glutamate 681, Biophys. J. 88 (2005) 2681–2691.
[11] W. Breuer, Reconstitution of a kidney chloride channel and its identification by covalent labeling, Biochim. Biophys. Acta. 1022 (1990) 229–236.
[12] T. Ahn, C.H. Yun, H.Z. Chae, H.R. Kim, H.J. Chae, Ca2+/H+ antiporter-like activity of human recombinant Bax inhibitor-1 reconstituted into liposomes, FEBS J. 276 (2009) 2285–2291.
[13] J.J. Garcia-Celma, I.N. Smirnova, H.R. Kaback, K. Fendler, Electrophysiological characterization of LacY, Proc. Natl. Acad. Sci. USA 106 (2009) 7373–7378.
[14] S.Y. Lee, J.A. Letts, R. MacKinnon, Functional reconstitution of purified human Hv1 H+ channels, J. Mol. Biol. 387 (2009) 1055–1060.
[15] M.R. Miranda, A.R. Choi, L. Shi, A.G. Bezerra Jr., K.H. Jung, L.S. Brown, The photocycle and proton translocation pathway in a cyanobacterial ion-pumping rhodopsin, Biophys. J. 96 (2009) 1471–1481.
[16] R.M. Ryan, E.L. Compton, J.A. Mindell, Functional characterization of a Na+-dependent aspartate transporter from Pyrococcus horikoshii, J. Biol. Chem. 284 (2009) 17540–17548.
[17] A. Wiedenmann, P. Dimroth, C. von Ballmoos, Functional asymmetry of the F(0) motor in bacterial ATP synthases, Mol. Microbiol. 72 (2009) 479–490.

[18] F. Zanotti, A. Gnoni, R. Mangiullo, S. Papa, Effect of the ATPase inhibitor protein IF1 on H+ translocation in the mitochondrial ATP synthase complex, Biochem. Biophys. Res. Commun. 384 (2009) 43–48.
[19] K.C. Duff, R.H. Ashley, The transmembrane domain of influenza A M2 protein forms amantadine-sensitive proton channels in planar lipid bilayers, Virology 190 (1992) 485–489.
[20] M.T. Tosteson, L.H. Pinto, L.J. Holsinger, R.A. Lamb, Reconstitution of the influenza virus M2 ion channel in lipid bilayers, J. Membr. Biol. 142 (1994) 117–126.
[21] L.H. Pinto, L.J. Holsinger, R.A. Lamb, Influenza virus M2 protein has ion channel activity, Cell 69 (1992) 517–528.
[22] C. Wang, K. Takeuchi, L.H. Pinto, R.A. Lamb, Ion channel activity of influenza A virus M2 protein: Characterization of the amantadine block, J. Virol. 67 (1993) 5585–5594.
[23] C. Wang, R.A. Lamb, L.H. Pinto, Direct measurement of the influenza A virus M2 protein ion channel activity in mammalian cells, Virology 205 (1994) 133–140.
[24] L.J. Holsinger, D. Nichani, L.H. Pinto, R.A. Lamb, Influenza A virus M2 ion channel protein: a structure-function analysis, J. Virol. 68 (1994) 1551–1563.
[25] R.A. Lamb, L.J. Holsinger, L.H. Pinto, The influenza A virus M2 ion channel protein and its role in the influenza virus life cycle, in: E. Wimmer (Ed.), Receptor-Mediated Virus Entry into Cell Cold Spring Harbor Press, Cold Spring Harbor, NY, 1994, pp. 303–321.
[26] I.V. Chizhmakov, F.M. Geraghty, D.C. Ogden, A. Hayhurst, M. Antoniou, A.J. Hay, Selective proton permeability and pH regulation of the influenza virus M2 channel expressed in mouse erythroleukaemia cells, J. Physiol. 494(Pt 2) (1996) 329–336.
[27] A.J. Hay, A.J. Wolstenholme, J.J. Skehel, M.H. Smith, The molecular basis of the specific anti-influenza action of amantadine, EMBO J. 4 (1985) 3021–3024.
[28] K.C. Duff, P.J. Gilchrist, A.M. Saxena, J.P. Bradshaw, Neutron diffraction reveals the site of amantadine blockade in the influenza A M2 ion channel, Virology 202 (1994) 287–293.
[29] C.S. Gandhi, K. Shuck, J.D. Lear, G.R. Dieckmann, W.F. DeGrado, R.A. Lamb, L.H. Pinto, Cu(II) inhibition of the proton translocation machinery of the influenza A virus M2 protein, J. Biol. Chem. 274 (1999) 5474–5482.
[30] J.A. Mould, J.E. Drury, S.M. Frings, U.B. Kaupp, A. Pekosz, R.A. Lamb, L.H. Pinto, Permeation and activation of the M2 ion channel of influenza A virus, J. Biol. Chem. 275 (2000) 31038–31050.
[31] P. Läuger, Kinetic properties of ion carriers and channels, J. Membr. Biol. 57 (1980) 163–178.
[32] C. Wang, R.A. Lamb, L.H. Pinto, Activation of the M2 ion channel of influenza virus: A role for the transmembrane domain histidine residue, Biophys. J. 69 (1995) 1363–1371.
[33] J.A. Mould, H.-C. Li, C.S. Dudlak, J.D. Lear, A. Pekosz, R.A. Lamb, L.H. Pinto, Mechanism for proton conduction of the M2 ion channel of influenza A virus, J. Biol. Chem. 275 (2000) 8592–8599.
[34] V. Vijayvergiya, R. Wilson, A. Chorak, P.F. Gao, T.A. Cross, D.D. Busath, Proton conductance of influenza virus M2 protein in planar lipid bilayers, Biophys. J. 87 (2004) 1697–1704.
[35] V. Vijayvergiya, J.K. Pearson, J. Goit, S. Rasmussen, T. Jones, F. Nielson, C.D.D. Larson, E. Peterson, A. Lowe, T. Ryser, P.F. Gao, T.A. Cross, D.D. Busath, Cation permeabilities of reconstituted influenza A M2 channels in planar bilayers. (In preparation).

[36] C. Schroeder, C.M. Ford, S.A. Wharton, A.J. Hay, Functional reconstitution in lipid vesicles of influenza virus M2 protein expressed by baculovirus: evidence for proton transfer activity, J. Gen. Virol. 75(Pt 12) (1994) 3477–3484.
[37] R. Dolin, R.C. Reichman, H.P. Madore, R. Maynard, P.N. Linton, J. Webber-Jones, A controlled trial of amantadine and rimantadine in the prophylaxis of influenza A infection, N. Engl. J. Med. 307 (1982) 580–584.
[38] J.J. Skehel, A.J. Hay, J.A. Armstrong, On the mechanism of inhibition of influenza virus replication by amantadine hydrochloride, J. Gen. Virol. 38 (1978) 97–110.
[39] J.J. Skehel, Influenza virus. Amantadine blocks the channel, Nature 358 (1992) 110–111.
[40] T.I. Lin, C. Schroeder, Definitive assignment of proton selectivity and attoampere unitary current to the M2 ion channel protein of influenza A virus, J. Virol. 75 (2001) 3647–3656.
[41] J.C. Moffat, V. Vijayvergiya, P.F. Gao, T.A. Cross, D.J. Woodbury, D.D. Busath, Proton transport through influenza A virus M2 protein reconstituted in vesicles, Biophys. J. 94 (2008) 434–445.
[42] C. Ma, A.L. Polishchuk, Y. Ohigashi, A.L. Stouffer, A. Schön, E. Magavern, X. Jing, J.D. Lear, E. Freire, R.A. Lamb, W.F. DeGrado, L.H. Pinto, Indentification of the functional core of the influenza A virus A/M2 proton-selective ion channel, Proc. Natl. Acad. Sci. USA 106 (2009) 12283–12288.
[43] R.M. Pielak, J.R. Schnell, J.J. Chou, Mechanism of drug inhibition and drug resistance of influenza A M2 channel, Proc. Natl. Acad. Sci. USA 106 (2009) 7379–7384.
[44] A.L. Stouffer, R. Acharya, D. Salom, A.S. Levine, L. Di Costanzo, C.S. Soto, V. Tereshko, V. Nanda, S. Stayrook, W.F. DeGrado, Structural basis for the function and inhibition of an influenza virus proton channel, Nature 451 (2008) 596–599.
[45] J.R. Schnell, J.J. Chou, Structure and mechanism of the M2 proton channel of influenza A virus, Nature 451 (2008) 591–595.
[46] S.D. Cady, C. Goodman, C.D. Tatko, W.F. DeGrado, M. Hong, Determining the orientation of uniaxially rotating membrane proteins using unoriented samples: A 2H, 13C, AND 15N solid-state NMR investigation of the dynamics and orientation of a transmembrane helical bundle, J. Am. Chem. Soc. 129 (2007) 5719–5729.
[47] S.D. Cady, M. Hong, Amantadine-induced conformational and dynamical changes of the influenza M2 transmembrane proton channel, Proc. Natl. Acad. Sci. USA 105 (2008) 1483–1488.
[48] S.D. Cady, M. Hong, Simultaneous extraction of multiple orientational constraints of membrane proteins by 13C-detected N-H dipolar couplings under magic angle spinning, J. Magn. Reson. 191 (2008) 219–225.
[49] S.D. Cady, T.V. Mishanina, M. Hong, Structure of amantadine-bound M2 transmembrane peptide of influenza A in lipid bilayers from magic-angle-spinning solid-state NMR: The role of Ser31 in amantadine binding, J. Mol. Biol. 385 (2009) 1127–1141.
[50] J. Hu, R. Fu, T.A. Cross, The chemical and dynamical influence of the anti-viral drug amantadine on the M2 proton channel transmembrane domain, Biophys. J. 93 (2007) 276–283.
[51] J. Hu, T. Asbury, S. Achuthan, C. Li, R. Bertram, J.R. Quine, R. Fu, T.A. Cross, Backbone structure of the amantadine-blocked trans-membrane domain M2 proton channel from Influenza A virus, Biophys. J. 92 (2007) 4335–4343.
[52] C. Li, M. Yi, J. Hu, H.X. Zhou, T.A. Cross, Solid-State NMR and MD simulations of the antiviral drug amantadine solubilized in DMPC bilayers, Biophys. J. 94 (2008) 1295–1302.
[53] R.C. Page, S. Kim, T.A. Cross, Transmembrane helix uniformity examined by spectral mapping of torsion angles, Structure 16 (2008) 787–797.

[54] R. Witter, F. Nozirov, U. Sternberg, T.A. Cross, A.S. Ulrich, R. Fu, Solid-state 19F NMR spectroscopy reveals that Trp41 participates in the gating mechanism of the M2 proton channel of influenza A virus, J. Am. Chem. Soc. 130 (2008) 918–924.
[55] J. Manor, P. Mukherjee, Y.S. Lin, H. Leonov, J.L. Skinner, M.T. Zanni, I.T. Arkin, Gating mechanism of the influenza A M2 channel revealed by 1D and 2D IR spectroscopies, Structure 17 (2009) 247–254.
[56] H. Chen, Y. Wu, G.A. Voth, Proton transport behavior through the influenza A M2 channel: Insights from molecular simulation, Biophys. J. 93 (2007) 3470–3479.
[57] T. Carpenter, P.J. Bond, S. Khalid, M.S. Sansom, Self-assembly of a simple membrane protein: coarse-grained molecular dynamics simulations of the influenza M2 channel, Biophys. J. 95 (2008) 3790–3801.
[58] R.B. Huang, Q.S. Du, C.H. Wang, K.C. Chou, An in-depth analysis of the biological functional studies based on the NMR M2 channel structure of influenza A virus, Biochem. Biophys. Res. Commun. 377 (2008) 1243–1247.
[59] P. Intharathep, C. Laohpongspaisan, T. Rungrotmongkol, A. Loisruangsin, M. Malaisree, P. Decha, O. Aruksakunwong, K. Chuenpennit, N. Kaiyawet, P. Sompornpisut, S. Pianwanit, S. Hannongbua, How amantadine and rimantadine inhibit proton transport in the M2 protein channel, J. Mol. Graph. Model. 27 (2008) 342–348.
[60] I.C. Yeh, M.A. Olson, M.S. Lee, A. Wallqvist, Free-energy profiles of membrane insertion of the M2 transmembrane peptide from influenza A virus, Biophys. J. 95 (2008) 5021–5029.
[61] M. Yi, T.A. Cross, H.X. Zhou, A secondary gate as a mechanism for inhibition of the M2 proton channel by amantadine, J. Phys. Chem. B 112 (2008) 7977–7979.
[62] Q.S. Du, R.B. Huang, C.H. Wang, X.M. Li, K.C. Chou, Energetic analysis of the two controversial drug binding sites of the M2 proton channel in influenza A virus, J. Theor. Biol. 259 (2009) 159–164.
[63] E. Khurana, M. Dal Peraro, R. DeVane, S. Vemparala, W.F. DeGrado, M.L. Klein, Molecular dynamics calculations suggest a conduction mechanism for the M2 proton channel from influenza A virus, Proc. Natl. Acad. Sci. USA 106 (2009) 1069–1074.
[64] C. Laohpongspaisan, T. Rungrotmongkol, P. Intharathep, M. Malaisree, P. Decha, O. Aruksakunwong, P. Sompornpisut, S. Hannongbua, Why amantadine loses its function in influenza m2 mutants: MD simulations, J. Chem. Inf. Model. 49 (2009) 847–852.
[65] H. Leonov, I.T. Arkin, Structure and dynamics of the influenza A M2 Channel: A comparison of three structures, J. Mol. Model. 2009 (in press).
[66] H. Leonov, I.T. Arkin, pH-driven helix rotations in the influenza M2 H(+) channel: A potential gating mechanism, Eur. Biophys. J. 2009 (in press).
[67] K. Nishimura, S. Kim, L. Zhang, T.A. Cross, The closed state of a H+ channel helical bundle combining precise orientational and distance restraints from solid state NMR, Biochemistry 41 (2002) 13170–13177.
[68] J. Hu, R. Fu, K. Nishimura, L. Zhang, H.X. Zhou, D.D. Busath, V. Vijayvergiya, T.A. Cross, Histidines, heart of the hydrogen ion channel from influenza A virus: Toward an understanding of conductance and proton selectivity, Proc. Natl. Acad. Sci. USA 103 (2006) 6865–6870.
[69] W. Luo, R. Mani, M. Hong, Side-chain conformation of the M2 transmembrane peptide proton channel of influenza a virus from 19F solid-state NMR, J. Phys. Chem. B 111 (2007) 10825–10832.
[70] D.A. Doyle, J.M. Cabral, R.A. Pfuetzner, A. Kuo, J.M. Gulbis, S.L. Cohen, B.T. Chait, R. MacKinnon, The structure of the potassium channel: Molecular basis of K(+) conduction and selectivity, Science 280 (1998) 69–77.

[71] A. Kolocouris, C. Zikos, R.W. Broadhurst, 19F NMR detection of the complex between amantadine and the receptor portion of the influenza A M2 ion channel in DPC micelles, Bioorg. Med. Chem. Lett. 17 (2007) 3947–3952.
[72] X. Jing, C. Ma, Y. Ohigashi, F.A. Oliveira, T.S. Jardetzky, L.H. Pinto, R.A. Lamb, Functional studies indicate amantadine binds to the pore of the influenza A virus M2 proton-selective ion channel, Proc. Natl. Acad. Sci. USA 105 (2008) 10967–10972.
[73] G. Zoidis, N. Kolocouris, L. Naesens, E. De Clercq, Design and synthesis of 1, 2-annulated adamantane piperidines with anti-influenza virus activity, Bioorg. Med. Chem. 17 (2009) 1534–1541.
[74] J. Wang, S.D. Cady, V. Balannik, L.H. Pinto, W.F. DeGrado, M. Hong, Discovery of spiro-piperidine inhibitors and their modulation of the dynamics of the M2 proton channel from influenza A virus, J. Am. Chem. Soc. 131 (2009) 8066–8076.
[75] L.H. Pinto, R.A. Lamb, Controlling influenza virus replication by inhibiting its proton channel, Mol. Biosyst. 3 (2007) 18–23.
[76] L.H. Pinto, R.A. Lamb, Influenza virus proton channels, Photochem. Photobiol. Sci. 5 (2006) 629–632.
[77] L.H. Pinto, R.A. Lamb, The M2 proton channels of influenza A and B viruses, J. Biol. Chem. 281 (2006) 8997–9000.
[78] M. Yi, T.A. Cross, H.X. Zhou, Conformational heterogeneity of the M2 proton channel: A structural model for channel activation, Proc. Natl. Acad. Sci. USA 2009 in press.
[79] L.J. Holsinger, R.A. Lamb, Influenza virus M2 integral membrane protein is a homotetramer stabilized by formation of disulfide bonds, Virology 183 (1991) 32–43.
[80] R.J. Sugrue, A.J. Hay, Structural characteristics of the M2 protein of influenza A viruses: evidence that it forms a tetrameric channel, Virology 180 (1991) 617–624.
[81] P.P. Panayotov, R.W. Schlesinger, Oligomeric organization and strain-specific proteolytic modification of the virion M2 protein of influenza A H1N1 viruses, Virology 186 (1992) 352–355.
[82] T. Sakaguchi, Q. Tu, L.H. Pinto, R.A. Lamb, The active oligomeric state of the minimalistic influenza virus M2 ion channel is a tetramer, Proc. Natl. Acad. Sci. USA 94 (1997) 5000–5005.
[83] W. Luo, M. Hong, Determination of the oligomeric number and intermolecular distances of membrane protein assemblies by anisotropic 1H-driven spin diffusion NMR spectroscopy, J. Am. Chem. Soc. 128 (2006) 7242–7251.
[84] G.G. Kochendoerfer, D. Salom, J.D. Lear, R. Wilk-Orescan, S.B. Kent, W.F. DeGrado, Total chemical synthesis of the integral membrane protein influenza A virus M2: role of its C-terminal domain in tetramer assembly, Biochemistry 38 (1999) 11905–11913.
[85] D. Salom, B.R. Hill, J.D. Lear, W.F. DeGrado, pH-Dependent tetramerization and amantadine binding of the transmembrane helix of M2 from the influenza A virus, Biochemistry 39 (2000) 14160–14170.
[86] J.G. Whitney, W.A. Gregory, J.C. Kauer, J.R. Roland, J.A. Snyder, R.E. Benson, E.C. Hermann, Antiviral agents: 1. Bicyclo[2.2.2]octan- and oct-2-enamines, J. Med. Chem. 13 (1970) 254.
[87] P.E. Aldrich, E.C. Hermann, W.E. Meier, M. Paulshock, W.W. Prichard, J.A. Synder, J.C. Watts, Antiviral agents. 2. Structure-activity relations of compounds related to 1-adamantanamine, J. Med. Chem. 14 (1971) 535–543.
[88] G. Fytas, P. Marakos, N. Kolocouris, G.B. Foscolos, N. Pouli, A. Vamvakides, S. Ikeda, E. De Clercq, 3-Cyclopentyl-1-adamantanamines and adamantanemethanamines. Antiviral activity evaluation and convulsions studies, Farmaco 49 (1994) 641–647.

[89] N. Kolocouris, G.B. Foscolos, A. Kolocouris, P. Marakos, N. Pouli, G. Fytas, S. Ikeda, E. De Clercq, Synthesis and antiviral activity evaluation of some aminoadamantane derivatives, J. Med. Chem. 37 (1994) 2896–2902.
[90] N. Kolocouris, A. Kolocouris, G.B. Foscolos, G. Fytas, J. Neyts, E. Padalko, J. Balzarini, R. Snoeck, G. Andrei, E. De Clercq, Synthesis and antiviral activity evaluation of some new aminoadamantane derivatives. 2, J. Med. Chem. 39 (1996) 3307–3318.
[91] A. Kolocouris, D. Tataridis, G. Fytas, T. Mavromoustakos, G.B. Foscolos, N. Kolocouris, E. De Clercq, Synthesis of 2-(2-adamantyl)piperidines and structure anti-influenza virus A activity relationship study using a combination of NMR spectroscopy and molecular modeling, Bioorg. Med. Chem. Lett. 9 (1999) 3465–3470.
[92] G. Stamatiou, A. Kolocouris, N. Kolocouris, G. Fytas, G.B. Foscolos, J. Neyts, E. De Clercq, Novel 3-(2-adamantyl)pyrrolidines with potent activity against influenza A virus-identification of aminoadamantane derivatives bearing two pharmacophoric amine groups, Bioorg. Med. Chem. Lett. 11 (2001) 2137–2142.
[93] A. Kolocouris, J.G. Outeirino, J.E. Anderson, G. Fytas, G.B. Foscolos, N. Kolocouris, The effect of neighboring 1- and 2-adamantyl group substitution on the conformations and stereodynamics of N-methylpiperidine. Dynamic NMR spectroscopy and molecular mechanics calculations, J. Org. Chem. 66 (2001) 4989–4997.
[94] A. Kolocouris, K. Dimas, C. Pannecouque, M. Witvrouw, G.B. Foscolos, G. Stamatiou, G. Fytas, G. Zoidis, N. Kolocouris, G. Andrei, R. Snoeck, E. De Clercq, New 2-(1-adamantylcarbonyl)pyridine and 1-acetyladamantane thiosemicarbazones-thiocarbonohydrazones: cell growth inhibitory, antiviral and antimicrobial activity evaluation, Bioorg. Med. Chem. Lett. 12 (2002) 723–727.
[95] I. Stylianakis, A. Kolocouris, N. Kolocouris, G. Fytas, G.B. Foscolos, E. Padalko, J. Neyts, E. De Clercq, Spiro[pyrrolidine-2, 2'-adamantanes]: Synthesis, anti-influenza virus activity and conformational properties, Bioorg. Med. Chem. Lett. 13 (2003) 1699–1703.
[96] G. Zoidis, N. Kolocouris, G.B. Foscolos, A. Kolocouris, G. Fytas, P. Karayannis, E. Padalko, J. Neyts, E. De Clercq, Are the 2-isomers of the drug rimantadine active anti-influenza A agents? Antivir. Chem. Chemother. 14 (2003) 153–164.
[97] G. Stamatiou, G.B. Foscolos, G. Fytas, A. Kolocouris, N. Kolocouris, C. Pannecouque, M. Witvrouw, E. Padalko, J. Neyts, E. De Clercq, Heterocyclic rimantadine analogues with antiviral activity, Bioorg. Med. Chem. 11 (2003) 5485–5492.
[98] A. Kolocouris, R.K. Hansen, R.W. Broadhurst, Interaction between an amantadine analogue and the transmembrane portion of the influenza A M2 protein in liposomes probed by 1H NMR spectroscopy of the ligand, J. Med. Chem. 47 (2004) 4975–4978.
[99] D. Setaki, D. Tataridis, G. Stamatiou, A. Kolocouris, G.B. Foscolos, G. Fytas, N. Kolocouris, E. Padalko, J. Neyts, E. De Clercq, Synthesis, conformational characteristics and anti-influenza virus A activity of some 2-adamantylsubstituted azacycles, Bioorg. Chem. 34 (2006) 248–273.
[100] G. Zoidis, C. Fytas, I. Papanastasiou, G.B. Foscolos, G. Fytas, E. Padalko, E. De Clercq, L. Naesens, J. Neyts, N. Kolocouris, Heterocyclic rimantadine analogues with antiviral activity, Bioorg. Med. Chem. 14 (2006) 3341–3348.
[101] D. Tataridis, G. Fytas, A. Kolocouris, C. Fytas, N. Kolocouris, G.B. Foscolos, E. Padalko, J. Neyts, E. De Clercq, Influence of an additional 2-amino substituent of the 1-aminoethyl pharmacophore group on the potency of rimantadine against influenza virus A, Bioorg. Med. Chem. Lett. 17 (2007) 692–696.
[102] N. Kolocouris, G. Zoidis, G.B. Foscolos, G. Fytas, S.R. Prathalingham, J.M. Kelly, L. Naesens, E. De Clercq, Design and synthesis of bioactive adamantane spiro heterocycles, Bioorg. Med. Chem. Lett. 17 (2007) 4358–4362.
[103] A. Kolocouris, P. Spearpoint, S.R. Martin, A.J. Hay, M. Lopez-Querol, F.X. Sureda, E. Padalko, J. Neyts, E. De Clercq, Comparisons of the influenza virus A M2 channel

binding affinities, anti-influenza virus potencies and NMDA antagonistic activities of 2-alkyl-2-aminoadamantanes and analogues, Bioorg. Med. Chem. Lett. 18 (2008) 6156–6160.
[104] G. Zoidis, A. Tsotinis, N. Kolocouris, J.M. Kelly, S.R. Prathalingam, L. Naesens, E. De Clercq, Design and synthesis of bioactive 1, 2-annulated adamantane derivatives, Org. Biomol. Chem. 6 (2008) 3177–3185.
[105] S. Kurtz, G. Luo, K.M. Hahnenberger, C. Brooks, O. Gecha, K. Ingalls, K. Numata, M. Krystal, Growth impairment resulting from expression of influenza virus M2 protein in Saccharomyces cerevisiae: Identification of a novel inhibitor of influenza virus, Antimicrob. Agents Chemother. 39 (1995) 2204–2209.
[106] K.M. Hahnenberger, M. Krystal, K. Esposito, W. Tang, S. Kurtz, Use of microphysiometry for analysis of heterologous ion channels expressed in yeast, Nat. Biotechnol. 14 (1996) 880–883.
[107] Q. Tu, L.H. Pinto, G. Luo, M.A. Shaughnessy, D. Mullaney, S. Kurtz, M. Krystal, R.A. Lamb, Characterization of inhibition of M2 ion channel activity by BL-1743, an inhibitor of influenza A virus, J. Virol. 70 (1996) 4246–4252.
[108] A.J. Hay, The action of adamantanamines against influenza A viruses: Inhibition of the M2 ion channel protein, Semin. Virol. 3 (1992) 21–30.
[109] K. Shiraishi, K. Mitamura, Y. Sakai-Tagawa, H. Goto, N. Sugaya, Y. Kawaoka, High frequency of resistant viruses harboring different mutations in amantadine-treated children with influenza, J. Infect. Dis. 188 (2003) 57–61.
[110] L.H. Pinto, G.R. Dieckmann, C.S. Gandhi, C.G. Papworth, J. Braman, M.A. Shaughnessy, J.D. Lear, R.A. Lamb, W.F. DeGrado, A functionally defined model for the M2 proton channel of influenza A virus suggests a mechanism for its ion selectivity, Proc. Natl. Acad. Sci. USA 94 (1997) 11301–11306.
[111] P. Astrahan, I. Kass, M.A. Cooper, I.T. Arkin, A novel method of resistance for influenza against a channel-blocking antiviral drug, Proteins 55 (2004) 251–257.
[112] C.F. Chew, A. Guy, P.C. Biggin, Distribution and dynamics of adamantanes in a lipid bilayer, Biophys. J. 95 (2008) 5627–5636.
[113] L.H. Pinto, R.A. Lamb, Understanding the mechanism of action of the anti-influenza virus drug amantadine, Trends Microbiol. 3 (1995) 271.
[114] K. Shimbo, D.L. Brassard, R.A. Lamb, L.H. Pinto, Ion selectivity and activation of the M2 ion channel of influenza virus, Biophys. J. 70 (1996) 1335–1346.
[115] V.B. Myers, D.A. Haydon, Ion transfer across lipid membranes in the presence of gramicidin A: II. The ion selectivity, Biochim. Biophys. Acta 274 (1972) 313–322.
[116] A. Chernyshev, R. Pomès, S. Cukierman, Kinetic isotope effects of proton transfer in aqueous and methanol containing solutions, and in gramicidin A channels, Biophys. Chem. 103 (2003) 179–190.
[117] R.H. Tredgold, R. Jones, A study of gramicidin using deuterium oxide, Biochim. Biophys. Acta 550 (1979) 543–545.
[118] J.O. Bockris, A.K.N. Reddy, Modern Electrochemistry I, Ionics, 2nd Ed., Plenum PublishingNew York, NY, 1998.
[119] N. Agmon, The Grotthuss mechanism, Chem. Phys. Lett. 244 (1995) 456–462.
[120] N. Agmon, Hydrogen bonds, water rotation and proton mobility, J. Chim. Phys. 93 (1996) 1714–1736.
[121] D. Busath, G. Szabo, Atypical gramicidin A channels have increased field strength at one binding site, Biophys. J. 45 (1984) 75–76.
[122] D. Busath, G. Szabo, Permeation characteristics of gramicidin conformers, Biophys. J. 53 (1988) 697–707.
[123] E.R. Decker, D.G. Levitt, Use of weak acids to determine the bulk diffusion limitation of H+ ion conductance through the gramicidin channel, Biophys. J. 53 (1988) 25–32.

[124] M. Mustafa, D.J. Henderson, D.D. Busath, Free-energy profiles for Ions in the influenza M2-TMD channel, Proteins Struct. Funct. Bioinf. 76 (2009) 794–807.
[125] M.D. Akeson, D.W. Deamer, Proton conductance by the gramicidin water wire. Model for proton conductance in the F1F0 ATPases? Biophys. J. 60 (1991) 101–109.
[126] Y. Tang, F. Zaitseva, R.A. Lamb, L.H. Pinto, The gate of the influenza virus M2 proton channel is formed by a single tryptophan residue, J. Biol. Chem. 277 (2002) 39880–39886.
[127] I.V. Chizhmakov, D.C. Ogden, F.M. Geraghty, A. Hayhurst, A. Skinner, T. Betakova, A.J. Hay, Differences in conductance of M2 proton channels of two influenza viruses at low and high pH, J. Physiol. 546 (2003) 427–438.
[128] A.L. Hodgkin, A.F. Huxley, The dual effect of membrane potential on sodium conductance in the giant axon of Loligo, J. Physiol. 116 (1952) 497–506.
[129] B. Chanda, O.K. Asamoah, R. Blunck, B. Roux, F. Bezanilla, Gating charge displacement in voltage-gated ion channels involves limited transmembrane movement, Nature 436 (2005) 852–856.
[130] P.S. Crozier, D. Henderson, R.L. Rowley, D.D. Busath, Model channel ion currents in NaCl-extended simple point charge water solution with applied-field molecular dynamics, Biophys. J. 81 (2001) 3077–3089.
[131] R.J. Sugrue, G. Bahadur, M.C. Zambon, M. Hall-Smith, A.R. Douglas, A.J. Hay, Specific structural alteration of the influenza haemagglutinin by amantadine, EMBO J. 9 (1990) 3469–3476.
[132] S. Grambas, A.J. Hay, Maturation of influenza A virus hemagglutinin—estimates of the pH encountered during transport and its regulation by the M2 protein, Virology 190 (1992) 11–18.
[133] C. Schroeder, H. Heider, E. Möncke-Buchner, T.I. Lin, The influenza virus ion channel and maturation cofactor M2 is a cholesterol-binding protein, Eur. Biophys. J. 34 (2005) 52–66.
[134] K.C. Duff, S.M. Kelly, N.C. Price, J.P. Bradshaw, The secondary structure of influenza A M2 transmembrane domain. A circular dichroism study, FEBS Lett. 311 (1992) 256–258.
[135] V. Vijayvergiya, S.L. Madson, P.F. Gao, T.A. Cross, D.D. Busath, 50th Biophysical Society Meeting, , 2006Salt Lake City, UT.
[136] L.J. Holsinger, M.A. Shaughnessy, A. Micko, L.H. Pinto, R.A. Lamb, Analysis of the posttranslational modifications of the influenza virus M2 protein, J. Virol. 69 (1995) 1219–1225.
[137] J.M. Thomas, M.P. Stevens, N. Percy, W.S. Barclay, Phosphorylation of the M2 protein of influenza A virus is not essential for virus viability, Virology 252 (1998) 54–64.
[138] D.D. Busath, J.G. Goit, S. Rasmussen, J. Kiriyama, V. Vijayvergiya, P.F. Gao, T.A. Cross, 50th Biophysical Society Meeting, 2006, Salt Lake City, Utah.
[139] F. Nielson, T. Harris, T. Jones, S. Rasmussen, P. Gao, T.A. Cross, D.D. Busath, 51st Biophysical Society Meeting, Baltimore, MD, 2007.
[140] M. Sharma, H. Qin, E. Peterson, C. Larson, W. Caywood, R. Rawlings, D. Busath, T.A. Cross, 52nd Biophysical Society Meeting, MA, Boston, 2009.
[141] J.M. Rausch, L.H. Pinto, Movements of Trp41 upon M2 activation, Biophys. J. 92 (2007) 120a.
[142] T. Betakova, F. Ciampor, A.J. Hay, Influence of residue 44 on the activity of the M2 proton channel of influenza A virus, J. Gen. Virol. 86 (2005) 181–184.
[143] D.J. Woodbury, Nystatin/ergosterol method for reconstituting ion channels into planar lipid bilayers, Methods Enzymol. 294 (1999) 319–339.
[144] D. Needham, D.A. Haydon, Tensions and free energies of formation of "solventless" lipid bilayers. Measurement of high contact angles, Biophys. J. 41 (1983) 251–257.

[145] W.D. Harkins, F.E. Brown, The determination of surface tension (free surface energy), and the weight of falling drops: the surface tension of water and benzene by the capillary height method, J. Am. Chem. Soc. 41 (1919) 499–524.
[146] A. Petelska, Z. Figaszewski, Interfacial tension of the two-component bilayer lipid membrane modelling of cell membrane, Bioelectrochem. Bioenerg. 46 (1998) 199–204.
[147] A.D. Petelska, Z.A. Figaszewski, Effect of pH on the interfacial tension of lipid bilayer membrane, Biophys. J. 78 (2000) 812–817.
[148] A.D. Petelska, Z.A. Figaszewski, Interfacial tension of bilayer lipid membrane formed from phosphatidylethanolamine, Biochim. Biophys. Acta 1567 (2002) 79–86.
[149] A.D. Petelska, Z.A. Figaszewski, Effect of pH on the interfacial tension of bilayer lipid membrane formed from phosphatidylcholine or phosphatidylserine, Biochim. Biophys. Acta 1561 (2002) 135–146.
[150] A.D. Petelska, M. Naumowicz, Z.A. Figaszewski, The interfacial tension of the lipid membrane formed from lipid-cholesterol and lipid-lipid systems, Cell Biochem. Biophys. 44 (2006) 205–211.
[151] A.D. Petelska, M. Naumowicz, Z.A. Figaszewski, Complex formation equilibria in two-component bilayer lipid membrane: Interfacial tension method, J. Membr. Biol. 228 (2009) 71–77.
[152] H.T. Tien, Interfacial chemistry of bilayer lipid membranes (BLM), in: K.L. Mittal (Ed.), Surfactants in Solution, Vol. 8 IBM US Technical Education, New York, 1989, pp. 133–178.
[153] H.T. Tien, Bilayer Lipid Membrane (BLM), Marcel Dekker, New York, 1974.
[154] H.G.L. Coster, R. Simon, Energy of formation of bimolecular lipid membranes, Biochim. Biophys. Acta 163 (1968) 234–239.
[155] C. Tanford, Hydrostatic pressure in small phospholipid vesicles, Proc. Natl. Acad. Sci. USA 76 (1979) 3318–3319.
[156] S.H. White, Small phospholipid vesicles: Internal pressure, surface tension, and surface free energy, Proc. Natl. Acad. Sci. USA 77 (1980) 4048–4050.
[157] F.M. Hochmuth, J.Y. Shao, J. Dai, M.P. Sheetz, Deformation and flow of membrane into tethers extracted from neuronal growth cones, Biophys. J. 70 (1996) 358–369.
[158] S.E. Feller, R.W. Pastor, On simulating lipid bilayers with an applied surface tension: Periodic boundary conditions and undulations, Biophys. J. 71 (1996) 1350–1355.
[159] F. Jahnig, What is the surface tension of a lipid bilayer membrane? Biophys. J. 71 (1996) 1348–1349.
[160] B. Roux, Commentary: Surface tension of biomembranes, Biophys. J. 71 (1996) 1346–1347.
[161] K. Tu, D.J. Tobias, J.K. Blasie, M.L. Klein, Molecular dynamics investigation of the structure of a fully hydrated gel-phase dipalmitoylphosphatidylcholine bilayer, Biophys. J. 70 (1996) 595–608.
[162] E.A. Evans, R. Waugh, Mechano-chemistry of closed, vesicular membrane systems, J. Colloid Interface Sci. 60 (1977) 286–298.
[163] E.A. Evans, R. Skalak, Mechanics and Thermodynamics of Biomembranes, CRC Press, Boca Raton, FL, 1980.
[164] R.V. Stahelin, F. Long, K. Diraviyam, K.S. Bruzik, D. Murray, W. Cho, Phosphatidylinositol 3-phosphate induces the membrane penetration of the FYVE domains of Vps27p and Hrs, J. Biol. Chem. 277 (2002) 26379–26388.
[165] T. Soderlund, J.M. Alakoskela, A.L. Pakkanen, P.K. Kinnunen, Comparison of the effects of surface tension and osmotic pressure on the interfacial hydration of a fluid phospholipid bilayer, Biophys. J. 85 (2003) 2333–2341.

[166] H.V. Ly, M.L. Longo, The influence of short-chain alcohols on interfacial tension, mechanical properties, area/molecule, and permeability of fluid lipid bilayers, Biophys. J. 87 (2004) 1013–1033.
[167] G. Koster, M. VanDuijn, B. Hofs, M. Dogterom, Membrane tube formation from giant vesicles by dynamic association of motor proteins, Proc. Natl. Acad. Sci. USA 100 (2003) 15583–15588.
[168] E. Glassinger, R.M. Raphael, Influence of thermally driven surface undulations on tethers formed from bilayer membranes, Biophys. J. 91 (2006) 619–625.
[169] A.D. MacGillivray, Nernst-Planck equations and the electroneutrality and Donnan assumptions, J. Chem. Phys. 14 (1968) 2903–2907.
[170] T. Teorell, Transport processes and electrical phenomena in ionic membranes, Prog. Biophys. Biophys. Chem. 3 (1953) 305–369.
[171] C. Tanford, Physical Chemistry of Macromolecules, John Wiley and Sons, New York, NY, 1961, pp. 225–227.
[172] P. Läuger, Electrogenic ion Pumps, Sinnauer Associates, Sunderland, MA, 1991, pp. 100–103.
[173] J.E. Raftos, B.T. Bulliman, P.W. Kuchel, Evaluation of an electrochemical model of erythrocyte pH buffering using 3P nuclear magnetic resonance, J. Gen. Physiol. 95 (1990) 1183–1204.
[174] A.R. Waldeck, P.W. Kuchel, 23Na-nuclear magnetic resonance study of ionophore-mediated cation exchange between two populations of liposomes, Biophys. J. 64 (1993) 1445–1455.
[175] J. Fischbarg, The plasma membrane transporters and channels of corneal endothelium, in: J. Tombran-Tink, C.J. Barnstable (Eds.), Ocular Transporters in Ophthalmic Diseases and Drug Delivery Humana Press, New York, NY, 2008, pp. 451–458.
[176] D.J. Woodbury, E.S. Richardson, A.W. Grigg, R.D. Welling, B.H. Knudson, Reducing liposome size with ultrasound: Bimodal size distributions, J. Liposome Res. 16 (2006) 57–80.
[177] E.S. Richardson, W.G. Pitt, D.J. Woodbury, The role of cavitation in liposome formation, Biophys. J. 93 (2007) 4100–4107.
[178] M.E. Hardy, C.E. Pollard, B.G. Small, M. Bridgland-Taylor, A.J. Woods, J.P. Valentin, N. Abi-Gerges, Validation of a voltage-sensitive dye (di-4-ANEPPS)-based method for assessing drug-induced delayed repolarisation in Beagle dog left ventricular midmyocardial myocytes, J. Pharmacol. Toxicol. Methods 60 (2009) 94–106.
[179] Y. Kapoor, B.A. Howell, A. Chauhan, Liposome assay for evaluating ocular toxicity of surfactants, Invest. Ophthalmol. Vis. Sci. 50 (2009) 2727–2735.
[180] J.M. Rausch, W.C. Wimley, A high-throughput screen for identifying transmembrane pore-forming peptides, Anal. Biochem. 293 (2001) 258–263.
[181] N. Duzgunes, Fluorescence assays for liposome fusion, Methods Enzymol. 372 (2003) 260–274.

CHAPTER TWO

Shape Transformations of Amphiphilic Membranes

W.T. Góźdź*

Contents

Abstract

We present theoretical calculations performed within the framework of the spontaneous curvature model describing the shape transformations of amphiphilic membranes. Possible shape transformations of lipid vesicles of spherical topology are reviewed. The deformation of the membrane shape caused by the

* Corresponding author. Tel.: +48 343 3242; Fax: +48 343 3333;
E-mail address: wtg@ichf.edu.pl

Institute of Physical Chemistry, Polish Academy of Sciences, Kasprzaka 44/52, 01-224 Warsaw, Poland

Advances in Planar Lipid Bilayers and Liposomes, Volume 10
ISSN 1554-4516, DOI: 10.1016/S1554-4516(09)10002-9

adhering colloidal particles or microtubules is examined. The effect of phase separation and diffusion of macromolecules on the shape deformation of multicomponent membrane is studied.

1. Introduction

Many types of stimuli can induce shape transformations of lipid membranes and liposomes. The change of temperature or osmotic pressure, the attachment of macromolecules to the liposome surface, interaction of liposomes with rigid surfaces or colloidal particles are examples of stimuli which cause shape transformations of liposomes. There are many examples of processes, which involve encapsulation of large particles located inside a biological cell and many mechanisms to attach the membrane of the cell to the particle. Viruses are expelled out of biological cells in the process of exocytosis, in which they are encapsulated in the cell membrane. Deformation of lipid vesicles or biological cells by rigid objects is also important when such objects are used to manipulate the cells, for example, in AFM experiments [1]. When a large particle touches the wall of a liposome, its shape is deformed due to binding the lipid membrane to the particle. That process was studied experimentally [2, 3], theoretically within the framework of the curvature energy [4–8], by Brownian dynamics computer simulations [9], and by dissipative particle dynamics [10]. The change of the liposome shape can be induced by adsorption of the vesicle to rigid surfaces [11] or by stretching the liposome by a microtubules. Microtubules are rigid, cylindrical aggregates of the protein tubulin. When microtubules are encapsulated inside lipid vesicles, they can grow due to the polymerization of the tubulin and deform vesicles when the size of a microtubule is larger than the distance between the walls of a vesicle [12–19]. A few types of deformations have been observed. When two ends of the rigid microtubule deform a vesicle, it may change its shape from a spherical one to a vesicle which resembles Greek letter ϕ or a dumbbell. It is also possible that only one end of the microtubule creates a protrusion. In such a case, a vesicle transforms into a new vesicle with the shape, which resembles a cherry.

The knowledge of possible shape deformations of the vesicles can be helpful in interpreting the shape transformations encountered in experiments or in biological systems. The shape of the liposomes observed in experiments can be mapped to some model situations predicted by theory. Such mapping may be useful in analyzing and understanding experimental results. We describe several examples of shape transformations of liposomes

calculated within the framework of the spontaneous curvature model and compare the predictions of the theory with a few known experimental situations. In Section 2, the theoretical model is presented. In Section 3, we describe the shape transformations resulting from the change of the volume and spontaneous curvature. In Section 4, we present how interactions of vesicles with rigid objects can influence shape transformations. In Section 5, shape transformation of multicomponent membranes is described.

2. Model

Lipid membranes are models of two-dimensional fluids [20]. The membrane forms a surface embedded in three-dimensional space. In the modeling on the mesoscopic scale, it is important to grasp the main feature of the studied system and disregard details, which have little or none influence on the investigated phenomenon. Such model has been developed for membrane built of amphiphilic molecules, where the bilayers are treated as mathematical surfaces and the stability of objects formed by the bilayers is estimated from the curvatures of the surfaces [21–23]. The energy $\mathcal{F}$ of objects built of bilayer membranes is the sum of the integrals of the mean curvature and the Gaussian curvature over the surface of a membrane.

$$\mathcal{F} = \frac{\kappa}{2}\int_S \mathrm{d}S(\mathcal{C}_1 + \mathcal{C}_2 - \mathcal{C}_0)^2 + \bar{\kappa}\int_S \mathrm{d}S\mathcal{C}_1\mathcal{C}_2, \tag{1}$$

where κ and $\bar{\kappa}$ are the bending and Gaussian rigidity, $\mathcal{C}_1$ and $\mathcal{C}_2$ are the principal curvatures, $\mathcal{C}_0$ is the spontaneous curvature, and the integral (1) is taken over the surface of a closed vesicle, S. The first integral describes elastic properties of the membrane. The second integral describes topological changes. If the topology does not change, the second integral is constant according to the Gauss–Bonet theorem. In most theoretical studies, the vesicles with rotational symmetry are investigated. Sometimes it is because the physics of the problem imposes such symmetry, sometimes it is because of the computational simplicity. It is important to choose convenient system of coordinates to describe the surface of the vesicle. The vesicle profile is parameterized with the angle, θ, of the tangent to the profile with the plane perpendicular to the axis of rotation, as a function of the arc length, s, as shown in Fig. 1. The parametric equations of the vesicle profile are given by:

$$z(s) = \int_0^s \mathrm{d}s' \sin(\theta(s')), \tag{2}$$

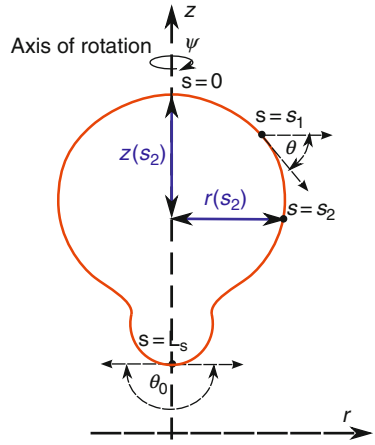

Figure 1 Schematic representation of a profile in the arc length parameterization $\theta(s)$. s is the arc length. L_s is the length of the profile.

$$r(s) = \int_0^s \mathrm{d}s' \cos(\theta(s')), \tag{3}$$

where the arc length s is the parameter.

The principal curvatures can be derived from the equations describing the surface of the vesicle. In the three-dimensional Euclidean space, the vector $\mathbf{R} = \{x(\psi, s), y(\psi, s), z(\psi, s)\}$ describing the points on a surface of revolution, parameterized with the function $\theta(s)$, is given by:

$$\mathbf{R} = \{\cos(\psi)r(s), \sin(\psi)r(s), z(s)\}. \tag{4}$$

The angle of rotation ψ and the arc length s are coordinates on the surface. x, y, and z are coordinates in three-dimensional Euclidian space. To calculate the principal curvatures $\mathtt{C}_1$ and $\mathtt{C}_2$ on the surface, the metric tensor g_{ij} is calculated in the following way [24, 25]:

$$g_{ij} = \begin{pmatrix} \frac{\partial \mathbf{R}}{\partial s}\cdot\frac{\partial \mathbf{R}}{\partial s} & \frac{\partial \mathbf{R}}{\partial \psi}\cdot\frac{\partial \mathbf{R}}{\partial s} \\ \frac{\partial \mathbf{R}}{\partial s}\cdot\frac{\partial \mathbf{R}}{\partial \psi} & \frac{\partial \mathbf{R}}{\partial \psi}\cdot\frac{\partial \mathbf{R}}{\partial \psi} \end{pmatrix} = \begin{pmatrix} 1 & 0 \\ 0 & (r(s))^2 \end{pmatrix}, \tag{5}$$

where

$$\partial\mathbf{R}/\partial s = \{\cos(\psi)\cos(\theta(s)), \cos(\theta(s))\sin(\psi), \sin(\theta(s))\}, \tag{6}$$

$$\partial\mathbf{R}/\partial\psi = \{-\sin(\psi)r(s), \cos(\psi)r(s), 0\}. \tag{7}$$

The unit normal $\mathbf{n}$ can be calculated from

$$\begin{aligned}\mathbf{n} &= \frac{(\partial\mathbf{R}/\partial\psi \times \partial\mathbf{R}/\partial s)}{\sqrt{\det(g_{ij})}} \\ &= \{-\cos(\psi)\sin(\theta(s)), -\sin(\psi)\sin(\theta(s)), \cos(\theta(s))\}.\end{aligned} \tag{8}$$

Next, $\mathbf{Y}$ and L_{ij} are defined as

$$\mathbf{Y} = \begin{pmatrix} \dfrac{\partial^2\mathbf{R}}{\partial s\partial s} & \dfrac{\partial^2\mathbf{R}}{\partial s\partial\psi} \\ \dfrac{\partial^2\mathbf{R}}{\partial\psi\partial s} & \dfrac{\partial^2\mathbf{R}}{\partial\psi\partial\psi} \end{pmatrix}, \tag{9}$$

$$L_{ij} = \mathbf{Y}\cdot\mathbf{n}. \tag{10}$$

L_{ij} are the coefficients of the second-fundamental form. The H_{ij} tensor is then

$$H_{ij} = g_{ij}^{-1}L_{ij} = \begin{pmatrix} \dfrac{\mathrm{d}\theta(s)}{\mathrm{d}s} & 0 \\ 0 & \dfrac{\sin(\theta(s))}{r(s)} \end{pmatrix}. \tag{11}$$

The trace of the tensor H_{ij} divided by 2 gives the mean curvature of the surface. Thus, $\mathcal{C}_1$ and $\mathcal{C}_2$ are:

$$\mathcal{C}_1 = \frac{\mathrm{d}\theta(s)}{\mathrm{d}s}, \tag{12}$$

$$\mathcal{C}_2 = \frac{\sin(\theta(s))}{r(s)}. \tag{13}$$

The bending energy $\mathcal{F}$ for the profile parameterized with the function $\theta(s)$ is given by the following formula

$$\mathcal{F}[\theta(s)] = \frac{\kappa}{2}\int_0^{2\pi}\mathrm{d}\psi\int_0^{L_s}\mathrm{d}s r(s)\left(\frac{\mathrm{d}\theta(s)}{\mathrm{d}s} + \frac{\sin(\theta(s))}{r(s)} - \mathcal{C}_0\right)^2, \tag{14}$$

where ψ is the angle of rotation. The surface area and the volume are calculated as follows:

$$S = 2\pi \int_0^{L_s} \mathrm{d}s r(s), \tag{15}$$

$$V = \pi \int_0^{L_s} \mathrm{d}s r^2(s) \sin\theta(s). \tag{16}$$

Sometimes it may be convenient to use different coordinate system to parameterize the shape of a vesicle. For example, the arc length may be replaced by the surface area of a rotationally symmetric vesicle a, as shown in Fig. 2. The equations for the parameterization of the shape profile have the following form:

$$z(a) = \frac{1}{2\pi} \int_0^a \mathrm{d}a' \frac{\sin(\theta(a'))}{r(a')}, \tag{17}$$

$$r(a) = \sqrt{\frac{\int_0^a \mathrm{d}a' \cos(\theta(a'))}{\pi}}. \tag{18}$$

The bending energy for the shape Eqs. (17), (18) is given by the following functional:

$$\mathcal{F}[\theta(a)] = \frac{\kappa}{2} \int_0^S \mathrm{d}a \left(\frac{\sin(\theta(a))}{r(a)} + 2\pi r(a) \frac{\mathrm{d}\theta(a)}{\mathrm{d}a} - \mathcal{C}_0 \right)^2, \tag{19}$$

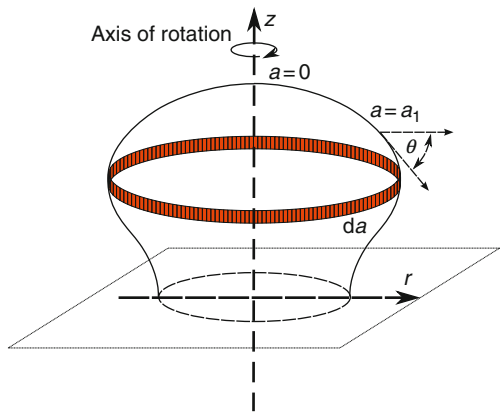

Figure 2 Schematic illustration of the parameterization of the vesicle shape. a is the surface area of some part of the vesicle, measured from the pole to some tangent point. $\theta(a)$ is the angle of the tangent to the shape profile with the line parallel to r-axis.

where $\mathcal{C}_0$ is the spontaneous curvature and S is the total surface area of the vesicle. Such parameterization is useful in investigation of the diffusion processes on lipid vesicles [26].

The volume, V_0, and the radius, R_0, of the sphere having the same surface area, S, as the investigated vesicle are chosen as the volume and the length units, respectively [11, 27],

$$R_0 = \sqrt{S/4\pi}, \tag{20}$$

$$V_0 = \frac{4}{3}\pi R_0^3. \tag{21}$$

The dimensionless, reduced volume v and the dimensionless spontaneous curvature c_0 are defined as follows:

$$v = V/V_0, \tag{22}$$

$$c_0 = \mathcal{C}_0 R_0. \tag{23}$$

In general analytic minimization of functional (1) is not possible. Therefore, the functional has to be minimized numerically. It can be done by solving differential equation [28]. However, for complex shapes this method is hard to implement. In all calculations presented here, we use the method which relies on expansion of the shape profile into appropriate Fourier series and minimization of the resulting functional with respect to the coefficients in the Fourier expansion. The proper series is the one which by construction fulfills boundary conditions for the shape profile, that is, $\theta(0) = 0$ and $\theta(L_s) = \pi$. The sine series almost perfectly fulfills the requirements for the set of functions, which we are looking for.

The following Fourier series is used to approximate the function $\theta(s)$:

$$\theta(s) = \theta_0 \frac{s}{L_s} + \sum_{i=1}^{N} a_i \sin\left(\frac{\pi}{L_s} i{\cdot}s\right), \tag{24}$$

where N is the number of the Fourier modes, and a_i are the Fourier amplitudes. For simple shapes like prolate vesicles it is enough to take 40 Fourier modes to get the bending energy with very high numerical accuracy. For complex shapes with narrow neck more than 100 modes is necessary. When Eq. (24) is inserted into Eqs. (2), (3), and (14), the functional minimization can be replaced by the minimization of the function of many variables. Functional (14) becomes the function of the amplitudes a_i and the length of the shape profile L_s. The minimization is performed under the constraints of constant surface area S and volume V. The constraints in numerical calculations are implemented by means of Lagrange multipliers.

We consider physical situations where the surface area of the liposome does not change. Thus, the liposome can be characterized by the reduced

volume and the spontaneous curvature. In this review, we concentrate on the liposomes with the rotational symmetry, but in general other nonaxisymmetric shapes are also possible. The simplest way to change the liposome shape is by changing the reduced volume or the spontaneous curvature. In experiments, the reduced volume can be varied by the change of the osmotic pressure, since the membrane is permeable to the water molecules. There are some evidence that the spontaneous curvature can be tuned by the change of temperature [29–31]. The change of temperature changes the spontaneous curvature globally on the whole surface of the vesicle. Attachment of the macromolecules at the surface of the liposome can induce the spontaneous curvature [32–36]. Macromolecules can be attached selectively to some part of the liposome surface. Thus, they can alter the spontaneous curvature selectively only on some region of the liposome.

3. Shape Transformation of Vesicles

If there are no external constraints, shapes of vesicles are governed by the reduced volume (Eq. 22) and the spontaneous curvature (Eq. 23). The phase diagram for axisymmetric vesicles with small spontaneous curvature has been already investigated [11, 27, 28, 37–40], but the phase diagram for large spontaneous curvature is still not thoroughly explored. The investigation of the transformations of vesicles with nonaxisymmetric shapes [41–44] and nonspherical topology [29, 45–47] reveals many interesting phenomena. Here, we focus on the discussion of the vesicles with the spherical topology and axisymmetric shapes. In Section 3.1, we review main results for small spontaneous curvature. Results for the shape transformations of vesicles with large spontaneous curvature are described in Sections 3.2–3.4. In Section 3.5, we present an example of shape transformation of membranes of nontrivial topology.

3.1. Transformations Induced by the Change of the Reduced Volume at Constant Spontaneous Curvature

In the simplest case where the spontaneous curvature is $C_0 = 0$, there are three basic shapes which minimize functional (1): stomatocytes, oblate, and prolate. For small reduced volume, stomatocyte vesicles have the lowest energy. For large reduced volume, prolate vesicles have the lowest energy and for intermediate values of the reduced volume oblate vesicles have the lowest energy.

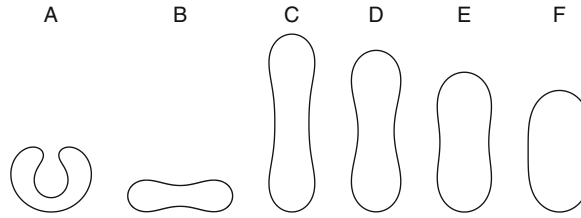

Figure 3 The profile of stomatocyte, oblate, and prolate vesicles for $\mathfrak{c}_0 = 0$ and different reduced volume: (A) $v = 0.6515$, (B) $v = 0.6515$, (C) $v = 0.6515$, (D) $v = 0.70$, (E) $v = 0.80$, (F) $v = 0.90$. The axis of rotation is in the vertical direction.

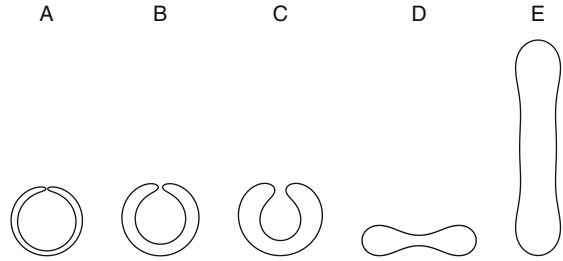

Figure 4 The shape profile of stomatocyte, oblate, and prolate vesicle for $\mathfrak{c}_0 = 0$ and different reduced volume: (A) $v = 0.20$, (B) $v = 0.40$, (C) $v = 0.5915$, (D) $v = 0.5915$, (E) $v = 0.5915$.

The change of the reduced volume results in discontinuous transitions. For the reduced volume $v = 0.6515$ and $v = 0.5915$, vesicles with different geometries exist and have approximately the same bending energy [28]. Figure 3 shows the vesicles with the reduced volume $v \geq 0.6515$. At $v = 0.6515$ the bending energy of the oblate (Fig. 3B) and the prolate (Fig. 3C) vesicle is approximately the same, but the stomatocyte vesicle (Fig. 3A) has higher energy. For smaller values of the reduced volume, oblate vesicles are stable, whereas for higher values of the reduced volume prolate vesicles are stable. Thus, at $v = 0.6515$ we have discontinuous transition which involves the change of geometry. The shape of prolate vesicles changes from elongated to spherical upon increasing the reduced volume (Fig. 3C–F).

Figure 4 shows vesicles for $v \leq 0.5915$: stomatocytes, oblate, and prolate. The bending energy for the stomatocyte (Fig. 4C) and the oblate vesicle (Fig. 4D) is approximately the same, but the bending energy of the prolate vesicle (Fig. 4E) is higher [28]. Stomatocyte vesicles are stable for smaller reduced volume and oblate vesicles are stable for larger reduced volume. Thus, at $v = 0.5915$ we have the second discontinuous transition which involves the change of the geometry and symmetry. The stomatocytes vesicles do not have up–down symmetry.

3.2. Transformations Induced by the Change of the Spontaneous Curvature at Constant Surface Area

To distinguish the role of the spontaneous curvature and the reduced volume in the process of shape transformations, one can examine the case where the surface area S of a vesicle is constant and the volume V is unconstrained. Such situation may hypothetically happen when a membrane is ideally permeable. Thus, the shape transformations are driven only by a change of the spontaneous curvature $\mathfrak{C}_0$. When the dimensionless spontaneous curvature $\mathfrak{c}_0$ is equal 2, the shape minimizing functional (1) is a sphere and the bending energy is zero, since $\mathfrak{c}_1 = \mathfrak{c}_2 = 1$ at every point of the surface. Increasing the spontaneous curvature beyond $\mathfrak{c}_0 = 2$ results in a series of transitions in which the sphere is transformed into chains of beads connected by small necks, as shown in Fig. 5.

The size, the number, and the shape of the beads are governed by the spontaneous curvature. The transitions are discontinuous, which can be easily seen from the plots of the reduced volume of the vesicles as a function of the spontaneous curvature, presented in Fig. 6. The lines of open circles denoted by letters from (A) to (J) in Fig. 6 show the values of the reduced volume and the spontaneous curvature for which a minimum of functional (14) was found. The letter (A) denotes the minima for spheres, (B) for dumbbells, (C) for tree-bead vesicles, and so on as indicated in Fig. 5. The minima of the functional are either global or local, since for the same parameters more than one solution is found. Comparing the curvature energy as a function of the spontaneous curvature for two configurations which differ by one bead, one finds the value of the spontaneous curvature for which the energies for the two configurations are equal. These values are marked by vertical arrows in Fig. 6. At these values, the configurations with a larger number of beads become global minima while the configurations with a smaller number of beads become local minima. For the configuration

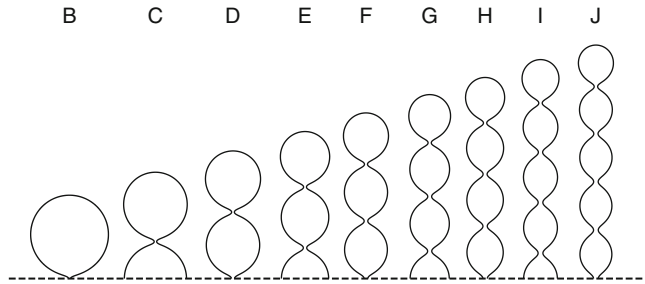

Figure 5 The profiles calculated for a constant surface area and different spontaneous curvature. The configurations with the minimal energy for a given number of beads are shown. No volume constraint is applied. The dashed line denotes the symmetry plane, only half of the vesicle is shown.

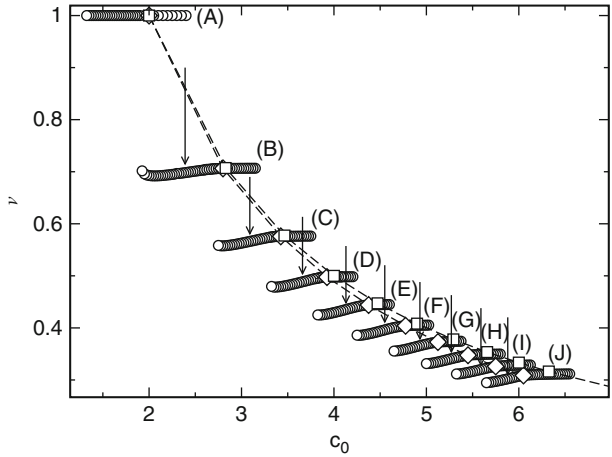

Figure 6 Reduced volume of the vesicles, $v = V/V_0$, versus the dimensionless spontaneous curvature, $c_0 = C_0 R_0$. Open circles denote the results of minimization without the volume constraint. Open squares represent configurations composed of touching spheres, with different numbers of spheres and the same total surface area. Open diamonds denote the configurations with minimal energy from Fig. 5. The dashed lines are added to guide the eye.

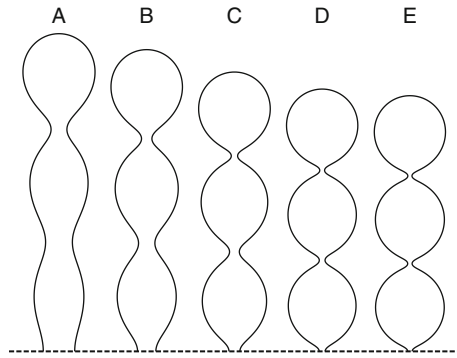

Figure 7 The profiles calculated for a constant surface area and different spontaneous curvature. The configurations with the minimal energy for a given number of beads are shown. No volume constraint is applied. The spontaneous curvature is, respectively: (A) $c_0 = 4.25$, (B) $c_0 = 4.45$, (C) $c_0 = 4.625$, (D) $c_0 = 4.775$, (E) $c_0 = 5.025$. The dashed line denotes the symmetry plane, only half of the vesicle is shown.

with a given number of beads, the decrease of the spontaneous curvature results in widening the necks in such a way that all the necks become wider simultaneously, see Fig. 7. Thus, by monitoring the width of the necks it is possible to monitor the change of the spontaneous curvature. The direction of the change of the spontaneous curvature can be also predicted.

The knowledge of such a dependence between the shape of a vesicle and the spontaneous curvature may be helpful in interpreting experimental results.

3.3. Transformation Induced by Spontaneous Curvature at Constant Reduced Volume

In the ensemble of constant surface area S, volume V, and spontaneous curvature C_0, the configurations, which resemble cylinder closed at the ends by hemispheres, become stable. The shape evolution driven by a change of the spontaneous curvature, for vesicles with small reduced volume, is particularly interesting because the transition from cylindrical vesicle to the vesicle composed of many beads proceeds gradually. For low values of the spontaneous curvature c_0, the vesicle is mainly cylindrical, as is shown in the configurations (A)–(F) in Fig. 8. Increasing the spontaneous curvature induces the beading process. The formation of beads begins at the ends and proceeds gradually toward the center. The beads have approximately the same size. Very similar process has been observed in the experiments on tubular polymersomes [30]. The transition observed in the experiments can be reproduced by changing the spontaneous curvature while keeping constant surface area and volume. Similar transformations of bilayer membranes which form cylindrical shapes into beads are often encountered in biological systems. The transformations are induced by different stimuli. For example, the action of laser tweezers [48–50], by UV irradiation [51], or the presence of hydrophilic polymers with hydrophobic side groups [34, 35] induces the transformations from cylinders to beads.

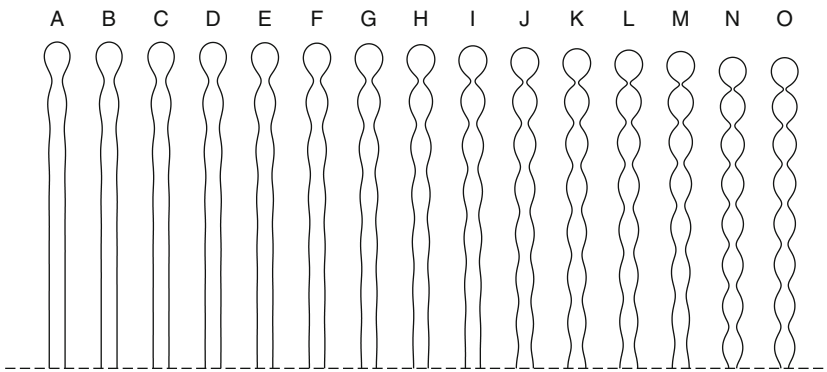

Figure 8 Shape transformation of a long tube induced by the change of the spontaneous curvature. Only upper half of the shape profile is shown since it is symmetric with respect to the horizontal axis. Reduced volume v is set to 0.235. The spontaneous curvature c_0 is (A) 6.05, (B) 6.15, (C) 6.25, (D) 6.35, (E) 6.45, (F) 6.55, (G) 6.65, (H) 6.75, (I) 6.85, (J) 6.95, (K) 7.05, (L) 7.15, (M) 7.25, (N) 7.35, (O) 7.45.

For the vesicles with small reduced volume, the morphological transition has been observed, in which the number of beads increases in the vesicle already covered with beads on its whole length. The transition is discontinuous, which can be seen by looking at the configurations (M) and (N) in Fig. 8. The configuration (M) in Fig. 8 is built of 15 beads, which are more pronounced at the ends and less pronounced in the middle. When the spontaneous curvature is increased, then the new configuration with 15 beads becomes metastable and next the solution with 15 beads no longer exists. There exists only the solution with 16 pronounced beads as presented in the configurations (N) and (O), but there is no continuous transition from the configuration with 15 beads to 16 beads at least in the situation modeled here. Such a transition exists also for the vesicles with different number of beads.

The curvature energy is lowered during the formation of beads and is the lowest when the whole vesicle is composed of beads as shown in Fig. 9. Two types of shape transitions can be distinguished by examining the dependence of the elastic energy on the spontaneous curvature: the first one, continuous transition from cylindrical vesicle to beads—configurations from (A) to (M); the second one, discontinuous transition, when the number of beads is changed from 15 beads in configuration (M) to 16 beads in configuration (N). Two different curves can be distinguished on the plot of the elastic energy as a function of the spontaneous curvature. The first curve which begins at $c_0 = 6.0$ and ends at $c_0 = 7.275$ represents the elastic energy change for the continuous transformation from cylindrical

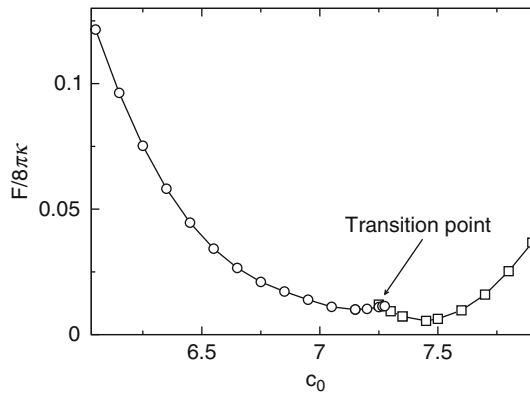

Figure 9 The elastic energy as a function of the reduced spontaneous curvature for the long vesicle obtained for the reduced volume $v = 0.235$. The lines are added to guide the eye. The open circles represent the evolution of the vesicle from the cylinder to the configuration with 15 beads. The open squares represent the configurations with 16 beads. The elastic energy is measured in units of the bending energy of a sphere ($8\pi\kappa$).

vesicle to the one composed of 15 beads. The second curve which begins at $c_0 = 7.25$ represents the energy change for the vesicle composed of 16 beads. Such a behavior is generic for the vesicles with small reduced volume and the exact number of beads is not crucial. Figure 10 shows the transformations for the vesicles with the reduced volume $v = 0.38, 0.39, 0.40$. Despite some differences, the shape transformation caused by the increase of the spontaneous curvature proceeds in a similar way. The tubular vesicles are transformed into vesicles composed of connected beads.

3.4. Breaking the Mirror Symmetry for Large c_o

When the spontaneous curvature becomes larger, an interesting phenomenon of breaking up–down symmetry for prolate vesicles is observed [28]. Figure 11. shows vesicles with $c_0 = 3.0$ at a few values of the reduced volume. When $v = 0.60, 0.70$ the prolate vesicle (Fig. 11A and B) has up

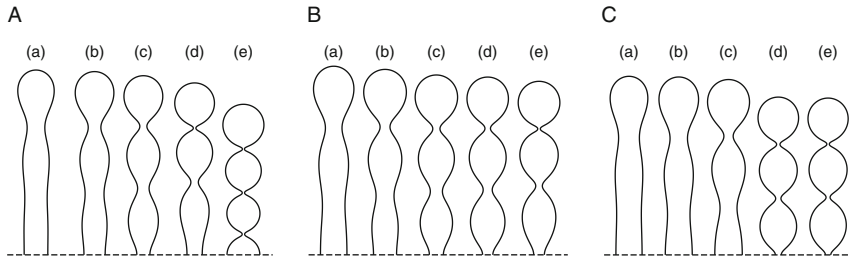

Figure 10 Shape transformations of a short tube induced by a change of the spontaneous curvature. The dashed line shows the symmetry plane, only upper half of a shape profile is presented. (A) the reduced volume $v = 0.38$—(a) $c_0 = 3.6$, (b) $c_0 = 4.1$, (c) $c_0 = 4.6$, (d) $c_0 = 5.1$, (e) $c_0 = 5.25$, (B) the reduced volume $v = 0.39$—(a) $c_0 = 3.8$, (b) $c_0 = 4.25$, (c) $c_0 = 4.30$, (d) $c_0 = 4.65$, (e) $c_0 = 5.25$, (C) the reduced volume $v = 0.40$—(a) $c_0 = 3.1$, (b) $c_0 = 3.6$, (c) $c_0 = 4.3$, (d) $c_0 = 4.7$, (e) $c_0 = 5.3$.

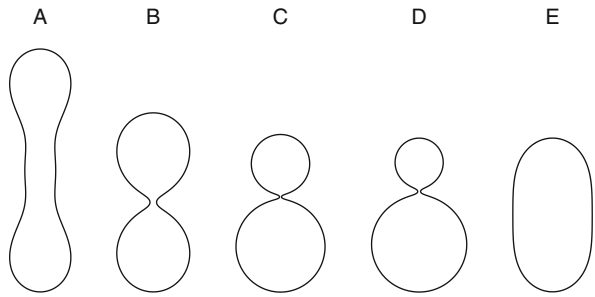

Figure 11 The profile of prolate vesicles for $c_0 = 3$ and different reduced volume: (A) $v = 0.60$, (B) $v = 0.70$, (C) $v = 0.75$, (D) $v = 0.80$, (E) $v = 0.90$.

and down symmetry, but for $v = 0.75$ (Fig. 11C) and $v = 0.80$ (Fig. 11D) the vesicles have pear-like shapes. For $v = 0.90$ (Fig. 11E) vesicles again have mirror symmetry at the equator. Experimentally, the shape transformation from ellipsoid to pear-like vesicles can be obtained by photoisomerization of photosensitive amphiphilic molecules [52].

Increasing the spontaneous curvature leads to the shapes which look like a chain of small beads connected with a larger sphere [31, 53, 54]. If the reduced volume is set constant, the size of beads and the number of beads depends on the spontaneous curvature. The larger the spontaneous curvature the larger the number of small beads is present in the configurations with the lowest energy. When the spontaneous curvature is sufficiently high, there exist many minima of functional (14) for the same set of parameters. Figure 12 shows the shape profiles for the minima of functional (14) at the reduced volume $v = 0.7$ and the spontaneous curvature $c_0 = 12$. All the configurations except the first one look similar, since they are composed of a large sphere connected with a chain of small beads. The size of small beads and the distance between the poles of the vesicle is different for each minimum. Of course, for a given spontaneous curvature, the size of the beads cannot be arbitrarily small. The existence of so many metastable states is possible due to the presence of the large sphere which acts as a volume and surface reservoir for the long protrusion. The global minimum is the configuration with eight small beads, but there exist local minima with a larger number of beads and thus with a larger distance between the poles of the vesicle, as shown in Fig. 13. Vesicles with such shapes are observed experimentally [19]. Similar vesicles have been considered in Refs. [27, 55, 56] but with a lower number of small beads.

It is interesting to note that on the energy–distance plot (Fig. 13), the points which represent configurations with smaller number of beads than the configuration which is the global minimum are very well approximated

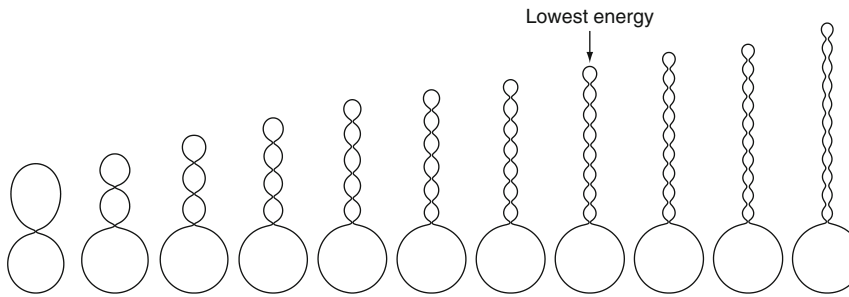

Figure 12 The shape profiles corresponding to the local minima of functional (14) for the reduced volume $v = 0.7$, the spontaneous curvature $c_0 = 12$, and without the constraint for the length. The solution with the lowest energy is the one with eight small beads.

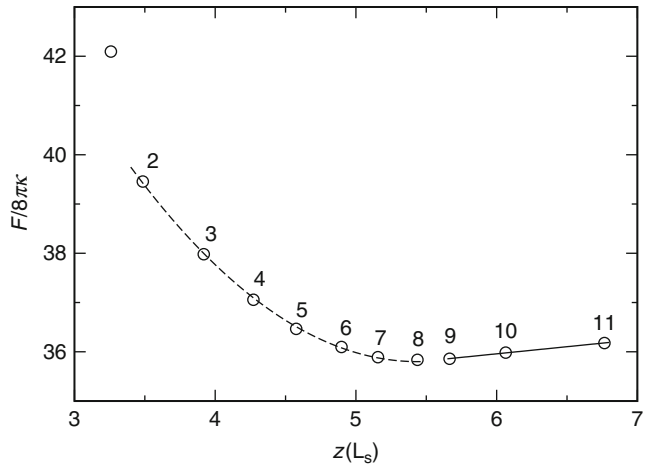

Figure 13 The local minima of the curvature energy F as a function of the distance between the poles of the vesicle $z(L_s)$. The open circles represent the minima of functional (14) corresponding to the profiles shown in Fig. 12. The dashed line is the fit to the points with 2, 3, 4, 5, 6, 7, 8 small beads of the parabolic curve $F = B/2\,(z - z_8)^2 + F_0$, where $B = 0.47 \times 8\pi\kappa$ and z_8 is the distance between the poles of the vesicle for the profile with eight small beads. The solid line is the fit to the points with 9, 10, 11 small beads of the straight line. The numbers above the symbols indicate the number of small beads.

with the parabolic curve shown by the dashed line. Thus, in some hypothetical process of compressing the stable configuration (the one with the lowest energy), the vesicle behaves asymptotically according to the Hook's law, that is, the force which causes the deformation is proportional to the change of the distance between the poles. The transitions between the minima with different number of beads will proceed through a series of metastable states. The energy of those metastable states will be in general a complex function of the pole-to-pole distance, which differs from the energy curve resulted from extrapolation of the minima with different number of beads, denoted by the dashed line in Fig. 13.

3.5. Deformation of Membranes of Complex Topology

Vesicles of spherical topology are most common, but there are also many types of vesicles with nonspherical topology [29, 45–47]. The simplest one is toroidal vesicles [45]. Very interesting are genus two vesicles due to the phenomenon of conformal diffusion [47]. To illustrate how fascinating can be shape transformations of membranes of complex topology we present possible shape transformations of a particular kind of high-genus vesicle [29]. These high-genus vesicles are closed objects built of two bilayers

connected by passages. The separation of the bilayers is small compared to the size of the vesicle. Although the shape of the membrane is complex, it can be easily parameterized by the following equation:

$$\cos\,\mathrm{h}^2(z) = a_0 + \sum_{i=1}^{N} a_i \sum_{i=1}^{N_i} \cos\left(\frac{2\pi}{L}\mathbf{k}_j^{(i)} \cdot \mathbf{r}\right), \tag{25}$$

where $\mathbf{r} = (x, y)$, and N is the number of Fourier amplitudes, a_i. There are N_i reciprocal lattice vectors $\mathbf{k}_j^{(i)}$ in the ith shell. L is the lattice constant. The shape of the high-genus vesicles may undergo significant transformations, for example, when the temperature is varied. Such transformations are observed in experiments and are predicted by theoretical calculations [29]. For high-genus vesicles there exist a few families of shapes which are stable for different values of the reduced volume and the spontaneous curvature, as presented in Fig. 14. The most common are the membranes connected by circular passages. It is surprising that there exist two families of such shapes for the same set of the reduced volume and the spontaneous curvature. They differ mainly by the size of the passage, where one family which we call small holes (Fig. 14A) is characterized by small size of the passage radius

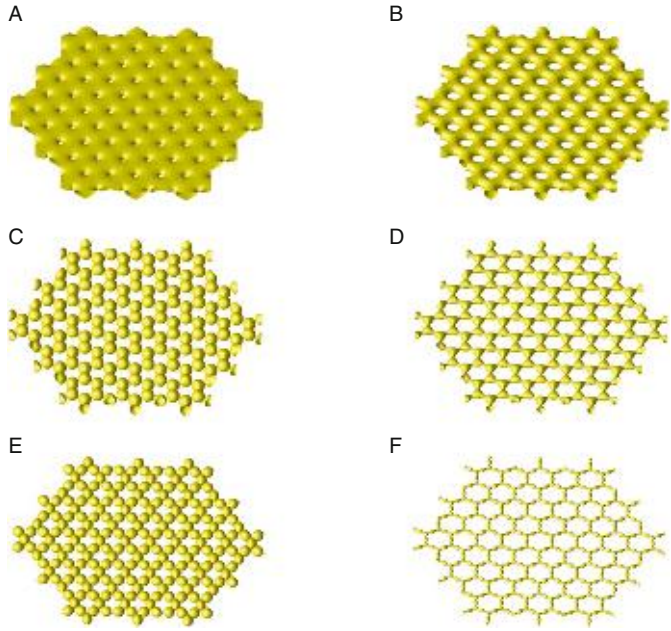

Figure 14 Different shapes of the membranes which forms the surface of the high-genus vesicles. (A) and (B)—circular passages, (C) and (D)—connected spheres (triangles), (E) and (F)—connected spindles.

compared to the distance between passages, while the other family—large holes, Fig. 14B—is characterized by the large ratio of passage radius to the distance between passages. The membrane with the small holes is the most stable for the small value of both reduced volume and spontaneous curvature, while the membrane with large holes is the most stable for large values of the reduced volume. The transition from the small holes to the large holes is continuous for high values of the reduced volume when the spontaneous curvature is changed. When reduced volume is smaller, the transition becomes discontinuous. For a certain range of the reduced volume and for large values of the spontaneous curvature, one observes another family of shapes which resembles spheres or triangles located in vertices of hexagons in a hexagonal lattice connected by small necks along the edges of hexagons as shown in Fig. 14C and D. Further decreasing of the reduced volume leads to a new family of shapes which are composed of spindle-like object located along the edges of hexagons on a hexagonal lattice joined in the vertices of hexagons as shown in Fig. 14E and F.

4. Deformation of Vesicles Subject to Constraints Resulted from Interactions with Rigid Objects

In this section, we discuss two model calculations for the deformations of vesicles by a microtubule and a colloidal particle. In Section 4.1, shape transformations of the vesicle with the reduced volume $v = 0.7$ and different values of the spontaneous curvature are described. In Section 4.2, the calculations based on functional (14) describing the deformations of lipid vesicles caused by small spherical particles are presented.

4.1. Deformation of Vesicles with Encapsulated Microtubules

Very interesting phenomena can be observed for vesicles with large spontaneous curvature with microtubules inside. For the vesicle with encapsulated microtubule, an additional constraint is applied in functional (14). The minimization is performed with constraint on the distance between the poles of the vesicle. It is assumed that microtubules are rigid and located inside a vesicle along the rotation axis [53]. We consider equilibrium states in which microtubules have a given length and do not shrink or grow and the shape of the vesicle has reached its equilibrium state. It is assumed that the growth of a microtubule is slower than the shape relaxation of the vesicle. The distance between the poles of a vesicle, which are located at the intersection of the rotation axis and the membrane surface, is always larger than the microtubule length T.

For the microtubule encapsulated in a vesicle with the reduced volume $v = 0.7$ and the spontaneous curvature $c_0 = 0$, the protrusion develops only at one pole of the vesicle. Thus, the mirror symmetry for the empty vesicle with respect to the symmetry plane located at the equator of the vesicle (see the first profile in Fig. 15) is spontaneously broken when a microtubule begins to deform the vesicle. The shape with protrusions on both poles of the vesicle is metastable [17]. This phenomenon is analogous to symmetry breaking with the increase of the spontaneous curvature for prolate vesicles. One can observe the transition from symmetric prolate vesicles to the vesicles with pear-like shape. Figure 15 shows the configurations of vesicles with microtubules of different length t, where $t = T/R_0$ is the length of the microtubule in dimensionless units.

Figure 16 shows the configurations of vesicles with different spontaneous curvatures and the same microtubule length $t = 7.0$. When the length of a microtubule is kept constant and the spontaneous curvature is varied, one may observe a certain tendency in the change of the vesicle shape. It changes in such a way that initially the protrusion remains cylindrical and the vesicle becomes more spherical. The volume and the surface area of the protrusion and the spherical part of the vesicle are changed. When the spontaneous curvature is sufficiently high for a given length of the protrusion, the beads are formed on the protrusion, such as on the last profile in Fig. 16. Thus, by

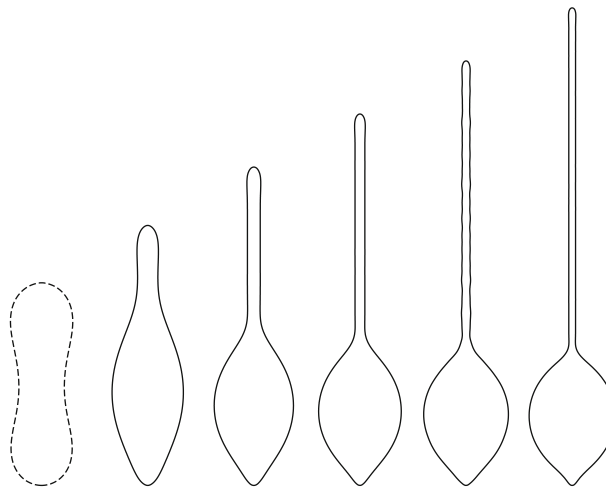

Figure 15 Shape profiles with different length of the encapsulated microtubule for the reduced volume $v = 0.7$ and the spontaneous curvature $c_0 = 0$. The first profile, denoted by the dashed line, represents the configuration without a microtubule. The length of the microtubule is $t = 4.9$, $t = 6.0$, $t = 7.0$, $t = 8.0$, $t = 9.0$ for the subsequent configurations from the left to the right.

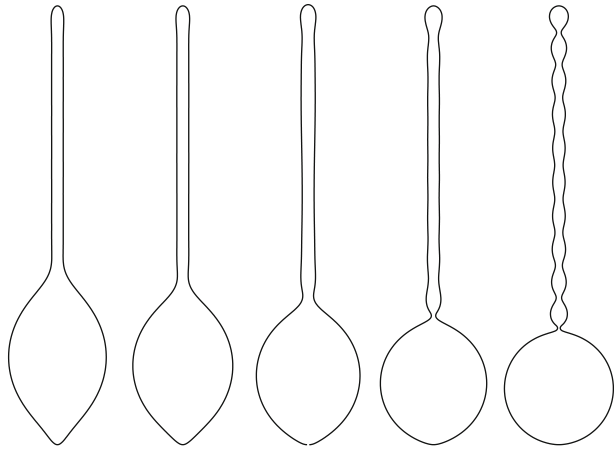

Figure 16 The influence of the spontaneous curvature on the shape of a vesicle containing a microtubule. The spontaneous curvatures for the presented shape profiles are $c_0 = 0$, $c_0 = 3$, $c_0 = 6$, $c_0 = 9$, $c_0 = 12$, starting from the left side. The length of the microtubules is $t = 7.0$, the reduced volume is $v = 0.7$. Three hundred and twenty amplitudes were used in the calculations.

analyzing the shapes of vesicles containing microtubules, one may gain some knowledge about the spontaneous curvature of the membrane.

In Section 3.4, it was demonstrated that for large spontaneous curvature $c_0 = 12$ and the reduced volume $v = 0.7$ there exist many solutions of functional (14) and the solution with the lowest energy is the vesicle composed of a chain of eight small beads attached to a large sphere. When we consider the situation in which the length of the microtubule T is larger than the distance between the poles of the vesicle with eight small beads (without the microtubule inside), it may be possible that in the case where the microtubule is inside the vesicle, a configuration with a number of beads larger than eight becomes the global minimum. Thus, the increase of the length of the microtubule may induce the shape transition. Indeed, it is possible to find more than one local minimum for the same values of the reduced volume v, the spontaneous curvature c_0, and the length of the microtubule t. Different minima correspond to different number of beads.

When the microtubule becomes sufficiently long, the protrusion which is formed of beads begins to change in such a way that the middle part of it becomes cylindrical and the beads are present only at the ends of the protrusion, as shown in Fig. 17. If it were possible to control the growth of the microtubule inside the vesicle with high spontaneous curvature, then it should be possible to change the structure of the protrusion from beads to cylinder and *vice versa*. Alternatively, it can be also done by pulling the

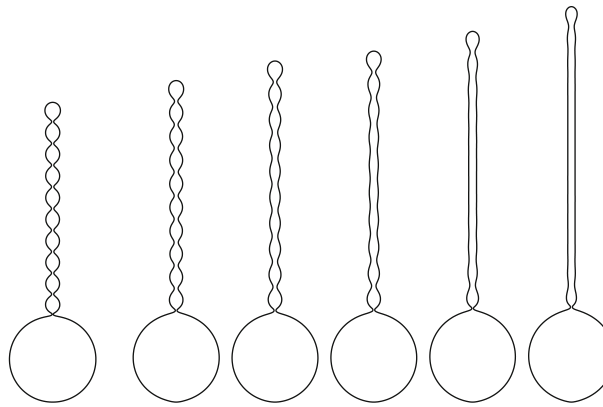

Figure 17 The deformation of the vesicle, composed of 10 small beads by microtubules of different lengths. The spontaneous curvature and the reduced volume are $c_0 = 12$ and $v = 0.7$, respectively. The first profile represents the configuration with 10 beads without the microtubule. In the subsequent profiles the length of the enclosed microtubule is $t = 6.5$, $t = 6.9$, $t = 7.1$, $t = 7.5$, $t = 8.0$.

protrusion. Further increase of the length of the microtubule leads to the cylindrical shape of the protrusion, with no beads at its ends. The radius of the cylindrical protrusion decreases with increasing length of the protrusion.

When the vesicle is stretched, the energy grows linearly with the distance when the protrusion has a structure of connected beads. The points representing energy for configurations with 8, 9, and 10 beads (denoted by diamonds, triangles, and squares) in Fig. 18 lie approximately on the straight lines. When the protrusion is sufficiently stretched, the beads disappear and the protrusion is cylindrical. A few minima with cylindrical protrusion calculated for a few lengths of the microtubule are very well approximated by the parabolic curve denoted by the dashed line in Fig. 18. The energy of stretching (or pulling) of the cylindrical protrusion is proportional to the squared distance. Thus, the vesicle behaves according to Hook's law. The knowledge of the geometry of the protrusion and the force required to pull the protrusion, for example, from an adhering vesicle can be used to examine the adhesion strength of the vesicle to the substrate [57].

During the stretching process of the vesicle with eight small beads, one should observe a series of shape transitions, two discontinuous from eight to nine and from nine to 10 beads, and finally the continuous transition from 10 beads to cylindrical protrusion. The continuous transition is pictured in Fig. 17. It has to be noted that the vesicle with 11 beads has higher curvature energy than the stretched vesicle with 10 beads. The differences in curvature energy between the local minima for configurations with 8, 9, or 10 beads and the encapsulated microtubule are very small, at most of the order

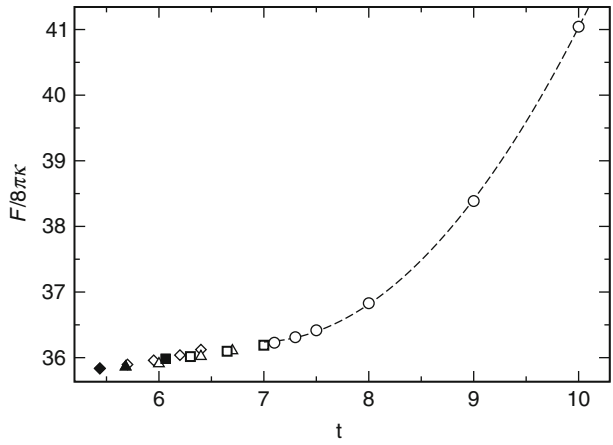

Figure 18 The curvature energy F, as a function of the microtubules length t, for the vesicle with the high spontaneous curvature, $c_0 = 12$ and the reduced volume $v = 0.7$. The solid diamond, triangle, and square represent the minima of functional (14) without the constraint on the tubule length, and with the corresponding profiles shown in Fig. 12, for eight, nine, and 10 small beads, respectively. The open diamonds, triangles, and squares represent the minima of functional (14) for configurations with eight, nine, and 10 small beads, respectively, with the microtubule inside the vesicle. The open circles represent the minima of functional (14) for the configuration with the cylindrical protrusion created by the microtubule. The dashed line is a fit of the parabolic curve to the points denoted by the open circles.

$0.06 \times 8\pi\kappa$. Therefore, one may expect that the shape transformations between them can be easily induced by small stimuli.

4.2. Deformations of Vesicles with Attached Colloidal Particles

The vesicle shape is deformed when a small spherical particle is encapsulated inside or outside the vesicle as shown schematically in Fig. 19. When only small fraction of the surface of the vesicle is deformed, that deformation is propagated over the whole vesicle. It is of particular interest whether the shape is deformed mainly locally in the vicinity of the attached particle or globally. How large are global changes of the shape, induced by binding the vesicle to a small particle and how the deformations resulting from that process propagate over the membrane which forms the vesicle. This process may be important for membrane mediated interactions between the inclusions or adsorbed particles [3].

Let us consider oblate and prolate vesicles with the reduced volume $v = 0.6515$. The radius K of the spherical particle in dimensionless units is $k = 0.1$, where $k = K/R_0$. The amount of the membrane which is bound to

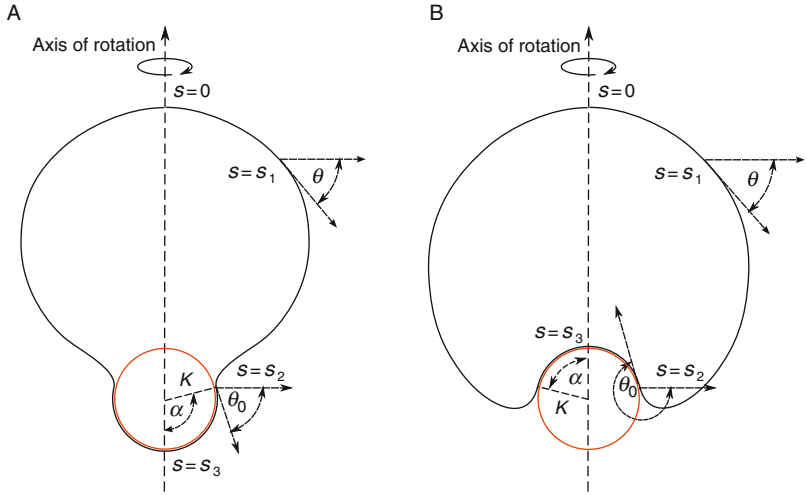

Figure 19 Schematic illustration of a spherical particle encapsulated inside and outside a vesicle. α is the wrapping angle, K the radius of the particle, θ the angle tangent to the profile, s the arc length, θ_0 the angle tangent to the profile at the point where the membrane touches the sphere. The spherical particle may be (A) inside or (B) outside the vesicle.

the colloidal particle is controlled by the wrapping angle α [58]. At $\alpha = 0$, the shape of the vesicle is not influenced by the spherical particle which is inside the vesicle since the particle is small enough to touch the surface of the vesicle only at one point, at the pole of the vesicle. The mean curvatures on the vesicle surface are smaller than the mean curvature of the spherical particle ($1/K$). Small deviations of the radius k from the value $k = 0.1$ do not change qualitatively the behavior of the studied system as long as the particle is significantly smaller than the vesicle itself.

Figures 20 and 21 show a few sequences of shape profiles for a few wrapping angles α for oblate, prolate, and stomatocyte vesicles. From the shape profiles, it can be inferred that the vesicles are deformed mainly locally, near the attached particles. The shape of prolate vesicles is deformed less than the shape of oblate vesicles. The global change of the shape for prolate and stomatocyte vesicles is less pronounced than for the oblate vesicles upon wrapping a spherical particle, as can be seen in Fig. 21.

At $\alpha = 0$ and at the reduced volume $v = 0.6515$, the bending energy for prolate and oblate vesicles is approximately the same. When the wrapping angle is significantly smaller than π, the prolate vesicle is the one with the lower energy. Thus, even small attraction of the membrane to the surface of a particle located inside the vesicle stabilizes particular (prolate) geometry. The energy of the stomatocyte vesicles with the spherical particle attached

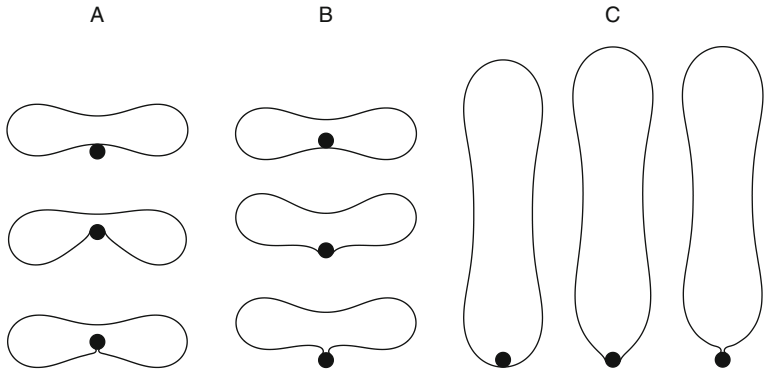

Figure 20 The profile of vesicles with the reduced volume $v = 0.6515$, obtained by minimization of the bending energy for different wrapping angle α. The radius of the attached spherical particle, shown as the black circle, is $k = 0.1$. The wrapping angle α in degrees for the profiles presented on the figures is appropriately: (A) $\alpha = 0.0$, 80.21, 160.42, (B) $\alpha = 0.09$, 63.12, 146.30, (C) $\alpha = 0.09$, 74.58, 154.79. The profiles are shown at the same scale.

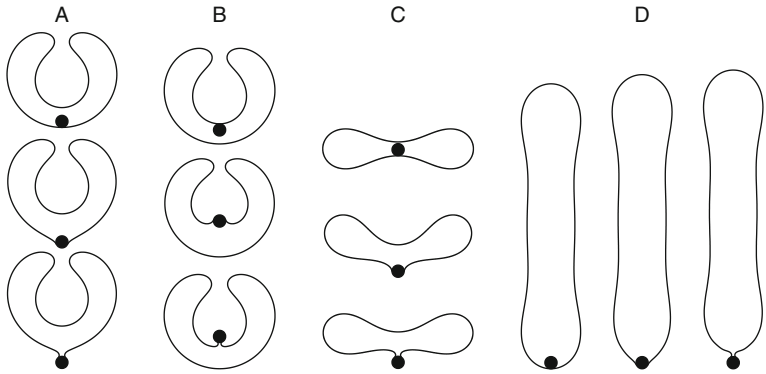

Figure 21 The profile of vesicle with the reduced volume $v = 0.5915$, obtained by minimization of the bending energy for different wrapping angle α. The radius of the attached spherical particle, shown as the black circle, is $k = 0.1$. The wrapping angle α in degrees for the profiles presented on the figures is appropriately: (A) $\alpha = 0.09$, 63.12, 140.47, (B) $\alpha = 0.09$, 68.85, 140.47, (C) $\alpha = 0.09$, 86.03, 143.33, (D) $\alpha = 0.09$, 63.12, 151.92. The profiles are shown at the same scale.

to the south pole (Fig. 21A) is the lowest among the vesicles of different geometries shown in Fig. 21.

For and empty vesicle with the reduced volume $v = 0.5915$, the oblate vesicle have lower energy then the prolate vesicle. However, for the complex colloid-vesicle for $\alpha > 0$, prolate vesicles become stable at some nonzero value of the wrapping angle α. If the difference of the bending energy for the wrapping angle $\alpha = 0$ is small, prolate vesicles may become

stable at some value α. Thus, binding the membrane to a colloidal particle may be exploited to switch the shape of the vesicle from prolate to oblate or *vice versa*.

For the reduced volume $v = 0.5915$ oblate vesicles have bending energy approximately the same as stomatocyte vesicles. From the analysis of the shapes presented on Fig. 21A and C it seems that the transformation from the oblate vesicle which has higher energy to the stomatocyte vesicle which has lower energy is probable. However, the energy barrier between stomatocyte and oblate vesicles is still significant for the configurations with similar shapes.

Prolate and oblate vesicles are symmetric with respect to the equator of a vesicle. Stomatocyte vesicles do not have up and down symmetry. Thus, attaching a spherical particle inside a vesicle at the north pole and at the south pole of the vesicle (see Fig. 21A and B) will differ, unlike in the case of oblate and prolate vesicles. The energy and the shape of the stomatocyte vesicles with a spherical particle of radius $k = 0.1$ attached at the south and north pole at the wrapping angle $\alpha = 0$ is exactly the same, since at the touching point the curvature of the spherical particle is higher than the curvature of the membrane. In the limit $\alpha = \pi$, the shapes should converge to the same configuration, but in between $(0 < \alpha < \pi)$ the evolution is completely different.

5. Deformation of Multicomponent Membranes

Multicomponent membranes compared to one component membranes have extra degrees of freedom associated with the distribution of components within the membrane. The distribution of membrane components influences the shape of the membrane [26, 59–68], but it is also possible that the shape of the membrane may influence the distribution of the components [64, 69–73]. Such mutual dependence of the membrane shape and distribution of components may lead to many interesting physical phenomena which are important for functioning biological systems. One may speculate that the change of the membrane shape may lead to the separation or mixing of membrane components due to minimization of the curvature energy. The components which are separated in a flat membrane may be mixed in a curved membrane which forms the vesicle (and *vice versa*).

5.1. Phase Separation Induced by the Shape of the Vesicle

In the case where the geometry of a vesicle influences the distribution of the components, the driving force for the separation is compatibility of the local curvature of a vesicle with the spontaneous curvatures of the components.

The energy of the multicomponent membrane can be described by the modified functional (14). The components are characterized by the spontaneous curvatures $\mathcal{C}_0^{\mathrm{A}}$ and $\mathcal{C}_0^{\mathrm{B}}$. The model may also describe the situation in which some molecules are attached to the membrane and form coherent regions. In that case, the attached molecules impose the spontaneous curvature on the membrane [34, 35, 74, 75]. It is assumed for simplicity that the bending rigidity and the Gaussian rigidity are the same for both components: $\bar{\kappa} = \bar{\kappa}^{\mathrm{A}} = \bar{\kappa}^{\mathrm{B}}$ and $\kappa = \kappa^{\mathrm{A}} = \kappa^{\mathrm{B}}$. In the limit of large bending rigidity, and low temperature the contribution to the free energy associated with the entropy of mixing is small compared to the curvature energy and is neglected in the calculations. The membrane shape may influence the distribution of the components in the membrane, which can lead to their segregation. On the other hand, the distribution of the components determines the membrane shape. These two processes are coupled in some complex way. In the simplest case, the spontaneous curvature is coupled to the concentration $\phi : \mathcal{C}_0(s) = \phi(s)(\mathcal{C}_0^{\mathrm{A}} - \mathcal{C}_0^{\mathrm{B}}) + \mathcal{C}_0^{\mathrm{B}}$, where $\mathcal{C}_0^{\mathrm{A}}$ and $\mathcal{C}_0^{\mathrm{B}}$ are the spontaneous curvatures of the membrane occupied by the first and the second component, respectively. Thus, the bending energy functional (14) depends on two functions which describe the concentration profile ϕ and the shape of the vesicle θ [73]. The spontaneous curvatures of the membrane components are used as material parameters. By varying the spontaneous curvature we can model the properties of the components which form the membrane.

We consider the situation where the composition (ϕ_{tot}) of the membrane is constant. The reduced volume $v = 0.655$ is chosen in such a way to obtain, for one component membranes with the spontaneous curvature equal 0, solutions with different geometries (oblate, prolate). The geometry of the vesicle influences the distribution of the components due to the coupling of the spontaneous curvature with the concentration profile. It is easy to distinguish in oblate vesicles two regions, where the local mean curvature is small and where the local mean curvature is large. In the vicinity of the poles, the local mean curvature is small while in the vicinity of the equator, the local mean curvature is much larger. Thus, to minimize the bending energy, the components with larger spontaneous curvature will occupy the region of the vesicle at the equator, and the components with smaller spontaneous curvature will occupy the poles of the vesicle. We consider vesicles that have rotational symmetry and the mirror symmetry with respect to the equator of the vesicle. Thus, the domains are distributed symmetrically in such a way that the domains of one component are located at the poles of the vesicle and are separated by the domain of the other component located along the equator.

Figure 22 shows the vesicle shapes for the total concentration $\phi_{\mathrm{tot}} = 0.50$ and a few values of the spontaneous curvature ($c_0^{\mathrm{A}} > 0$) for component A. The spontaneous curvature ($c_0^{\mathrm{B}} = 0$) for component B is always zero.

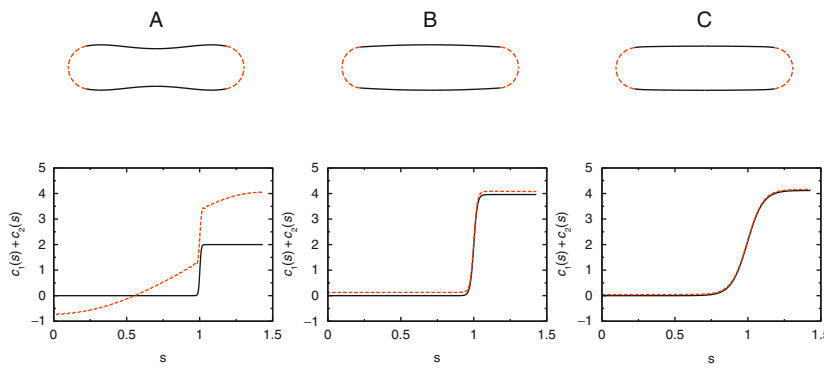

Figure 22 The shape profiles and corresponding local curvature and spontaneous curvature profiles for oblate vesicles with the reduced volume $v = 0.655$ and a few values of the spontaneous curvature c_0^A are presented in the upper row. The dashed lines and the solid lines represent the region of the vesicle occupied by the components with positive spontaneous curvature c_0^A, and $c_0^B = 0.0$, respectively. The lines meet at the inflection point of the spontaneous curvature profile $c_0(s)$. The total concentration $\phi_{tot} = 0.5$. The spontaneous curvature is, respectively: (A) $c_0^A = 0.0$, (B) $c_0^A = 3.96$, (C) $c_0^A = 4.12$. The correspondent spontaneous curvature profiles $c_0(s)$ (solid lines) and the local curvature $c_1(s) + c_2(s)$ (dashed lines) are shown in the lower row. The profiles presented here start at the pole of the vesicles $s = 0$ and end the equator of the vesicles $s = L_s/2$.

The vesicle shape changes smoothly with the change of the spontaneous curvature c_0^A. The first profile is chosen for small values of the spontaneous curvature where the interface width is narrow (Fig. 22A). The other two profiles show the vesicles just before the rapid change of interface width (Fig. 22B) and just after the rapid change of the interface width (Fig. 22C). The second and the third profiles are very similar, despite large change of the interface width. Thus, the change of the interface width is not noticeably reflected in the shape of the vesicle. The bending energy is the lowest when the interface width is wide for the membranes built of components characterized by large difference in the spontaneous curvature. The jump of the spontaneous curvature at a very sharp interface may be unfavorable for minimizing the bending energy, when the difference of the spontaneous curvatures is large. The bending energy may be minimized in such a case by widening the interface between the domains.

The lower row of Fig. 22 shows the sum of the principal curvatures $c_1(s) + c_2(s)$ and the local spontaneous curvature $c_0(s)$ which is a function of the concentration profile $\phi(s)$. The curves shown by the dashed lines represent the functions which minimize the curvature energy functional [73]. The concentration profiles presented in Fig. 22 describe two domains of different spontaneous curvatures separated by an interface. The functions are not arbitrary, one should remember about the constraints resulting from

the physics of the problem, imposed on the shape of those function. It is interesting to note that the optimal value of the bending energy is obtained when the curve which describes the local curvature is parallel to the curve which describes the spontaneous curvature profile and is the lowest when they overlap.

The overall behavior remains similar when the geometry of the vesicles is changed from oblate to prolate. However, for prolate vesicles, the distribution of components $\phi(s)$ and therefore the distribution of the spontaneous curvatures $c_0(s)$ cannot be so easily matched to the local curvatures, because of the constraints imposed on the shape of the vesicle[73].

5.2. Deformation of Membranes Caused by Phase Separation of Their Components

The components in multicomponent membranes may phase separate, for example, when the temperature is changed. The separated components may form domains of different shapes [70, 71, 76–80]. The shape of the domains depends on the concentration of the components and their properties. Usually, one observes stripe-like and circular domains. The phase separation of two component membrane under week tension has been studied within the framework of the spontaneous curvature model [66]. The component was characterized by different spontaneous curvature. It has been predicted that for small concentration of component A or B the domains with circular shape are preferred, as shown in Fig. 23A and C. Stripe-like domains, Fig. 23B, are the most stable for comparable concentration of components and for not large ratio of the spontaneous curvatures. It has been observed experimentally that by changing the tension of the membrane may lead to phase transition between circular and stripe-like domains [79]. If the ratio of the spontaneous curvatures is large, the phases formed of circular domains are dominant. Increasing the concentration of one component leads to budding, as shown in Fig. 24. It is interesting to note that not only the buds with one bead are stable but also the buds with more than one bead, see Fig. 24D

Figure 23 Circular and stripe-like domains. The ratio of the spontaneous curvatures is $c_0^{\mathrm{A}}/c_0^{\mathrm{B}} = -1$. The concentration of the components in the domains is (A) 0.1, (B) 0.4, (C) 0.8. The dark grey and light grey mark the membrane area occupied by component A and B.

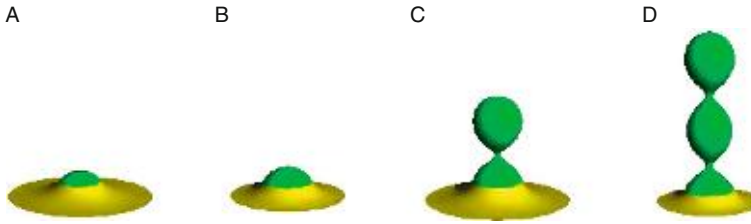

Figure 24 The circular domains. The ratio of the spontaneous curvatures is $c_0^A/c_0^B = -3$. The concentration of the components in the domains is (A) 0.1, (B) 0.22, (C) 0.42, (D) 0.72. The dark grey and light grey mark the membrane area occupied by component A and B.

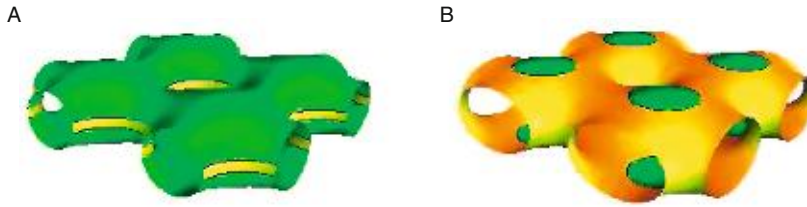

Figure 25 Phase separation in membranes of nontrivial topology. The ratio of the spontaneous curvatures is $c_0^A/c_0^B = 3$. The dark grey and light grey mark the membrane area occupied by component A and B. The concentration of components is, respectively: (A) $\phi = 0.93$, (B) $\phi = 0.11$.

The process of the phase separation in membranes of nontrivial topology can be quite complex since the separated components can form not only circular domain but also ring-like domains as shown in Fig. 25. Thus, the component which prefer high curvature regions may form the ring-like domains and the other components may occupy more flat part of the membrane [64, 65]. It is interesting to note that the change of the concentration and thus the domain size results in the change of the membrane shape. One can vary the size of the passage radius by changing the size of the domains.

5.3. Deformation Induced by Diffusion of Macromolecules

Proteins or polymers [32, 34–36, 81, 82] can deform in their neighborhood the shape of the membrane. When the macromolecules diffuse on the lipid vesicle, its shape is changed in time. The diffusion of the macromolecules influences the shape of the vesicle and *vice versa*. Coupling the distribution of the membrane components with the shape of the vesicle is an important and interesting phenomenon present in biological systems [61, 64–67, 74, 75,

83–86]. The macromolecules can influence the shape of the vesicles, but also the shape may lead to segregation of the macromolecules of different species [69, 72, 73, 87]. The change of the vesicle shape can be induced by the macromolecules which diffuse on the surface of lipid vesicles. Such phenomena have been observed in experiments [35] where the polymers injected near the lipid vesicle were anchored to the membrane causing its deformation. The polymer which is attached to the membrane can increase its configurational entropy if the membrane is bent away from the polymer. Such mechanism leads to inducing the spontaneous curvature [32]. Not only polymers but also large macromolecules attached to the membrane may induce the spontaneous curvature. It is challenging to model a general phenomenon of diffusion of macromolecules on a fluid membrane and in particular examining how diffusing macromolecules can influence the shape of the membrane and the shape of the membrane can influence the process of diffusion [26, 82].

Here we present model calculations where, the macromolecules may change the shape of the surface when the distribution of the macromolecules is altered during the diffusion process. The macromolecules continue to diffuse on a membrane with a changed shape. Since the diffusion of the macromolecules on a lipid membrane is modeled by solving the diffusion equation on a membrane surface, not only the shape of the membrane is adjusted to the distribution of the molecules, but also the diffusion is modified by continuous change of the membrane shape. Coupling of the concentration of membrane components with its shape may be used in biological systems to modify behavior of biological cells. For example, by slowing down the diffusion process or forming long lasting concentration gradients. In the mathematical model, the shape of the vesicles is governed by the bending energy and the diffusion is described by the diffusion equation. The spontaneous curvature is coupled to the concentration of the macromolecules $\phi(a)$:

$$\mathcal{C}_0(a) = \mathcal{C}_0\phi(a), \tag{26}$$

where $\mathcal{C}_0$ is the spontaneous curvature induced by the macromolecules, a is the surface area of the vesicle. Such concentration dependent spontaneous curvature is used in the expression for the bending energy in Eq. (19). In the mesoscopic description, the properties of the macromolecules are reflected in the value of the spontaneous curvature. In the mathematical model used in the calculations [26], the detailed knowledge of the microscopic structure of the macromolecules and the bilayer is not necessary. In particular, it is irrelevant whether the macromolecules are embedded in the bilayer or they are attached to the one side of the bilayer. In the model, it is only considered how strong is the influence of the macromolecules on the spontaneous curvature. It is assumed that the evolution of the concentration profile $\phi(a, \tau)$ in time is governed by the diffusion equation:

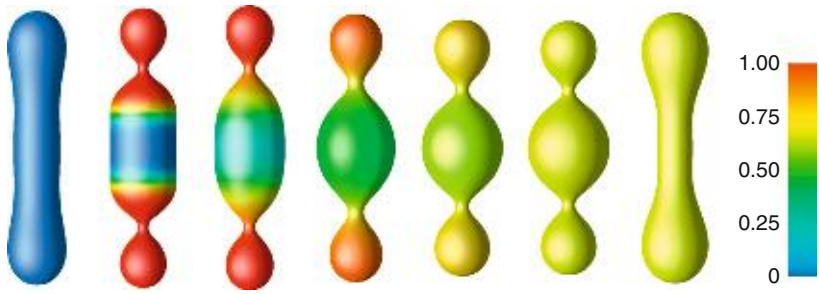

Figure 26 The change in time of the vesicle shape caused by diffusing macromolecules. The reduced volume of the vesicle is $v = 0.6$. The spontaneous curvature induced by the macromolecules is $c_0 = 4.0$. The total concentration of macromolecules is $\phi_{\text{tot}}^{(1)} = 0.682$. The shades of grey reflect the value of the concentration of the macromolecules on the vesicles according to the grayscale map. The first vesicle is the vesicle without the macromolecules on its surface. Next vesicles represents the shapes after 1, 11, 51, 200 time steps for prolate vesicles. The last two vesicle are the vesicle with uniform distribution of the macromolecules, where the first is metastable and the second is the stable one.

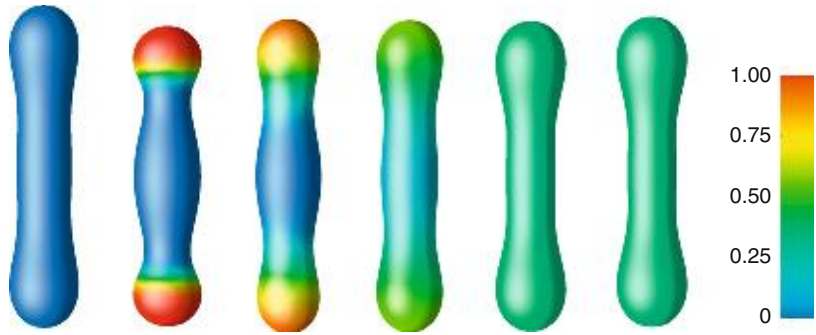

Figure 27 The change in time of the vesicle shape caused by diffusing macromolecules. The reduced volume of the vesicle is $v = 0.6$. The spontaneous curvature induced by the macromolecules is $c_0 = 4.0$. The total concentration of macromolecules is $\phi_{\text{tot}}^{(1)} = 0.363$. The shades of grey reflect the value of the concentration of the macromolecules on the vesicles according to the grayscale map. The first vesicle is the vesicle without the macromolecules on its surface. Next vesicles represents the shapes after 1, 11, 51, 200 time steps for prolate vesicles. The last vesicle is the vesicle with uniform distribution of the macromolecules.

$$\frac{\partial}{\partial \tau}\phi = D\nabla_s^2\phi, \tag{27}$$

where ∇_s^2 is surface Laplacian operator, D is the surface diffusion coefficient, and τ is time.

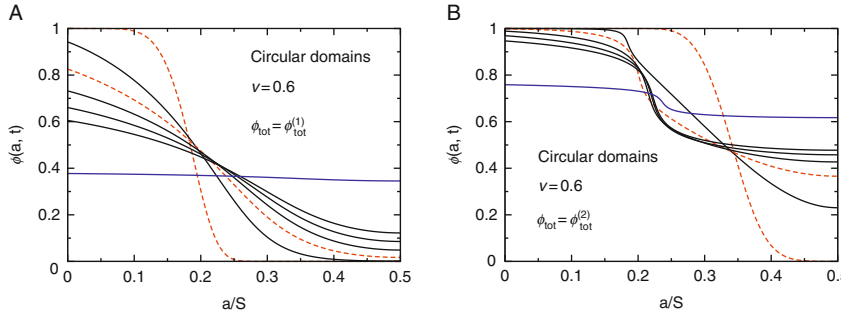

Figure 28 The distribution of the macromolecules $\phi(t, a)$ after 1, 11, 21, 31, 41, 51, 200 time steps for prolate vesicles. The time step $dt = 0.01$. The reduced volume of the vesicle is $v = 0.6$. The spontaneous curvature induced by the macromolecules is $c_0 = 4.0$. The total concentration of macromolecules is $\phi^{(1)}_{tot} = 0.363$—(A), and $\phi^{(2)}_{tot} = 0.682$—(B), respectively. S is the total surface area of the vesicle.

Figures 26 and 27 show the shapes of the vesicles calculated for different distribution of the macromolecules on the surface of the vesicles. The value of the concentration of the macromolecules is reflected on the surface of the vesicle by its color calculated according to the color maps included in the figures. The evolution of the concentration profiles is also presented in Fig. 28 on plots of the concentration $\phi(a)$ as a function of the surface area of the vesicle a. From Figs. 26 and 27, we see that the macromolecules are initially distributed on the poles of the vesicle. When they diffuse on the surface of the vesicle, they cause the deformation of its surface. When the surface is deformed, the diffusion process is altered because the macromolecules have to diffuse on the vesicle with a new geometry. The narrow necks can slow down the diffusion process, because smaller number of macromolecules can diffuse over the surface of the necks with small radius. The small necks can lead to the concentration gradients of the macromolecules on the part of the vesicles separated by the narrow necks. This can be easily seen by analyzing the concentration profiles on Fig. 28B, It is interesting to note that the diffusion process may lead to obtain the vesicles in a metastable state as presented in Fig. 26.

6. Summary

We have presented several possible shape transformations of vesicles of simple and complex topology built of amphiphilic molecules. All the calculations were performed within the framework of the spontaneous curvature model. In a few cases, we compared the theoretical calculations with the experimental results. We hope that the model calculations presented here when combined with the experimental results will help in better

understanding complex phenomena encountered in investigations of lipid membranes and liposomes.

REFERENCES

[1] A. Boulbitch, Enforced unbinding of a bead adhering to a biomembrane by generic forces, Europhys. Lett. 59 (2002) 910–915.
[2] C. Dietrich, M. Angelova, B. Pouligny, Adhesion of latex spheres to giant phospholipid vesicles: Statics and dynamics, J. Phys. II France 7 (1997) 1651–1682.
[3] I. Koltover, J.O. Rädler, C.R. Safinya, Membrane mediated attraction and ordered aggregation of colloidal particles bound to giant phospholipid vesicles, Phys. Rev. Lett. 82 (1999) 1991–1994.
[4] R. Lipowsky, H.-G. Döbereiner, Vesicles in contact with nanoparticles and colloids, Europhys. Lett. 43 (1998) 219–225.
[5] M. Deserno, W.M. Gelbart, Adhesion and wrapping in colloid-vesicle complexes, J. Phys. Chem. B 106 (2002) 5543–5552.
[6] M. Deserno, T. Bickel, Wrapping of a spherical colloid by a fluid membrane, Europhys. Lett. 62 (2003) 767–773.
[7] M. Deserno, Elastic deformation of a fluid membrane upon colloid binding, Phys. Rev. E 69 (2004) 031903.
[8] S. Das, Q. Du, Adhesion of vesicles to curved substrates, Phys. Rev. E 77(1) (2008) 011907.
[9] H. Noguchi, M. Takasu, Adhesion of nanoparticles to vesicles: A Brownian dynamics simulation, Biophys. J. 83(1) (2002) 299–308.
[10] K.A. Smith, D. Jasnow, A.C. Balazs, Designing synthetic vesicles that engulf nanoscopic particles, J. Chem. Phys. 127(8) (2007) 084703.
[11] U. Seifert, R. Lipowsky, Adhesion of vesicles, Phys. Rev. A 42 (1990) 4768–4771.
[12] H. Hotani, H. Miyamoto, Dynamic features of microtubules as visualized by dark-field microscopy, Adv. Biophys. 26 (1990) 135.
[13] D. Kuchnir Fygenson, J.F. Marko, A. Libchaber, Mechanics of micotubule-based membrane extension, Phys. Rev. Lett. 79 (1997) 4497–4500.
[14] V. Emsellem, O. Cardoso, P. Tabeling, Vesicle deformation by microtubules: A phase diagram, Phys. Rev. E 58 (1998) 4807–4810.
[15] R. Morikawa, Y. Saito, H. Hyuga, Monte carlo study of a vesicle morphology caused by microtubule assembly, J. Phys. Soc. Jpn. 68 (1999) 760–1768.
[16] H. Hotani, F. Nomura, Y. Suzuki, Giant liposomes: From membrane dynamics to cell morphogenesis, Curr. Opin. Colloid Interface Sci. 4 (1999) 358–368.
[17] A. Shibuya, Y. Saito, H. Hyuga, Morphology of axisymmetric vesicles with encapsulated filaments and impurities, J. Phys. Soc. Jpn. 71(7) (2002) 1780–1788.
[18] H. Hotani, T. Inaba, F. Nomura, S. Takeda, K. Takiguchi, T.J. Itoh, T. Umeda, A. Ishijima, Mechanical analyses of morphological and topological transformation of liposomes, Biosystems 71(1–2) (2003) 93–100.
[19] T.G. D'Onofrio, A. Hatzor, A.E. Counterman, J.J. Heetderks, M.J. Sandel, P.S. Weiss, Controlling and measuring the independence of local properties in biomembranes/publications, Langmuir 19 (2003) 1618–1623.
[20] A. Ciach, W.T. Góźdź, Nonelectrolyte solutions exhibiting structure on the nanoscale, Annu. Rep. Prog. Chem. Sect. C 97 (2001) 269314.
[21] P.B. Canham, The minimum energy of bending as a possible explanation of the biconcave shape of the human red blood cell, J. Theor. Biol. 26 (1970) 61–81.

[22] W. Helfrich, Elastic properties of lipid bilayers: Theory and possible experiments, Z. Naturforsch. 28c (1973) 693–703.
[23] E. Evans, Bending resistance and chemically induced moments in membrane bilayers, Biophys. J. 14 (1974) 923–931.
[24] J. Stoker, Differential Geometry, Vol. XX of Pure and Applied Mathematics, (1969) Wiley, New York.
[25] O.-Y. Zhong-can, W. Helfrich, Bending energy of vesicle membranes: General expressions for the first, second, and third variation of the shape energy and applications to spheres and cylinders, Phys. Rev. A 39(10) (1989) 5280–5288.
[26] W.T. Góźdź, Diffusion of macromolecules on lipid vesicles, Langmuir 24(21) (2008) 12458–12468.
[27] L. Miao, B. Fourcade, M. Rao, M. Wortis, Equilibrium budding and vesiculation in the curvature model of fluid lipid vesicles, Phys. Rev. A 43 (1991) 6843–6856.
[28] U. Seifert, K. Berndl, R. Lipowsky, Shape transformations of vesicles: Phase diagram for spontaneous-curvature and bilayer-coupling models, Phys. Rev. A 44 (1991) 1182–1202.
[29] C.K. Haluska, W.T. Góźdź, H.-G. Doebereiner, S. Foerster, G. Gompper, Giant hexagonal superstructures in diblock-copolymer membranes, Phys. Rev. Lett. 89 (2002) 238302-1-4.
[30] A.A. Reinecke, H.-G. Doebereiner, Slow relaxation dynamics of tubular polymersomes after thermal quench, Langmuir 19 (2003) 605–608.
[31] W.T. Góźdź, Spontaneous curvature induced shape transformations of tubular polymersomes, Langmuir 20 (2004) 7385–7391.
[32] C. Hiergeist, R. Lipowsky, Elastic properties of polymer-decorated membranes, J. Phys. II France 6 (1996) 1465–1481.
[33] R. Lipowsky, H.-G. Dobereiner, C. Hiergeist, V. Indrani, Membrane curvature induced by polymers and colloids, Physica A 249 (1998) 536–543.
[34] I. Tsafrir, D. Sagi, T. Arzi, M.-A. Guedeau-Boudeville, V. Frette, D. Kandel, J. Stavans, Pearling instabilities of membrane tubes with anchored polymers, Phys. Rev. Lett. 86 (2001) 1138–1141.
[35] I. Tsafrir, Y. Caspi, M.-A. Guedeau-Boudeville, T. Azri, J. Stavans, Budding and tubulation in highly oblate vesicles by anchored amphiphilic molecules, Phys. Rev. Lett. 91(2003) 138102-1-4.
[36] A. Iglič, T. Slivnik, V. Kralj-Iglič, Elastic properties of biological membranes influenced by attached proteins, J. Biomech. 40 (2007) 24922500.
[37] H.J. Deuling, W. Helfrich, Red blood cell shapes as explained on the basis of curvature elasticity, Biophys. J. 16(8) (1976) 861–868.
[38] H. Deuling, W. Helfrich, The curvature elasticity of fluid membranes: A catalogue of vesicle shapes, J. Phys. 37(11) (1976) 1335–1345.
[39] W. Harbich, H. Deuling, W. Helfrich, Optical observation of rotationally symmetric lecithin vesicle shapes, J. Phys. 38(6) (1977) 727–729.
[40] R. Morikawa, Y. Saito, H. Hyuga, Monte Carlo study of an axially symmetric vesicle, J. Phys. Soc. Jpn. 66 (1997) 2513–2520.
[41] W. Wintz, H.-G. Döbereiner, U. Seifert, Starfish vesicles, Europhys. Lett. 33(5) (1996) 403–408.
[42] Y. Jie, L. Quanhui, L. Jixing, O.-Y. Zhong-Can, Numerical observation of nonaxisymmetric vesicles in fluid membranes, Phys. Rev. E 58(4) (1998) 4730–4736.
[43] Y. Zhang, X. Zhou, J. Zhou, Z.-c. Ou-Yang, Triconcave solution to the helfrich variation problem for the shape of lipid bilayer vesicles is found by, ''Surface Evolver'' Int. J. Mod. Phys. B 16 (2002) 511–517.
[44] X. Michalet, Equilibrium shape degeneracy in starfish vesicles, Phys. Rev. E 76(2) (2007) 021914.

[45] M. Mutz, D. Bensimon, Observation of toroidal vesicles, Phys. Rev. A 43(8) (1991) 4525–4527.
[46] F. Jülicher, U. Seifert, R. Lipowsky, Conformal degeneracy and conformal diffusion of vesicles, Phys. Rev. Lett. 71(3) (1993) 452–455.
[47] F. Jülicher, The morphology of vesicles of higher topological genus: Conformal degeneracy and conformal modes, J. Phys. II 6(12) (1996) 1797–1824.
[48] R. Bar-Ziv, E. Moses, Instability and "pearling" states produced in tubular membranes by competition of curvature and tension, Phys. Rev. Lett. 73 (1994) 1392–1395.
[49] R. Bar-Ziv, E. Moses, P. Nelson, Dynamic excitations in membranes induced by optical tweezers, Biophys. J. 75 (1998) 294–320.
[50] P. Nelson, T. Powers, U. Seifert, Dynamical theory of the pearling instability in cylindrical vesicles, Phys. Rev. Lett. 74 (1995) 3384–3387.
[51] E. Brückner, P. Sonntag, H. Rehage, Light-induced shape transitions of unilamellar vesicles, Langmuir 17(8) (2001) 2308–2311.
[52] T. Hamada, Y. Sato, K. Yoshikawa, T. Nagasaki, Reversible photoswitching in a cell-sized vesicle, Langmuir 21(17) (2005) 7626–7628.
[53] W.T. Góźdź, Influence of spontaneous curvature and microtubules on the conformations of lipid vesicles, J. Phys. Chem. B 109 (2005) 21145–21149.
[54] W.T. Góźdź, Shape transformations of vesicles built of amphiphilic molecules, Biophys. Rev. Lett. 3 (2008) 1–24.
[55] B. Božič, G. Gomišček, V. Kralj-Iglič, S. Svetina, B. Žekš, Shapes of phospholipid vesicles with beadlike protrusions, Eur. Biophys. J. 31 (2002) 487–496.
[56] V. Kralj-Iglič, A. Iglič, G. Gomišček, F. Sevšek, V. Arrigler, H. Hägerstrand, Microtubes and nanotubes of a phospholipid bilayer membrane, J. Phys. A: Math. Gen. 35 (2002) 15331549.
[57] A.-S. Smith, E. Sackmann, U. Seifert, Pulling tethers from adhered vesicles, Phys. Rev. Lett. 92(20) (2004) 208101.
[58] W.T. Góźdź, Deformations of lipid vesicles induced by attached spherical particles, Langmuir 23 (2007) 5665–5669.
[59] D. Andelman, T. Kawakatsu, K. Kawasaki, Equilibrium shape of two-component unilamellar membranes and vesicles, Europhys. Lett. 19 (1992) 57–62.
[60] F. Jülicher, R. Lipowsky, Domain-induced budding of vesicles, Phys. Rev. Lett. 70 (19) (1993) 2964–2967.
[61] T. Taniguchi, K. Kyozi Kawasaki, D. Andelman, T. Kawakatsu, Phase transitions and shapes of two component membranes and vesicles II: Weak segregation limit, J. Phys. II France 4 (1994) 1333–1362.
[62] F. Jülicher, R. Lipowsky, Shape transformations of vesicles with intramembrane domains, Phys. Rev. E 53(3) (1996) 2670–2683.
[63] P.B. Sunil Kumar, G. Gompper, R. Lipowsky, Budding dynamics of multicomponent membranes, Phys. Rev. Lett. 86(17) (2001) 3911–3914.
[64] W.T. Góźdź, G. Gompper, Composition-driven shape transformation of membranes of complex topology, Phys. Rev. Lett. 80 (1998) 4213–4216.
[65] W.T. Góźdź, G. Gompper, Composition-driven shape transformation of membranes of complex topology, Phys. Rev. E 59 (1999) 4305–4316.
[66] W.T. Góźdź, G. Gompper, Shape transformations of two component membranes under weak tension, Europhys. Lett. 55 (2001) 587–593.
[67] W.T. Góźdź, G. Gompper, Phase behavior of two-component membranes, Coll. Surf. A: Physicochem. Eng. Aspects 208 (2002) 241–251.
[68] J. Stavans, Instabilities of membranes with anchored polymers, Physica A 306 (2002) 368.
[69] U. Seifert, Curvature-induced lateral phase segregation in two-component vesicles, Phys. Rev. Lett. 70 (1993) 1335–1338.

[70] T. Baumgart, S.T. Hess, W.W. Webb, Imaging coexisting fluid domains in biomembrane models coupling curvature and line tension, Nature 425 (2003) 821–824.
[71] T. Baumgart, S. Das, W.W. Webb, J.T. Jenkins, Membrane elasticity in giant vesicles with fluid phase coexistence, Biophys. J. 89 (2005) 1067–1080.
[72] A. Roux, D. Cuvelier, P. Nassoy, J. Prost, P. Bassereau, B. Goud, Role of curvature and phase transition in lipid sorting and ssion of membrane tubules, EMBO J. 24 (2005) 1537–1545.
[73] W.T. Góźdź, The interface width of separated two-component lipid membranes, J. Phys. Chem. B 110 (2006) 21981–21986.
[74] H.T. McMahon, J.L. Gallop, Membrane curvature and mechanisms of dynamic cell membrane remodelling, Nature 438 (2005) 590–596.
[75] J. Zimmerberg, M.M. Kozlov, How proteins produce cellular membrane curvature, Nat. Rev. Mol. Cell. Biol. 7 (2006) 9–19.
[76] S.L. Veatch, S.L. Keller, Organization in lipid membranes containing cholesterol, Phys. Rev. Lett. 89 (2002) 268101.
[77] S.L. Veatch, S.L. Keller, Separation of liquid phases in giant vesicles of ternary mixtures of phospholipids and cholesterol, Biophys. J. 85 (2003) 3074–3083.
[78] S.L. Veatch, I.V. Polozov, K. Gawrisch, S.L. Keller, Liquid domains in vesicles investigated by NMR and fluorescence microscopy, Biophys. J. 86 (2004) 2910–2922.
[79] S. Rozovsky, Y. Kaizuka, J.T. Groves, Formation and spatio-temporal evolution of periodic structures in lipid bilayers, J. Am. Chem. Soc. 127(1) (2005) 36–37.
[80] S.L. Veatch, K. Gawrisch, S.L. Keller, Closed-loop miscibility gap and quantitative tie-lines in ternary membranes containing diphytanoyl PC, Biophys. J. 90(12) (2006) 4428–4436.
[81] F. Campelo, A. Hernández-Machado, Model for curvature-driven pearling instability in membranes, Phys. Rev. Lett. 99 (2007) 08810.
[82] F. Campelo, A. Hernández-Machado, Polymer-induced tubulation in lipid vesicles, Phys. Rev. Lett. 100 (2008) 158103.
[83] S. Leibler, Curvature instability in membranes, J. Phys. France 47 (1986) 507–516.
[84] S. Leibler, D. Andelman, Ordered and curved meso-structures in membranes and amphiphilic films, J. Phys. France 48 (1987) 2013–2018.
[85] T. Kawakatsu, D. Andelman, K. Kyozi Kawasaki, T. Taniguchi, Phase transitions and shapes of two component membranes and vesicles I: Strong segregation limit, J. Phys. II France 3 (1993) 971–997.
[86] T. Taniguchi, Shape deformation and phase deformation dynamics of two-component vesicles, Phys. Rev. Lett. 76 (1996) 4444–4447.
[87] A. Iglič, H. Hägerstrand, P. Veranič, A. Plemenitaš, V. Kralj-Iglič, Curvature-induced accumulation of anisotropic membrane components and raft formation in cylindrical membrane protrusions, J. Theor. Biol. 240 (2006) 368–373.

Subject Index